BIO-ALGORITHMS AND MED-SYSTEMS

Vol. 6, No. 12
2010

JOURNAL EDITED BY JAGIELLONIAN UNIVERSITY - MEDICAL COLLEGE - KRAKOW – POLAND

http://www.bams.cm-uj.krakow.pl

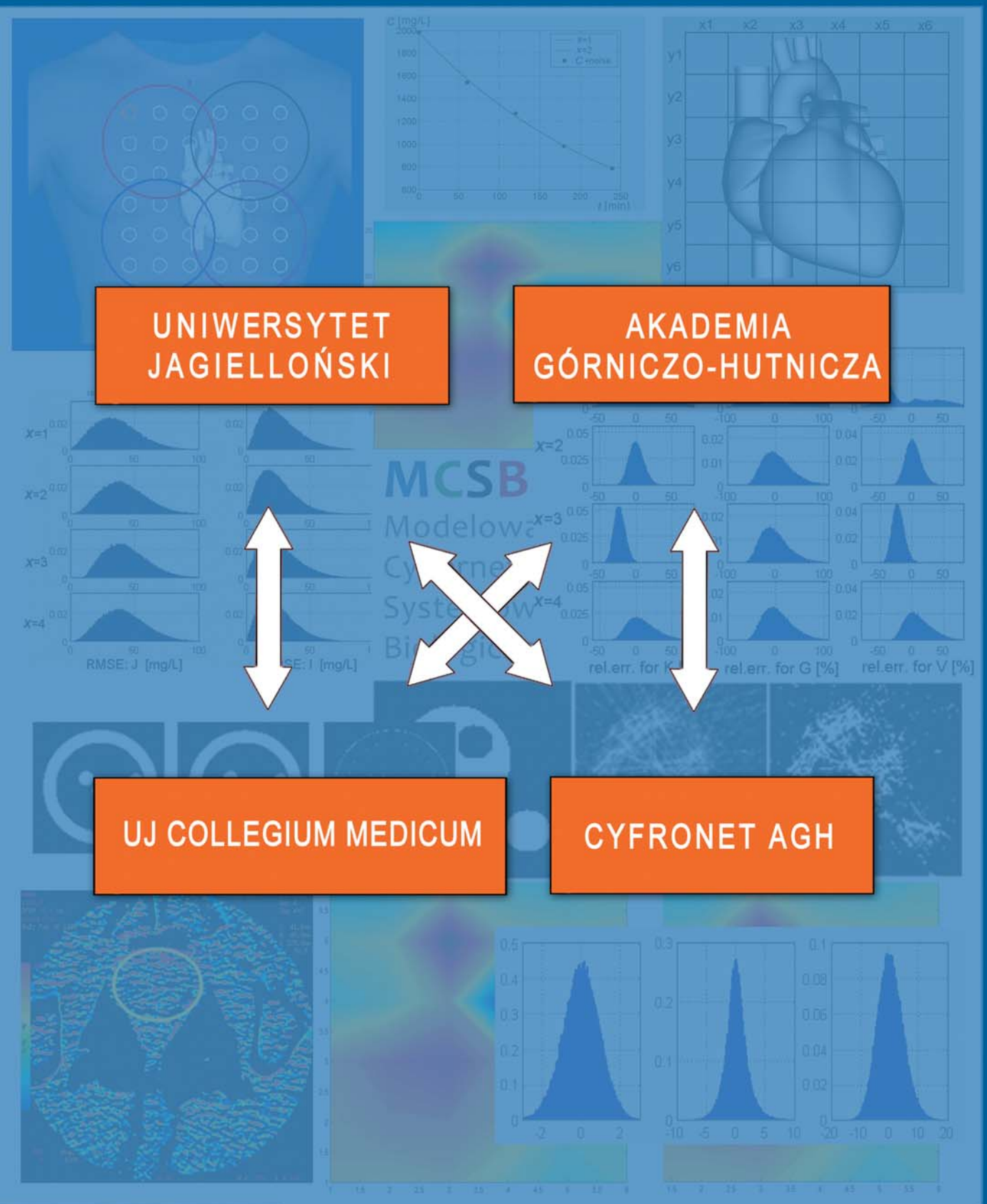

EDITORIAL BOARD

Polish Ministry of Science and Higher Education journal rating: 4.000

Sustaining institution: Ministry of Science and Higher Education

Edition: 300 copies

ISSN 1895-9091 (print version)
ISSN 1896-530X (electronic version)

http://www.bams.cm-uj.krakow.pl

Contents

PHYSIOLOGY IN SILICO

AGRICULTURE

BIO-ALGORITHMS AND MED-SYSTEMS
JOURNAL EDITED BY MEDICAL COLLEGE – JAGIELLONIAN UNIVERSITY
Vol. 6, No. 12, 2010, pp. 5–13.

IMAGE ENHANCEMENT TASKS IN CAPSULE ENDOSCOPY

Krzysztof Duda[1,4], Mariusz Duplaga[2,4], Tomasz Zieliński[3,4]

[1]Department of Measurement and Instrumentation,
[2]Collegium Medicum, Jagiellonian University, Grzegorzecka Str. 20, 31-531 Kraków, Poland,
e-mail: mmduplag@cyf-kr.edu.pl
[3]Department of Telecommunications, AGH University of Science and Technology,
Al. Mickiewicza 30, 30-059 Kraków, Poland, e-mail: {kduda, tzielin}@agh.edu.pl
[4] Centre of Innovation, Technology Transfer and University Development, Jagiellonian University,
Czapskich Str. 4, 31-110 Kraków, Poland

Abstract: Improving quality of images from endoscopic capsules is discussed in the paper. The quality of the images acquired during endoscopic examination may be severely affected by different factors. We consider the most typical cases of geometrical lens distortion, limited resolution of the sensor and blur caused by the defocus and motion. We present remedies for the above obstacles. They are, respectively, identification and correction of the geometrical lens distortion, super-resolution of images, and blur identification and removing. We also describe the designed algorithms, particularly for the case of the capsule endoscopy, and show preliminary results obtained with artificial test data.
Keywords: endoscopic capsule, digital images, camera distortion correction, super-resolution, blur identification and removing

Introduction

Endoscopic examination of gastrointestinal (GI) tract is one of the main diagnostic procedures in gastroenterology, enabling the evaluation of the presence of pathological lesions and sampling of tissue for pathological assessment. In search of diagnostic tools allowing for examination of these parts of GI tract, which are less accessible with standard endoscopy performed with fiber endoscope and which would be more acceptable by patients, the capsule endoscopy was developed and introduced to gastrointestinal diagnostics. Although first indications for capsule endoscopy were quite narrow, currently it is perceived as a tool enabling diagnostic assessment of upper and lower part of GI. There are plans of coupling the capsule with optical or tissue biopsy options in order to increase its diagnostic impact. The capsules used currently for GI endoscopy are equipped with on-board light source, camera and memory. Low resolution images are registered during the passage of the capsule through GI tract. Then, they are browsed and analyzed.

Research activities presented in the paper were conducted within the VECTOR project (Versatile Endoscopic Capsule for gastrointestinal TumOr Recognition and therapy) carried out within 6th Framework Research and Development Programme of European Union and aimed at design the next generation endoscopic capsule. The main functionalities of the VECTOR capsule include: 1) active movement and 2) real-time transmission of a high resolution video stream. The video is used not only for medical diagnosis, but also for automatic image based navigation and computer aided diagnosis.

The quality of the images obtained from the VECTOR capsule can be deteriorated by the distortions resulting from the optical system (wide angle lenses), spatial resolution of the sensor, blur effects caused by defocus or/and motion, non-uniform light conditions and others. Advanced image enhancement and restoration methods are applied as a remedy to these problems. The paper is focused on design, implementation and testing of the following image enhancement algorithms:

1) correction of geometrical lens distortion,
2) super-resolution (SR),
3) blur estimation and suppression.

Correction of geometrical lens distortion

The algorithm for correction of geometrical camera lens distortion is fully automatic, but some interaction of the user are required for setting appropriate values of parameters (e.g. the threshold value during converting gray scale to binary image, which depends on the lighting conditions during taking the picture). The parameters of geometrical camera distortion are estimated only once. After identification of lens distortion model, the correction may be computed in real time by dedicated software. The algorithm was successfully validated with the recordings from the standard Given Imaging PillCam camera.

Camera lens distortion model

It is known from previous studies [1-3], that for correction of wide angle endoscope camera geometrical distortion it is sufficient to consider only radial distortion (i.e. tangential distortion is typically neglected). The distortion model is determined by: 1) the center of distortion (which is not necessary the geometrical center of the image), and 2) distortion polynomial. The distortion polynomial relates to distances between the center of distortion and the current pixel in undistorted and distorted image. The objective is to find the center of distortion and distortion polynomial, and than relocate the pixels to obtained corrected image.

Designed correction algorithm

The test image recorded by the PillCam is presented in Fig.1. It can be seen that the lines that should be straight are bent. In optimization procedure the points which should lie on the straight line are selected and fitted to this line (in least-squares sense). The error of the fit is minimized by changing the parameters of distortion model.

Manual selection of appropriate points is too tedious and time consuming. Typically, the corners of the squares are selected. During experiments we find out that selecting the centers of the squares is a more robust and precise approach, especially when the image is defocused (like the center part of Fig.1). Selecting the centers of the squares is also easier for automatic implementation.

The developed algorithm for correction of camera distortion consists of the following steps.

1. Converting RGB image into gray scale image and adaptive histogram equalization. Removal of inscriptions.
2. Computing Radon transform of the image (depicted in Fig.2) and using it for detecting the straight lines in the image. Maximum values of the Radon transform, denoted by blue circles in the Fig.2, are automatically detected.
3. Finding the centers of white squares. The gray scale image is converted to the binary one and, next, morphological labeling is used for finding objects in the image. As a default value of the threshold for image binarization, 75% of its maximum intensity is set. This value may require same adjustment for test images taken in non-uniform lighting conditions. However, the test image may be taken in standard laboratory conditions, as identification of geometrical lenses distortion is performed only once. Centers of the white squares are mean values of their X and Y coordinates.
4. Grouping points into lines. The points that should form the line are grouped based on their distance

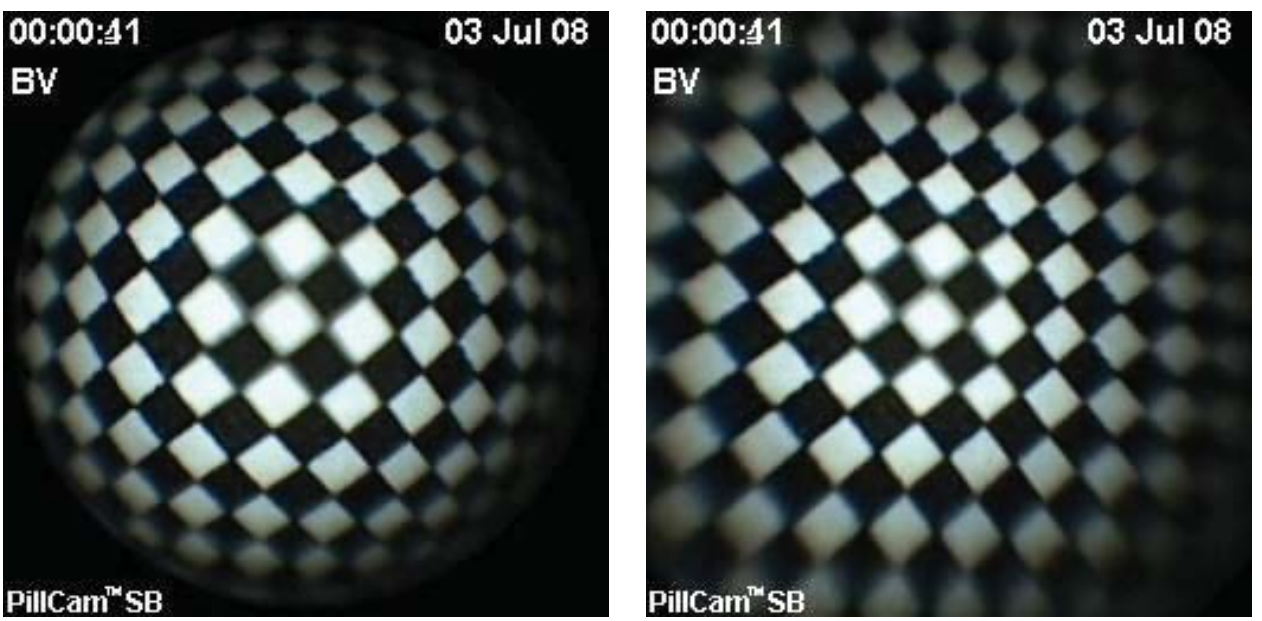

Fig. 1. Test image before correction (left) and after correction (right)

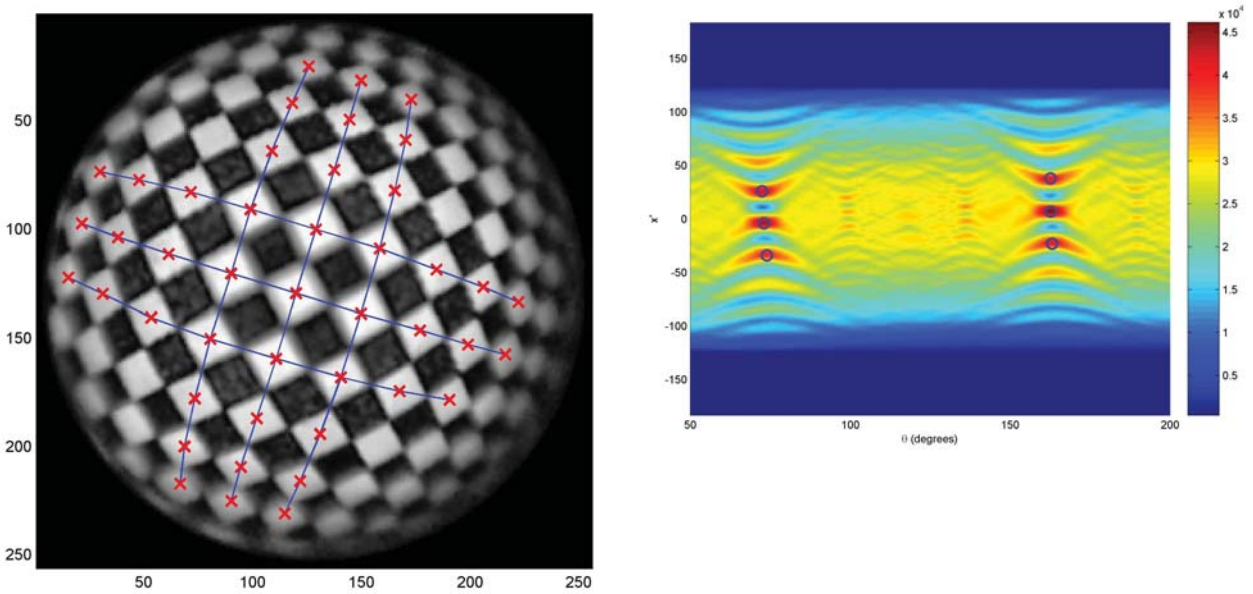

Fig. 2. Processed image with automatically detected points and lines (left). Radon transform of the processed image (right)

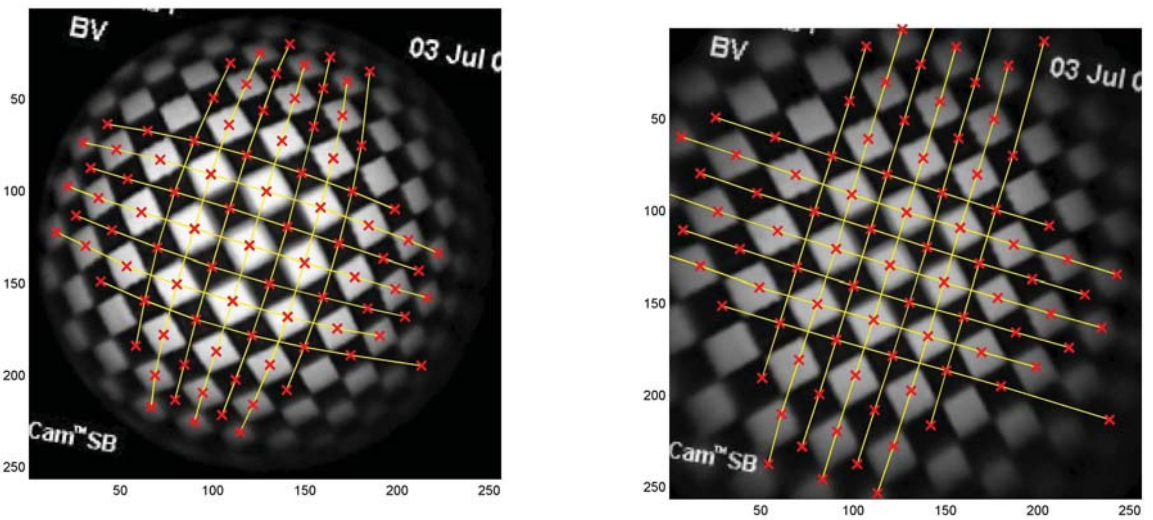

Fig. 3. Images and selected lines before (left) and after (right) optimization

from the lines previously computed. Fig.2 depicts automatically selected six groups of points that should form lines.

5. Steps 1-4 are repeated for the image negative in order to take advantage of the dark squares as well. Fig.3 shows points grouped in lines that stand for an input to the optimization procedure.
6. Optimization. We consider 3rd order distortion polynomial. The cost function is defined as the sum of the squared distances of the points to the straight lines. The results of optimization are: 1) the center of distortion and 2) coefficients of the distortion polynomial. Test image with control points before and after optimization is depicted in Fig.3.
7. Computing a correction polynomial and a correction look-up table. The correction polynomial

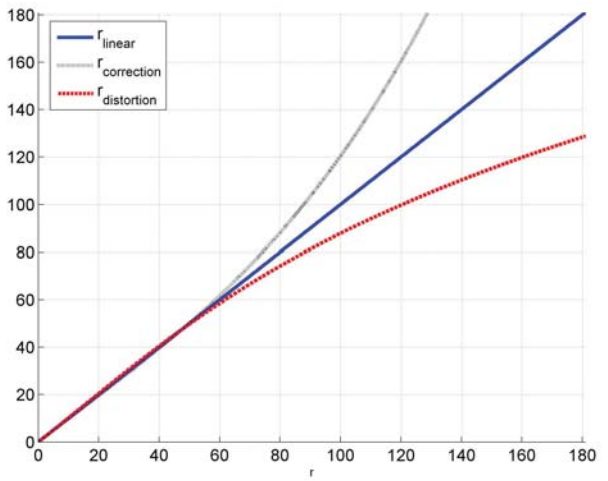

Fig. 4. Distortion polynomial and correction polynomial

is computed by fitting to data generated from the distortion polynomial. Both polynomials are depicted in Fig.4. Using correction polynomial, new locations for pixels are computed and stored in the look-up table. For example, if the distance of the pixel from the distortion center in distorted image equals 100 (OX axis), it means that it should be moved to the distance of 120 in corrected image, as shown in Fig.4.

Super-Resolution

Super-resolution (SR) is the term used in literature for many image processing algorithms aimed at enlarging (magnification) of images with simultaneous improvement of higher frequency content, i.e. with the reconstruction of the details [4-9]. SR is expected to overcome limitations of sensors and optics technology. Main application fields of the SR are: video (e.g. surveillance or forensic purposes), satellite imaging, and medical imaging (e.g. CT and MRI). Although SR is very promising and powerful technique one should notice that, [4]: "*Generally, the SR image reconstruction approach is an ill-posed problem because of an insufficient number of low resolution images and ill-conditioned blur operators"*. We propose to use SR techniques to improve the quality of LR (Low Resolution) images from the capsule. For the VECTOR capsule we consider a multi-frame-based SR algorithm. Multi-frame SR algorithms reconstruct a HR (High Resolution) image from the set of LR images of the same scene. The fundamental assumption in multi-frame SR algorithms is that the LR frames are aliased and sub-pixel shifted in respect to each other. The assumption about aliasing in images is a weak requirement because low-pass optical filters are in general not used in cameras, as opposed to lowpass electrical filters that are always used before analog to digital conversion. The assumption about sub-pixel shifts is particularly well suited for the capsule traveling inside human body, as e.g. camera motion, heart beat, breathing and peristaltic motions, will be sources of natural camera dither (i.e. potentially sub-pixel shifts of the scene between frames).

A typical SR algorithm consists of 3 stages: 1) image registration, 2) interpolation and reconstruction, and 3) restoration. Unfortunately, many SR algorithms presented in literature assume that relative sub-pixel shifts between LR images are known and consider the problem of reconstructing HR image from blurred and noisy LR images. In practical application image registration is a crucial part of any SR algorithm.

The SR algorithms are typically formulated as optimization problems with significant computational burden which disables real-time applications. SR is a computationally intensive problem, typically involving tens of thousands unknowns, e.g. super-resolving a sequence of 50 × 50 pixel LR frames by a factor of 4 in each spatial dimension involves 200 × × 200 = 40000 unknown pixel values in the HR image. Furthermore, the matrix system is typically underdetermined and ill-conditioned, which can aggravate system noise and blurring effects. The computation time can be a significant limitation for real-time SR application. Computation times reported in literature are as follows: 5-7 minutes for 256×256 images and 4 times upsampling in [5]; 17.7 seconds for 43×43 images and 4 times upsampling in [10]; 26 minutes for registration and 38 seconds for MAP (Maximum a posteriori) algorithm for 128 × 128 "cameraman" image and 2 times upsampling in [11]. These times cannot be fairly compared since different SR models and computer platforms were applied, but they illustrate the computational scale of the SR problem. In contrast to above references, our algorithm does not exploit computationally extensive optimization theory, but relays on simple averaging or interpolation on non-uniform grid of upsampled and registered LR images.

Developed SR algorithm

In our implementation, the HR image is reconstructed from the current *i*-th LR image and *n* previous LR images. First, LR images are upsampled to the desired spatial resolution. Next, previous images are registered to the current image. Registered images are then averaged with weights depending on registration quality factor. (The other option, with more complex computation, is interpolation on HR grid based on LR upsampled images, which we discus next). Details of the algorithm are given in [12]. For

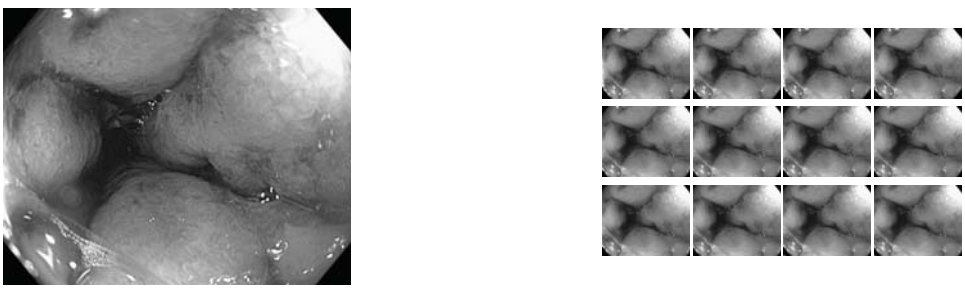

Fig. 5. HR endoscope test image (600×480) (left) and the set of LR test images (150×120) (right)

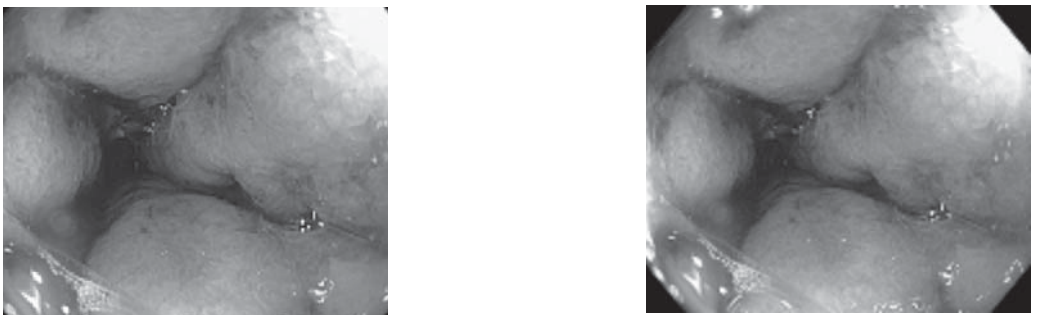

Fig. 6. SR reconstruction PSNR = 38.08 dB (left); Bilinear interpolation PSNR = 37.04 dB (right)

image registration we assumed rigid affine model and image similarity was measured by normalized mutual information [13].

Fig. 5 presents HR endoscope test image of size 600×480 and the set of LR images. The LR images were artificially prepared by taking every 4-th pixel from HR image in OX and OY directions. Before downsampling, the HR image was: a) shifted by 1 pixel in OX and OY directions (upper rows in Fig. 5); b) scaled (simulation of forward camera movement) and shifted in OX and OY directions (middle rows in Fig. 5) and c) skewed, scaled and shifted in OX and OY directions (lower rows in Fig. 5). Thus sub-pixel shifts of LR images were generated with additional camera movement.

Image registration stage is the most time consuming part of our SR algorithm. For faster evaluation, the registration is based on the central part of the image instead of the whole image. SR reconstruction results for the proposed algorithm are depicted in Fig. 6. Objective reconstruction quality is measured by peak signal-to-noise ratio (PSNR) computed with respect to the HR test images from Fig. 5. For comparison, Fig. 6 shows bilinear interpolation of the LR image from Fig. 5 (first row, first column).

Artifacts visible on the image border in Fig.6 are caused by the image registration stage. During registration LR images are fitted to the selected reference LR frame. Most often LR images do not cover the same scene exactly, e.g. consider the reference image and the image to be registered taken a little closer to the same scene; then we have to zoom in this image to fit it to the reference image, and when

Fig. 7. LR image (320×240) and reconstructed HR image (640×480)

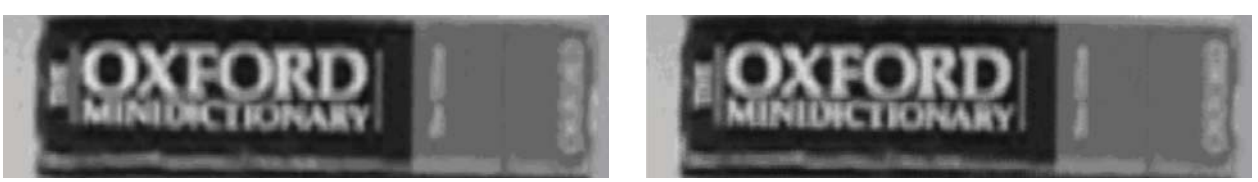

Fig. 8. Interpolation (left) and SR (right), the world MINIDICTIONARY is better visible for the SR

combining them we may have distortion near the image border, because the images do not overlap near it.

The implemented SR algorithm was also tested with real world LR data. Video recording was taken with digital camera Canon A430 4MP in 320×240 resolution. Fig. 7 shows the original LR image and reconstructed HR image. In Fig. 7 we present the scene that, due to geometrical content, is easier for subjective quality evaluation than anatomical structure from Fig. 5. For reconstructing the pixel values in HR image we use non-uniformly spaced interpolation (alternatively, previously described averaging that is computationally simpler may be used). In Fig. 8 the SR result is compared to bilinear interpolation of one LR image. It is seen that the world MINIDICTIONARY is better visible when the SR reconstruction is applied.

The simulations performed with test images confirmed better performance of the proposed algorithm in comparison to the bilinear interpolation method. Magnification of one LR endoscopic image (from 150×120 to 600×480 resolution) using standard Pentium 3.2 GHz with 1GB RAM in Matlab™ 7.1 environment was taking approximately 2.5 seconds. In case of parallel implementation of image registration, this computation time can be further reduced. SR reconstructed images are at least as good in PSNR as interpolated ones but usually have greater amount of high-frequency details.

Blur estimation and suppression

In the VECTOR capsule, main sources of image blur are: 1) camera or scene motion during exposition; 2) defocus of optics; 3) wide-angle lenses; and 4) anatomical liquids on the lenses. We have implemented an algorithm for estimating and removing the blur from images able to retrieve their diagnostic value.

Deblurring with known PSF

It is assumed that a blurred image can be approximately described by the equation:

$$\mathbf{g} = \mathbf{H} * \mathbf{f} + \mathbf{n} \quad (1)$$

where: **g** – is the blurred (distorted) image; **f** – is the original true image, i.e. the image taken with a perfect image acquisition conditions; **H** – is the distortion operator, also called the Point Spread Function (PSF). Notation **H*f** means 2D convolution; **n** – is additive noise, introduced during image acquisition that corrupts the image. Based on model (1), the fundamental task of deblurring is to deconvolve the blurred image with the PSF that exactly describes the distortion. The main difficulty in applying model (1) is proper estimation of the PSF, which is unknown. Once the PSF is known, the number of methods is available for deblurring. For example, Matlab™ Image Processing Toolbox includes four deblurring functions based on:

1. Wiener filter (least squares solution).
2. Regularized filter (constrained least squares solution).
3. Lucy-Richardson algorithm.
4. Blind deconvolution algorithm without knowledge of the PSF.

Deblurring with estimated PSF

Two cases of the blur are well described in literature: the blur caused by defocus (when PSF has the form of cylinder) and blur caused by motion (when PSF has the form of rectangle, possibly rotated) [14-17]. In our implementation the radius of the cylinder or the size of the rectangle are estimated in power cepstrum domain, where the convolution has the form of addition. The real cepstrum of the image $g(x, y)$ is defined as:

$$C\{g(x,y)\} = F^{-1}\{\log | F\{g(x,y)\} |\} \quad (2)$$

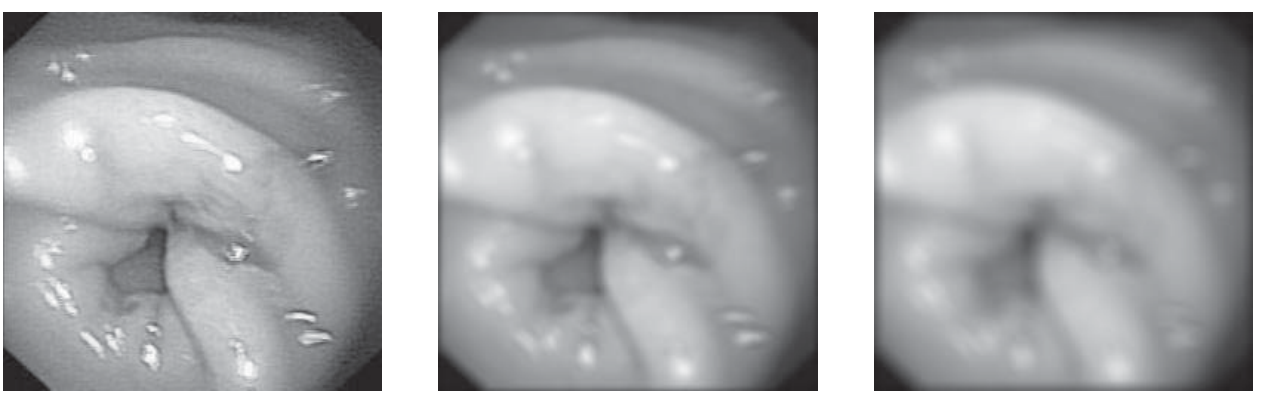

Fig. 9. Test image of 256 × 256 pixels (left); test image blurred with the rectangular PSF 7 × 9 rotated by 30 degrees (middle), and test image blurred with the cylindrical PSF with radius 8 (right)

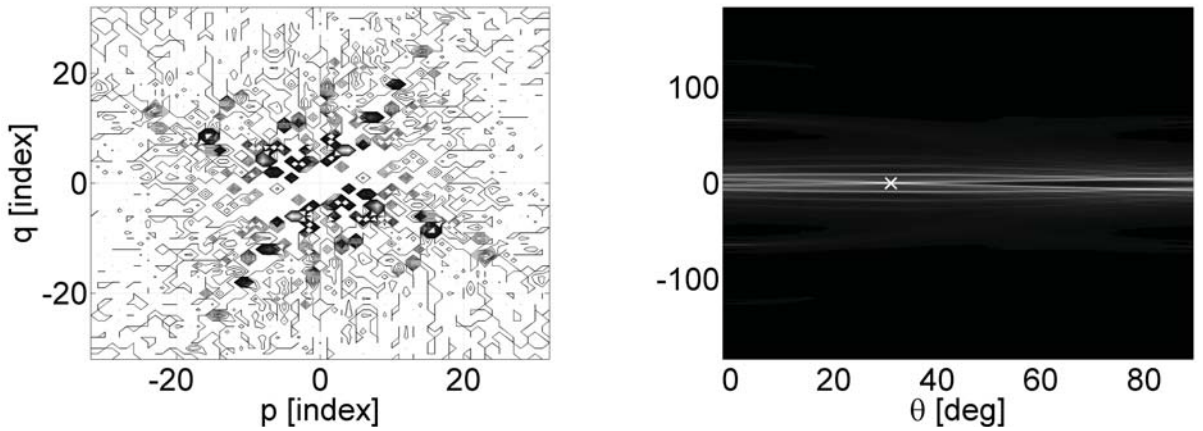

Fig. 10. Power cepstrum of the blurred image from Fig. 9 – middle; the cepstrum is rotated by 30 degrees to p and q axes (left); Radon transform of the power cepstrum – maximum denoted by 'x' is for the angle 30 degrees (right)

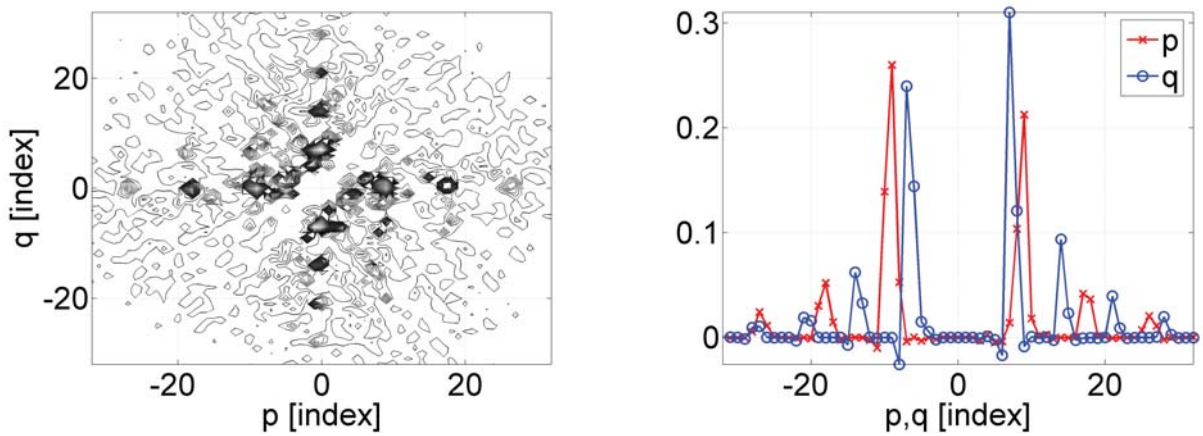

Fig. 11. Power cepstrum of the blurred image from Fig. 9 – middle – after correction of rotation (left); cross section of the power spectrum along p and q axes, the spikes determine the size of PSF (right)

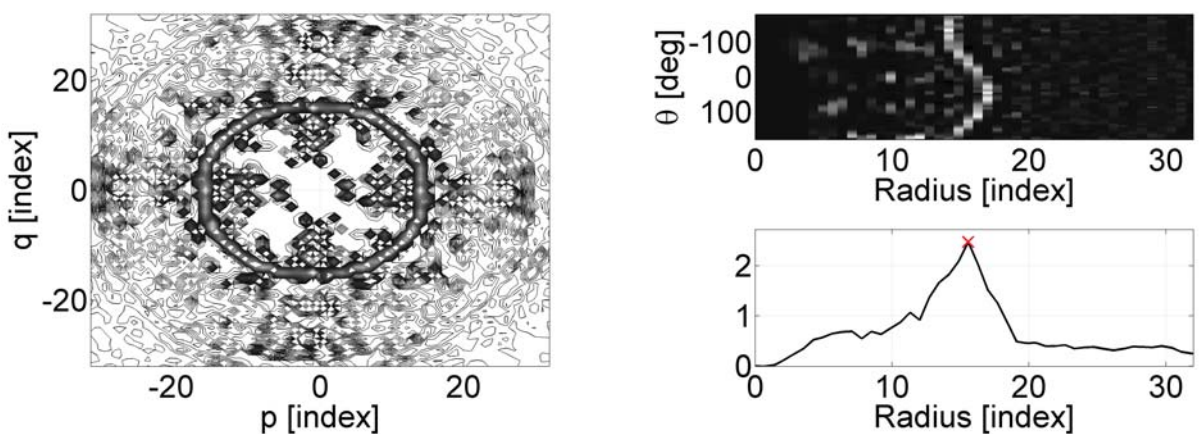

Fig. 12. Power cepstrum of the blurred image from Fig. 9 – right (left); Power cepstrum in polar coordinates and smooth curve of summation for constant radius, the maximum determines the radius of PSF (right)

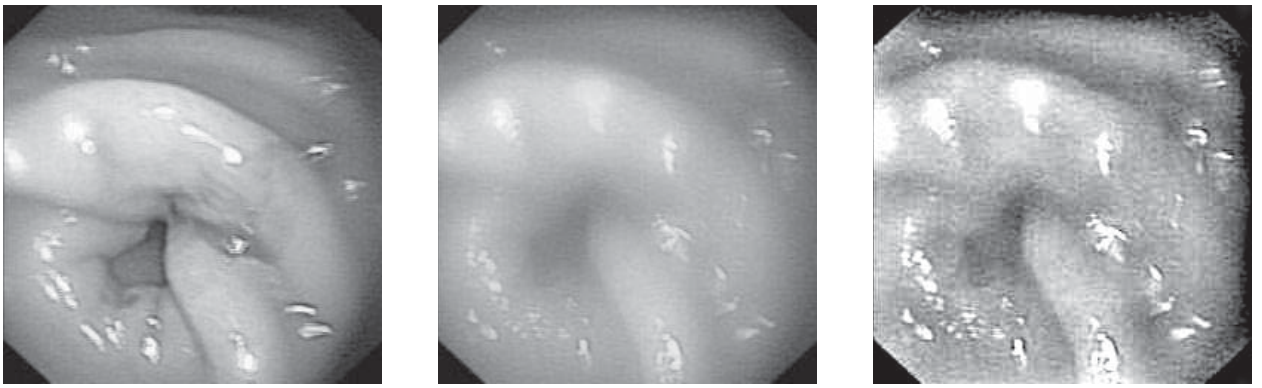

a) b) c)

Fig. 13. Illustration of image deblurring for 256×256 images taken from gastroscopy recording: a) frame no 2575 without blur; b) frame no 2576 with blur; c) frame no 2576 with blur removed by the implemented method

Denotations of the axis are as follows: pixel coordinates are *x* and *y*; frequency axes in Fourier domain are *u* and *v* with the range of digital frequency <-*π*, *π*>; and finally, cepstrum axes are *p* and *q* in pixels. For the case when $|F\{g(x, y)\}|=0$ we add some small positive value, e.g. 10^{-16}, before computing logarithm in (2).

Fourier transform of the rectangle with size *a*×*b* contains functions sin(*x*)/*x* on the axes *u*, *v*. The cepstrum of the rectangle has negative spikes on the *p*, *q* axes in *a*, 2*a*,… and *b*, 2*b*,… In figures presented below the sign of the cepstrum was reversed for better visualization.

Fourier transform of the cylinder contains Bessel functions of the first kind that are similar to sin(*x*)/*x,* with the difference that those functions are 'nearly' symmetric. The cepstrum of the cylinder has the form of concentric rings with the radiuses almost equal 2*a*, 4*a*,…

Based on Fourier transform convolution property it is obvious that:

$$\begin{aligned} C\{g(x,y) * h(x,y)\} &= F^{-1}\left\{\log\left|G(u,v)H(u,v)\right|\right\} = \\ &= F^{-1}\left\{\log\left|G(u,v)\right|\right\} + F^{-1}\left\{\log\left|H(u,v)\right|\right\} = \\ &= C\{g(x,y)\} + C\{h(x,y)\} \end{aligned} \quad (3)$$

and this means that convolution is additive in cepstrum domain. This property is used for determining the kind and the size of PSF. Details of the algorithm are given in [18].

The estimation of PSF is illustrated for a 256×256 gastroscopy image shown in Fig. 9. In experiments the following scenario has been used: 1) blurring the image with known PSF, 2) estimating this PSF, and 3) deblurring the image. The PSF estimation is automatic and does not require user interaction.

Fig. 9 (middle) shows an image blurred by a rectangle PSF with size 7×9, rotated by 30 degrees. Power cepstrum for this case is presented in Fig. 10. The power cepstrum is rotated against *p*, *q* axes. For automatic detection of this rotation we use Radon transform depicted in Fig. 10; the maximum value correctly determines the 30 degrees rotation. In the next step the rotation is compensated in cepstrum domain as shown in Fig. 11. The spikes on *p*, *q* axes determine the size of the PSF; in our case 7 and 9 pixels.

Fig. 9 (right) shows an image blurred by cylinder PSF with radius 8. Power cepstrum for this case is presented in Fig. 12. For automatic detection of the radius power cepstrum is mapped to polar coordinates and the polar plane is summed by columns, i.e. for constant radius. The summation curve presented in Fig. 12 has a maximum for the radius 15.55, thus the radius of PSF, after dividing by 2 and rounding, equals 8. The result is not exactly equal 16, because the estimation is performed in Cartesian coordinates, which are not well suited for representing cylinders, especially with small radius.

During experimentation phase it turned out that standard deconvolution algorithms (e.g. available in Matlab™ or the inverse filter from [17]) are very sensitive to the PSF estimation error. Best results for real data were obtained with a simple deconvolution filter with amplitude function defined by:

$$|H_i| = \frac{1+\varepsilon}{|H(u,v)|+\varepsilon}, \quad 0 < \varepsilon < 1 \quad (4)$$

where $|H(u, v)|$ is estimated amplitude function of the blur filter. In Fig. 13 are presented results from deblurring gastroscopy video: (left) – video frame without blur shown only for comparison, (middle) – test frame with real blur, (right) – test frame with blur removed by the implemented algorithm.

Two main conclusions resulting from the presented study are as follows:

– the estimation of PSF is the most important and difficult part of any deblurring process,
– the blur is always connected with lowpass filtering, but not necessary caused by defocus or motion.

In the Fig. 13 the blur is rather caused by some fluid on camera lenses. Nevertheless, deblurring operation is quite successive. We presume that possibility of 'digital cleaning' of camera lenses exists; this means the image can be cleaned not by using windscreen wiper on the camera lenses, but in algorithmic way, using proper image deconvolution.

Summary

We have designed and performed initial tests of three methods of image enhancement, which are to be applied to processing data coming from gastrointestinal capsule. They address the following operations: 1) geometrical lenses distortion correction, 2) improving the spatial resolution of the camera by Super-Resolution algorithm, and 3) blur identification and removal. The methods were designed for automatic performance, i.e. without the interaction of the physician, which is an important feature since typically thousands of frames come from a single capsule examination. All methods can work in real-time.

However, the designed and presented methods need further broad testing and validation. At the time of their first implementation, software and hardware development activities of the VECTOR project were conducted simultaneously and the prototype of the capsule was not yet available. For this reasonwe used test data from other sources, i.e. from the Giving Imaging PillCam capsules, and algorithms' validation by physicians was not done. Nevertheless, the preliminary results shown in the paper make a promising basis for clinical validation of the presented methods.

References

1. Vijayan A. K., Kumar S., Radhakrishnan D. (1999), A New Approach for Nonlinear Distortion Correction in Endoscopic Images Based on Least Squares Estimation. *IEEE Trans. on Medical Imaging* 18/4, 345-354.
2. Helferty J. P., Zhang C., McLennan G., Higgins W. E. (2001), Videoendoscopic Distortion Correction and Its Application to Virtual Guidance of Endoscopy. *IEEE Trans. on Medical Imaging* 20/7, 605-617.
3. Socha M., Duda K., Zieliński T. P., Duplaga M. (2005), Algorithmic Correction of Geometric Distortion of Bronchoscope Camera. Modelling and measurements in medicine, XV Symposium, Krynica, 18-22 września (in Polish).
4. Park S. C., Park M. K., Kang M. G. (2003), Super-resolution image reconstruction. A technical overview. *IEEE Signal Processing Magazine* 20/3, 21-36.
5. Woods N. A., Galatsanos N. P., Katsaggelos A. K. (2006), Stochastic methods for joint registration, restoration, and interpolation of multiple undersampled images. *IEEE Transactions on Image Processing* 15/1, 201-213.
6. Farsiu S., Elad M., Milanfar P. (2006), Multiframe demosaicing and super-resolution of color images 15/1, 141-159.
7. Nhat N., Milanfar P., Golub G. (2001), A computationally efficient superresolution image reconstruction algorithm. *IEEE Transactions on Image Processing* 10/4, 573-583.
8. Farsiu S., Robinson M. D., Elad M., Milanfar P. (2004), Fast and robust multiframe super resolution. *IEEE Transactions on Image Processing* 13/10, 1327-1344.
9. Xiaochuan P., Lifeng Y., Chien-Min K. (2005), Spatial-resolution enhancement in computed tomography. *IEEE Trans. on Medical Imaging* 24/2, 246-253.
10. Nguyen N., Milanfar P., Golub G. (2001), A computationally efficient superresolution image reconstruction algorithm. *IEEE Transactions on Image Processing* 10/4, 573-583.
11. Chantas G. K., Galatsanos N. P., Woods N. A. (2007), Super-Resolution Based on Fast Registration and Maximum a Posteriori Reconstruction. *IEEE Transactions on Image Processing* 16/7, 1821-1830.
12. Duda K., Zieliński T., Duplaga M. (2008), Computationally Simple Super-resolution Algorithm for Video from Endoscopic Capsule. ICSES, Kraków, 197-200.
13. Pluim J. P. W., Maintz J. B. A., Viergever M. A. (2003), Mutual-information-based registration of medical images. A survey. *IEEE Trans. on Medical Imaging* 22/8, 986-1004.
14. Kundur D., Hatzinakos D. (1996), Blind Image Deconvolution. *IEEE Signal Processing Magazine*, May 1996, 43-64.
15. Kundur D., Hatzinakos D. (1996), Blind Image Deconvolution Revisited. *IEEE SP Magazine*, Nov. 1996, 61-63.
16. Rom R. (1975), On the Cepstrum of Two-dimensional Functions. *IEEE Transactions On Information Theory* 21/2, 214-217.
17. Cannon M. (1976), Blind Deconvolution of Spatially Invariant Image Blurs with Phase. *IEEE Transactions on Acoustics, Speech and Signal Processing* 24/1, 58-63.
18. Duda K., Duplaga M. (2009), Blur identification and removing for images from endoscopic capsule. Modelling and measurements in medicine, IX Symposium, Krynica, 10-14 May, 157-160 (in Polish).

BIO-ALGORITHMS AND MED-SYSTEMS
JOURNAL EDITED BY MEDICAL COLLEGE – JAGIELLONIAN UNIVERSITY
Vol. 6, No. 12, 2010, pp. 15–20.

ANALYSIS OF RAMIFICATIONS AND CARINA SHAPE IN BRONCHOSCOPIC IMAGES*

Zbigniew Mikrut, Mariusz Duplaga

AGH University of Science and Technology, Institute of Automatics, Mickiewicza Ave., 30-059 Krakow, Poland; e-mail: zibi@agh.edu.pl
Jagiellonian University, Medical College, Grzegorzecka Str. 20, 31-531 Krakow, Poland, e-mail: mmduplag@cyfronet.pl

Abstract: Because of the growing volume of digital registrations obtained from bronchoscopic examinations it proved necessary to summarize ("brief") their results, namely to mark the parts that are relevant and/or irrelevant for medical diagnosis. The parts in which the ramification areas of bronchial tree are visualized belong to the first group. The paper presents an automatic method for detection of the areas where next level orifices of bronchial tree are visible. The applied algorithms allow the shape evaluation for both orifices and the area located between them (carina). In both cases *backpropagation* type neural networks are used as classifiers.
Keywords: bronchoscopic video, video summarization, digital image analysis, multi-thresholding, shape descriptors

Introduction

Modern medical equipment almost routinely offers registration of the examination results in the form of digital images or video sequences. Well known examples are computer tomography, angiography or endoscopy [7]. Along with further development of these techniques, the problems with storing and browsing enormous data volumes become really serious.

During the bronchoscopic examinations carried out as a part of BRONCHOVID project [1] several hundreds of digital video sequences have been registered. They have been stored in a dedicated data base, and described with respect to the presence of selected disease entities. Selected video frames have been used for construction of algorithms for automatic detection of specific disease symptoms.

Browsing of videos and manual selection of interesting video frames is a very tiresome and time consuming job. Dominant parts of each video contain video frames that are out of focus or are irrelevant from the diagnostic point of view. Therefore, a method has been proposed for summarization of videos, which comprises mainly marking of video parts that are uninteresting or – on the opposite – video frame sequences that are very essential [3].

The approach to summarization of the video recording of the bronchoscopic examinations may be based on the use of the significant point in the topography of the tracheobronchial tree. The frames with the images of the ramifications of bronchial tree belong to such points. The detection of ramifications may help in positioning the bronchoscope tip (camera head) in the bronchial tree. From the diagnostic point of view it is very essential to determine the shapes of the next level openings, in particular to detect any strictures, i.e. reductions of the orifice area. The second important task is the shape analysis of the carina, i.e. the area between the next level orifices of the bronchial tree.

Both tasks have been realized by the image analysis algorithms, described in the present paper. Section 2 describes the multi-threshold binarization method, which has been applied to detection of next level orifices in the bronchial tree. Section 3 presents the algorithm for carina shape evaluation, based on the cross-section area analysis. For classification of the orifice and carina shapes, the *backpropagation* type neural networks have been used. All the necessary calculations have been carried out in the Matlab environment, using appropriate toolboxes of the software [10].

* The research of the first author has been supported by the AGH UST grant No. 11.11.120.612. The second author wishes to acknowledge financial support from the Ministry of Science and Higher Education of the Republic of Poland, under the project "BRONCHOVID" (Grant No. R13 011 03).

Ramifications of the bronchial tree

The image of the division of the bronchus as seen by the bronchoscope camera may be compared to two or more black holes corresponding with the orifices of next level bronchi. For their detection a multi-threshold binarization algorithm has been used. For consecutively increasing thresholds, the segmentation and labeling of detected objects is carried out. The detailed preprocessing has been realized using the Matlab Image Processing Toolbox [10] and is described in [4]. Every object detected has been described using four shape descriptors:

– Haralick circularity descriptor [2]

$$Har = \mu_R / \sigma_R \tag{1}$$

where μ_R and σ_R are the mean and standard deviation of distances from the center of the object to any part of its perimeter,

– descriptor based on the Malinowska's factor [8]:

$$W8 = \frac{2\sqrt{\pi S}}{L} \tag{2}$$

where *S* and *L* are the object area and perimeter respectively,

– Blair-Bliss descriptor:

$$\boldsymbol{B} = \frac{S}{\sqrt{2\pi \sum_S (r)^2}} \tag{3}$$

where *r* is the distance between the center of the object and any object pixel,

– m7 – a geometric moment [7, 5] (in [6] is referred to as I_8):

$$m7 = \frac{\left(m_{20} - \frac{m_{10}^2}{m_{00}}\right)\left(m_{02} - \frac{m_{01}^2}{m_{00}}\right) - \left(m_{11} - \frac{m_{10}\, m_{01}}{m_{00}}\right)^2}{m_{00}^4}, \quad m_{pq} = \sum i^p j^q \tag{4}$$

where *i, j* are the coordinates of binary object pixels.

With changing binarization thresholds, the object shape and thus the values of coefficients describing the object also change (see Fig. 1). In the algorithms discussed here it has been assumed that if the shape descriptors do not change for several consecutive binarization thresholds, then they really describe the actual shape of the object. That assumption has been verified by analyzing consecutive values of the coefficients in a moving window. The analysis comprised calculation of average value and standard deviation in a three element window (see Fig. 2).

For every step (binarization threshold) the standard deviation values, calculated for all the coefficients, were summed up. For such function a global minimum was determined. The minimum position indicated the corresponding threshold value, and for that value the respective shape coefficients were stored. In Fig. 2 the threshold value obtained from such calculations is marked by the arrow.

In Fig. 3 consecutive stages of multithreshold binarization are presented. For threshold value equal to 50 (and below) the coefficients have not been calculated, because the areas of the objects were too small (see Fig. 1). For threshold value equal to 59 two objects were detected. The object No. 1, referred to in Figs. 1 and 2, has been marked by an arrow. Binarization at threshold value equal to 77 resulted in detection of three objects. Object No. 1 was merged with the neighboring object after reaching binarization threshold value equal to 97. The algorithm's working range for the threshold value was limited

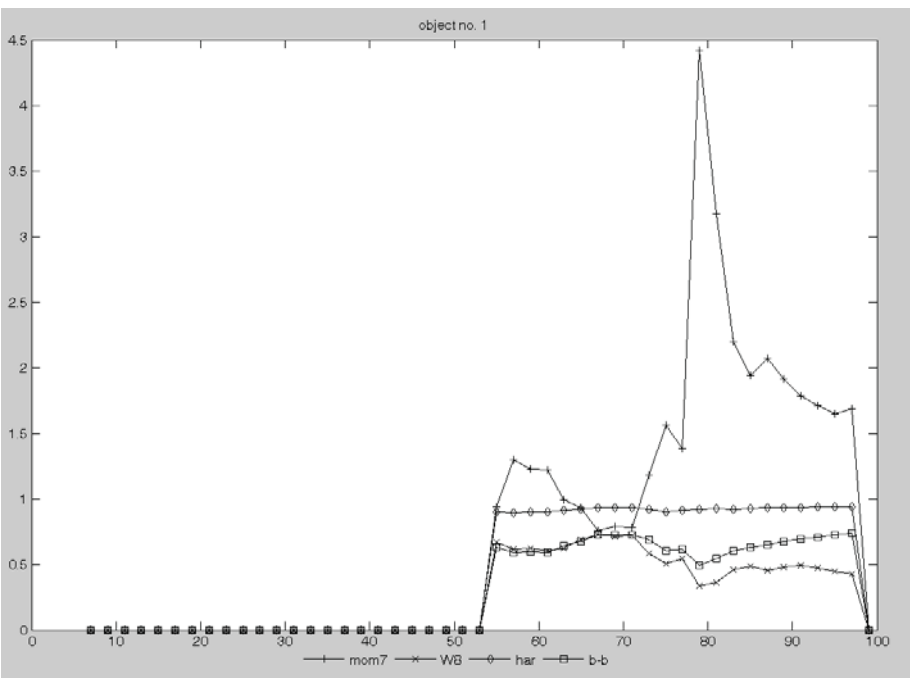

Fig. 1. Plots of value changes for the four shape descriptors of object No. 1

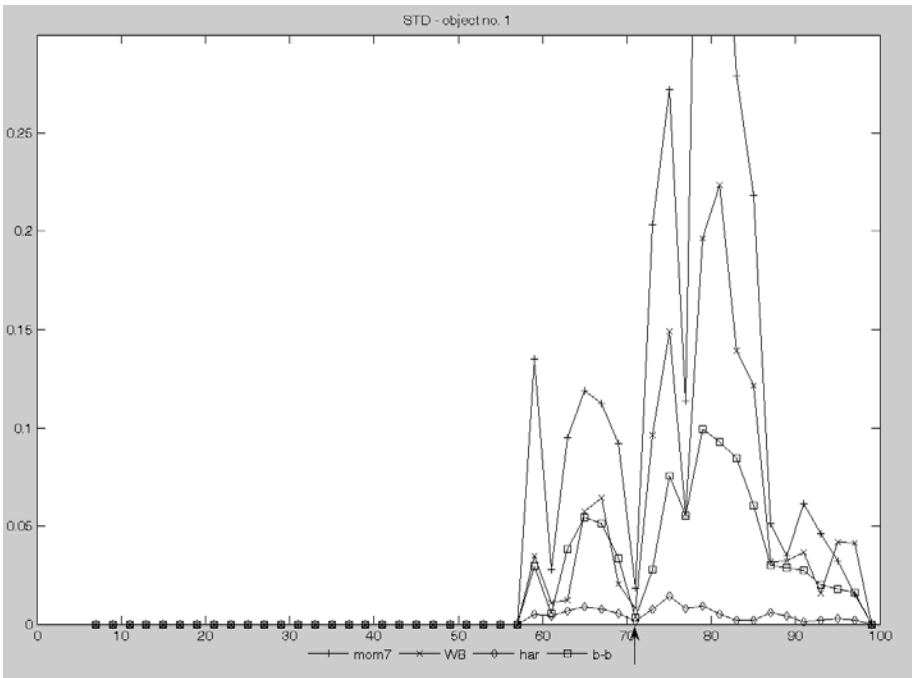

Fig. 2. Standard deviations calculated for the shape descriptors in the window of size 3

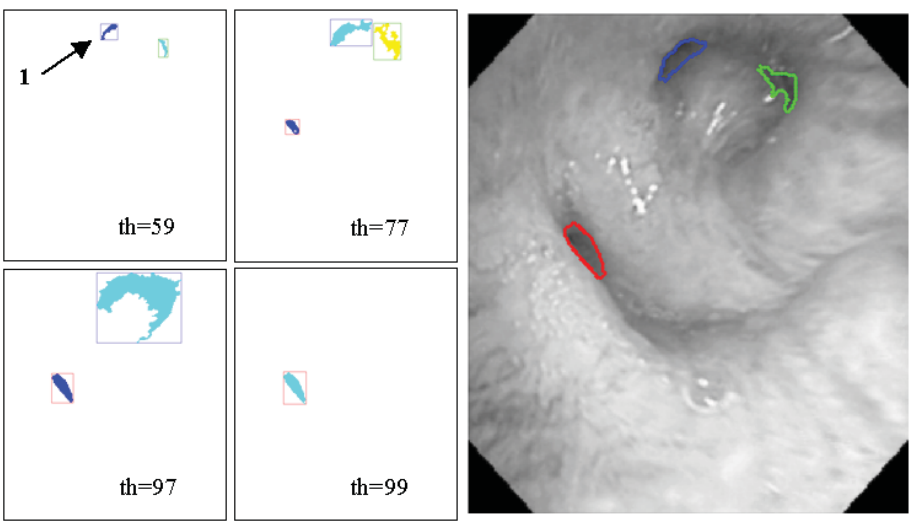

Fig. 3. Selected stages of binarization, segmentation and the final result. The necessary details can be found in the text

by value of 99. After completing the procedure only one object was left: the two objects with lower indices, merged together, have been removed because they touched the window border. The analysis of the shape descriptors variation, discussed above, allows the determination of threshold value that reflects the actual shape for every object detected. For these threshold values the object edges were determined, which later have been superimposed on the original images (see Fig. 3).

The algorithm described above has been used for analysis of several tens of video frames. For each object detected four shape descriptors have been stored, together with the accompanying user provided information, concerning the object stenosis. The completed data set has been divided into the learning part, consisting of 74 object descriptions, and the test set comprising 63 data records

For detection of orifice stenosis *backpropagation* type neural network has been used, which is regarded as one of the most efficient classifiers [9]. In order to obtain best results, the internal structure of the network has been varied – namely the size of the hidden layer. For the 4-x-2[1] structures, where x = 3, 6, 8, 10...13, the learning set has been recognized in 97.30%, while the test set in 92.06%.

1 notation: size of the input – hidden – output layers respectively

Analysis of the carina shape

After detection of bronchial tree orifices, distances were calculated between the detected objects. In the present version of the algorithm, the image section exhibiting maximum distance between the objects is selected for further analysis. For the present analysis it has been also assumed that the cross-section function approximately determines the actual shape of the carina. Carina shapes that are narrow and exhibit sharply defined edges, which reflect steep slopes of the orifice, are treated as regular. Carina shapes with diffused, wide edges, slowly merging into the orifices, are probably illness symptoms.

In most video frames the bronchoscope tip is not located exactly above the carina. Therefore the shape of the cross-section function is not symmetric. Fig. 4 presents the stages of the initial cross-section processing. In the first step the algorithm tries to detect the top-most area (plateau), approximating the area around the top (global maximum) by a flat segment. Then the cross-section function is truncated at both ends at the levels taken from binarization threshold values of the detected objects (see horizontal segments in Fig. 4). The cross-section part that is better visible (the longer one) is smoothed. If it is located at the right-hand side of the top then its mirror reflection is created. Such a situation is presented in Fig. 4. The final stage of the preliminary processing consists of the construction of secant line – the line connecting the start point of the cross-section with the beginning of the flat part (see the dashed line in Fig. 4).

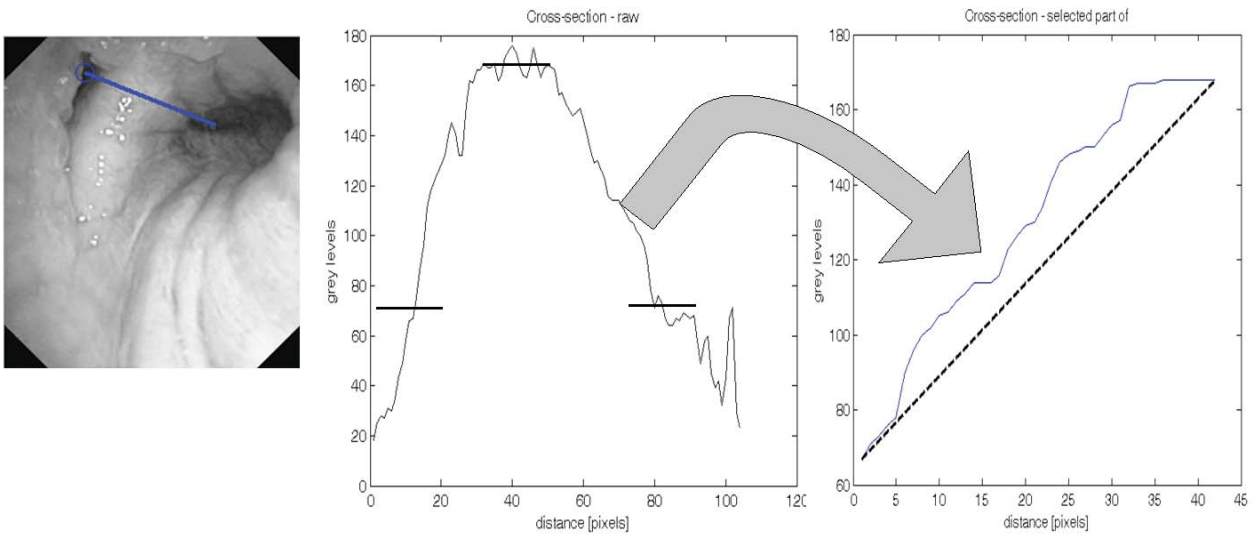

Fig. 4. The stages of preliminary cross-section processing near the carina image area (details can be found in the test)

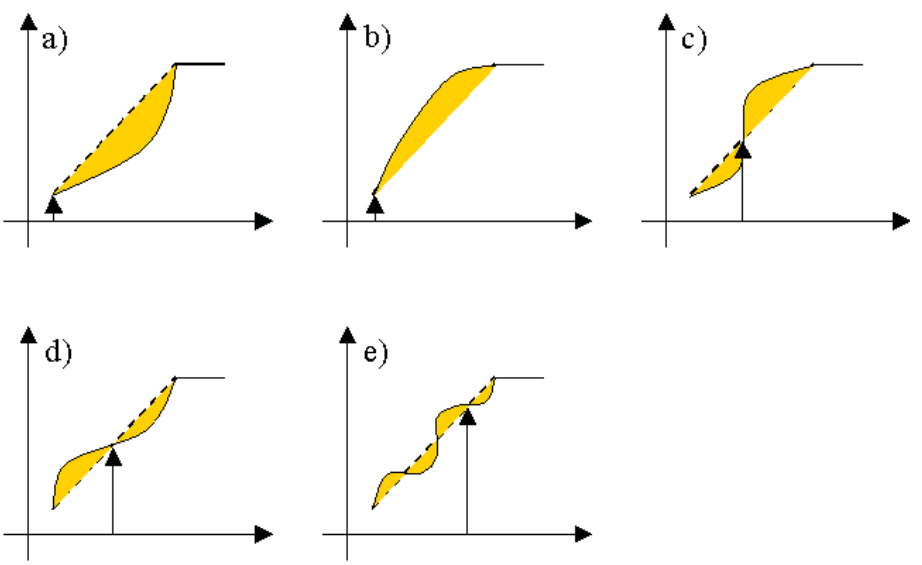

Fig. 5. Exemplary arrangements of carina cross-section and the secant line:
a), d) – regular carina shape, b), c) – abnormal carina shape,
e) problematic situation, secant line angle and/or plateau length are then decisive

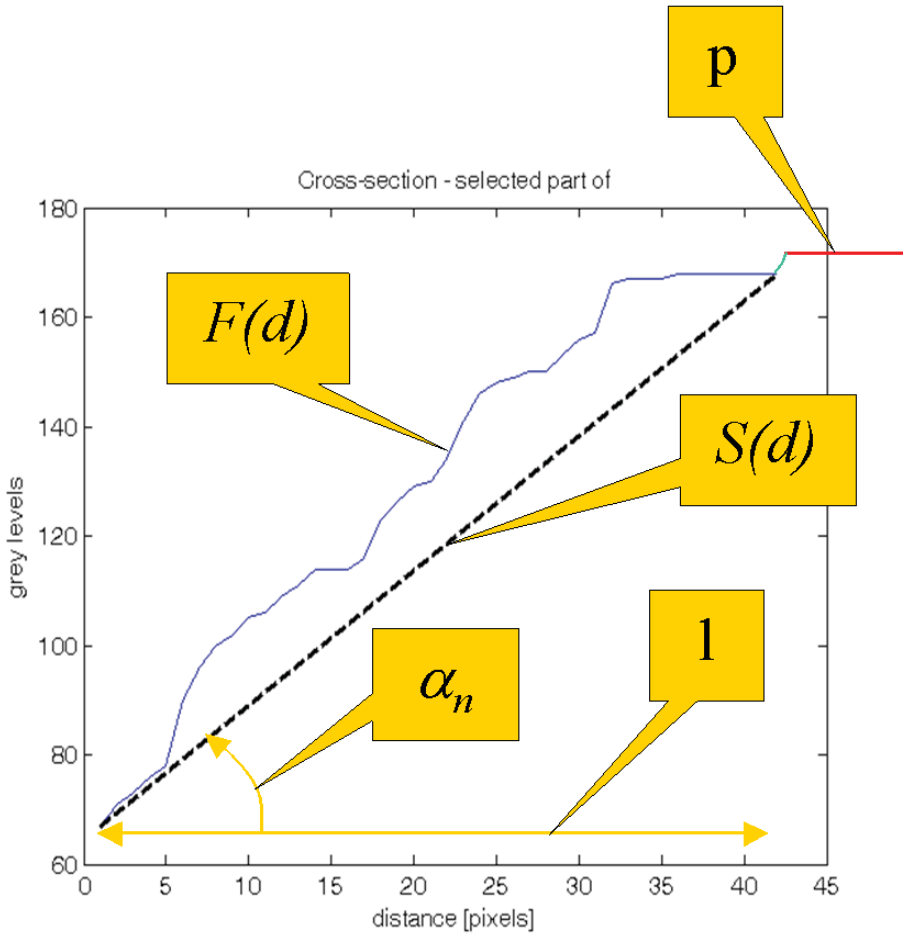

Fig. 6. Labeling of the cross-section function parameters

The concept of detailed shape analysis for the preliminarily processed cross-section area has been presented in Fig. 5. The picture presents several versions of relative location of the secant line and the cross-section function and the respective diagnosis proposals.

In order to classify the data set, several coefficients have been proposed, describing the situations presented in Fig. 5.

If the analyzed cross-section function is denoted as *F(d)* and the secant function as *S(d)* then:

$$f^{\uparrow} = \sum_{d=1}^{d=l} \begin{cases} F(d) - S(d) \; if \; F(d) > S(d) \\ 0 \; otherwise \end{cases} \tag{5}$$

$$f^{\downarrow} = \sum_{d=1}^{d=l} \begin{cases} S(d) - F(d) \; if \; S(d) > F(d) \\ 0 \; otherwise \end{cases} \tag{6}$$

where *l* is the domain for both functions (see Fig. 6).

Similarly binary form is determined for relations (5) and (6)

$$f_B^{\uparrow} = \sum_{d=1}^{d=l} \begin{cases} 1 \; if \; F(d) > S(d) \\ 0 \; otherwise \end{cases} \tag{7}$$

$$f_B^{\downarrow} = \sum_{d=1}^{d=l} \begin{cases} 1 \; if \; S(d) > F(d) \\ 0 \; otherwise \end{cases} \tag{8}$$

If l_L denotes the point on *X* axis, in which the one-before-last crossing of *F(d)* and *S(d)* functions took place (see also the arrows in Fig.5), then:

$$f_L = \sum_{d=l_L}^{d=l} \begin{cases} 1 \; if \; F(d) > S(d) \\ -1 \; otherwise \end{cases} \tag{9}$$

Taking into account relations (7) – (9) one can determine the following normalized coefficients:

$$C_1 = \frac{f^{\uparrow}}{f^{\uparrow} + f^{\downarrow}} \tag{10}$$

$$C_2 = \frac{f_B^{\uparrow}}{f_B^{\uparrow} + f_B^{\downarrow}} \tag{11}$$

$$C_3 = 0.5 + \frac{f_L}{2l} \tag{12}$$

$$C_4 = \frac{p}{l} \tag{13}$$

where *p* is the plateau length,

$$C_5 = \alpha_n \tag{14}$$

where α_n is the slope angle between the secant line and the *X* axis, normalized to the [0, 1] range.

As in the case of shape evaluation for bronchial tree orifices for the classification of cross-sections the *backpropagation* type neural networks have been used. Neural network with a 5–3–2 structure has achieved 100% recognition in the learning set (33 vectors) and recognition of 76.79% in the test set (56 vectors).

Conclusions

In the present paper an algorithm has been described for detection of bronchial tree ramifications, based on the analysis of selected video frames. Multi-threshold binarization accompanied by calculation and analysis of shape descriptors allowed the determination of actual shapes of the detected orifices. By using *backpropagation* type neural networks, the detected orifices have been classified with the respect to their shape into constricted and the other ones (rounded or irregular). The achieved recognition rate of 92% for the test set is found to be a satisfactory result. This result can be improved after analysis of recognition reliability and application of rejections.

The carina shape analysis has been carried out by analysis of the image cross-section taken along a straight segment connecting the two most distant orifices of the bronchial tree. A preliminary processing method has been proposed in order to extract the most informative cross-section parts. After some considerations regarding the expected carina shapes, five descriptors have been defined, describing the analyzed cross-section function. Classification into normal and abnormal carina shapes has been carried out using an artificial neural network. The recognition rate of 77% does not fully satisfy the authors of the paper. It seems that the main stage of the preliminary processing requires improvement, namely a more precise generation of the image cross-section and plateau length determination. It will be the subject of further research activity. The achievement of better classification results seems very essential, because it is widely considered that the widening or other distortions of carina shape is a serious symptom indicating a possibility of carcinoma presence.

References

1. Duplaga M., Bułat J., Leszczuk M., Romaniak P., Socha M., Turcza P. (2010), The BRONCHOVID computer system supporting bronchoscopy laboratory. Proc. 2nd International Conference on Information Technologies in Biomedicine, Kamień Śląski, Springer-Verlag, 511-522, in press.
2. Haralick R.M. (1974), A measure of circularity of digital figures. *IEEE Trans. Systems, Man and Cybernetics* 4, 394--396.
3. Leszczuk M., Grega M. (2010), The prototype software for video summarization of bronchoscopy procedures (leaving the most representative fragments) with the use of mechanisms designed to identify, index and search. Proc. 2nd International Conference on Information Technologies in Biomedicine, Kamień Śląski, Springer-Verlag, 587-598, in press.
4. Mikrut Z., Duplaga M. (2010), Analysis of Images of Bronchial Tree Ramifications for Summarization of Bronchoscopic Videos. Proc. 2nd International Conference on Information Technologies in Biomedicine, Kamień Śląski, Springer-Verlag, 583-586, in press.
5. Pilch J. (1991), *Analysis of the selected shape descriptors. PhD Thesis*. Kraków: AGH UST (in Polish).
6. Sluzek A. (1995), Identification and inspection of 2-D objects using new moment-based shape descriptors. *Pattern Recognition Letters* 16, 687-697.
7. Tadeusiewicz R. (ed.) (2008), *Biomedical engineering. A book of modern magic knowledge – a nice and approachable version*. Kraków: AGH UST.
8. Tadeusiewicz R. (1992), *Vision systems for industrial robots*. Warszawa: WNT (in Polish).
9. Tadeusiewicz, R. (1993), *Neural Networks*. Warszawa: RM Academic Publishing House (in Polish).
10. Thompson C.M., Shure L. (1995), Image Processing Toolbox for use with Matlab. Natick: The Math-Works.

BIO-ALGORITHMS AND MED-SYSTEMS
JOURNAL EDITED BY MEDICAL COLLEGE – JAGIELLONIAN UNIVERSITY
Vol. 6, No. 12, 2010, pp. 21–24.

GLOBAL EXTREMES ANALYSIS IN APPLICATIONS OF DISCRETE TOMOGRAPHY

Leszek Nowak, Bartosz Zieliński

Faculty of Physics, Astronomy and Applied Computer Science, Jagiellonian University, ul. Reymonta 4, 30-059 Kraków, dr.leszek.nowak@gmail.com
Institute of Computer Science, Jagiellonian University, ul. Łojasiewicza 6, 30-348 Kraków, bartosz.zielinski@uj.edu.pl

Abstract: One of the most important problems in discrete tomography is to reconstruct function $f: a \rightarrow \{0,1\}$, where a is a finite subset of $\mathbb{Z}^n$ $(n \geq 2)$, from the finite set of projections. There are a lot of methods dedicated for this problem, which employ basic methods of discrete mathematic, distribution theory, and even evolutionary algorithms. In this paper, new approach to this problem, based on global extremes analysis, is presented. It is competitive with the other algorithms, due to the fact that it returns projections identical with the original ones and is most effective in case of images with consistent objects.
Keywords: Discrete Tomography, Function Reconstruction, Image Reconstruction, Global Maxima Analysis

Introduction

The computerized tomography (CT) is a technique to reconstruct internal structures of a body from data collected outside of it. This means that computer tomography provides a very good method to investigate the internal structure of the analyzed object without destroying it. Obviously that kind of method is very important in medicine [Hau1994].

Theoretically it is possible to reconstruct the internal structure from the finite number of filtered back projections (FBP) – FBP are simply the projections that run back through the original image to obtain a rough approximation of it. This steams from the fact that such projections interact constructively in regions that correspond to the emissive sources of the original image. In medical tomography the section images are obtained by moving an X-Ray beam around the object (patient) and record the projection on a film positioned diametrically opposed to the X-Ray beam (see Fig. 1). This method is mostly used in medicine, but also in other fields like archeology, biology, geophysics, materials science, industrial inspection, etc. Moreover different types of signal acquisition can be used, not only X-Rays. However, no matter what we study and what we use for this purpose, the computer algorithms are very similar.

Usually FBP need several hundreds of projections. It is time consuming, expensive and may damage the object. Moreover, in certain applications, the range of the function to be reconstructed is discrete and known – in case of discrete tomography only from 2 to 10 projections are needed. That is why discrete tomography was introduced.

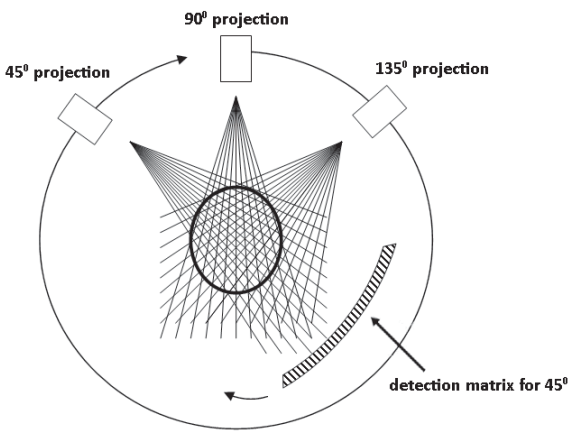

Fig. 1. CT Action Scheme

Problem description

One of the most important problems in discrete tomography is to reconstruct function $f: a \rightarrow \{0,1\}$, where a is a finite subset of $\mathbb{Z}^n$ $(n \geq 2)$, from the finite set of projections [HerKub2007]. To simplify, the problem of reconstruction when using a small number of projections is that there are a large number of solutions, which need somehow to be diminished based on the domain and type of the object. Thus, a priori information is used, such as convexity, connectedness, round-

ness, etc. So, practically, the aim of binary tomography is to reconstruct a binary image, where the object is represented in white and the background in black, using projections of the image from few different angles (see Fig. 2).

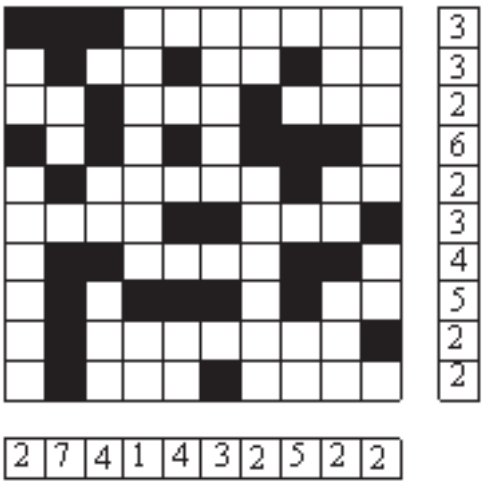

Fig. 2. Sample binary image with two orthogonal projections

State of Art

There are a lot of different methods dedicated for this problem, which employ basic methods of discrete mathematic [HerKub1999, HerKub2007], distribution theory [Haz2008], and even evolutionary algorithms for f function reconstruction. One of the most known algorithms was proposed by Ryser [Rys1957] and consists of four steps: ordering the columns in a non increasing way, filling the rows from left to right, shifting elements from the rightmost columns in a proper way and reordering the columns accordingly to the first step. On the other hand, evolutionary algorithm proposed by Balázs and Gara [BalGar2009] assumes that the original image is composed of a ring centered on the image, with some disjoint disks inside of it. The objects are represented by list of triplets, which represents the center of the disk and its radius. The evolutionary algorithm is used to minimize the difference between projections of reconstructed and original image. Difference between them is the fitness function (see Fig. 3).

Fig. 3. Original image, reconstructed image and difference between them

Discrete tomography reconstruction problem can also be solved using Kaczmarz method for Algebraic Reconstruction Technique (ART) [StrVer2009, Kac1937]. This iterative method was created for solving linear equation system. It is based on the fact that the convergence rate of Kaczmarz method can be significantly improved when the algorithm sweeps through the rows of image in a random manner, rather than in sequential order. Moreover, this method can be applied not only to binary, but also to a grayscale images (Fig. 4).

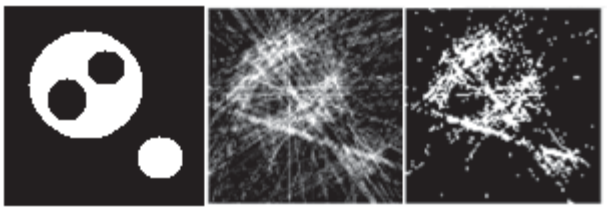

Fig. 4. Original image and its grayscale and binary reconstructions

Global extremes analysis algorithm

In this paper, a new algorithm for function f reconstruction is proposed. It analyses global extremes of two projections. For this purpose, it is assumed that initial values of function f are equal 0 for every point.

The reconstruction process starts with searching the global maxima of both projections (see Fig. 5a, indexes max1 and max2) and computing the initial point of analysis (see Fig. 5a, point C). Function value for this point is set to 1 and values of projections in corresponding indexes are decremented (in this case for indexes max1 and max2).

In the next step, points belonging to neighborhood of point C (see Fig. 5a, points N, E, S and W) are analyzed in the same way as point C. However, if value of projection in corresponding indexes equals 0 the point is no longer considered. Otherwise value of function f in this point is set to 1. Then, similar analysis is conducted for points obtained by shifting points N, E, S and W by vectors [0, 1], [1, 0], [0, -1] and [-1, 0], respectively. As a result of such operation, projection values in the indexes corresponding to point C are equal 0 (see Fig. 5b).

In the final step, successive point C is calculated using global maxima of both projections. The analysis stops when value of projections in every index is equal 0.

Discussion

Presented algorithm promotes the regions of image which contains the biggest number of object points. Series of experiments have been conducted to prove the algorithm effectiveness. Some of them are shown in Fig. 6. It can be noticed that the algorithm is very effective in case of images with consistent objects. Reconstructed images in the other cases slightly differ from original ones, however, their projections are identical (see Fig. 6).

Due to the characteristic of the proposed algorithm, it is possible to apply it into a number of problems [HerKub1999]. Biplane angiography, used for the visualization of a cardiac ventricles, can be pointed as one of them. In this case a standard procedure is to inject Roentgen contrast agent into cardiac ventricles and to take X-ray image. The aim is to determine the three-dimensional structure, therefore every two dimensional cross-section need to be reconstructed from two orthogonal

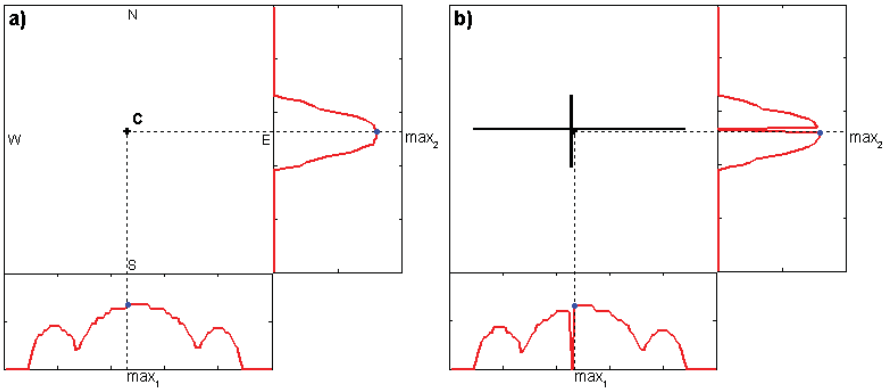

Fig. 5. Initial point of analysis (point C) and its corresponding indexes before (a) and after (b) first step of analysis

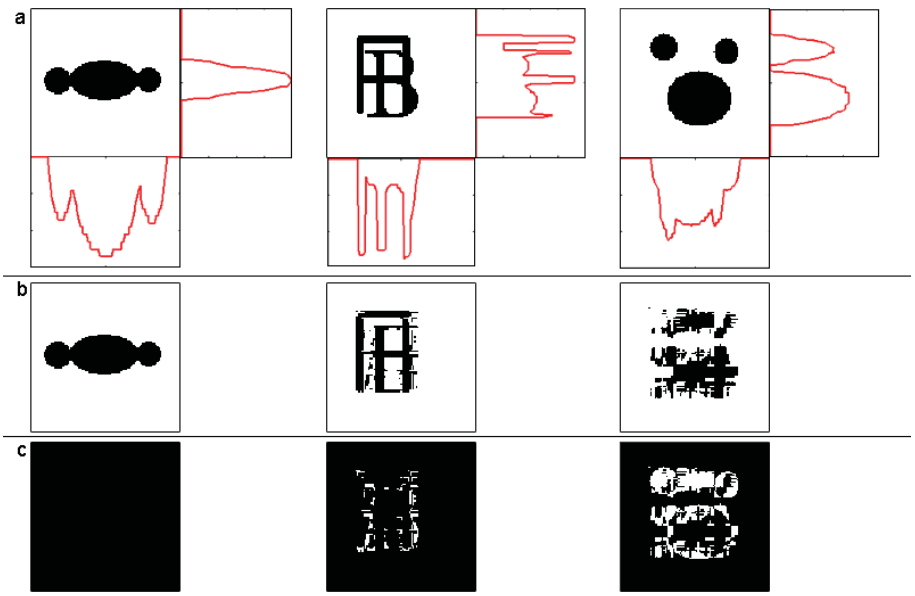

Fig. 6. Original images with projections (row a) reconstructions (row b) and difference between original image and reconstruction

projections. Moreover, it can be also applied to reconstruct structures from on the base of projections generated by electron microscopy. In this case projections are obtained by emitting electrons towards the studied object and recording them by detectors. Both applications concern the consist objects and therefore given algorithm can be used with good results.

In the future works the authors will conduct research on the effectiveness of the presented method. For this purpose, angiography images will be obtained and pre-processed to obtain binary images which separate cardiac ventricle from the neighborhood. Then presented algorithm will be applied and the result of reconstruction will be verified by a radiologist.

Conclusion

In this paper, original method of function f reconstruction from two projections has been presented. The algorithm bases on extremes analysis. It is competitive with the other algorithms [HerKub1999, HerKub2007, Haz2008, BalGar2009], due to the fact that it is effective, returns projections identical with original ones and is most effective in case of images with consistent objects. Therefore it can be used in practical applications of discrete tomography, as most reconstructed images in this domain are consistent.

References

1. [Bal2007] Balázs P. (2007), A decomposition technique for reconstructing discrete sets from four projections. *Image and Vision Computing* 25 (10), 1609-1619.
2. [BalGar2009] Balázs P., Gara M. (2009), An Evolutionary Approach for Object-Based Image Reconstruction Using Learnt Priors. *Lecture Notes in Computer Science* 5575, 520-529.

3. [Hau1994] Hausenblas E. (1994), The Salzburg NTN--Method for the Radon Transform. Technical report. Institute of Softwaretechnology, Salzburg.
4. [Haz2008] Hazama F. (2008), Discrete tomography through distribution theory. *Publications of the Research Institute for Mathematical Sciences* 44 (4), 1069-1095.
5. [HerKub1999] Herman G.T., Kuba A. (1999), Discrete Tomography: Foundations, Algorithms and Applications. Birkhäuser, Boston.
6. [HerKub2007] Herman G.T., Kuba A. (2007), Advances In Discrete Tomography and Its Applications. Birkhäuser, Boston.
7. [Kac1937] Kaczmarz S. (1937), Angenäherte Auflösung von Systemen linearer Gleichungen. *Bulletin of the Polish Academy Of Sciences Mathematics*, 335-357.
8. [Rys1957] Ryser H. J. (1957), Combinatorial properties of matrices of zeros and ones. *Canadian Journal of Mathematic* 9, 371-377.
9. [Smi2002] Smith S.W. (2002), Digital Signal Processing: A Practical Guide for Engineers and Scientists. California Technical Publishing, San Diego.
10. [StrVer2009] Strohmer T., Vershynin R. (2009), A randomized Kaczmarz algorithm with exponential convergence. 262-278.

BIO-ALGORITHMS AND MED-SYSTEMS
JOURNAL EDITED BY MEDICAL COLLEGE – JAGIELLONIAN UNIVERSITY
Vol. 6, No. 12, 2010, pp. 25–29.

A NEW ALGORITHM FOR FINGERPRINT FEATURE EXTRACTION WITHOUT THE NECESSITY TO IMPROVE ITS IMAGE

Piotr Rapta[1], Khalid Saeed[2]

Faculty of Physics and Applied Computer Science, AGH University of Science and Technology, Krakow, Poland ([1]piotr.rapta@gmail.com, [2]saeed@agh.edu.pl)

Abstract: Based on Gabor filter, an algorithm is worked out and presented in this work. The algorithm uses ridge endings and ridge bifurcation to represent a fingerprint image. The experimental results have proven the algorithm completion in preparing the fingerprint image for simple classification and hence high success rate of recognition. Spurious features from detected set of minutiae are deleted by a postprocessing stage. The detected features are observed to be reliable and accurate. The algorithm was implemented in Matlab and therefore it is under steady modification and improvement as each step can be easily visualized graphically to check for further analysis. The best feature of the algorithm is the unnecessity for noise removal, brightness or contrast improvement, normalization or even histogram equalization.
Keywords: biometrics, feature extraction, fingerprints, minutiae, Gabor filtering, feature vector

Introduction

There are mainly two methods for fingerprint identification. The first is based on examining the geometric pattern of the fingerprint minutiae and comparing (matching) it with the patterns available in the database for classification and hence recognition. In the other sort of methods only some particular elements of the minutiae (called the characteristic points or the features) are analyzed instead. In both approaches, the fingerprint image is described by a set of information data of definite structure [5]. The difficulty in the image analysis process lies in the enormous changeability of the structure in the successive registrations of the same fingerprint. The techniques used in the classification and matching of fingerprints can be of the same nature in both methods. The same procedure and steps are used before taking the decision of image identification or verification.

Fingerprint individuality can be expressed by the nature of its minutia, precisely by their kind, location and orientation [9]. The most applied minutiae are ridge endings and ridge bifurcation (Fig. 1).

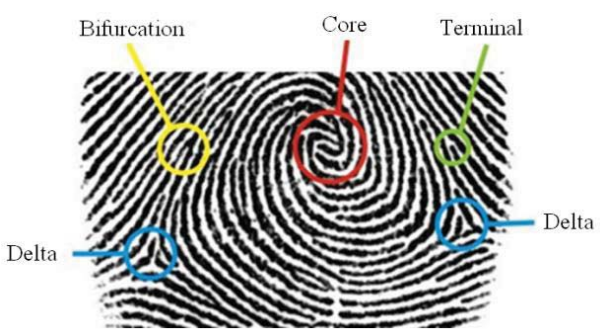

Fig. 1. Example of minutiae

Proposed algorithm

Many fingerprint recognition methods use preprocessing steps, like noise removal, brightness and contrast improvement or

Fig. 2. Original fingerprint image (256x280 pixels)

equalizing the image histogram to improve the image quality before filtering. However, the presented in this paper algorithm does not require any of these preprocessing steps. The authors have shown that a correctly selected effective filter can successfully replace these time consuming steps.

Analyzing the state of the art in the available literature, one can conclude that the best results can be achieved by applying a complex filtering system that takes into consideration both the direction and frequency of the image to be filtered. Based on Gabor filter and other works [2, 3, 7, 11] an algorithm is worked out and presented in this work. The experimental results have proved the algorithm perfection in improving the quality of the original fingerprint images.

Figure 3 shows the steps of the suggested algorithm.

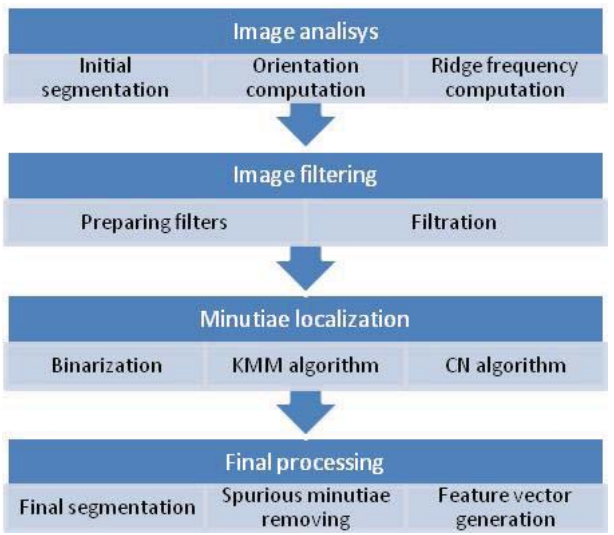

Fig. 3. The general structure of the worked out algorithm

Image analysis

Initial segmentation separates the region of interest from the background. The method of initial segmentation is very simple and based on the principle statistical functions: mean value and mean variation (Fig. 4).

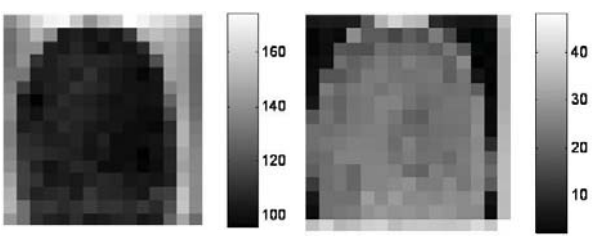

Fig. 4. Segmentation of image: mean value (a) and mean variation (b) for each image block [11]

The computation of the statistical values in each block is needed for image segmentation. Because of the fact that the major part of the fingerprint image is the region of interest, we can assign parameters in describing the range of statistical values to decide about the adherence of each block.

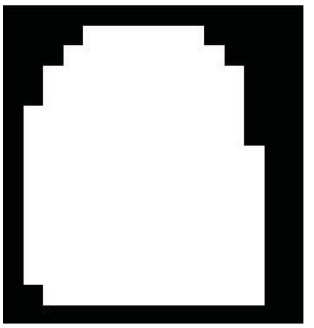

Fig. 5. Segmentation regions: the white colour – area of interest, the black colour – backround

Figure 5 presents the result of segmentation. White blocks respond to the region of interest, black blocks respond to the background.

The next step in the algorithm is to compute the orientation matrix for the input image. To do that Sobel operator is used, which represents a gradient filter.

For the computation of directional map (Fig. 6), we use images without filtration. That is why some regions may occur with error values (especially in ridges with very high distortion). To avoid errors in the region of interest, Gaussian filter is used.

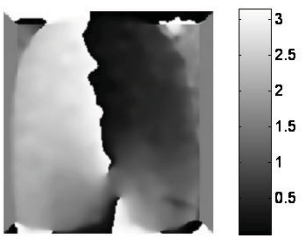

Fig. 6. Visualization of filtered fingerprint directional map (radian scale)

Core and delta localization is very important because both are reference points for minutiae. In very large databases, comparison of fingerprint takes more time. To reduce the computing time, we classify fingerprints in the registration stage. After localizing core and delta in the fingerprint image, one can easily classify the image of the fingerprint. There are many algorithms for fingerprint classification, for example „pointcare method", or „line search based method", both widely described in [6].

The proposed algorithm is built on the „line search based method", known for high precision and short time of computing. Number of delta or core depends on the fingerprint type. In the first stage we use the directional map and quantize tit in four directions as shown in Fig. 7.

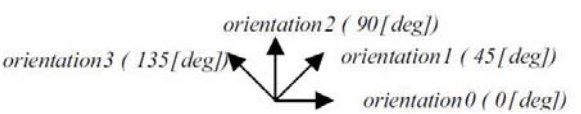

Fig. 7. Quantized direction for directional map [6]

In the quantized direction map, we search for pixels that are neighboring pixels in another direction. In effect, we receive a list of delta or core candidates (Fig. 8).

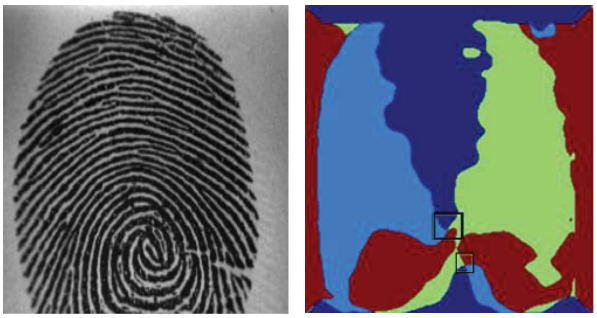

(a) (b)

Fig. 8. Fingerprint image (a) and its quantized directional map (b) with regions of delta or core candidates (squares)

The decision whether the analyzed pixel is a delta or a core candidate is determined by values distribution of the neighbor pixels. The localization of focal points is determined by mean localization of delta or core candidate.

To compute ridge frequency (differs from region to another) the input image is divided into blocks (size 16x16 pixels). For each region we calculate the mean direction and count local maxima in the orthogonal direction. In this way we obtain the ridge amount in each block. Ridge frequency is the ratio of ridge amount to the length of the block edge. This method is very sensitive to the direction computed incorrectly, so we take into account only the region of interest. When the ridge frequency for each block is computed, we tag this into the frequency matrix (Fig. 9).

(a) (b)

Fig. 9. Fingerprint image (a) and its corresponding frequency map (b)

Image filtering

Image filtering using a single Gabor filter precisely keeps the frequency band and direction. Fingerprint image consists of high ridge frequency and ridge directions, so we need many Gabor filters (a bank of filters). Filtration by Gabor filters improves the image quality and completes the disconnection in ridge flow [3, 8, 9, 11]. This helps reduce the size of false minutia list detected in the next step of the algorithm.

$$G(x, y; \theta, f) = \exp\{-\frac{1}{2}[\frac{x_0^2}{\sigma_x^2} + \frac{y_0^2}{\sigma_y^2}]\}\cos(2\Pi f x_0)$$

$$x_0 = x\cos\theta + y\sin\theta$$

$$y_0 = -\sin\theta + y\cos\theta$$

In this equation, θ represents the orientation of the normal to the parallel stripes of a Gabor function, σ is the standard deviation of the Gaussian envelope in x or y direction, f is filter frequency.

Gabor filter bases on spatial frequency and ridge direction. Ridges in fingerprint images have always the frequency and direction well defined, that is why Gabor filtering gives very good results. Gabor filter is defined as a harmonic function multiplied by Gaussian function. Thanks to this modulation, points localized near the middle of the ridge are amplified, while the others are damped (Fig. 10).

(a) (b)

Fig. 10. Original fingerprint image (a) filtered by Gabor filters bank (b)

Minutiae extraction

To apply the minutiae searching algorithm, the filtered image goes through two processes: binarization and thinning (Fig. 11). Binarization is necessary before the image thinning process.

(a) (b)

Fig. 11. Original image (a) and its thinned by KMM algorithm [10] form (b)

The next step is minutiae detection. Here we follow the widely used CN algorithm [5] as shown in Fig. 12.

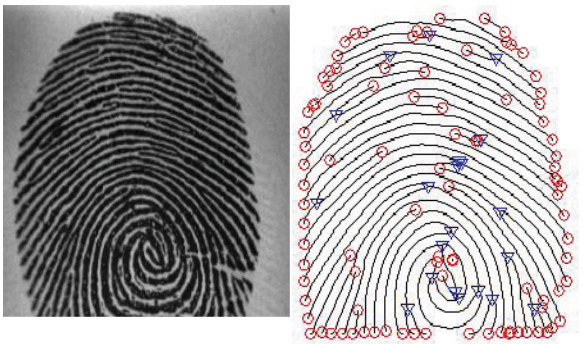

(a) (b)

Fig. 12. Original image (a) and its thinned form (b) with minutiae marked on it (CN algorithm)

Final processing steps

The final processing includes final segmentation and spurious minutiae removing. There are mainly two reasons why spurious minutiae usually exist. The first is the noise coming from dirty fingers or scanners [4]. The second is the deformation caused by filtration and thinning (Fig. 13). It is easy to effectively remove these spurious minutiae.

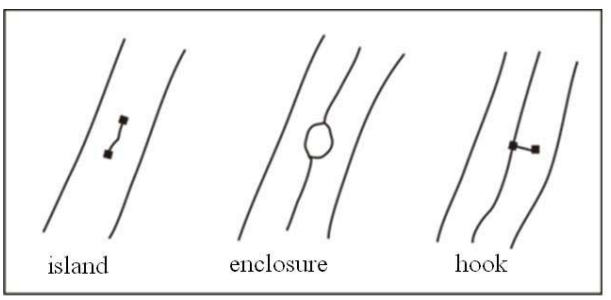

Fig. 13. False ridge termination and bifurcation, generated by other minutiae

In Fig. 13 one can see three types of false minutiae, caused by improper filtration. Authors' proper false minutiae removal method is based on the distance between the original minutiae and the work in [7].

Feature vector

The final step of the algorithm is the feature vector generation. Feature vector consists of three elements. The first corresponds to the localization and orientation of ridge terminals. The second corresponds to bifurcation in the same way. The last element (optional) implies focal points localization (a core or a delta).

An example that illustrates the final results is presented in Fig. 14.

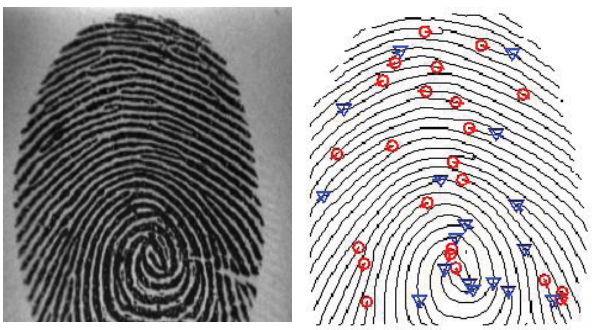

(a) (b)

Fig. 14. The original fingerprint image (a) and its thinned form (b) with the minutiae and their direction marked on it. The circles refer to the termination while the triangles refer to the bifurcation

Comparison and analysis of algorithm results

The results of the algorithm were compared with the results of other methods, such as Fourier filtration, histogram alignment and Hong algorithm [1]. We tested the algorithms at various quality images. Below we present the results of the algorithm for a fingerprint image of middle quality (Fig. 15).

Fig. 15. Middle quality fingerprint image used for algorithms testing

The comparison with the described in [1] algorithms has shown that algorithms based on Fourier filtration and histogram alignment give very poor results. An image without correct filtration cannot be thinned and analyzed by CN algorithm.

However, very good results can be observed from authors' and Hong algorithms, because both are based on Gabor filtration. The difference in the image quality is therefore only caused by other parameters and the method of direction map generation. Table 1 presents the results of the comparison between the sub-algorithm of minutiae detection (Fig. 15).

Analyzing the results given in Table 1, one can conclude that both the authors' and Hong algorithms give very good results. In both algorithms spurious minutiae detection was unnecessary.

Tab. 1. Results of comparison between algorithms from minutiae point of view. The numbers present terminations/bifurcations

Algorithm	Fourier	Histogram alignment	Hong	Authors'
After segmentation	52/56	84/46	16/4	19/3
After spurious minutiae removal	12/18	30/14	16/4	19/3

Conclusion

In this paper a new algorithm for fingerprint feature extraction was presented. This algorithm does not need all steps of image preprocessing. It was implemented in Matlab in its educational version. As a result, a feature vector (with focal points) is obtained and used as the input to the classification step for fingerprint identification or verification. The algorithm was tested on various image qualities and has proven to be promising.

Feature work implies working out a system that recognizes the fingerprint image from image acquisition to classification for identification and verification.

References

1. Bućko Ł. (2009), Identyfikator linii papilarnych. Praca magisterska. Białystok: Politechnika Białostocka.
2. Greenberg S., Aladjem M., Kogan D., Dimitrov I. (2002), Fingerprint Image Enhancement using Filtering Techniques. *Real-Time Imaging* 8/3, 227-236.
3. Hong L., Wan Y., Jain A. (1998), Fingerprint Image Enhancement: Algorithm and Performance Evaluation. *IEEE Transactions on Pattern Analysis and Machine Intelligence* 20/8, 777-789.
4. Kim S., Lee D., Kim J. (2001), Algorithm for Detection and Elimination of False Minutiae in Fingerprint Images. In: *Lecture Notes in Computer Science*. Berlin: Springer, 235--240.
5. Maltoni D., Jain A. K., Maio D., Prabhakar S. (2003), Handbook of finterprint recognition. New York: Springer.
6. Ohtsuka T., Watanabe D., Aoki H. (2007), Fingerprint Core and Delta Detection by Candidate Analysis. *MVA2007 IAPR Conference on Machine Vision Applications, Tokyo, Japan*, 130-133.
7. Porwik P., Wiecław Ł. (2008), Local binarization and fingerprint area extraction in recognition systems. In: *BIOMETRYKA*. Warszawa: Institute of Mathematical Machines, 97-106.
8. Porwik P., Wiecław Ł. (2009), A new fingerprint ridges frequency determination method. *IEICE International Journal Electronics Express* 6/3, 154-160.
9. Ratha N., Bolle R. (2004). Automatic Fingerprint Recognition Systems. New York: Springer.
10. Saeed K., Tabędzki M., Rybnik M., Adamski M. (2010), K3M – A Universal Algorithm for Image Skeletonization and a Review of Thinning Techniques. *International Journal of Applied Mathematics and Computer Science* 10/2, 317--335.
11. Thai R. (2003), Fingerprint Image Enhancement and Minutiae Extraction. The University of Western Australia.

BIO-ALGORITHMS AND MED-SYSTEMS
JOURNAL EDITED BY MEDICAL COLLEGE – JAGIELLONIAN UNIVERSITY
Vol. 6, No. 12, 2010, pp. 31–35.

PERFUSION COMPUTED TOMOGRAPHY IN THE PROSTATE CANCER DIAGNOSIS

JACEK ŚMIETAŃSKI

Institute of Computer Science, Jagiellonian University, 6 Łojasiewicza St., 30-348 Kraków, e-mail: jacek.smietanski@ii.uj.edu.pl

Abstract: One of the main causes of – still high – mortality among patients who suffer from the prostate cancer is the too late detection of its presence. The existing diagnostic difficulties induce to seek new, better diagnostic methods, for example specific biomarkers or advanced imaging techniques. One of the proposals with the potential to increase an early detection of prostate cancer is the perfusion computed tomography. This method has been tested for some years in the Oncology Center, Cracow. Unfortunately, the perfusion prostate images are not clear and difficult to interpret. Therefore an attempt was made to develop algorithms using the image processing and pattern recognition techniques, which – as it seems – can greatly facilitate the process of searching the correct cancer location.

The results of the proposed algorithm are promising, but the test data were not fully representative, because of too few cases, including few healthy patients analyzed. Hence the need for more research on a larger group of patients is obvious. It means that the simple method for automatic verification of the proposed locations, with confirmed indications made using another technique, must be created. The most reliable verification technique is a histological evaluation of postoperative specimens. However, it cannot be used in all cases, also a different plane of imaging causes additional difficulties.

Keywords: prostate cancer, perfusion computed tomography, medical image analysis, pattern recognition

Streszczenie: Jedną z głównych przyczyn wciąż wysokiej śmiertelności wśród chorych na raka prostaty jest zbyt późne wykrycie obecności tego nowotworu. Istniejące trudności diagnostyczne skłaniają do poszukiwania nowych, lepszych metod, np. specyficznych biomarkerów czy technik zaawansowanej diagnostyki obrazowej. Jedną z propozycji mających potencjał do zwiększenia wykrywalności wczesnego raka prostaty jest perfuzyjna tomografia komputerowa. Metoda ta od kilku lat testowana jest w krakowskim oddziale Centrum Onkologii. Jednak perfuzyjny obraz stercza jest mało wyrazisty i trudny w interpretacji, dlatego podjęto próbę opracowania algorytmów wykorzystujących techniki komputerowego przetwarzania i rozpoznawania obrazów, co – jak się wydaje – może wydatnie ułatwić proces poszukiwania i właściwej lokalizacji nowotworu.

Zaproponowany algorytm uzyskał obiecujące wyniki na danych testowych, te jednak nie do końca były reprezentatywne, uwzględniały bowiem zbyt małą liczbę przypadków, w tym mało osób zdrowych. Stąd konieczność rozszerzenia badań na szerszą grupę pacjentów, co wiąże się z potrzebą opracowania prostej metody automatycznej weryfikacji wskazań algorytmu z potwierdzoną inną metodą lokalizacją nowotworu. Najbardziej wiarygodną metodą porównawczą jest ocena histopatologiczna preparatów pooperacyjnych. Nie może być ona jednak stosowana u wszystkich pacjentów, a odmienna płaszczyzna obrazowania nastręcza dodatkowych trudności.

Słowa kluczowe: rak prostaty, perfuzyjna tomografia komputerowa, przetwarzanie obrazów, sztuczna inteligencja

Introduction

There is no doubt that the prostate cancer (PCa) is one of the most important medical problems. Although there exist numerous methods and procedures for treating that malignancy, their successfulness strongly depends on the tumor progression. Only the PCa detected in enough early stage – before the metastasis occurs – can be successfully cured. Although its detectability is much better than several years ago, the diagnostic techniques are still insufficient and often fail.

Nowadays the most popular diagnostic procedures of PCa are the PSA protein measure and the DRA *(per rectum)* examination [3,12]. Both suffer from too low level of sensitivity and specificity. The higher the PSA level, the greater the likelihood of cancer. But the problem lies in the fact that the increase in the concentration of this protein is also observed in benign diseases, it is also a natural process associated with the patient's age. Hence the results cannot imply the clear diagnostic decision. Also the second method – the DRA study – can capture only those changes which are perceptible in the peripheral zone of prostate apex.

The only technique which allows to confirm the existence of PCa is biopsy, at which a small portion of the gland is taken for histological examination. Of course, such a confirmation is possible only when the biopsy needle successfully hits into the pathologically changed part of the gland. Routinely accompa-

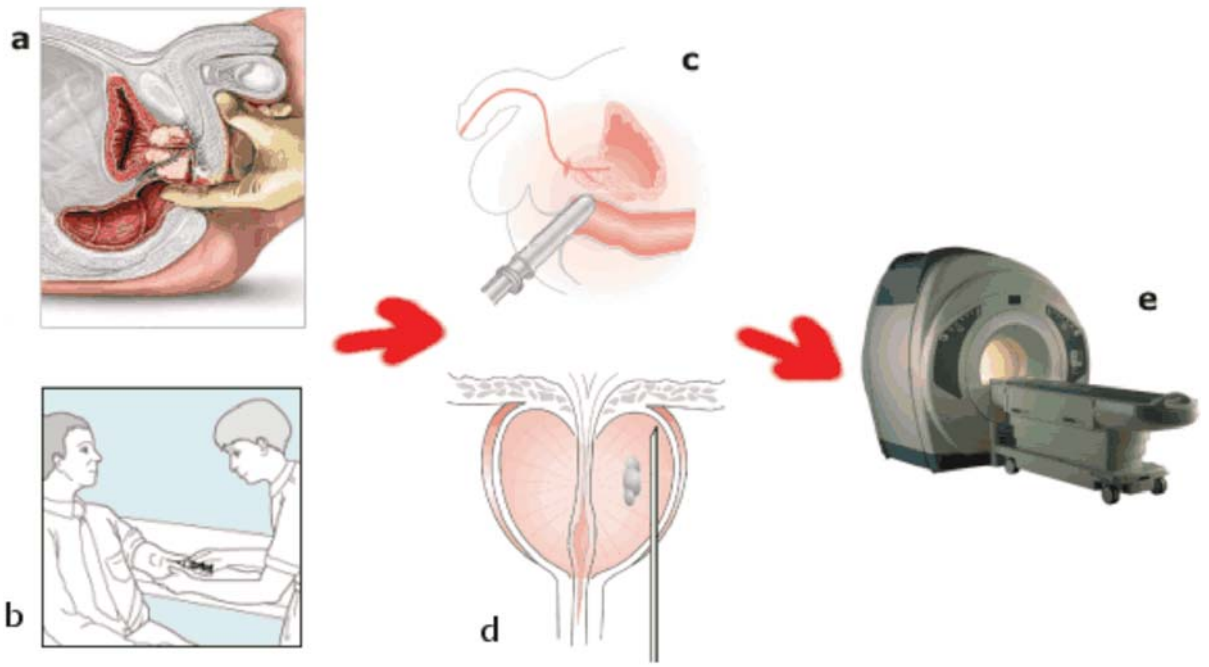

Fig. 1. The scheme of PCa diagnosis: a) ***per rectum*** examination (DRE); b) blood examination (PSA measure); c) transrectal ultrasound (TRUS); d) biopsy; e) additional radiology diagnostic

nying biopsy transrectal ultrasound examination (TRUS) can help to indicate the suspected region, however, it often does not work (when the changes are izoechogenic, invisible in TRUS). In such cases, a diagnostician is forced to collect tissue from randomly selected fragments of the gland, which is burdensome for the patient and may be fatal in consequences when the decision is incorrect [13,14].

An additional radiological diagnostic, like conventional computed tomography (CT), can help only with detection of metastasis in advanced PCa.

Perfusion computed tomography

The perfusion computed tomography (p-CT) technique enables to measure some parameters of blood flow within diagnosed organs. In this method the patient is injected the bolus and repeated scans using the multislice CT scanner are made. The measured parameters are: blood flow (BF), blood volume (BV), mean transit time (MTT), and permeability surface (PS) [1,18].

Nowadays the p-CT examination is used mainly in diagnosis of the brain acute stroke [5,10], but the usefulness of this method was also tested on other organs including prostate [4,6,7,11]. Its application to detecting cancerous lesions is based on the effect of angiogenesis – the documented evidence for creation of new blood vessels in tumor [2,8,9]. Although prostate is not highly vascularized, it is supposed that the p-CT can indicate these suspicious areas also in this gland.

Experiments

In the author's previous work the set of p-CT prostate images was analyzed. The p-CT examination was held by experienced radiologists in the Cracow branch of the Oncology Center. Totally over 50 patients with proved or suspected PCa and 1 patient without any pathological or suspected changes within prostate were diagnosed. The images were generated using *Advantage Workstation*, the part of the tomographic system.

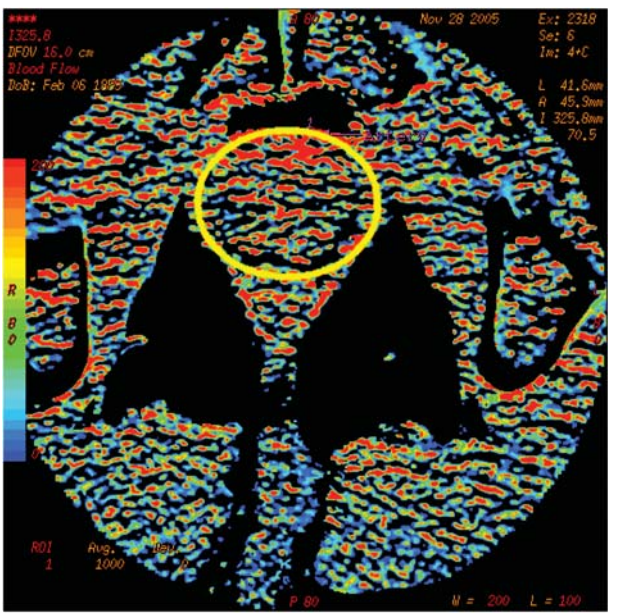

Fig. 2. The example of p-CT image – the minor pelvis cross-section. The oval marks the area of the prostate

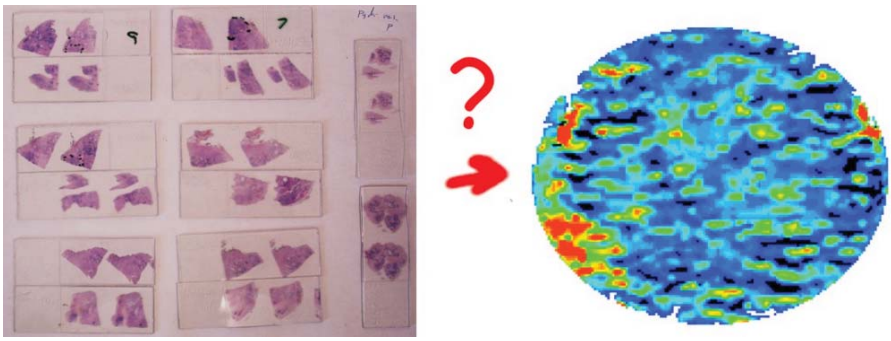

Fig. 3. How to transform information from histological specimens (left) into the p-CT prostate image (right)?

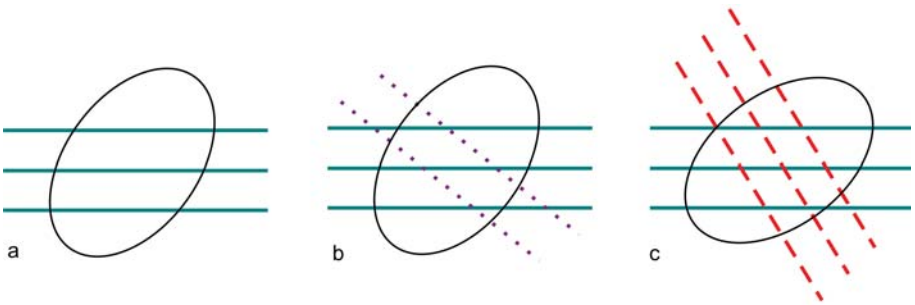

Fig. 4. a) the p-CT images are created in axial plane of the minor pelvis (solid line); b) images of postoperative specimens are not in the same plane (dotted line); c) for another prostate gland the plane for create histological images (dashed line) may differ

Each image, sized 512x512 pixels, presents the whole cross-section of the minor pelvis. The prostate is located in its central area (fig. 2).

From such images the prostate area was manually selected and used for further analysis. More details about images, used preprocessing methods and recognition algorithm were described in our earlier works [15,16,17] and are not important for our present discussion. The only thing which should be noted is that only 59 out of 159 images[1] accepted for analysis have tumor location confirmed. Is means that only a small part of images could be used for testing and estimate the algorithm effectiveness.

However, the recognition results were promising (86% of correct recognitions – sensitivity 92%, specificity 67%). Therefore an attempt to improve used algorithm and repeat the experiment on a large set of images acquired from representative group of patients with surely confirmation of the cancer presence and (if yes) its precise location.

Cancer confirmation

The aforementioned task seems to be very difficult. Although the PCa location may be confirmed using postoperative histological specimens, it must be done by hands, which is a very time consuming and not always possible process. In view of this the most important task is to improve the technique for comparison of those two types of images. For example, to create an automatic or semiautomatic system enabling fast transformation of the histological result into the p-CT image (fig. 3).

Unfortunately, we met a number of problems, partially connected to insufficient information about source images. The most important are:

- inconsistent image scaling;
- different and not determined levels of p-CT examination;
- not determined angle of imaging.

The first issue is the effect of scaling p-CT source image. As it was said, each cross-section was transformed into 512x512 pixels image, regardless of the patient's body shape and circuit. It means that fat men's prostate seemed to be smaller than the same size prostate of rather thin men. Additionally, the prostate was stretched into an ellipse. As it is known, scaling means loss of some important image information. Moreover, we cannot rescale it into the original size as we do not know the scaling parameters. The postoperative specimens were given in its natural size, so their comparison is not easy.

The second problem is more difficult to alleviate. It occurs because in the p-CT imaging we usually do not diagnose the whole prostate gland, but only a two centimeters wide fragment. We do not have any information which part of prostate was exactly scanned. It was said that the examination levels correspond with the apex, middle and base of the gland. But it is only an approximation. The real position of the diagnosed levels remains unknown.

Also the third problem must be solved in some way. It is connected with different imaging angles. The p-CT images were taken always in axial plane, but the histological speci-

1 The total number of patients were 57, for each patient 3 images (for each parameter) were generated. It makes 57*3=171 images. However, some of them were not good enough to accept for analysis, so the final number was 159.

mens are created certainly from apex to base. This angle is not only different from that in which the p-CT image is created, but may differ for each analyzed prostate.

Of course, the 3D reconstruction is not a real problem, but to do it well we should know the angle in which the postoperative images are created, the scaling parameters for the p-CT image, and levels of p-CT examination. Without such information, the reconstruction and comparison of the two images may be extremely hard.

There is one thing more – the postoperative histology specimens are available only for people with detected PCa and removed prostate gland. How about data from people who were not operated or the PCa was not proven (but we are not certain if it really does not exist)?

More problems

One of the advantages of the p-CT method is its availability. Especially if compared with other imaging techniques, like MRI or PET. It is also much cheaper than other methods. However, it must be noted that p-CT examination cannot be done anytime for every patient. We use X-ray and the contrast bolus, which may have negative impact on the patient's health. Therefore this kind of diagnosis should be used carefully, only in justified cases. Especially healthy people should not be examined. This implies ethical problems. Should we conduct the experiments on healthy patients or rather not?

Another question is, how may p-CT images be useful in everyday diagnostic. Suppose we have a reliable computational system, capable to correctly point out the cancerous regions. Is the p-CT precise enough to specify the PCa staging and grading? This is necessary for take up appropriate treatment. If not, the biopsy should be conducted. However, the biopsy may be successful only if the biopsy needle correctly hits into cancerous region. It is problematic in general. Could the p-CT help in pointing out the proper region for biopsy? Is the biopsy under p-CT control possible?

The results of p-CT examination depend on CT scanner work parameters, like voltage, time of examination, amount and rate of bolus administration. Also the selection of input function [18] is important for result calculation. Which parameters are the best? Could the results achieved by different tomographs be compared? To answer to this question, more and more experiments are needed.

Conclusions

Although the results of previous research are promising, the usefulness of p-CT technique in prostate cancer imaging may be limited due to the discovered problems with the histological confirmation of cancer location for a large set of images. Additionally, due to ethical problems it may be difficult to achieve images of healthy prostates, which are necessary to construct ra eliable control group for testing.

This, and other problems presented in this paper, make the p-CT not clearly useful. More experiments must be taken to asses the value of this examination. Therefore we conclude that the p-CT method may be practical, but firstly the improvement of this technique is needed.

Particularly, the whole prostate should be analyzed. Additionally, the image creation technique by tomographic system must be improved. Also all the information which enables a comparison of the p-CT image with the histological specimens must be calculated and presented. A good idea may lay in the 3D image creation, based directly on p-CT signal analysis. The 3D model may be easier to compare with postoperative histological data. This guarantees a fast and simply confirmation of the usefulness of the p-XT image recognition algorithms.

References

1. Cenic A., Nabavi D.G., Craen R.A. et al. (2000), CT method to measure hemodynamics in brain tumors: validation and application of cerebral blood flow maps. *Am. J. Neuroradiol*. 21, 462-470.
2. Charlesworth P., Harris A. (2006), Mechanisms of disease: angiogenesis in urologic malignancies. *Nature Clinical Practice Urology* 3(3), 157-169.
3. Chwaliński T. (2001), Rak stercza: rozpoznanie i leczenie. *Nowa Medycyna* 113, 5-6.
4. Henderson E., Milosevic M.F., Haider M.A., Yeung I.W. (2003), Functional CT imaging of prostate cancer. *Psys. Med. Biol.* 38, 3085-3100.
5. Hoeffner E.G., Case I., Jain R. et al. (2004), Cerebral perfusion CT: technique and clinical applications. *Radiology* 231(3), 632-644.
6. Ives E.P., Burke M.A., Edmonds P.R. et al. (2005), Quantitative computed tomography perfusion of prostate cancer: correlation with whole-mount pathology. *Clinical Prostate Cancer* 4(2), 109-112.
7. Łuczyńska E., Anioł J., Stelmach A., Jaszczyński J. (2008), The value of perfusion CT in evaluating locoregional staging in post-radical prostatectomy patients with elevated serum PSA level. *Pol. J. Radiol*. 73(2), 13-17.
8. Miles K.A. (1999), Tumour angiogenesis and its relation to contrast enhancement on computed tomography: a review. *Eur. J. Radiol*. 30, 198-205.
9. Miles K.A. (2002), Functional computed tomography in oncology. *European Journal of Cancer* 38, 2079-2084.
10. Miles K.A., Griffiths M.R. (2003), Perfusion CT: a worthwhile enhancement? *Br. J. Radiol*. 76, 220-231.
11. Prando A., Wallace S. (2000), Helical CT of prostate cancer: early clinical experience. *American Journal of Roentgenology* 175(2), 343-346.
12. Roscigno M., Scattoni V., Bertini R. et al. (2004), Diagnosis of prostate cancer. State of the art. *Minerva Urol. Nefrol*. 56(2), 123-145.
13. Scattoni V., Zlottab A.R., Nava L. et al. (2002), Prostatic transrectal ultrasound (TRUS) guided biopsy schemes and TRUS prostatic lesion-guided biopsies. *European Urology Supplements* 1, 28-34.
14. Sudoł-Szopińska I., Szopiński T. (ed.) (2005), Diagnostyka ulstrasonograficzna gruczołu krokowego. Praktyczna Ultrasonografia. Warszawa – Zamość: Roztoczańska Szkoła Ultrasonografii.
15. Śmietański J., Tadeusiewicz R. (2009), Computational Analysis of Prostate Perfusion Images – a Preliminary Report. *Bio-Algorithms and Med-Systems* 5(10), 25-30.

16. Śmietański J., Tadeusiewicz R., Łuczyńska E. (2010), Texture Analysis in Perfusion Images of Prostate Cancer – Case Study. *International Journal of Applied Mathematics and Computer Science* 20(1), 149-156.
17. Śmietański J., Tadeusiewicz R. (2010), System automatycznego wykrywania i lokalizacji raka stercza na obrazach perfuzyjnej tomografii komputerowej. *Automatyka*.
18. Wintermark M., Maeder P., Thiran J.-P. et al. (2001), Quantitative assessment of regional cerebral blood flows by perfusion CT studies at low injection rates: a critical review of the underlying theoretical models. *Eur. Radiol.* 11, 1220--1230.

BIO-ALGORITHMS AND MED-SYSTEMS
JOURNAL EDITED BY MEDICAL COLLEGE – JAGIELLONIAN UNIVERSITY
Vol. 6, No. 12, 2010, pp. 37–42.

PERFUSION CT IN PROSTATE CANCER DIAGNOSTIC – COMPARATIVE DISCUSSION

Jacek Śmietański*, Ryszard Tadeusiewicz**

** Institute of Computer Science, Jagiellonian University, ul. Łojasiewicza 6, 30-438 Kraków, e-mail: jacek.smietanski@ii.uj.edu.pl*
*** Department of Automatics, AGH University of Science and Technology, al. Mickiewicza 30, 30-059 Kraków, e-mail: rtad@agh.edu.pl*

Abstract: The improvement of tomographic techniques, such as spiral tomography, multi-slice tomography and finally perfusion computed tomography (p-CT) methods, allows us to acquire not only anatomical but also functional information about diagnosed internal organs. This state-of-the-art technique becomes more and more applicable, enabling fast evaluation of larger and larger fragments of the body without significant increase of unnecessary radiation and the amount of injected bolus.
The usefulness of the p-CT diagnostic in detection of early prostate cancer (PCa) is still debatable. During last decade there were only few publications concerning this problem. In addition, those works lead to completely different conclusions. However, as it is shown in this article, most of those researches were held on too small and non-representative groups of patients. In addition, some of the statistical interpretations of the results were insufficient or incorrect. In this article we show a counterexample to reasoning described in one of those works.
Keywords: perfusion computed tomography, prostate cancer diagnostics

Streszczenie: Dynamiczny rozwój technik tomografii komputerowej, takich jak tomografia spiralna, wielorzędowa, czy w końcu perfuzyjna tomografia komputerowa (p-CT) sprawia, że obecnie możliwe jest uzyskanie nie tylko precyzyjnych danych anatomicznych poszczególnych organów wewnętrznych, ale też określenie ich funkcjonowania. Wraz z postępującym rozwojem, technologia p-CT staje się coraz bardziej użyteczna, umożliwiając szybką diagnozę coraz większych fragmentów ciała bez znaczącego wzrostu przyjętej dawki promieniowania czy ilości zastosowanego środka kontrastowego.
Tym niemniej przydatność tej metody (p-CT) w diagnozie wczesnego raka prostaty jest wciąż dyskusyjna. W ciągu ostatniej dekady pojawiło się zaledwie kilka prac dotykających tego problemu, a prace te prowadziły do sprzecznych wniosków.
W niniejszym artykule dokonano porównania tych dotychczas opublikowanych prac, wskazując na fakt, iż większość badań prowadzona była na bardzo niewielkiej, niereprezentatywnej grupie pacjentów, a statystyczna analiza wyników była czasem niewystarczająca lub błędna. Istotnym elementem naszej pracy jest wskazanie kontrprzykładu wykazującego błędne rozumowanie w jednej z przytoczonych tutaj publikacji.

Introduction

The difficulties in detecting prostate cancer (PCa) using routine diagnostics methods (measure of PSA, digital rectal examination, transrectal ultrasound, biopsy) [1-3] leads to attempts to find another techniques which could manage in the hardest cases, where standard, mentioned above, methods fail. One of those methods under investigation is perfusion computer tomography (p-CT).

Measuring tissue perfusion allows us for a quantitative analysis of blood flow in individual parts of the diagnosed organ. Initially, the methods based on the measurement of perfusion level were formed to help with diagnostic of diseases connected with reduced or declined blood flow through the tissue, but they became also useful in oncology, where the p-CT method is now able also to point out the angiogenic regions [4].

The p-CT imaging is a relatively new and still not enough known method. Most of the procedures have not been standardized yet, what makes it problematic to compare results achieved in different diagnostics centers. However, such attempts to define certain procedures, especially in brain diagnosis, have already been taken [5]. Another problem lies in ambiguous terminology (especially in early literature, where the currently most common word “perfusion” was seldom in use) [6].

The perfusion imaging can be held using different diagnostic methods. The most widely it is used in MRI imaging [7,8], but perfusion was tested also with PET [9], SPECT [10], Xe-CT [11] and other techniques [12]. Nevertheless, because of the expensive equipment, low accuracy and difficulties in results evaluation, the usefulness of those methods is limited [13].

General outlook of p-CT imaging

Nowadays the researches focus more often on the p-CT method. It seems to be better than perfusion MRI and other perfusion methods because of lower cost, better availability and more precise results (p-CT is the quantitative method). However the p-CT examination, like all tomographic methods, is connected with radiation, so it should be taken only in justified cases. Fortunately, the radiation absorbed dose is not much higher than in traditional CT [14]. Another risk in p-CT is connected with contrast, injected to artery before examination [15,16], so there are usually more expensive but also safer non-ionic contrast media in use [17].

The limitation of the p-CT technique is the relatively little width of the area which can be examined at one time. Actually, depending on the class of tomograph it cannot be wider than 10-40 mm. However, the fast evolution of this technology suggests that it will be soon possible to perform examinations of such organs as brain, liver, kidneys or heart entirely. [18]

First of all, this method has found applications in diagnosis of brain acute stroke [14,19,20] where it enables a more precise and earlier determination of changes within brain, what has a critical meaning in therapy planning. The usefulness of this method was also researched with reference to other organs, e.g. in diagnostics of gliomas [21], cancer of head and neck [22], liver [23], spleen and lymph nodes [24], pancreas and kidney [25], lung [26], rectum [27], or in research of blood flow in heart [28]. In most of these studies, researchers focused on the detection of metastases, differentiation of benign from malignant lesions, and assessment of therapeutic response.

The p-CT examination can be made together with other imaging techniques to take the advantages of complimentary information. For example, in PET/CT we achieve information about cancer metabolism, while the p-CT could point out angiogenic regions. Those complementary information are useful while estimating the tumor therapy efficiency. [29]

The purpose of this paper is to summarize the results achieved in different studies on p-CT in prostate cancer diagnosis.

p-CT in prostate investigations

According to the authors' best knowledge at the moment of writing this paper (the end of 2009), there were four teams who addressed this problem [30-34].

The first published work (Prando, Wallace 2000) [30] describes examinations taken for 35 patients, where 25 had confirmed PCa and 10 had increased PSA level or positive DRE examination result, but in biopsy there were no pathological changes. At the obtained p-CT images the areas around the edge of both prostate lobes were analyzed. The authors searched for suspected sites of asymmetric flow. Unfortunately, they neither indicate the size of the analyzed ROI (region of interest), nor the qualification criteria of the suspect area. Their results were compared to results obtained during the biopsy, and show 58% efficiency of detection the PCa areas.

The research by Henderson et al (2003) [31], conducted on a group of 9 patients, focus on the evaluation and the detection of differences in the obtained values. The proposed method of determining ROI on the given image is based on the analysis of the brightness level of the points inside the prostate – the borders of the ROI pixels showed the blood flow $BF > 0.3 \frac{ml}{\min\ g}$, and the border had to be a continuous area containing of at least 10 pixels. The ROI designated in this way was called a "hot spot". For comparison a symmetric "cold spot" area was designated on the opposite lobe of the prostate. The average and standard deviation of pixels brightness were calculated both for the entire prostate, as well as for the regional "hot spot" and "cold spot". Those values were compared, obtaining statistically significant differences in the values of the blood flow *(BF)* and blood volume *(BV)* parameters. The assessment of accuracy of selecting the "hot spot" areas and its compliance with the location of cancer were based on the biopsy and physical examination (DRE) results. However, it was rather coarse, and certainly not enough – it was rated only the location of the suspicious lobe, not the exact location of cancer.

In the work by Ives et al (2005) [32] the p-CT results for 10 patients with confirmed prostate cancer, qualified for surgical treatment, were analyzed. The calculations were done at three levels corresponding to the basis, middle and apex of the gland. On each image two regions near the prostate boundary area with the highest value of perfusion (one on the left, one on the right lobe) were indicated. The blood flow perfusion values (*BF*) were compared with the tumor volume (*v*) observed on postoperative histopathological samples for each of the 6 considered ROI. The correlation coefficient between *BF* and *v* was calculated for each ROI and for each patient. The published results indicate a statistically significant ($p<0.05$) relationship between the perfusion values and the tumor volume only in large, advanced cancer.

Critical discussion and counterexample

For the last mentioned research (Ives et al, 2005 [32]) we noted, however, that the statistical analysis was too simplified and did not include cancerous areas located outside the analyzed ROIs. Moreover, the selection of ROIs strongly prefers large monofocal tumors. It is because the investigator had to indicate the suspicious areas on each image, even if the differences in perfusion values were not significantly large. Below we present a simply **counterexample** to the reasoning presented in the cited work. In this theoretical (but possible) situation we assume a linear relationship between the value of perfusion *(BF)* and the tumor volume *(v)* as it is shown in equation 1 and figure 1a.

$$BF = v + 0.1 \tag{1}$$

We present two possible situations:

1. Tumor with multiple small foci – in each ROI one small focus ($v=0.1$) is located. According to the mentioned above relationship, the *BF* values in each ROI are equal or close to *0.2* (table on fig. 1b).

2. Large monofocal tumor – in this example the cancer is presented only in one of the 6 analyzed ROIs, and its volume is large ($v=0.9$). According to the relationship (eq.1, fig.1a) the *BF* value in this ROI is close to *1*, and in each of the remaining ROIs *BF* is close to *0.1*.

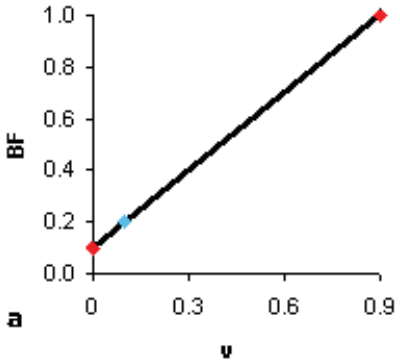

b

v	BF
0.1	0.198
0.1	0.199
0.1	0.200
0.1	0.200
0.1	0.201
0.1	0.202

c

v	BF
0.0	0.098
0.0	0.099
0.0	0.100
0.0	0.101
0.0	0.102
0.9	1.000

Fig. 1. Hypothetical relationship between perfusion and tumor volume: a) chart with data points marked b) table for tumor with multiple small foci – the calculation for the ROIs indicated in the table shows a complete lack of correlation between ***BF*** and ***v*** (***r = 0***), c) table for large monofocal tumor – the results of calculations indicate a strong correlation between ***BF*** and ***v*** (***r > 0.99***). Description in the text

In the first situation there is a complete lack of correlation between *BF* and *v* (correlation coefficient *r = 0*), but in the second one we have a strong correlation between *BF* and *v* (*r > 0.99*).

p-CT investigations performed in Krakow

The last discussed here team – Łuczyńska et al (2006) [33] is located in Krakow and authors of this paper sometimes cooperate with this research group. Łuczyńska et al described a case of a patient to whom both biopsy and periodically performed TRUS did not show any change. Only the p-CT measurements were able to detect the PCa – thanks to the visible difference in blood flow parameters, the diagnostician could put the biopsy needle into the appropriate area and confirm the existence of cancer. Thus appears that perfusion imaging can significantly assist in diagnosis. However, a single case cannot be generalized.

In the second work of Łuczyńska's team (2008) [34] there are presented results for 24 patients. All of them had confirmed PCa and were operated. Similar to the Ives' work [32] the diagnosed regions were split into three levels. The pathological changes were searched independently on each level of each lobe in the peripheral zone of the prostate. Unfortunately, the histopathological verification was not accurate. The authors were able only to say in which lobe (left or right) the foci were detected. In the cited work the four perfusion parameters were taken into consideration: blood flow (*BF*), blood volume (*BV*), mean transit time (*MTT*) and permeability surface (*PS*). Unfortunately, we do not know how the different kinds of images were analyzed and how the various components from those parameters were joint into a final result for the patient. The result takes one of four possible values:

I. suspicious areas present in both lobes;
II. suspicious areas only in right lobe;
III. suspicious areas only in left lobe;
IV. suspicious areas not found.

The final analysis was limited only to determining the correlation coefficients between the PSA level, the Gleason score and the described above perfusion images observations. The authors show a correlation between PSA level and the number of lobes suspected for the presence of cancer. However, it must be said that such an analysis is of very little or even no value. The sense of p-CT imaging lies in its potential ability to point out an accurate localization of PCa. It is obviously not enough to know only in which half of the gland the tumor exists. In addition, the presented correlation results are not very reliable, since a single outlier has a significant impact on them. It is also worth to note the fact (not mentioned in the cited work), that even such generalized results show only 46% accuracy with the histopathological results.

Especially interesting are the results for patients with the mucinous carcinoma [35] – the rare variety of PCa. A comparison of the histopathological findings with the results of p-CT gave the worst results in studies by Ives et al [32] (which was explained by unusualness of this cancer variety, but probably was the effect of the aforementioned errors in the results interpretation), while only the p-CT method was able to detect the mucinous carcinoma in the Cracow Oncology Center [33].

Comparison of results presented by different researchers

Table 1 summarizes and compares the techniques and research methodologies presented in the discussed above papers.

Also the researches on the usefulness of the p-CT method to monitor the effectiveness of treatment were taken. Harvey et al [36,37] diagnosed patients undergoing radiotherapy before the start, 1-2, and 5-6 weeks after the exposure. Perfusion study was able to detect an acute hyperemic response, which is one of the possible effects of radiation.

Conclusion

The p-CT is a medical visualization method which is best known as a tool for the brain diagnosis. It is because the brain is very well blooded and the brain p-CT images are quite easy to interpretation. However, the studies on p-CT used for other organs were also published, including the papers concerning

Tab. 1. Comparison of published p-CT prostate studies

team	Prando, Wallace (2000)	Henderson (2003)	Ives (2005)	Łuczyńska (2008)
total number of patients	35	9	10	24
patients with confirmed PCa	25	9	10	24
patients with suspected PCa	10	0	0	0
healthy patients	0	0	0	0
age of patients	45-72	59-80	42-69	49-72
area of examination	7 mm	10 mm	?	?
CT operating parameters	120 kVp, 240 mAs	120 kVp, 100/200 mAs[1]	120 kVp, 180 mAs	?
contrast volume	120 ml	1.5 ml/kg [2]	100 ml	50 ml
contrast: dose of iodine	300 mgI/ml	300 mgI/ml	300 mgI/ml	370 mgI/ml
rate of contrast administration	3 ml/s	3.5-4.5 ml/s	4 ml/s	5 ml/s
scanning	immediately after last dose of contrast	immediately after initiation of dosing contrast	20 s after initiation of dosing contrast	5-7 s after initiation of dosing contrast
time of examination	50 s	4 or 8 min[3]	40 s	50 s
time between successive scans	?	1 or 2,3 s [4]	10 s	?
determined parameters	-	BF, BV, MTT, PS, TTP	-	BF, BV, MTT, PS
method of results interpretation	comparing values on symmetrical ROIs	comparing the average and std. dev. within ROIs	correlation between perfusion and tumor volume	correlation analysis between PSA, Gleason score, and p-CT result
authors' conclusions	cancerous changes are visible in p-CT	perfusion values indicate cancerous area	not useful, detects only large, advanced tumors	correlation between PSA and positive p-CT result

1 For two patients the examination was taken on a GE Hi-Speed Advantage tomograph (100 mAs), for other patients on a Picker PQ5000 tomograph (200mAs).
2 The contrast volume depends on the patients weight.
3 Two patients on a GE tomograph – 4 min; the others on a Picker tomograph – 8 min.
4 Two patients (GE tomograph): scan every second in the first 2 min, then every 10s; the other patients (Picker tomograph): scan every 2,3s in the first 70s, then every 15s.

the use of the p-CT method in the PCa diagnosis. Unfortunately, the results presented in those papers lead to completely different conclusions. Those differences may be connected with the use of different types of tomograph and different examination parameters. Also the selection of diagnosed patients was often not representative and their number can be too small to get statistically well founded conclusions. Finally, there were also some mistakes in the results analyses.

Therefore, there is a need to verify the aforementioned results and prepare the research project of p-CT prostate diagnosis for a large, representative set of patients.

In presented papers only the cancerous or suspected to be cancerous patients were diagnosed. Therefore, we do not have a control group, necessary for proper comparisons. This problem cannot be easily solved. There is an ethical problem related to p-CT examination of every healthy person because of radiation and contrast medium used in this technique. Due to those negative aspects, the p-CT examination should be applied only in justified cases. However, the information about perfusion level in a healthy prostate would be very valuable.

The main goal in the p-CT diagnosis is to point out correctly the region of the gland where the PCa exists. While the prostate p-CT images are very difficult for interpretation, there is a need to use advanced computational methods, for example those known from the artificial intelligence field.

References

1. Hricak H., Choyke P., Eberhardt S. et al. (2007), Imaging Prostate Cancer. A Multidisciplinary Perspective. *Radiology* 243/1, 28-53.
2. Roscigno M., Scattoni V., Bertini R. et al. (2004), Diagnosis of prostate cancer. State of the art. *Minerva Urol Nefrol* 56/2, 123-145.
3. Selley S., Donovan J., Faulkner A. et al. (1997), Diagnosis, management and screening of early localised prostate cancer. *Health Technol Assess* 1, 1-96.
4. Miles K.A., Griffiths M.R. (2003), Perfusion CT: a worthwhile enhancement? *Br. J Radiol* 76, 220-231.
5. Procedure Guidelines for CT/MR Perfusion Imaging 2006, http://mr-proj2.umin.jp/data/guidelineCtpMrp2006-e.pdf.
6. Lev M.H. (2002), CT/MR Perfusion imaging and alphabet soup: an appeal for standardized nomenclature. *American Journal of Neuroradiology* 23, 746-747.
7. Jędrzejewski G. (2006), MRI-based methods for perfusion imaging. *J Radiol* 71/4, 52-54.
8. Thomas D., Lythgoe M.F., Pell G.S. et al. (2000), The measurement of diffusion and perfusion in biological systems using magnetic resonance imaging. *Phys Med Biol* 45, (R97–R138).
9. Di Carli M.F., Dorbala S., Meserve J. et al. (2007), Clinical myocardial perfusion PET/CT. *J Nucl Med* 48/5, 783-793.
10. Ito H., Iida H., Bloomfield P.M. et al. (1995), Rapid calculation of regional cerebral blood flow and distribution volume using iodine-123-iodoamphetamine and dynamic SPECT. *J Nucl Med* 36, 531-536.
11. Joseph M., Nates J.L. (2000), Stable xenon computed tomography cerebral blood flow measurement in neurological disease: review and protocols. *The Internet Journal of Emergency and Intensive Care Medicine* 4/2, http://www.ispub.com/ostia/index.php?xmlFilePath=journals/ijeicm/vol4n2/xenon.xml.
12. Latchaw R.E., Yonas H., Hunter G.J. et al. (2003), Guidelines and recommendations for perfusion imaging in cerebral ischemia: a scientific statement for healthcare professionals by the Writing Group on Perfusion Imaging, From the Council on Cardiovascular Radiology of the American Heart Association. *Stroke* 34, 1084-1104.
13. Wintermark M., Maeder P., Thiran J.P. et al. (2001), Quantitative assessment of regional cerebral blood flows by perfusion CT studies at low injection rates: a critical review of the underlying theoretical models. *Eur Radiol* 11, 1220--1230.
14. Hoeffner E.G., Case I., Jain R. et al. (2004), Cerebral perfusion CT: technique and clinical applications, *Radiology* 231/3, 632-644.
15. Morcos S.K. (2005), Acute serious and fatal reactions to contrast media: our current understanding. *BJR* 78, 686--693.
16. Thomsen H.S., Bush W.H., Jr. (1998), Treatment of the adverse effects of contrast media. *Acta Radiologica* 39, 212-218.
17. Thomsen H.S., Dorph S. (1993), High-osmolar and low-osmolar contrast media. An update on frequency of adverse drug reactions. *Acta Radiologica* 34/3, 205-209.
18. Becker C. (2006), Application of perfusion CT, Training in Advances in Radiology. *Aarhus*, http://www.star-program.com/data-star-program/upload/star_abstracts_1086_ApplicationofPerfusionCT.pdf.
19. Hartel M., Dziubińska-Basiak M., Konopka M. et al. (2006), Kompleksowa diagnostyka obrazowa udaru niedokrwiennego mózgu – opis przypadku. *Udar Mózgu* 8/2, 81-86.
20. Rosenberg R., Wojtek P., Konopka M. et al. (2004), Kliniczne zastosowanie obrazowania perfuzyjnego metodą tomografii komputerowej oraz obrazowania dyfuzyjnego i perfuzyjnego metodą rezonansu magnetycznego w wykrywaniu wczesnych zmian w udarze niedokrwiennym mózgu. *Udar Mózgu* 6/2, 71-78.
21. Dziubińska M., Basiak M., Konopka M. et al. (2006), Rola obrazowania perfuzji w tomografii komputerowej w diagnostyce glejaków ośrodkowego układu nerwowego. *Neurologia i Neurochirurgia Polska* 40/1, 51-56.
22. Groell R., Doerfler O., Schaffler G.J., Habermann W. (2001), Contrast-enhanced helical CT of the head and neck. Improved conspicuity of squamous cell carcinoma on delayed scans. *American Journal of Roentgenology* 176, 1571-1575.
23. Dugdale P.E., Miles K.A. (1999), Hepatic metastases: the value of quantitative assessment of contrast enhancement on computed tomography. *Eur J Radiol* 30, 206-213.
24. Fukuya T., Honda H., Hayahi T. et al. (1995), Lymph-node metastases: efficacy of detection with helical CT in patients with gastric cancer. *Radiology* 197, 705-711.
25. Blomley M.J., Coulden R., Bufkin C., Lipton M.J., Dawson P. (1993), Contrast bolus dynamic computed tomography for the measurement of solid organ perfusion. *Invest Radiol* 28 (suppl. 5), S72-S77.
26. Zhang M., Kono M. (1997), Solitary pulmonary nodules: Evaluation of blood flow patterns with Dynamic CT. *Radiology* 205/2, 471-478.
27. Sahani D.V., Kalva S.P., Hamberg L.M. et al (2005), Assessing tumor perfusion and treatment response in rectal cancer with multisection CT: initial observations. *Radiology* 234, 785-792.
28. Wolfkiel C.J., Ferguson J.L., Chomka E.V. et al. (1987), Measurement of myocardial blood flow by ultrafast computed tomography. *Circulation* 76, 1262-1273.
29. Miles K.A., Griffiths M.R., Fuentes M.A. (2001), Standardized perfusion value: universal CT contrast enhancement scale that correlates with FDG-PET in lung nodules. *Radiology* 220, 548-553.
30. Prando A., Wallace S. (2000), Helical CT of prostate cancer: early clinical experience. *American Journal of Roentgenology* 175/2, 343-346.
31. Henderson E., Milosevic M.F., Haider M.A., Yeung I.W. (2003), Functional CT imaging of prostate cancer, *Psys Med Biol* 38, 3085-3100.
32. Ives E.P., Burke M.A., Edmonds P.R. et al. (2005), Quantitative computed tomography perfusion of prostate cancer: correlation with whole-mount pathology. *Clinical Prostate Cancer* 4/2, 109-112.
33. Łuczyńska E., Anioł J., Szczudło J. et al. (2006), Perfusion of prostate cancer: correlation between p-CT and whole--mount pathology – case report. *Pol J Radiol* 71/4, 70-73.
34. Łuczyńska E., Anioł J., Stelmach A., Jaszczyński J. (2008), The value of perfusion CT in evaluating locoregional staging in post-radical prostatectomy patients with elevated serum PSA level. *Pol J Radiol* 73/2, 13-17.

35. Epstein J.I., Lieberman P.H. (1985), Mucinous adenocarcinoma of the prostate gland. *Am J Surg Pathol* 9/4, 299--308.
36. Harvey C., Dooher A., Morgan J. et al. (1999), Imaging of tumour therapy responses by dynamic CT. *Eur J Radiol* 30/3, 221-226.
37. Harvey C.J., Blomley M.J., Dawson P. et al. (2001), Functional CT imaging of the acute hyperemic response to radiation therapy of the prostate gland: early experience. *J Comput Assist Tomogr* 25/1, 43-49.

BIO-ALGORITHMS AND MED-SYSTEMS
JOURNAL EDITED BY MEDICAL COLLEGE – JAGIELLONIAN UNIVERSITY
Vol. 6, No. 12, 2010, pp. 43–51.

MCG DATA PREPROCESSING

Kamila Baron-Pałucka

AGH, Katedra Automatyki, al. Mickiewicza 30, 30-059 Kraków

Abstract: In order to enable further analysis of magnetocardiographic data (MCG), it is necessary to export it from the software that was used to collect data from MCG device, and to convert it to the format that can be used in Matlab application for map sequence generation. This paper describes details of all phases of data conversion – from raw device data to magnetic field (MF) and pseudo-current density (PCD) maps sequences generation.

Introduction

Magnetocardiographic examination registers intensity of the magnetic field generated during cardiac electrical activity. Electrical impulses, flowing through human heart and causing the contraction and relaxation of atria and chambers, are according to Maxwell equations the source of the magnetic field that is oriented perpendicularly to the electrical field [1]. In course of the examination patient is placed on a special amagnetic bed that can be positioned in three perpendicular directions against rigid and static sensors' set-up. All components of typical magnetocardiograph are presented in Figure 1.

It should be emphasized that, discounting research installations [4], for economical reasons, many commercially available solutions offer only few channels (sensors) that register the intensity of the magnetic field generated by heart. In order to span the whole area of the heart, those devices need to perform few sequential measurements and patient's bed is moved in between of those measurements so that consecutive heart area is placed below sensors for the consecutive measurement. To obtain the final magnetic field map (MF map) it is necessary to perform a series of calculations that account for the fact that data collected from different measuring positions is shifted in time. In the CMI 2409 device CardioMag Imaging Inc., that was used to collect data presented in this publication, the head consists of 9 sensors and in course of the examination signals are registered in four measuring positions, as presented in Figure 2.

In course of the examination the values of the intensity of the magnetic field are registered in form of time runs – each measuring point over patient torso is associated with one time run. Morphological features of MCG and ECG time runs are lot alike – on MCG time runs there are parts similar to P wave, QRS complex and T and U waves from ECG time run – there is also timing correlation between those elements. The significant difference is the fact, that in measuring points placed over lower thorax, in proximity of the midsternal plane, time runs with normal orientation of R and T waves are registered, whereas in measuring points placed over upper left thorax, time runs have reversed orientation (compare in Figure 3: time runs from box 3 and 4 with time runs from box 1).

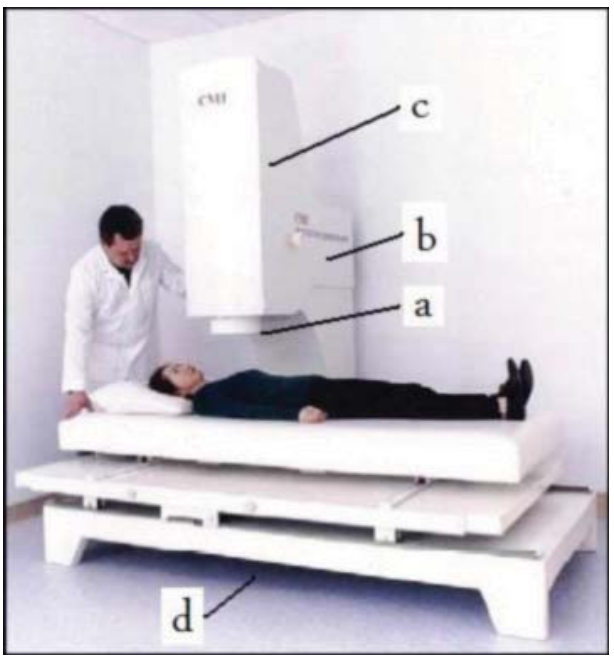

Fig. 1. Magnetocardiograph. On the basis of CardioMag Imaging brochure. a) SQUIDs (Superconducting Quantum Interference Devices) – sensors, b) interference compensation, c) dewar, d) bed

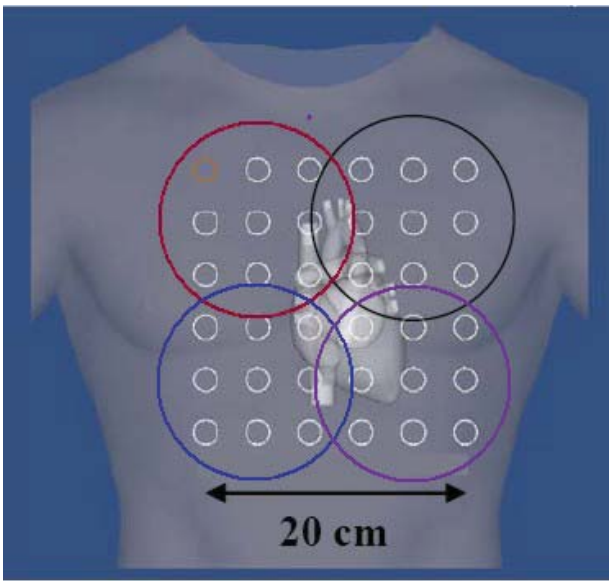

Fig. 2. Localizations of four consecutive measurements that span the whole area of the heart. Big circles represent positions of the device's head, little circles represent positions of nine sensors placed on that head. Based on CardioMag Imaging brochure

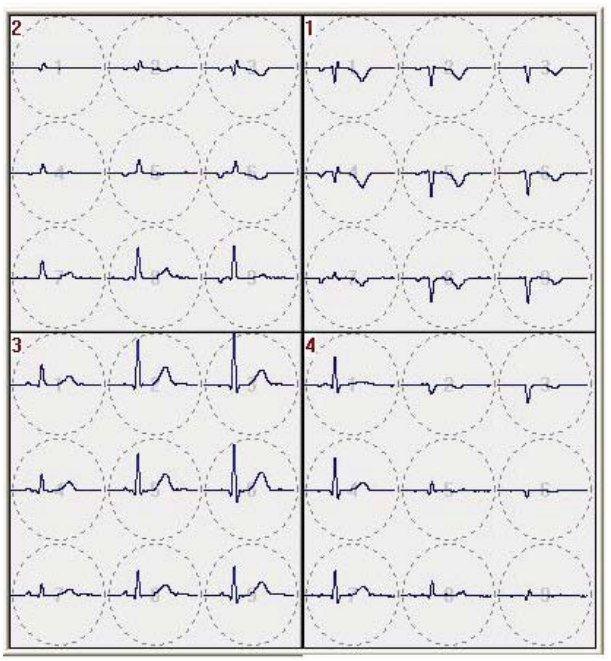

Fig. 3. MCG time runs from 9 channels, collected sequentially in four consecutive measuring positions. In measuring points over lower thorax (3 and 4) in proximity of the midsternal plane, registered signals have normal orientation of R and T waves, whereas in points over upper left thorax (1) R and T waves are reversed. On the basis of MCG, CardioMag Imaging application

Since the CMI 2409 device's head comprises of 9 sensors and registers signals in four different measuring positions, then after completion of the examination we have data from 36 measuring channels.

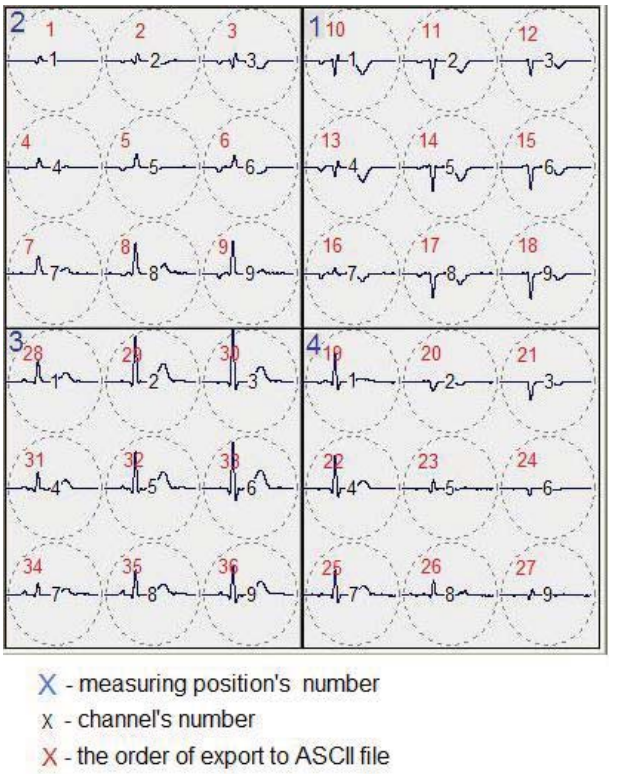

Fig. 4. The order in which data from consecutive channels is exported to output ASCII file

By virtue of similarities between ECG and MCG time runs, MCG data in time runs format can be interpreted basing on rules created for ECG data [3], but the alternative approach is to convert it to map format that could be subject of further analysis in Matlab application. This conversion can be accomplished with operations described in the next chapter.

The phases of MCG data conversion

This chapter presents the basic operations that convert data registered in course of the diagnostic MCG examination to optimized form that enables it to be used and analyzed in Matlab application.

Phase 1: Raw MCG data exported to ASCII format

Raw data collected in course of MCG examination is initially processed. Data from each channel is filtered with the use of low-pass filter of the FIR type with the cutoff frequency of 20 Hz, so that unwanted interference could be removed. Afterwards, for each channel QRS complexes are discovered – based on those complexes the signal can be averaged, so that for each channel there would be one averaged heart cycle. As a result we obtain spatial grid 6x6 with averaged heart cycles in grid's knots, that correspond to a measuring position in which data for certain cycle was registered (compare Figure 4). Averaged data can be exported from CardioMag MCG application – consequently we obtain ASCII file that contains 36 averaged time runs of registered magnetic field intensity values.

Each of averaged time runs consists of 1000 samples and data for consecutive channels is placed in ASCII file in sequence described in Figure 4.

The output ASCII file contains in the first thousand lines data samples from channel 1 registered in second measuring position, and in the last thousand lines data samples from channel 9 registered in third measuring position – in total 36 000 lines plus 36 additional marker lines in the following format:

```
„Position=2 Channel=1 NSamples=1000
FSampling=1000Hz CalibrCoef_
pT=0.000186264”.
```

This exemplary marker line denotes that next thousand lines contain data samples registered in second measuring position from the first out of nine channels, with 1000 Hz sampling frequency and calibration coefficient 0.000186264 that was used to equalize differences in gain of the current channel in respect to gains of remaining channels.

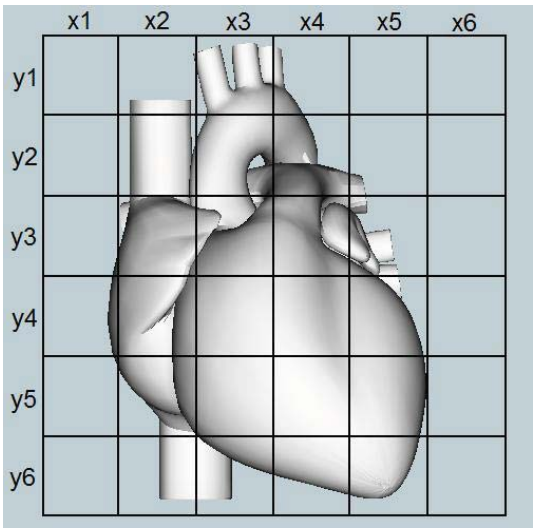

Fig. 5. The correspondence between coordinates *x* and *y* of the output matrix *out_data* and the actual situation of patient's heart

Phase 2: Converting ASCII file to format corresponding with spatial arrangement

The ASCII file is converted with the use of author's application to DAT format file that instead of 36036 lines, consists of 36 lines each 1000 samples long – the original order of channels is preserved but marker lines are deleted.

Such DAT file can be used by following Matlab function in which final conversion to three dimensional matrix 6x6x1000 is performed. The output matrix corresponds to spatial and temporal data arrangement:

The data correspondence in spatial terms means that data samples from 36 lines of DAT file were arranged in a way where data in output matrix *out_data* corresponds to spatial arrangement that is presented in Figure 4 – so that first row of output matrix *out_data* contains data samples from 1st, 2nd and 3rd channel registered in second measuring position followed by data samples from 1st, 2nd and 3rd channel registered in first measuring position, whereas sixth row of output matrix *out_data* contains data samples from 7th, 8th and 9th channel registered in third measuring position followed by data sam-

```
function [out_data] = load_and_convert(in_data_file)
% ----------------------------------
% Basing on file name given in in_data_file it loads appropriate .dat file
% and then converts it so that matrix structure is in accordance with
% spatial and temporal set-up from MCG examination.
% ----------------------------------
% in_data_file : name of the .dat file (e.g. ‘sample_data.dat’)
% out_data : 3 dimensional matrix with converted data from in_data_file

data=load(in_data_file);
out_data=zeros(6,6,1000);
for x=1:6
    for y=1:6
        for t=1:1000
            if (x<=3 && y<=3)
                out_data(x,y,t)=data(3*(x-1)+y,t);
            end
            if (x<=3 && y>3)
                out_data(x,y,t)=data(9+3*(x-1)+y-3,t);
            end
            if (x>3 && y<=3)
                out_data(x,y,t)=data(27+3*(x-4)+y,t);
            end
            if (x>3 && y>3)
                out_data(x,y,t)=data(18+3*(x-4)+y-3,t);
            end
        end
    end
end
clear in_data;
end
```

ples from 7thm 8th and 9th channel registered in fourth measuring position.

The coordinates *x* and *y* of the output matrix *out_data* are of a spatial type – point (*x1, y1,* ▪) corresponds to upper left corner of examination area and point (*x6, y6,* ▪) corresponds to lower right corner of that area – compare Figure 5.

The *t* coordinate of the output matrix *out_data* is of a temporal type – (▪, ▪, *t1*) is a first data sample of an averaged heart cycle for chosen channel whereas (▪, ▪, *t1000*) is the last data sample of that cycle.

Phase 3: Interpolation

In order to create a magnetic field map, available data needs to be interpolated – we need to find values of the magnetic field intensity in points of the heart that were in between magnetocardiograph's sensors and in a way complement data among 36 available channels. Interpolation can be performed with the use of any method available in Matlab, e.g. 'linear', 'spline' or 'nearest neighbor'. Simultaneously, to reduce computational complexity, for each channel only subset of samples that are evenly distributed in time is chosen – e.g. every tenth, twentieth or with any other sampling density.

Interpolation with simultaneous reduction of time samples amount is accomplished in Matlab application with the use of the following function – for instance if every fiftieth time sample is chosen (sample_density = 50) and interpolation step is set to 0.1 (interpol_step = 0.1), then original matrix 6x6x1000 is transformed to output matrix 51x51x20 – operating on sequence that consists of 20 instead of 1000 maps (when every fiftieth is chosen) significantly reduces computational complexity of subsequent operations without compromising the character of the sequence as a whole.

The above function implements 'spline' interpolation of data from matrix *input_data* to output matrix *interpolated_data* with any chosen interpolation step (*interpol_step*) and any chosen sampling density (*density_of_samples*) that reduces the number of maps in the sequence.

The matrix obtained as a result of the described function can be used to draw final MF map. It can be accomplished with the use of one of the following Matlab functions:

- *contour()* – contour map
- *contourf()* – filled contour map
- *scatter()* – map created from single points

Figures 6, 7 and 8 present the comparison of the maps created from the same original data set, but with different drawing functions, interpolation methods and interpolation steps.

Phase 4: Conversion to PCD format

PCD (Pseudo Current Density) maps were introduced to enable such representation of the magnetic field intensity values, that would reflect the source of the measured values – the distribution of the density of the heart's currents [5]. The conversion to that format is accomplished by applying to B_z component of the magnetic induction vector the HC (Hosaka-Cohen) transformation, which allows to obtain the value of the so-called pseudo current density [2].

The application of PCD maps in visualization of MCG data results in maps, where localization of the point with the largest signal amplitude is equivalent to the localization of the electrical dipole of the heart, and orientation of this point's pseudo current density vector is in accordance with orientation of electrical dipole of the heart. Therefore, PCD map is intuitive for

```
function [ interpolated_data, counter ] = interpolate( input_data,...
    density_of_samples, interpol_step)
% ----------------------------------
% to decrease computational effort it picks data from original data table
% (according to density_of_samples parameter) – from 1000 time samples
% (1000 maps of the dimension 6x6) every n-th is taken
% and then it interpolates it so instead of 6x6=36 data points on the map,
% we get 501x501=251001 (from 1 to 6 with the step 0.01)
% ----------------------------------
% input_data :  3 dimensional matrix with MF data
% density_of_samples : every n-th time sample is taken for each from 36 canals
% interpolated_data :  input data after interpolation
% counter : calculated based on density, if every n-th sample is taken then
%           there is x maps in total (x time samples for each of 36 canals)

counter=round(1000/density_of_samples);
[X,Y]=meshgrid(1:6,1:6);
Z=zeros(6,6,counter);
for a=1:counter
    for i=1:6
        for j=1:6
            Z(i,j,a)=input_data(i,j,1+density_of_samples*(a-1));
        end
    end

    [Xi,Yi]=meshgrid(1:interpol_step:6,1:interpol_step:6);

    interpolated_data(:,:,a)=interp2(X,Y,Z(:,:,a),Xi,Yi,'spline');
end
clear input_data;
end
```

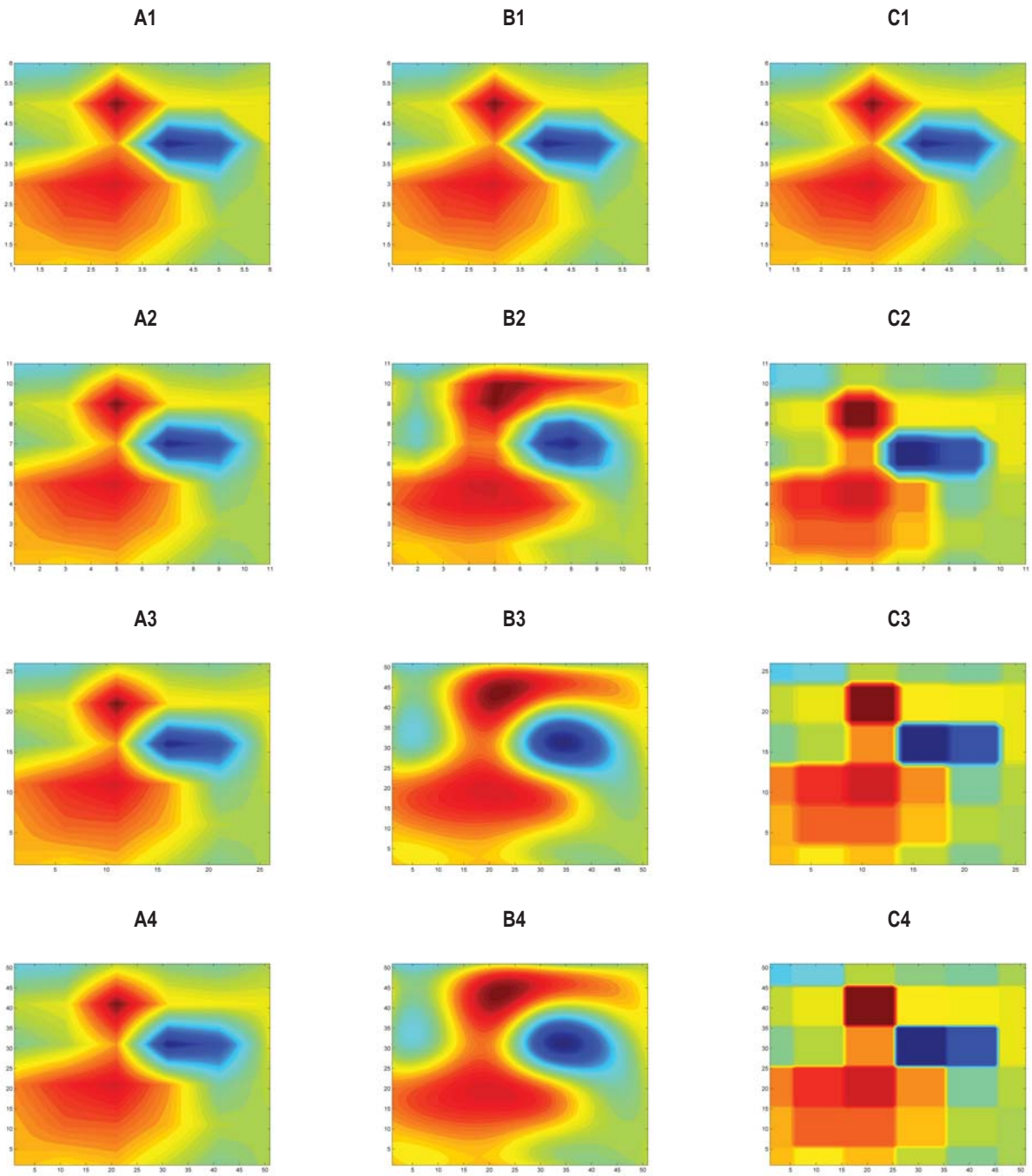

Fig. 6. The comparison of maps drawn with function *contourf()* from the same original data set, but with different interpolation methods and steps. A – 'linear' interpolation, B – 'spline' interpolation, C – 'nearest neighbor' interpolation. Row 1 – interpolation step equals 1 (only original data samples are used to draw map), row 2 – interpolation step equals 0.5, row 3 – interpolation step equals 0.2, row 4 – interpolation step equals 0.1

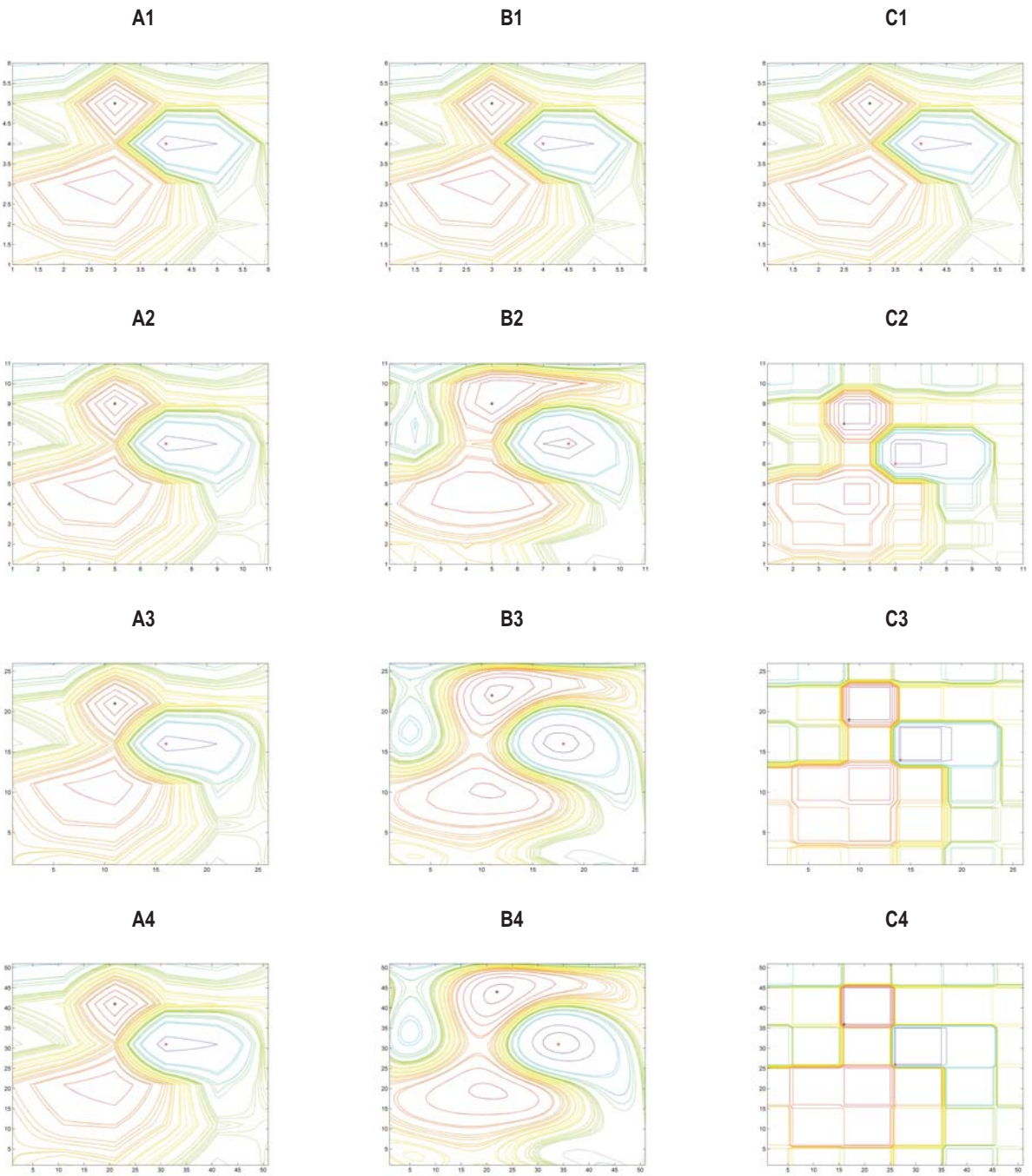

Fig. 7. The comparison of maps drawn with function *contour()* from the same original data set, but with different interpolation methods and steps. A – 'linear' interpolation, B – 'spline' interpolation, C – 'nearest neighbor' interpolation. Row 1 – interpolation step equals 1 (only original data samples are used to draw map), row 2 – interpolation step equals 0.5, row 3 – interpolation step equals 0.2, row 4 – interpolation step equals 0.1

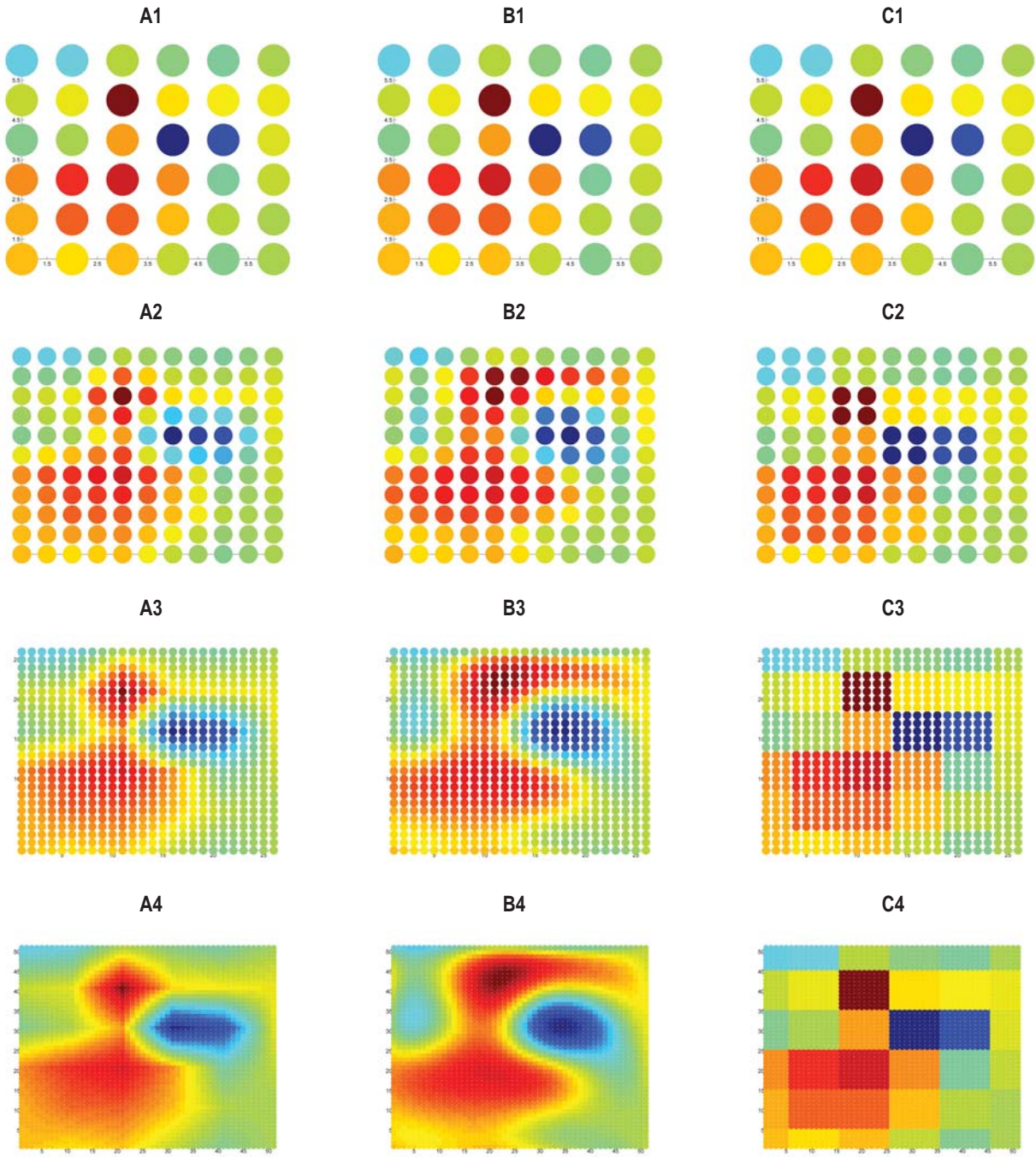

Fig. 8. The comparison of maps drawn with function *scatter()* from the same original data set, but with different interpolation methods and steps. A – 'linear' interpolation, B – 'spline' interpolation, C – 'nearest neighbor' interpolation. Row 1 – interpolation step equals 1 (only original data samples are used to draw map), row 2 – interpolation step equals 0.5, row 3 – interpolation step equals 0.2, row 4 – interpolation step equals 0.1

doctor's interpretation, since it reflects the areas of the heart which are active at the given moment.

Transformation from MF to PCD format is described by following equation:

$$\vec{c} = \frac{\partial B_z}{\partial y} \cdot \vec{e}_x - \frac{\partial B_z}{\partial x} \cdot \vec{e}_y \quad (1)$$

where:

$\vec{c}$ – pseudo current density

B_z – component of the magnetic induction vector (registered in course of MCG examination)

$\vec{e}_x, \vec{e}_y$ – versors of the coordinate system

The conversion can be implemented in Matlab with the use of the following function:

```
function [ pcd_data ] = convert_mf_to_pcd( mf_data, counter )
% ------------------------------
% converts Magnetic Field data to Pseudo-Current Density data
% ------------------------------
% mf_data : 3 dimensional matrix with MF data
% counter : calculated based on chosen density of samples,
%           if every n-th sample is taken then there is x maps in total
%           (x time samples for each of 36 canals)
% pcd_data : converted PCD data in form of 3 dimensional matrix

for a=1:counter
    [px,py]=gradient(mf_data(:,:,a));
    pcd_data(:,:,a)=py-px;
end
clear mf_data;
end
```

This function computes appropriate gradients on MF data to accomplish transformation described by equation *(1)* and as a result convert data to PCD format.

Phase 5: MF and PCD maps sequence generation

The last step on the path to obtaining complete map sequence, that can be later used for patient's classification to respective test groups, is the generation of all maps that constitute the sequence. This means that in case of matrix of dimensions 51x51x20, which was described earlier, in order to generate the complete sequence we have to draw 20 maps of dimensions 51x51. Since previously described method of decreasing the number of time samples was accomplished by choosing every fiftieth sample, then obtained sequence of 20 maps correspond to time samples evenly distributed along the whole cycle of the heart's activity – first maps of the sequence illustrate the magnetic field of the heart in course of contraction of atria and the last maps of the sequence illustrate the relaxation phase.

Figure 9 demonstrates the second half of PCD maps sequence that was obtained for the chosen patient – this means maps of numbers from 11 to 20 from the complete set of 20 maps.

Conclusion

This paper describes all phases ofe conversion from raw MCG data to the output format of MF or PCD maps sequence, which can be a subject of more advanced analysis. The paper presents not only the details of the conversion of original data to format corresponding with spatial arrangement, but also the details of the method of choosing the subset of maps that decrease the computational complexity of later operations on sequences. It was also presented how data can be converted from MF to PCD format. In conclusion, the influence of the choice of interpolation method and interpolation step on the quality of obtained maps was presented, as well as comparison of different types of maps that can be created in Matlab application.

References

1. Baron-Pałucka K. (2008), Magnetocardiography – measurement conduction, data formats and diagnostic applications. *Bio-Algorithms and Med-Systems* 4/7, 25–34.
2. Baron-Pałucka K. (2008), Wybrane problemy akwizycji i analizy danych diagnostycznych z badań magnetokardiograficznych. *Elektrotechnika i Elektronika* 27, 63–75.
3. Chen J., Thomson P., Nolan V. (2004), Age and sex dependent variations in the normal magnetocardiogram compared with changes associated with ischemia. *Annals of Biomedical Engineering* 32/8, 1088–1099.
4. Fenici R., Brisinda D., Meloni A. (2003), First 36-channel Magnetocardiographic Study of CAD Patients in an Unshielded Laboratory for Interventional and Intensive Cardiac Care. *Lecture Notes on Computer Science* 2674, 122–131.
5. Haberkorn W., Steinhoff U., Burghoff M. (2006), Pseudocurrent density maps of electrophysiological heart, nerve or brain function and their physical basis. *BioMagnetic Research and Technology* 4, 5.

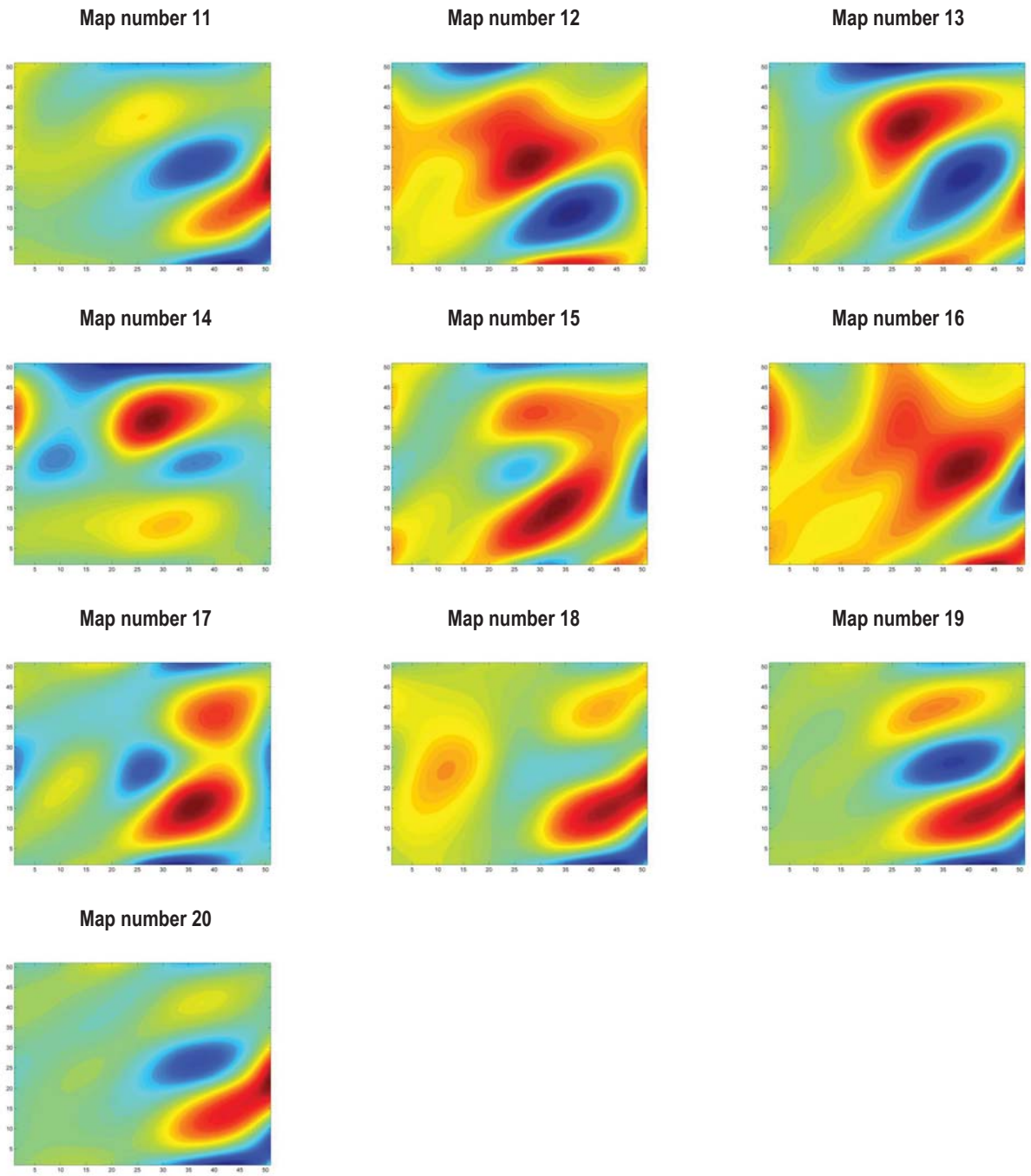

Fig. 9. The second half of the complete sequence of 20 PCD maps (maps number 11-20)

BIO-ALGORITHMS AND MED-SYSTEMS
JOURNAL EDITED BY MEDICAL COLLEGE – JAGIELLONIAN UNIVERSITY
Vol. 6, No. 12, 2010, pp. 53–57.

IMAGE BASED REGION RECOGNITION IN GASTROINTESTINAL ENDOSCOPY

Rafał Frączek[1], Mariusz Duplaga[1,2]

[1]Centre of Innovation, Technology Transfer and University Development, Jagiellonian University, Czapskich Str.4, 31-110 Kraków, Poland, e-mail: rafalfr@agh.edu.pl
[2]Collegium Medicum, Jagiellonian University, Grzegórzecka Str. 20, 31-531 Kraków, Poland, e-mail: mmduplag@cyf-kr.edu.pl

Abstract: Capsule endoscopy was introduced to gastroenterology with the aim of improvement of the diagnostics means for these parts of gastrointestinal tract which are difficult to reach with a classical endoscopy. Modern capsules are equipped with an on-board light source and a camera. Acquired images are transmitted to a video recorder. The next generation capsule, which is developed within the VECTOR (Versatile Endoscopic Capsule for gastrointestinal TumOr Recognition and therapy) project, will also make it possible to transmit a video stream in real-time. The video recording generated by the endoscopic capsule during its passage through gastrointestinal tract is of a considerable length and the automatic detection of its specific regions would enhance diagnostic capacity of the procedure. Therefore, a special algorithm has been developed and implemented in C++. The algorithm is meant to be used for automatic region classification within video recordings (streams) whichcan be obtained with an endoscopic capsule.
Keywords: image recognition, neural networks, endoscopy, mpeg-7
Słowa kluczowe: rozpoznawanie obrazów, sieci neuronowe, endoskopia, mpeg-7

Introduction

Capsule endoscopy was invented in the end of the 20th century. It is one of the first micro-devices enabling exploration of the human body with minimum level of invasiveness and discomfort for a patient [1] – [5]. The capsule was introduced to diagnostics in gastroenterology with the aim of improvement of localization of these parts of gastrointestinal tract, which are difficult to reach with classical endoscopy. Current research and development activities are focused on development of the next generation capsule with extended functionality, including autonomous locomotion system, tissue sampling, optical biopsy and potentially treatment delivery. Most of these objectives are covered by the VECTOR project (Versatile Endoscopic Capsule for gastrointestinal TumOr Recognition and therapy) carried out within the 6th Framework Program of the European Commission.

In the paper, selected aspects of signal processing in the gastrointestinal (GI) capsule are highlighted. The authors explore the issue of capsule localization on the basis of image features acquired with the use of standard MPEG-7 image descriptors.

Nowadays, capsules used in medical practice offer the resolution of acquired GI images which is significantly lower than the resolution provided by modern fiberoptic endoscopes. The paper describes the options for the support of usage scenario of the capsule developed within the VECTOR project. Developed approach was tested on the images obtained from the GI tract with fiberoptic endoscopy techniques.

Method description

The process of the assessment of the whole video record registered during the passage of endoscopic capsule through GI tract is time-consuming. The functionality of detection of non-informative frames and automatic capsule localization could bring benefits in terms of the optimization of these tasks. Non-informative frames make usually a considerable part of all frames recorded during classical and capsule endoscopy. The detection of such frames and their exclusion from the video recording would significantly reduce the time necessary for the evaluation of the resulting video and for its automatic analysis. To achieve this goal, the authors developed an algorithm that detects and marks non-informative frames, and then recognizes the region of GI tract in which the capsule is located. This approach is depicted in fig. 1.

In the subsequent chapters, detailed information on each step of the algorithm is presented.

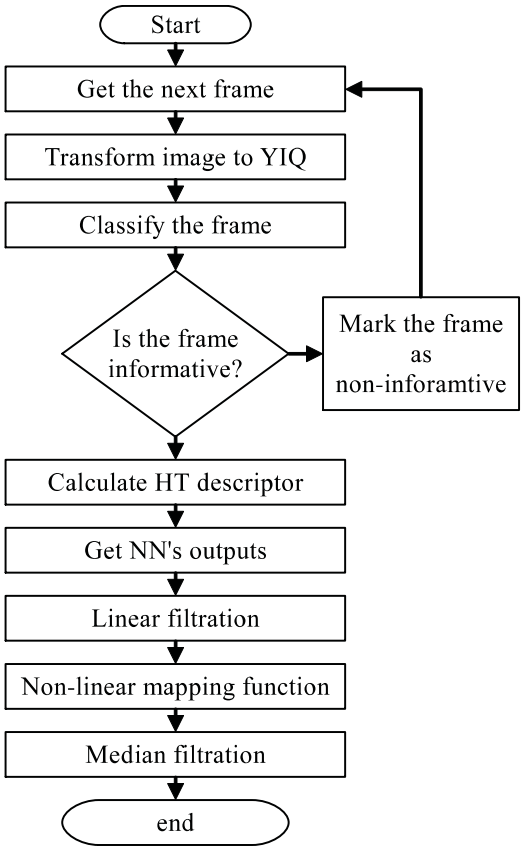

Fig. 1. The algorithm flowchart

Detection of non-informative frames

At this stage, non-informative frames resulting from poor visibility or unfavorable condition, e.g. light reflections, are detected. Exclusion of such frames from further processing is important because they can cause additional errors during the classification stage. Two examples of such frames are shown in the table 1.

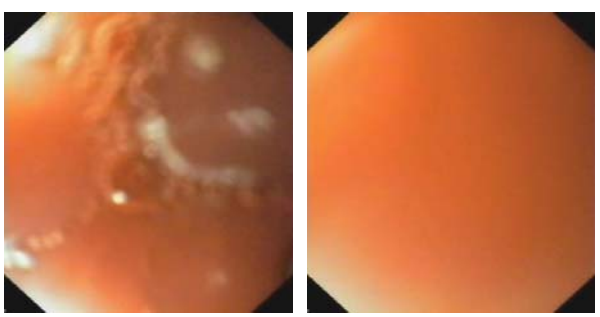

Fig. 2. Examples of non-informative frames

The detection of non-informative frames is based on pixel color distribution. In order to find the most suitable color space for the detection, three color spaces have been tested: HSV, YCrCb and YIQ. In addition, several representative video frames were manually segmented into two separate classes: informative and non-informative ones. Then pixel values for both regions were extracted and converted to the three color spaces. Three separate data sets were obtained in this way. For classification purposes, three neural networks were trained. Three-layer non-linear neural networks were used. Each pixel in a image is analyzed by a neural network. The network returns high value if a pixel belongs to the informative region and low value in case of non-informative region. Since the best results were obtained for the YIQ color space, it was applied in further steps.

In the next stage, the effectiveness and credibility of detection of non-informative frames in the video sequence was evaluated. A frame was considered non-informative if more than 50% pixels are classified as artifacts. The threshold was arbitrarily chosen by authors. Two sets of frames originating from video recordings of endoscopic procedures were manually segmented by authors into informative and non-informative frames. All frames were processed with a previously trained neural network and automatically classified into the two classes. The results are presented in the table 2.

Tab. 1. Results for non-informative frames detection

Informative frames		Non-informative frames	
correct	Incorrect	correct	Incorrect
99.10%	0.9%	99.30%	0.70%

Region detection

To perform the region classification, the following method was developed. The region detection is based on analysis of image descriptors calculated for the subsequent frames. In order to find the most suitable descriptor and classification method, several well-known image descriptors and classification methods have been examined. In the case of image descriptors, the most suitable mpeg-7 [6] –[7] descriptors together with some well-known image features not belonging to the mpeg-7 standard were tested. The following descriptors were used: Dominant Color (DC), Color Structure (CS), Color Layout (CL), Edge Histogram (EH), Homogenous Texture (HT), Scalable Color (SC), Scale-Invariant Feature Transform (SIFT), Steerable Filters (SF), Moment Invariants (MI), Differential Invariants (DI). In order to obtain illumination invariance, the 128-dimensional SIFT descriptor [8] was normalized (divided by the square root of the sum of all squared components). Steerable filters [9] were computed with Gaussian derivatives up to the 4^{th} order and as a result the descriptor had 13 elements. Moment invariants [10] were computed up to the 2^{nd} order and the 2^{nd} degree, giving a 10-dimensional descriptor. Differential invariants [11] were computed up to the 3^{rd} order (8-dimensional descriptor). For the purpose of classification, the following methods were tested: C-means (CM), Fuzzy c-means (FCM) [12], Gustafson-Kessl algorithm (GK) [13], Support Vector Machine (SVM) [14] and neural networks [15]. The purpose of the experiment was to perform automatic classification of gastrointestinal track regions within the frames obtained from fiberoptic GI endoscopy, using all available descriptors and all classification methods. The overall data set was composed of 4644 video frames (two video recordings). It was randomly divided into two subsets: one for training and the other for testing. For each descriptor-classification method pair, the percentage of correctly classi-

fied frames was calculated. Obtained results are shown in the table 3.

Tab. 2. Test results

Classifier descriptor	CM	FCM	GK	SVM	NN
HT	86	87	85	94	95
DC	87	88	88	89	89
CS	69	72	65	77	78
CL	78	78	75	88	88
EH	79	79	80	81	81
SC	82	84	85	92	93
SIFT	87	88	88	93	93
SF	70	71	71	77	77
MI	70	70	72	75	76
DI	74	77	65	80	80

The results show that the Homogeneous Texture descriptor combined with a neural network as a classifier yield the best results: they were both implemented in the final algorithm implementation.

Since the method uses neural networks, it is necessary to train them before the method can be applied. There are four networks – each one is trained to recognize one specific region of the GI track (in other words, each neural network is associated with one recognizable region). When a new frame is analyzed, the descriptor is calculated and then its value is processed by the four previously trained neural networks. As a result, four output values are obtained. The neural network output value is high (near 1.0) when it is fed with a descriptor calculated for a frame associated with the network. Otherwise the output value is low (near 0.0). The signal of raw neural networks outputs is formed in this way.

Classification enhancement by non-linear filtration

Since it is not possible to filter out all non-informative frames at the first stage, the raw output signals from neural networks are noisy. This may result in false region classifications. In order to overcome this problem, an enhancement procedure was designed. It consists of three steps: low-pass signal filtration, non-linear mapping function and median filtration.

The first step is a 5-point low pass filter. The next step is a non-linear mapping function, which maps the smoothed out neural networks outputs to a one-dimensional signal. The mapping function has the following form:

$$\mathbf{x} = [x1, x2, x3, x4],$$

$$y = f(\mathbf{x}) = \sum_{i=1}^{4} i \cdot H\left(x_i - \max_i\{x_i\}\right) \quad H(i) = \begin{cases} 0 & if \quad x < 0 \\ 1 & if \quad x \geq 1 \end{cases} \quad (1)$$

The purpose of the mapping function is to provide a clear region indicator, that shows in which part of the gastrointestinal track the capsule is currently localized. The mapping has the property that its value is 1 when capsule is in region A, value is 2 when capsule is in region B and so forth.

Finally, the function values are filtered by the median filter. The reason for using the median filter is that it removes duplicate pikes that may appear in the function output whereas it preserves the sharp signal edges on the region boundaries.

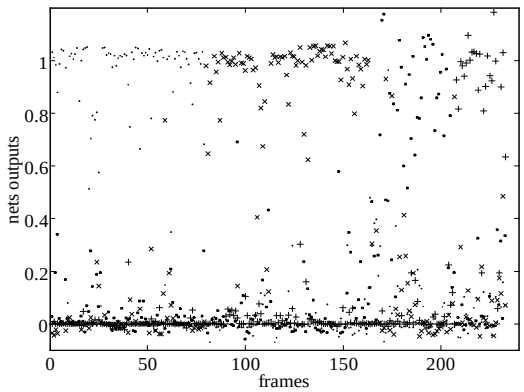

Fig. 3. Raw neural networks outputs

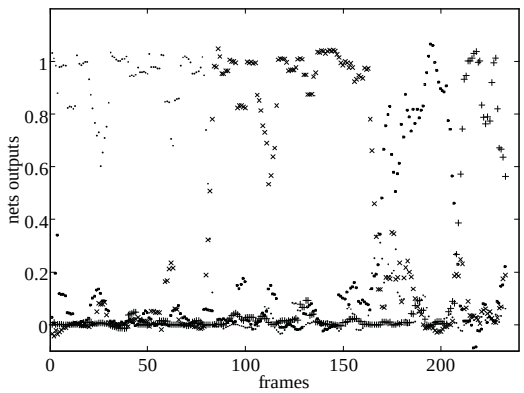

Fig. 4. Filtered neural networks outputs

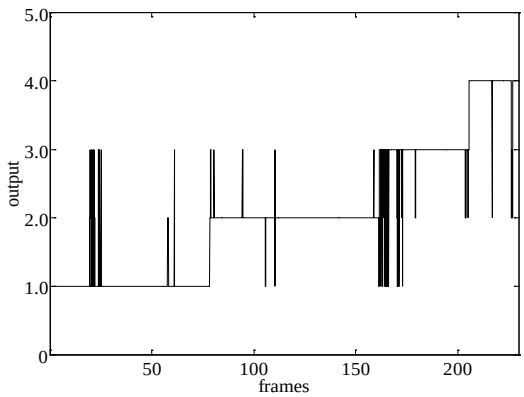

Fig. 5. Non-linear mapping function output

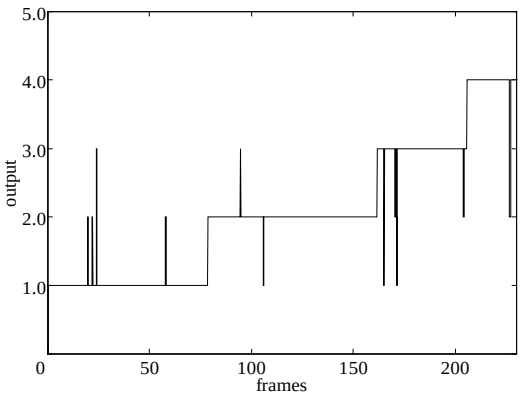

Fig. 6. Median filtered output

Signals at subsequent steps are presented on fig. 2 – 5. On fig. 2 and 3, outputs from each neural network is denoted by a different mark (e.g. the output from the 4th network is denoted by "+").

In order to test the efficiency of the method, the following test was carried out. The data set in the experiment was composed of two sets of frames originating from endoscopy video recordings. Each video recording was divided by a physician into four regions. Then both videos were processed with the developed method.

The obtained results show that the overall region classification accuracy is 90%.

Fast implementation of image-based capsule localization in c++

The algorithm was implemented in form of a plug-in for VirtualDub program. Fig. 6 shows a screenshot of the VirtualDub window with the running plug-in.

In order to boost the code performance in terms of execution speed, some implementation optimizations have been applied. The first possible program enhancement is to fully utilize modern multi-core processors. This goal can be achieved by employing all extensions provided by the OpenMP library, which makes it easy to parallelize some loops.

In our work, we have used an advanced hyperplane method [16], which utilizes possible dependencies among nested loops. As a result, some changes have been applied in the image descriptors source code.

However, the code parallelization can yield the best results if it is applied to these parts of code which are computationally ineffective.

Obtained results show that image features extraction (Homogenous Texture descriptor) is the most computationally intensive step. Other program blocks are fast enough and they do not require any specific optimization.

After applying all possible changes, a 30% speed-up has been obtained. The improvement is not very significant, because the source code has many parts which can not be easily parallelized by means of the techniques described above.

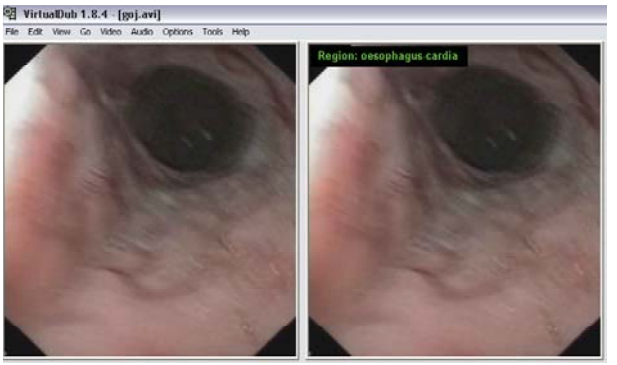

Fig. 7. VirtualDub screenshot with a running plug-in

Tests

In order to examine the accuracy of the proposed method, a test was carried out. The plug-in was fed with two different video files. Each video file had been annotated by an experienced endoscopist prior to the test. The obtained results are shown in table 4.

Tab. 3. Test results

region	A	B	C	D
A	91	2	1	3
B	6	93	5	7
C	1	2	93	2
D	2	3	1	88

Each table cell represents the percentage of video frames from one region (row) classified as second region (column). The meanings of regions are as follows: A – oesophagus and cardia, B – corpus of the stomach, C – pylorus, D – duodenal cap.

Conclusion

A new method for automatic region recognition in a gastrointestinal track is presented. The method uses Homogeneous Texture descriptor for features extraction. In the preceding step, the features vector is analyzed by a set of four neural networks. The output signal from networks is then mapped into four recognizable regions. The entire algorithm is optimized and implemented in C++ as a plug-in for VirtualDub video editor.

Test results show that the method yields over 90% recognition accuracy. Future development will include very fast implementation on Nvidia CUDA platform.

Acknowledgments:The research presented in the paper was performed within the activities of the VECTOR project (Versatile Endoscopic Capsule for gastrointestinal TumOr Recognition and therapy), Contract No 033970. The authors thank Professor Krzysztof Fyderek and Dr Kinga Kowalska-Duplaga from Department of Pediatrics, Gastroenterology and Nutrition, University Child Hospital in Kraków, for provision of samples of video sequences from endoscopic procedures.

References

1. D. Panescu (2005), Emerging technologies. An imaging pill for gastrointestinal endoscopy, IEEE Eng. *Medicine and Biology Magazine* 24/4, 12-4.
2. EC IST Vector Project Home Page: http://www.vector-project.com/.
3. Given Imaging Home Page: www.givenimaging.com, http://best-programs.net/.
4. G. Iddan, G. Meron, A. Glukhovsky, P. Swain (2000), Wireless capsule endoscopy. *Nature*, 405-417.
5. M. Mylonaki, A. Fritscher-Ravens, P. Swain (2003), Wireless capsule endoscopy: a comparison with push enteroscopy in patient with gastroscopy and colonoscopy negative gastrointestinal bleeding. *Gut Journal* 52/8, 1122-1126.
6. B. S. Manjunath, P. Salembier, T. Sikora (2002), Introduction to MPEG-7 Multimedia Content Description Interface. John Wiley & Sons, Chichester, England.
7. J. M. Martinez, R. Koenen, F. Pereira (2002), MPEG-7: the generic multimedia content description standard. *IEEE Multimedia* 9/2, 78-87.
8. D. G. Lowe (2004), Distinctive image features from scale-invariant keypoints. *International Journal of Computer Vision* 2/60, 91-110.
9. W. Freeman, E. Adelson (1991), The design and use of steerable filters. *IEEE Transactions on In Pattern Analysis and Machine Intelligence* 13/9, 891-906.
10. L. Van Gool, T. Moons, D. Ungureanu (1996), Affine/photometric invariants for planar intensity patterns. *European Conference on Computer Vision* 1, 642-651.
11. J. Koenderink, A. van Doorn (1987), Representation of local geometry in the visual system. *Biological Cybernetics* 55/6, 367-375.
12. J. C. Bezdek (1981), Pattern Recognition with Fuzzy Objective Function Algorithms. Springer.
13. R. Babuska et al. (2002), Improved Covariance Estimation for Gustafson–Kessel Clustering. *IEEE International Conference on Fuzzy Systems* 2, 1081-1085.
14. N. Cristianini, J. Shawe-Taylor (2000), An Introduction to Support Vector Machines and Other Kernel-based Learning Methods. Cambridge: Cambridge University Press.
15. Ch. M. Bishop (1996), Neural Networks for Pattern Recognition. Oxford: Clarendon Press.
16. M. Paliwoda (2008), Automatically loops parallelized, efficiency of parallelized code. *PAK* 54/8.

BIO-ALGORITHMS AND MED-SYSTEMS
JOURNAL EDITED BY MEDICAL COLLEGE – JAGIELLONIAN UNIVERSITY
Vol. 6, No. 12, 2010, pp. 59–66.

THE APPLICATION OF FLICKER NOISE SPECTROSCOPY FOR ANALYSIS OF EEG SIGNAL RELATED TO MOVEMENT IMAGINATION

Anna Broniec

broniec@novell.ftj.agh.edu.pl
Faculty of Physics and Applied Computer Science, AGH University of Science and Technology, Kraków, Poland

Abstract: In the paper the Flicker Noise Spectroscopy (FNS) method has been applied for analysis of EEG signal related to movement imagination. The results of the experiment, consisting of fifty repetition of right hand movement imagination, have been presented at time-frequency maps. Consecutively, the electroencephalography signal averaged by a number of repetitions has been parameterized in accordance with the FNS method. The analysis of the parameters describing the signal shows changes in their values at the moment of hand movement imagination. FNS also allows to analyze correlations between signals measured at different points of space (different electrodes) in time.
Keywords: electroencephalography (EEG), Flicker Noise Spectroscopy (FNS), movement imagination, time-frequency maps, cross-correlations

Streszczenie: W artykule zastosowano metodę FNS do analizy sygnału elektroencefalograficznego związanego z wyobrażeniem ruchu prawą ręką. Wynik doświadczenia polegającego na pięćdziesięciokrotnym powtórzeniu wyobrażenia ruchu prawą ręką został przedstawiony w postaci mapy czasowo-częstościowej. Następnie uśredniony po liczbie powtórzeń sygnał elektroencefalograficzny poddany został parametryzacji w czasie, zgodnie z założeniami metody FNS. Analiza parametrów opisujących sygnał pozwala zaobserwować zmiany wartości parametrów w chwili wyobrażenia ruchu prawą ręką. Metoda FNS pozwoliła dodatkowo na analizę korelacji występujących pomiędzy sygnałem otrzymanym z różnych elektrod w czasie.
Słowa kluczowe: elektroencefalografia (EEG), FNS, wyobrażenie ruchu, mapy czasowo-częstościowe, korelacje

Introduction

People who are physically disabled and suffer from severe motor disabilities need alternative way of communication technology. For those who are completely paralyzed direct communication between brain and computer (without any muscle control) is indispensable. For this reason, the brain-computer interface (BCI) systems are an impressively developing subject of scientific research from about 15 years. BCI integrates many fields of knowledge, such as engineering, exact and biomedical sciences [1]. One of the most essential stages of BCI development is extraction of specific features or parameters from EEG signal, which allows to translate brain activity into device control signal. The detailed knowledge about brain activity during imagination of the movement and the movement itself opens new possibilities in communication between man and machine. Finding such repeatable features occurring during movement imagination opens prospect to implementation of sensorimotor rhythm to control the machine, e.g. cursor control [2].

In the present paper, the EEG signal related to movement imagination is analyzed by the Flicker Noise Spectroscopy (FNS). The FNS method was applied in many various fields where natural signals are considered, particularly in investigation of physicochemical, electrochemical, corrosion and bioelectorochemical processes. So far the method was applied to parametrization of the images produced by atomic force microscopy (AFM) [3], analysis of geological signals measured in seismic areas (determination of precursors of earthquake) [4,5], determination of precursors for electric breakdowns in thin porous silicon films [6], and analysis of electric potential fluctuations in electromembrane systems [7]. The FNS method was also successfully applied for some problems in medicine. It is worth to mention the usage of FNS to analyse the effect of different types of medical treatment on the dynamics of index finger tremor for a Parkinsonian patient [8]. The rate of tremor signal change was measured after two types of treatment, one of them was medication (L-Dopa) and the second was the electromagnetic stimulation by the implanted in the patient's brain electrode. The flicker-noise spectroscopy approach was also used to analyze the electroencephalograms. Timashev et al. [9] used FNS to compare electroencephalogram from two patients, a healthy child and one with schizophrenic symptoms. Recently, the same authors used the FNS method for identification of photosensitive epilepsy by analyzing the magnetoencephalographic (MEG) signal [10]. They suggested that the FNS methodology is a promising method of early diagno-

sis, not only for photosensitive epilepsy but also for other neurodegenerative diseases, such as Parkinson's, Alzheimer's, Huntington's, amyotrophic lateral sclerosis, schizophrenia and epilepsy.

In the present paper the FNS method is used to analyze the electroencephalogram signals related to right hand movement imagination.

The flicer-noise specroscopy method

let us assume that the signal of interest is described by dynamic variable during time interval . In our case it corresponds with the electroencephalography signal. The basic idea of the FNS method is the assumption that main information about a system under study is provided by specific "resonant" and "chaotic" components including sequences of different types of irregularities, such as spikes and jumps and discontinuities in their derivatives of different orders [11]

$$V(t) = V_r(t) + V_{cS}(t) + V_{cJ}(t) \tag{1}$$

where corresponds to the signal formed by resonant components and are the chaotic components corresponding to spikes and jumps, respectively.

The main tool to extract and analyze the information contained in the signal is the power spectrum (the cosine transform) of the autocorrelation function

$$S(f) = \int_{-T/2}^{T/2} \psi(\tau)\cos(2\pi f\tau)\,d\tau \tag{2}$$

where is the time lag and is the autocorrelation function which can be expressed in the form

$$\psi(\tau) = \langle V(t)V(t+\tau)\rangle_{T-\tau} \tag{3}$$

The angular brackets in equation (3) is the average over time interval

$$\langle(...)\rangle_{T-\tau} = \frac{1}{T-\tau}\int_0^{T-\tau}(...)\,dt\,. \tag{4}$$

Additionally, to extract complete information from the difference moments (transient structural function) is required

$$\phi^2(\tau) = \left\langle [V(t) - V(t+\tau)]^2 \right\rangle_T \tag{5}$$

Note that all information extracted from above expressions are averaged over time interval . In real experiment can be subinterval of , where corresponds to whole duration of the experiment. It is obvious that the value of the autocorrelation function can depend on the position of subinterval in the. If there is no such dependence then the evolution process can be called "stationary". For stationary process equation (5) can be written in the form [9]

$$\phi^2(\tau) = 2[\psi(0) - \psi(\tau)] \tag{6}$$

Notice that the transient structural function contains information about the jumps, while the power spectrum contains information about jumps as well as spikes of the dynamic variable [8].

The FNS method can be applied for different classes of problems described below.

(A) Determination of parameters which characterized the dynamics of a system.

The FNS method is successfully applied for determination of parameters describing the dynamics of the system. All these parameters can be extracted from chaotic components of and using appropriate interpolations formulas presented underneath.

If we consider that chaotic component of signal consists exclusively of spikes and jumps, the interpolation formula for chaotic component of transient structural function can be expressed as

$$\phi_c^2(\tau) \approx 2\sigma^2\left[1 - \Gamma^{-1}(H_1)\Gamma\left(H_1, \frac{\tau}{T_1}\right)\right]^2 \tag{7}$$

where $\Gamma(x)$ are the complete and incomplete gamma functions, respectively is the standard deviation of the measured variable, is the Hurst constant and is the correlation time. As it was mentioned before is formed only by jumps, therefore in the case of transient structural function we can assume that component originating from spikes is equal to zero. On the other hand, the interpolation function for chaotic power spectrum component should be separated into two independent parts related to spikes and jumps

$$S_{cS}(f) = \frac{S_{cS}(0)}{1 + (2\pi f T_0)^{n_0}} \tag{8}$$

$$S_{cJ}(f) = \frac{S_{cJ}(0)}{1 + (2\pi f T_1)^{2H_1+1}} \tag{9}$$

where are parameters and can be expressed as

$$S_{cJ}(0) = 4\sigma^2 T_1 H_1\left\{1 - \frac{1}{2H_1\Gamma^2(H_1)}\int_0^\infty \Gamma^2(H_1,\xi)d\xi\right\} \tag{10}$$

Parameters H_1, T_1, n_0 have specific physical interpretations as follow: determines the characteristic time during the measured values gets "forgotten", describes the "law" of correlation loss and describe correlation "loss" in frequency coordinate [11].

(B) Determination of the precursors of abrupt changes in the state.

To investigate the nonstationary processes occurring in real experiment the changes in and in the interval, where should be taken into consideration. In this case the considered window with interval is shifted by in each step. For each step all parameters of the FNS method should be determined. One of the method for investigation of the nonstationary processes is determination of the precursor of abrupt changes, which can be calculated using formula

$$C(t_{k+1} + T) = \frac{Q_{k+1} - Q_k}{\Delta T} \times \frac{2T}{Q_{k+1} + Q_k} \tag{11}$$

$$Q_k = \frac{1}{\alpha T}\int_0^{\alpha T} \phi^2[(\tau)]_k \, d\tau$$

where α is parameter, is the time interval shifted by along time axis.

(C) Determination of cross-correlations between signals simultaneously measured in different points in space.

The FNS method allows also to determine correlation characterizing the links between and using expression

$$q_{ij}(\tau;\Theta_{ij}) = \left\langle \left[\frac{V_i(t) - V_i(t+\tau)}{\sqrt{\phi_i^2(\tau)}}\right]\left[\frac{V_j(t+\Theta_{ij}) - V_j(t+\Theta_{ij}+\tau)}{\sqrt{\phi_j^2(\tau)}}\right]\right\rangle_{T-\tau-|\Theta_{ij}|} \quad (12)$$

where is the lag time and is the time shift parameter.

The parameter in (eq. 12) describes the cause and effect relation between signals. > 0 means that signal flows from to source while for the signal flows from to. Thus the analysis of can be used to investigate the flow dynamics between sources.

All formulas presented above and algorithm to determine parameters from the signal are presented in details in [10].

Experimental paradigm

The investigation of EEG phenomena related to the movement imagination necessitates a sensibly planned experiment, focused on specification of method applied afterwards. One, a 26 years old, right-handed healthy volunteer participated in the study. The experiment consisted of fifty repetitions of right hand movement imagination. The duration time of single trial was seven seconds and consisted of three periods. The first period from 0 to 3 s was the relaxation time, the second period from 3 to 4 s indicated the imagination of hand movement by sound signal, and the third one from 4 to 7 s was relaxation time again. Subject was requested to relax the muscle and suppress eye blinking to avoid EMG and EOG activity artefacts. The trials with evident artefacts were excluded from further analysis. One 50-trials experiment takes less than 6 minutes. The configuration of the electrodes used for data acquisition is shown in Fig. 1. EEG activity was recorded from 16 of the standard electrode locations (international extended 10/20 electrode system) distributed mainly over sensorimotor cortex. All 16 channels were referenced to the average of the right and left ear's signals (electrode and). The sampling frequency was 500 Hz.

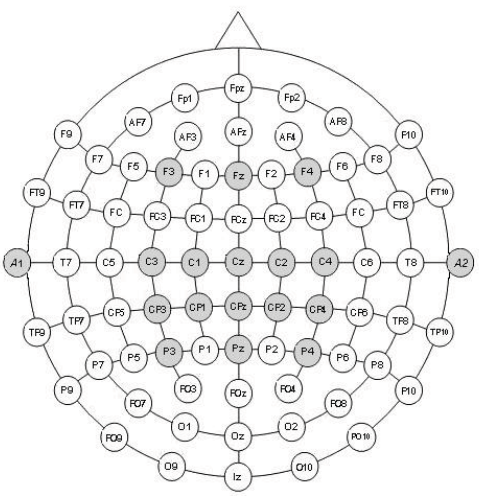

Fig. 1. The international extended 10/20 electrode system. The electrodes used for data acquisition are marked in gray circle. The ear's electrodes are the referencing ones

Results

The detailed knowledge about brain activity during the movement or the movement imagination and the movement itself opens new possibilities in communication between man and machine. It is well known that during movement or movement imagination the changes of brain activity occur in the alpha (8-13 Hz) as well as the beta frequency range (15-20 Hz)[12, 13]. For description of the power changes on a spatiotemporal maps, the event-related desynchronization (ERD) and event-related synchronization (ERS) are defined [14]. ERD/ERS maps inform about the power decrease/increase, averaged over trials in relation to power in a reference time interval. In case of experiment with hand movement, ERD appears in both alpha and beta bands before movement (imagination of movement), while ERS appears usually in the beta band as post-movement beta synchronization (β-rebound) after the end of movement (imagination of movement). Since human somatotopic organization indicates that human limbs are controlled by contralateral brain hemispheres, we expect that the most important changes in brain activity occur mainly at C3 electrode, which lies over left hemisphere of motoric cortex. For better illustration of conralateral brain activity, the signal from C4 electrode is also taken into consideration.

In the present experiment subject had to perform the task of imagination of right hand clench fifty times. The EEG signal obtained from the experiment was prepared for further analysis in three steps. Firstly, all evident artefacts were excluded from the signal, secondly – the signal was spatially and then temporally filtered between 5-35 Hz using Butterworth bandpass filter. Finally, the signal was averaged over all trials. The averaged signal for electrodes C3 and C4 is shown in Fig. 2. In both figures the time interval of sound signal, which indicates the imagination of hand movement, is marked by dashed line.

Using averaged signal for C3 and C4 electrodes, the ERD/ERS maps are calculated and presented in Fig. 3. By analogy, the time interval of sound signal, which indicates the imagination of hand movement, is marked by dashed line. As we expected, the bilaterally α-ERD (11-12 Hz) before and during imagination of movement can be observed. On the other hand, the contralateraly β-ERD (20-30 Hz) appears during imagination of movement from 3.5 to 4.5 second and after the end of imagination from 5 to 6.5 second as the post-movement beta synchronization (β-rebound).

The ERD/ERS maps are the classical way of brain activity presentation in the experiment in which the sensorimotor cortex behaviour is investigated. The aim of this paper is to present that FNS can be an alternative method to analyze the data related to the movement imagination in different manner. Using formula (2), the power spectrum (the cosine transform)

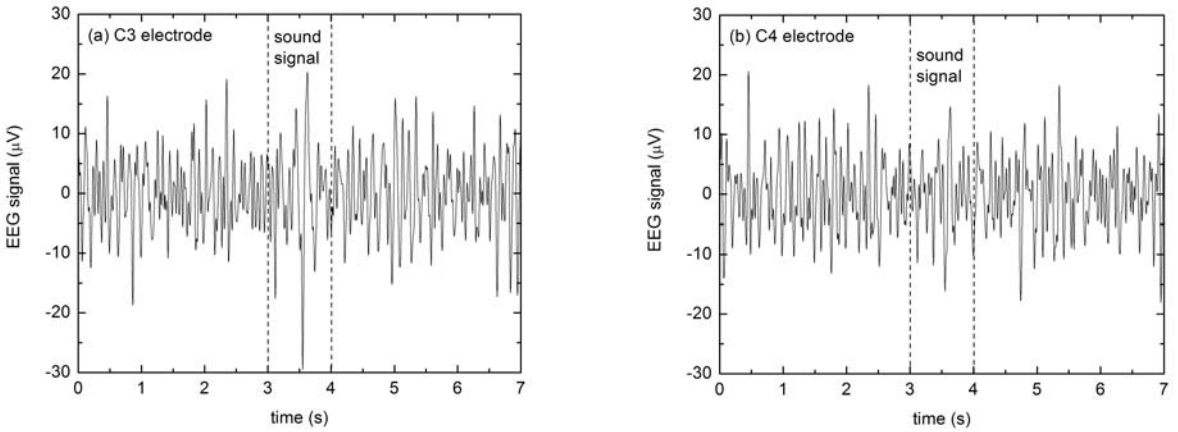

Fig. 2. Original EEG signal related to right hand movement imagination and averaged over trials for electrode C3 (a) and electrode C4 (b)

of the autocorrelation function was calculated. In the Fig. 4 the power spectrum for C3 electrode in two time intervals is presented. In both cases calculations were performed with T = 1*s*. In the first time interval, from 4.4 to 5.4 s, corresponding to movement imagination, we can observe the domination of alpha rhythm with frequency 9-11 Hz. The second period between 5.5 and 6.5 s after movement imagination is dominated by beta rhythm with frequency 18-20 Hz. It is worth to mention that in the relax stage of brain, the characteristic of the power spectrum is inversely proportional to the frequency.

Another application of the FNS method is parameterization of chaotic components of the signal. As we presented in theoretical section, for stationary problem we are able to obtain set of parameters which describe dynamics of the system. It is obvious that in case of movement imagination the assumption of stationarity in entire time interval is not satisfied. To solve the problem of nonstationarity, the entire time interval was divided into small ones. It can be assumed that in each of these small intervals the stationary condition is fulfilled, therefore all interpolating formulas presented above can be applied. For the same time intervals as in the case of power spectrum analysis, namely for the imagination of movement and post-movement beta rhythm, the structural functions and parameters were calculated. The parameters for time interval 4.4 – 5.4 s amount: $S_{cS}(0) = 32.73\,\mu V$, $n_0 = 3$, $T_0 = 11.7 \times 10^{-3}\,s$, $H_1 = 0.72$, $T_1 = 8.9 \times 10^{-3}\,s$, while those parameters for time interval 5.5 – 6.5 s are: $S_{cS}(0) = 25.22\,\mu V$, $n_0 = 3$, $T_0 = 18.2 \times 10^{-3}\,s$, $H_1 = 1.72$, $T_1 = 9.2 \times 10^{-3}\,s$. In fig. 5 the experimental structural function (marked by line) and its interpolation (marked by dots), obtained using determined parameters, are presented. It can be observed that function has completely different behaviour for movement imagination (Fig. 5(a)) and post-movement β-rebound (Fig. 5 (b)). The closer inspection of parameters for both intervals does not indicate great changes in their values, except of the Hurst constant. Its value changes from $H_1 = 0.72$ for the first interval to $H_1 = 1.72$ for the second one.

Additionally, the FNS method allows to calculate the cross-correlations in a specified time interval (eq. 12). The Θ_{ij} parameter in equation (12) means the time shift between i-th and

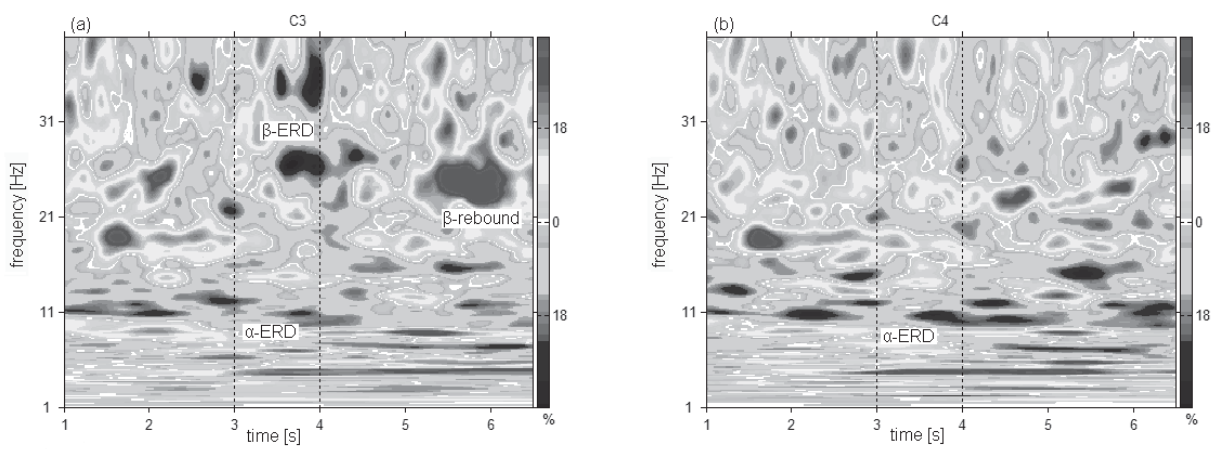

Fig. 3. Time-frequency maps of ERD/ERS related to right hand movement imagination for electrode C3 (a) and electrode C4 (b). The estimation of the time-frequency distribution of energy density is scalogram (Continuous Wavelet Transform). The reference period is 0-1 s

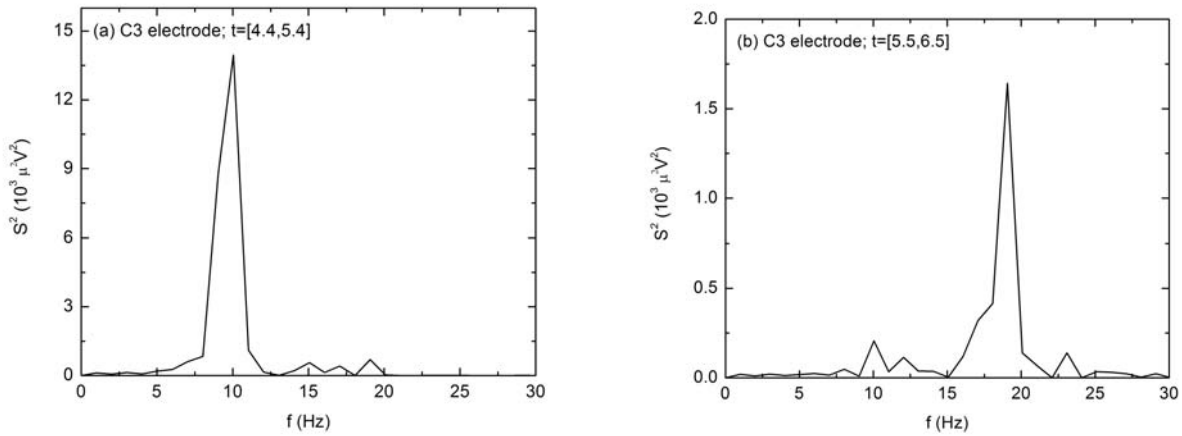

Fig. 4. The power spectrum (the cosine transform) of the autocorrelation function calculated for electrode C3 and time interval t = 4.4-5.4 s, which correspond to the task of movement imagination task (a) and time interval t = 5.5-5.5 s, which corresponds to post movement β-rebound (b)

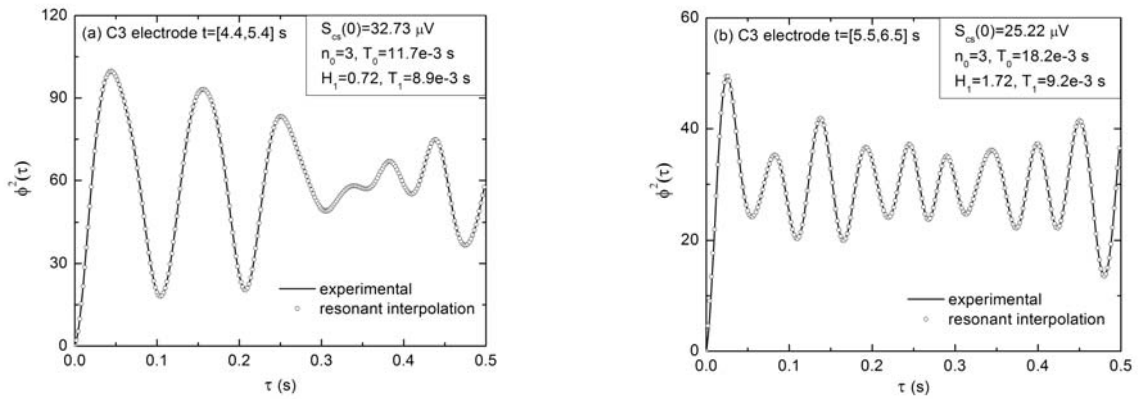

Fig. 5. The experimental structural function (marked by line) and its interpolation (marked by dots) for electrode C3 in time intervals corresponding to movement imagination (a) and post- movement β-rebound (b)

j-th electrode. If we consider signal with frequency occurring on both electrodes, it is easy to show that correlation equal to one corresponds to situation when the signals from i-th and j-th are in phase, while correlation equal to minus one corresponds to opposite situation, when i-th and j-th electrodes are in antyphase. Thus, analysis of cross-correlation maps gives as an additional information about dominant frequency occurring on both electrodes simultaneously. In Fig. 6 the cross-correlations between two electrodes C3 and C1 and four different time intervals (a)1.8-2.8 s, (b)3.5-4.5 s, (c) 4.5-5.5 s, (d) 5.5-6.5 s are illustrated. Both electrodes lie over the motor cortex on left brain hemisphere, in a distance about 3 cm from each other. Figure 6(a) presents the cross-correlation in the time interval before the sound signal in the relax state with expectation on performing the task, while the figure 6(b) shows the correlations related to sound signal. It shows the uniform distribution of maxima and minima. The distance between maximum and minimum corresponds to the frequency of alpha rhythm, which is dominant in this time interval. Then, in Fig. 6(c) the cross-correlation changes, which is probably related to regrouping of neurons oscillations frequency during performing the task. The last figure 6(d) shows the cross-correlation after the imagination of movement. The distance between maximum and minimum corresponds to frequency of beta rhythm, which is related to the post movement beta activity, known as β-rebound. For better illustration of the distances between extreme points in cross-correlation maps, the sections through $\tau = 0.26\,s$ are presented in Fig. 7.

As we treat the performance of movement imagination as some disturbance in relax brain activity, it seems natural to expect some precursor of those changes. In Fig. 8 the nonstationary precursor, calculated using equation (11) for electrodes C3 and C4 with two different combination of parameters, is presented. In all figures the time interval of sound signal, which indicates the imagination of hand movement, is marked by a dashed line. For both sets of parameters, abrupt changes in *C* precursor as a function of time occur at electrode C3. At the same time, amplitude of precursor *C* on the electrode C4 is much lower. The changes of precursor in electrode C3 can be associated with reorganization of neurons oscillations occur-

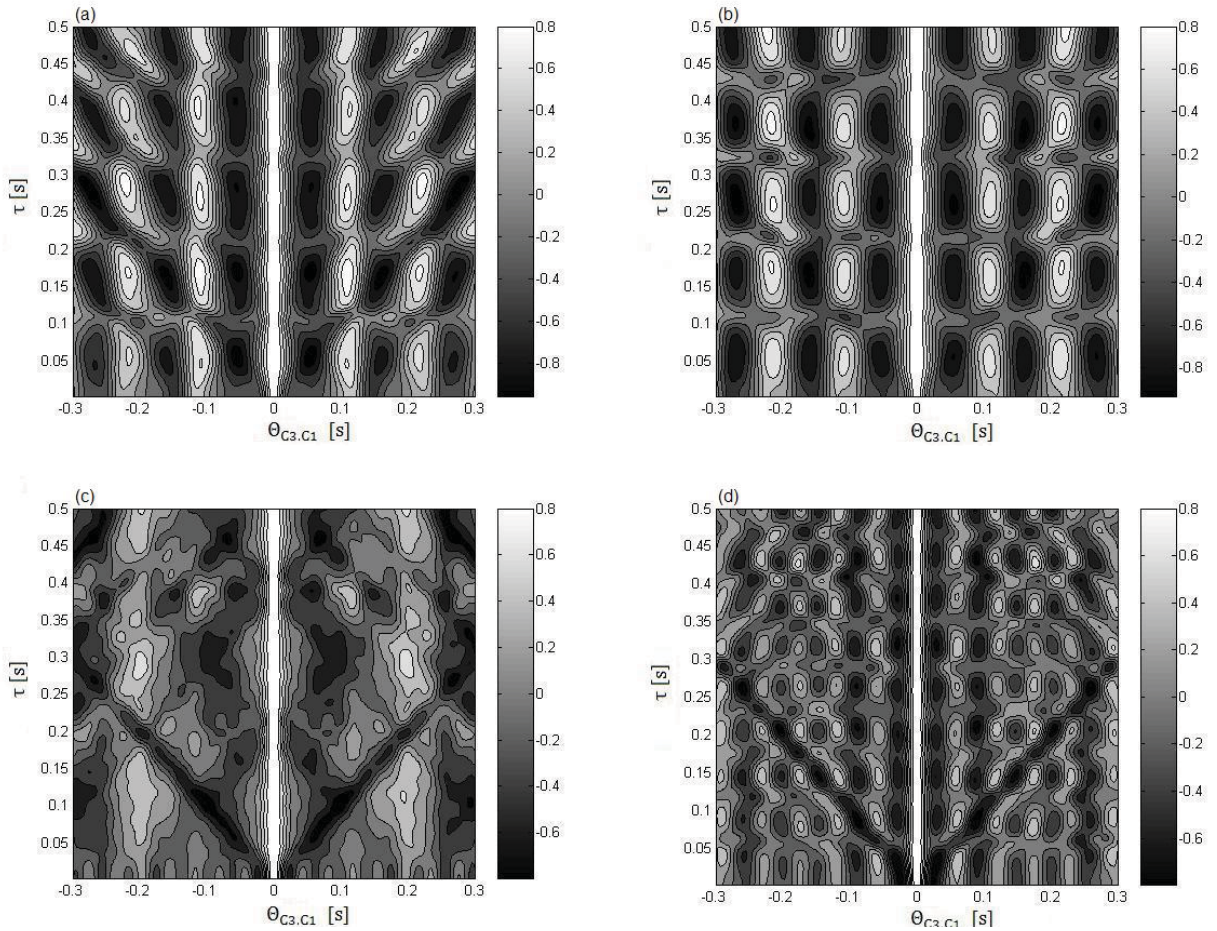

Fig. 6. The cross-correlations between two electrodes C3 and C1 in four different time intervals: (a) 1.8-2.8 s, (b) 3.5-4.5 s, (c) 4.5-5.5 s, (d) 5.5-6.5 s

ring before movement imagination, which in case of right hand, corresponds mainly to electrode C3.

Conclusion

The analysis presented above shows that the Flicker-Noise Spectroscopy can be applied to study the electroencephalography signal. In the present paper the FNS method was applied for analysis of EEG signal related to movement imagination. The analysis of power spectrum of autocorrelation function and cross-correlation maps allows to observe the changes in brain activity during movement imagination. The parameterization of chaotic components of signal for two time intervals corresponds to movement imagination and post-movement β-rebound was performed. Additionally, abrupt changes in precursor as a func-

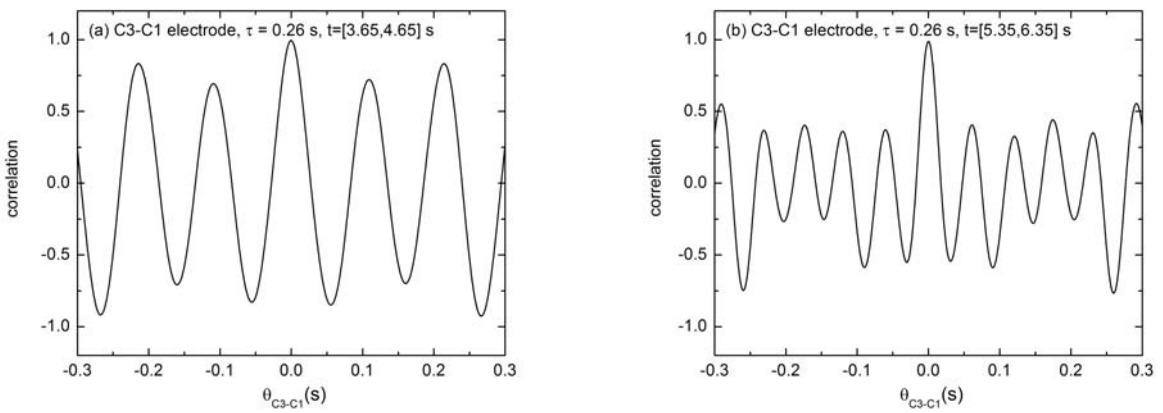

Fig. 7. Sections of cross-correlation maps through $\tau = 0.26\,s$ in time intervals (a) 3.5-4.5 s and (b) 5.5-6.5 s related to Fig. 6(b) and 6(d), respectively

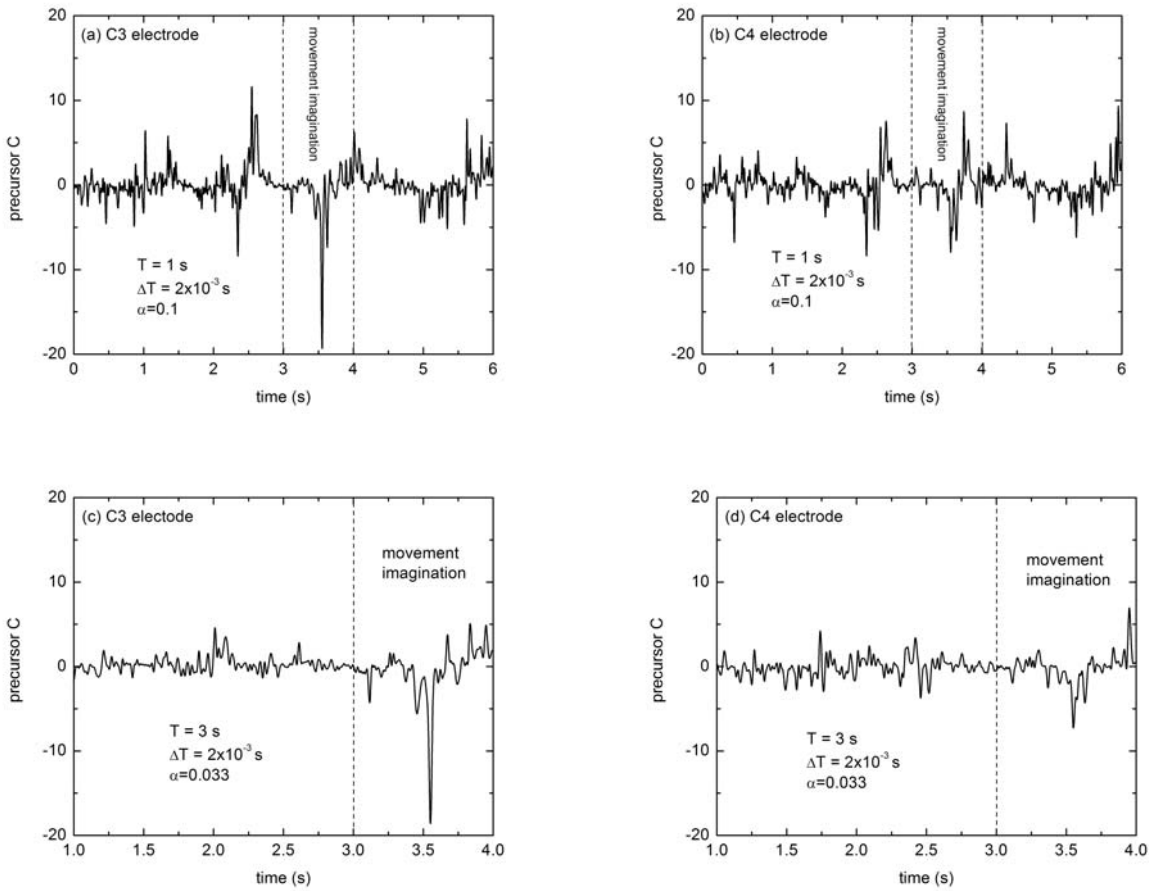

Fig. 8. The nonstationary precursor for electrodes C3 (a),(c) and C4 (b), (d) with two different combination of parameters

tion of time has been found. It gives hope for an effective differentiation between right and left hand movement imagination for future implementation for the BCI application.

Acknowledgements

This paper has been supported by research project No. N N518 426736.

References

1. Schalk G., McFarland D.J., Hinterberger T., Birbaumer N., Wolpaw J.R. (2004), BCI2000: A General-Purpose Brain--Computer Interface (BCI) System. IEEE Trans Biomed Eng 51 (6), 1034-43.
2. Huang D., Lin P., Fei D., Chen X., Bai O. (2009), Decoding human motor activity from EEG single trials for a discrete two-dimensional cursor control. J Neural Eng 6/046005 (12pp) doi:10.1088/1741-25.
3. Timashev S.F., Belyaev V.E., Timashev P.S., Solovieva A.B. (2006), On parameterization of surface structures. Colloid J 68, 481-493.
4. Descherevsky V., Lukk A.A., Sidorin A.Y., Vstovsky G.V., Timashev S.F. (2003), Flicker-noise spectroscopy in earthquake prediction research. Natural Hazards and Earth System Sciences 3, 159-164.
5. Telesca L., Lapenna V., Timashev S., Vstovsky G., Martinelli G. (2004), Flicker-noise spectroscopy: a new approach to investigate the time dynamics of geoelectrical signals measured in seismic areas. Physics and Chemistry of the Earth 29, Issues 4-9, 389-395.
6. Parkhutik V., Rayon E., Ferrer C., Timashev S., Vstovsky G. (2003), Forecasting of electrical breakdown in porous silicon using flicker noise spectroscopy. Physica Starus Solidi (A) 197, 471-475.
7. Timashev S.F., Vstovskii G.V. (2003), Flicker-Noise Spectroscopy for Analyzing Chaotic Time Series of Dynamic Variables: Problem of Signal-to-Noise Relation. Russian Journal of Electrochemistry, Chemistry and Materials Science 39/2.
8. Yulmetyev R.M., Demin S.A., Panischev O.Y., Hanggi P., Timashev S.F., Vstovsky G.V. (2006), Regular and stochastic behavior in Parkinsonian pathological tremor signals. Physica A: Statistical Mechanics and its Applications 369/2, 655-678.
9. Timashev S.F., Polyakov Y.S. (2008), Analysis Of Discrete Signals with Stochastic Components Using Flicker Noise Spectroscopy. International Journal of Bifurcation and Chaos (IJBC) in Applied Sciences and Engineering 18/9, 2793-2797.

10. Timashev S.F., Polyakov Y.S., Yulmetyev R.M., Demin S.A., Panischev O.Y., Shimojo S., Bhattacharya J. (2009), Analysis of biomedical signals by flicker-noise spectroscopy: Identification of photosensitive epilepsy using magnetoencephalograms. Las Phys 19.
11. Timashev S.F. (2001), Flicker-noise spectroscopy as a tool for analysis of fluctuations in physical systems. In: Noise in Physical Systems and 1/f Fluctuations – ICNF 2001, ed. by G. Bosman. World Scientific, New Jersey-London, 775--778.
12. Crane N.E., Miglioretti D.L., Gordon B., Sieracki J.M., Wilson M.T., Uematsu S. (1998), Functional mapping of human sensorimotor cortex with electrocorticographic spectral analysis: I. Alpha and beta event-related desynchronization. Brain 121, 2271-99.
13. Alegre M., Gurtubay I.G., Labarga A., Iriarte J., Valencia M. Artieda J. (2004), Frontal and central oscillatory changes related to different aspects of the motor process: a study in go/no-go paradigms. Exp Brain Res 159, 14-22.
14. Pfurtsheller G., da Silva F.L. (1999), Handbook of Electroencephalography and Clinical Neurophysiology, Revised Series. Elsevier Science B.V.

BIO-ALGORITHMS AND MED-SYSTEMS
JOURNAL EDITED BY MEDICAL COLLEGE – JAGIELLONIAN UNIVERSITY
Vol. 6, No. 12, 2010, pp. 67–73.

TRANSCRANIAL MAGNETIC STIMULATION TMS VERUS ELECTROCONVULSIVE THERAPY ECT IN THERAPY OF DEPRESSIONS – ADVANTAGES AND DISADVANTAGES OF COMPUTER MODELING

Tomasz Zyss[1], Andrzej Krawczyk[2], Paweł Drzymała[3], Bartosz Sawicki[4], Jacek Starzyński[5]

[1] *Department of Adult Psychiatry, University Hospital, Medical College of Jagiellonian University, Kraków; e-mail: mzzyss@cyf-kr.edu.pl*
[2] *Central Institute for Labour Protection – National Research Institute, Unit for Bioelectromagnetism, Warszawa*
[3] *Institute of Mechatronics and Information Systems, Technical University of Lodz, Łódź*
[4] *Institute of Theory of Electrical Engineering, Measurement and Information Systems, Warsaw University of Technology, Warszawa*

Abstract: The work describes the results of our own investigations on computer modeling of two physical methods of depressions treatment: electroconvulsive therapy ECT and transcranial magnetic stimulation TMS. The model studies allowed us to explain why the effectiveness of magnetic stimulation is lesser than that of electric stimulation. There are, however, several aspects that could not be analyzed or explained with the help of modeling techniques.
Keywords: depression; ECT, TMS, computer modeling, advantages, disadvantages

Streszczenie: Praca opisuje wyniki badań własnych nad komputerowym modelowaniem dwóch metod fizykalnego leczenia depresji: zabiegów elektrowstrząsowych EW oraz przezczaszkowej stymulacji magnetycznej TMS. Badania modelowe pozwoliły wyjaśnić, dlaczego skuteczność stymulacji magnetycznej jest mniejsza niż elektrycznej. Istnieje jednak kilka aspektów, które nie mogły być wyjaśnione czy też przeanalizowane za pomocą technik modelowania.

Introduction

Transcranial magnetic stimulation (TMS) is a neurophysiological method using a strong time varying magnetic field to stimulate brain structures. It was introduced into clinical practice in 1985 and initially used in neurological diagnostics. Due to its safety and on-invasive character, the transcranial magnetic stimulation technique became a valuable instrument used in functional studies on the brain [1].

Studies on the potential antidepressant effect of TMS have been conducted since the beginning of the 1990s. In its assumptions, magnetic stimulation TMS was to become a method of treatment of depressive disorders alternative to electroconvulsive therapy (ECT) and safer than the latter, since it did not evoke seizure activity [2].

After nearly two decades of our own investigations and studies of other authors on TMS it has become known that the psychiatrists' hopes pinned on this method have been shattered. It turned out that the antidepressant effect is weak. Thanks to the techniques of computer modeling it was possible to analyze the phenomena accompanying both magnetic stimulation TMS and the reference method, namely, ECT [3].

Computer modeling of electric and magnetic brain stimulation

The development of computer techniques which have taken place in recent decades have provided researchers with powerful research instruments that allow for more or less faithful modeling of biophysical phenomena which take place within biological objects. In neurophysiological studies it became possible to construct models of complex biological structures like the human head, and, moreover, particular models of the head can be characterized by different levels of complexity, issuing from its structural and bioelectric heterogeneity [4, 5]. The constructed model of the head may be later subjected to the processes of electric or magnetic stimulation. Thus, it is possible to observe in this computer model the biophysical phenomena

which accompany the two methods of physical treatment of depression, namely electroconvulsive therapy (ECT) and transcranial magnetic stimulation (TMS). The former method (ECT) has its recognized and confirmed position in the catalogue of psychiatric therapies [6] while the latter (TMS) has been examined in regards to its antidepressant effectiveness since the 1990s [7], as it is one of the newest experimental neuromodulating methods [8].

Before TMS was introduced into clinical practice, the technique of electric stimulation of the head and brain was subject to various attempts at being modeled. The results of experiments on electrical brain stimulation are a kind of comparison data to the studies on magnetic stimulation [9-12]. It should be mentioned that apart from ECT modeling, studies also exist aimed at the analysis of methods of non-convulsive electric stimulation, i.e., a procedure executed with the use of stimulation parameters that do not bring about a convulsive seizure activity. In ECT modeling it is the dispersion of the current under the electrodes that is interesting, and the process of modeling itself "stops" just before the triggering of seizure activity in the brain, which is undesirable in the magnetic stimulation technique and belongs to a separate domain of studies on models of epilepsy.

The investigations demonstrated that the density of the current excited as a result of electric head stimulation decreases with the increase of the depth (i.e. approaching the center of the brain) – which is understandable. Current flows through the more superficial layers and the further it is from the stimulating electrodes, the lesser its density becomes (the current does not reach the "center" of the brain or only a small proportion reaches it). In the superficial layers the density of the current increased in direct correlation with a decrease in distance between the electrodes. This effect can be explained by the "bending" of the path of the current flow between the electrodes. When the electrodes are close to each other, the pathway of the current flow gets bent; the majority of the current tends to flow between the electrodes in the shallow, superficial layers. In turn, when the distance between the electrodes is greater, it forces the current to flow through a larger part of the brain – its density in the superficial layers decreases and its density in the deeper layers increases.

Studies modeling the phenomena accompanying magnetic stimulation started later than those regarding electric stimulation [13-15].

There are, however, relatively few works in which the TMS and ECT techniques were directly compared. They include the study by Nadeem et al. [16] who used an extremely complicated spatial model of the head consisting of as many as 24 different anatomical structure components in their investigations. The researchers showed that in ECT the values of current density and the electric field strength are ca. four times as high as those obtained during TMS; therefore the physical impulse in ECT may penetrate further and be more effective in the deep structures of the brain. Yet, the authors stated that TMS can also achieve biologically active values of current density and electric field strength in brain structures, but only in superficial ones.

Own model studies – on a simple model of the head

Our first model experiments were carried out on a simple spherical three-dimensional (3D) model of the head [17]. The software package Opera-3D+ (a product of the English company Vector Fields Ltd., at present: Cobham Technical Services) was used for the spatial analysis of physical processes which accompany electric and magnetic head simulation. The created model was based on a set of Helmholtz's differential equations solved numerically with the finite element method.

Our first step in the research consisted of creating a three-dimensional structure of the head, which was to be submitted to the process of electric or magnetic stimulation. To simplify the procedure, we resigned from analyzing the electric anisotropy (various electric properties of tissues towards directions) of particular layers, including the layer of soft tissues of the head: the scalp, and the layer of bone integument of the scull. In the constructed model, we introduced another simplification, introducing an ideal spherical shape of the head and all its layers (in natural conditions a head is an ellipse/ellipsoid with the longest radius in the front-back projection). The geometrical model applied in magnetic stimulation was slightly different from that used in electric stimulation. The difference consisted in application of different elements constituting subsequent layers, but their electric properties as well as the thickness of particular layers were preserved.

The second step in our research consisted of submitting the created model of the head to the procedures of electric and magnetic stimulation. Qualitative evaluation was conducted as regards current density (J, [A/m^2]) – a physical value reflecting the effectiveness of current flow in biological structures better than its "ordinary" value of current (I, [A]).

The research showed that during ECT course, two crawling/spreading effects occur, which consist of the fact that the current flows mainly in a direction parallel to and not perpendicular to the surface of the brain. In other words, the current has no tendency to penetrate the brain structures, but – due to certain bioelectric properties of the head – it flows through its more superficial layers. The above mentioned crawling/spreading effect can be detected not only in the skin layer, but also in the cerebrospinal fluid layer.

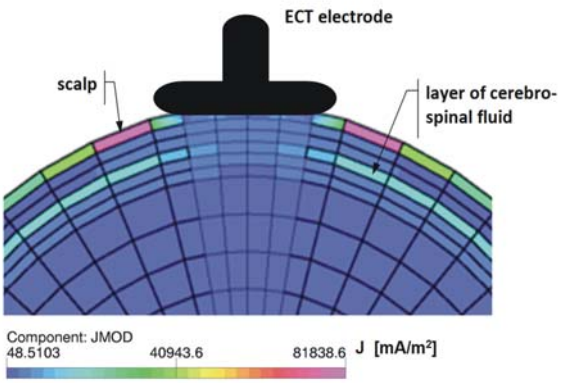

Fig. 1. Higher values of current density indicates a crawling/spreading effect in two head layers during ECT

Ultimately, the multi-layer structure of the head with alternating layers of high and low specific conductance (electrical conductivity or specific conductance is a measure of the ability of a material, in this case particular layers of the head, to conduct an electric current; the opposite of electrical resistance) causes a significant part of the electric current (85-90%) applied via electrodes during an ECT procedure to become lost in the more superficial layers and as a result only a small amount reaches the cortical layers of the brain. If the electrodes were placed not on the opposite poles of the head (180^0; e.g., bitemporally) but at a much lesser distance, e.g., bifrontally, as it is done in clinical practice (= 90^0), the strongest current flow would occur in the scalp layer. In such a situation only a minimal quantity of the applied current reaches the deeper layers.

In the method of magnetic stimulation (TMS), it is also electric current that is the physical factor stimulating nerve cells. This current, however, comes from a source completely different than that of the current applied in ECT. The current flowing in the applicator (stimulating coil placed close to the head) causes the occurrence of magnetic field, which can freely penetrate the stimulated area of the head. The strong, time varying magnetic field pulses influencing the conductor (here: closed circuits of neuronal net – brain tissue) causes that in its surroundings there occurs electric field of intensity E.

The current flowing in the conductor will be of intensity I (in fact, current density J [A/m^2]), directly proportional to the field intensity E ([V/m]) and conductivity of medium σ ([S/m]): $J = \sigma E$.

Having exceeded a definite threshold value, this current (wire current) is able to stimulate nerve cells, whose activation can be evaluated with the help of various neurophysiological or biochemical methods.

Current density in the cortex layer was 0,1-1 mA/mm^2, which suggests a lesser current load than that observed during electric stimulation (ECT technique). Since it was assumed then that TMS would have antidepressant effectiveness [18] the obtained results mainly demonstrated the greater safety of the TMS technique. But it must be stated clearly, however, that the safety of a definite therapeutic method is a factor of secondary importance. The most important element is the effectiveness of a given method of treatment. If the method is not (or only slightly) effective in regards to its therapeutic action, all considerations and assessments concerning its safety fall to the wayside.

Own model studies – on a realistic model of the head

After a break, our own model investigations were continued using a more complex, actual model of the head [19-24].

After having constructed the model of the head, we proceeded to construct models of electrodes and stimulation coils (for ECT and TMS respectively), with which it was possible to subject the model of the head to the appropriate form of stimulation. The construction of a model of an electrode or a coil, thanks to their less complex geometry, is much simpler than that of a model of the head. Technical data of the original elements used in ECT and TMS procedures provided the appropriate patterns.

Having constructed models of the head, ECT stimulating electrodes, and TMS coils we could begin direct comparison of the two techniques. During the initial comparative studies, several indices were worked out which allowed for the comparison of particular configurations (location of the electrodes, positioning and types of coils) in both kinds of stimulations as well as the examination of their equivalence. The analysis was carried out on the basis of a three dimensional electric model of the head taking into account the electrical conductivity of particular layers.

The investigations covered various configurations of electrodes and coils. Two cases (presented in table 1) were selected for comparative studies. ECT-TT refers to bilateral ECT procedures with the electrodes located in bi-temporal positions, while TMS is transcranial magnetic stimulation with a round coil near the temporal region.

To compare the techniques of ECT and TMS, the standard technical parameters of medical equipment for electric stimulation (ECT machines) and magnetic stimulation (TMS stimulators) used in clinical practice were modeled. The aim was to calculate the actual distributions of the electromagnetic field inside the human head.

The broad range of variation in various settings of the machinery as well as the sizes of the applicators posed certain problems. Calculating every possible combination would have been far too time consuming and, moreover, it seemed unnecessary for the initial comparison. It was decided to execute calculations for three combinations of parameters only: minimum (min.), at which the generated field E (current density) was the weakest; maximum (max.) – generating the strongest field, and medium (med.) – using the medium settings of the medical devices. Calculations in the extreme cases guaranteed that the entire range of possible solutions would be covered. Details of the settings in each calculated case are presented in table 1. Parameters of the ECT devices and TMS stimulators were discussed in separate works [25-28].

From a medical point of view, the maximum values of the electric field which occur in particular tissues, i.e. the skin, the skull and the brain, are the important elements. The strength of the electric field (E) is a quotient of current density (J) and electrical conductivity (gamma). The parameter of current density J was selected for presentation because, due to the low electrical conductivity, the strength of the electric field (E) reaches its highest values in the bone tissue, dominating the solutions in the soft tissues.

In regards to the comparison of ECT and TMS, it can be seen clearly that the values of current density obtained during ECT are much higher than those achieved during magnetic stimulation.

An analysis shows that in the layer of the brain (in its anterior areas) electric stimulation via ECT generated currents of density amounting to 150-400 A/m^2. On the other hand, magnetic stimulation via TMS enables electric currents with a density of ca. 7-15 A/m^2 to be generated in the nerve tissue of the brain. This clearly demonstrates the advantage of the electric method over the magnetic method. The difference between the densities of the currents generated in these two methods may explain both the safety of TMS and its lower effectiveness in comparison to ECT. From a clinical point of view, however, it is hard to appreciate the fact that TMS does not evoke any serious side effects or that they are much more limited than those caused by ECT if, at the same time, it hardly manifests any clinical effectiveness. It could be compared to the appreciation

Tab. 1. Geometrical and electrical parameters of different variants of stimulation. Parameter indices: min., med. and max. – refer to the values of energy transferred to the stimulated objects; description of abbreviations and symbols – in the text

Model	Parameters	Parameter values
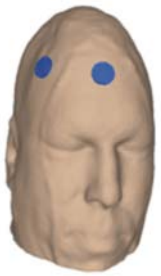 **ECT-FT**	**min.**	U = 50 V R = 1,5 cm; t_{width} = 1 ms; f = 50 Hz
	med.	U = 200 V R = 1,5 cm; t_{width} = 1 ms; f = 50 Hz
	max.	U = 400 V R = 1,5 cm; t_{width} = 1 ms; f = 50 Hz
 **ECT-TT**	**min.**	U = 50 V R = 1,5 cm; t_{width} = 1 ms; f = 50 Hz
	med.	U = 200 V R = 1,5 cm; t_{width} = 1 ms, f = 50 Hz
	max.	U = 400 V R = 2,5 cm; t_{width} = 1 ms, f = 50 Hz
 **TMS**	**min.**	I = 4 kA n = 5; r = 1 cm, R = 3 cm, h = 1 cm t_{rise} = 100 µs, f = 10 Hz
	med.	I = 7 kA n = 7; r = 1 cm, R = 5 cm, h = 1 cm t_{rise} = 100 µs, f = 10 Hz
	max.	I =9 kA n = 10; r = 2 cm, R = 7 cm, h = 2 cm t_{rise} = 100 µs, f = 10 Hz

of the fact that techniques such as Giljarowski's electrosleep [29], Cranial Electrotherapy Stimulation CES [30] or transcranial direct current stimulation tDCS [31] do not evoke convulsions without paying attention to the ineffectiveness of this method in comparison to ECT.

The results of numerical calculations have been listed in table 2.

An analysis of the results reveals several interesting facts. Comparison of results from two different ECT electrode locations confirmed that a shorter distance between the electrodes (fronto-temporal = unilateral ECT; ECT-FT) forces a stronger current flow in the superficial layer (skin) than the longer distance (temporo-temporal = bilateral ECT; ECT TT). A greater distance between the electrodes, on the other hand, results in better penetration into the deeper layers of the head, i.e., the brain, which seems to correspond with the better clinical effectiveness of the procedures executed with the bilateral method.

The broad ranges of variability of the parameters in both types of stimulation – represented in table 1 – cause the result bands to partly overlap. This could mean that selecting the settings which ensure maximum magnetic stimulation via TMS would make it possible to achieve values of the electric field in the brain equal to those obtained with the weakest ECT settings.

However, from a clinical point of view we cannot compare the minimum parameters of ECT stimulation with the maximum parameters of TMS. ECT procedures executed with minimum parameters bring about only abortive seizures (non-convulsive or EEG seizures with an inadequate length of duration), which are clinically ineffective, i.e., have no antidepressant efficacy.

Tab. 2. Results of the maximum density of electric current in three layers of the human head model for different stimulation variants

		ECT-FT			ECT-TT			TMS		
		min	med.	max.	min.	med.	max.	min.	med.	max.
skin	J_{max} [A/m^2]	917	3778	7557	604	2416	4843	9	50	210
skull		129	517	1034	75	296	933	0,7	4	20
brain		70	287	575	101	443	1538	3	10	120

Secondly, as it has already been stated, most commercial stimulators for TMS work at "medium" rather than "maximum" stimulation parameters.

This means that, in fact, an optimum ECT stimulation causes the generation of currents with density amounting to 1000 A/m^2 in the superficial areas of the brain layer while TMS with a stimulating coil charged with electric current of 5-7 kA allows for generation of up to 10 A/m^2 on the surface of the brain. Thus, the analysis of the data presented in table 2 shows that the current density flowing through the brain layer in the TMS technique is ca. 100 (40-150) times lower than that obtained in ECT.

The presented results of modeling [32, 33] are pivotal for the explanation of the relatively low clinical effectiveness of TMS [34, 35].

The differences in the values of currents flowing in particular layers of the head manifested themselves in both computer models. The results of the earlier studies conducted in the spherical model were misinterpreted as a proof of safety of magnetic stimulation. The same mistake was made by several other authors studying this problem in the 1990s. The results of those investigations did not inhibit the newly started clinical studies on the role of TMS in therapy of depressions as the method that has to be – due to the results of numerical investigations – little effective or, at least, less effective than ECT. It was only the little effectiveness revealed by the numerous clinical studies conducted in the subsequent years that forced the researchers to carry out a new critical analysis of the results – including also those obtained in computer models. It has become clear that safety of a given therapeutic method is of lesser importance in the face of little or no effectiveness of this method.

Limitations of numerical methods

The techniques of computer modeling are obviously a valuable research instrument that allows us to understand various phenomena of biological nature. However, possible limitations of numerical methods must not be neglected. Some of these limitations are listed below.

1. In the case of electroconvulsive therapy (ECT), the process of computer modeling ends just before a self-sustaining after-discharge (seizure activity) is triggered in the neuronal network of the brain. A discharge of this kind does not usually occur during TMS procedures, but it basically modifies the current conditions within the brain – in comparison with the seizure method, namely, ECT. Obviously, modeling of the phenomena of seizure activity is also possible [36], but they seem to help identify the differences between the discussed techniques to a very limited extent.
2. In the modeling process of ECT and TMS it is necessary to create virtual models of electrodes or coils – the elements of the stimulation system for application of physical stimuli to the patient's head. Models, however, hardly correspond with real life.

   Thus, from the technical point of view it is easier and safer to control the currents applied in ECT procedures (20-450 V, < 1A) than those used in TMS (1-3 kV, do 8 kA).

   Theoretically, it is possible to design (and this was executed in our investigations [37]) a system of a stimulator for TMS – that would allow for generation of a magnetic field strong enough to evoke within the head the electric conditions similar to those occurring during ECT procedures. Yet, construction of such a stimulator seems practically impossible. Today, the commercial stimulators for TMS work within the range of extreme technical conditions. The modeled stimulator for TMS would have to be a source of the electric current reaching tens of thousands ampere that would flow through a coil placed close to (or even touching the surface of) the head. This kind of coil would have to satisfy the conditions of electric safety (i.e. be protected from leakage – which is rather difficult for the relatively thin layers of insulator and the coil shell), thermal safety (carry away the enormous excess of heat and not get burnt – even in the modern coils there occur problems with effective cooling), and mechanical safety (not break into pieces under the influence of high electromechanical forces) [38].
3. The process of modeling does not take into account any non-linear relations between the parameters of stimulation (especially the frequency) and the obtained biological effect. Studies on electric stimulation show that certain frequencies of stimulation (approx. 60-120 Hz) are optimum, that is, a stimulus of the minimum amplitude is able to evoke biological response [39, 40]. In the case of stimulation with the frequencies lower or higher than the optimum the excitability threshold of neuronal structures increases – which requires application of stimuli with higher amplitudes. In the case of TMS technique, this effect has been studies less thoroughly than in the case of electric stimulation. However, observations confirm that at the higher frequencies of TMS stimulation, the risk of evoking seizure activity increases – and it was its absence that was recognized as the main advantage of this technique [41-43]. Triggering of a seizure in a patient protected with general anesthesia and muscle relaxation (as it is done in ECT) differs from an incidental evoking of an epileptic seizure in a conscious patient (as it may happen in TMS).
4. Computer modeling was not able to foresee the results using the techniques of functional neuroimaging in the patients with depression [44, 45]. These studies – executed within the last few years – have shown that the patients with depressive disorders suffer from metabolic dysfunctions in various areas of the brain [46]. These areas may be different in individual patients. Little is known about the topographical stability of this dysfunction, i.e., whether the metabolic disorder in each recurrence of depression originated from the same area. In the case of ECT these observations are of little importance since the generalized seizure activity initiated by electric stimulation reaches all the structures of the brain (including the metabolically disturbed ones). Yet, in the case of the focal TMS [47], functional diagnostics, which is both expensive and hardly accessible, becomes necessary. TMS may be effective only if it is conducted not at random or over an area determined a priori (the left dorsolateral prefrontal area was recognized as one for many years [48]), but over the area which constitutes the actual metabolic target of depression in a given patient. Moreover, in order to increase the precision of stimulation, TMS should not be performed "by hand" (i.e., with the coil held in the hand), but with the use of neuronavigation techniques, which makes TMS even less friendly to its potential recipient [49, 50]. Additionally, the metabolically

disturbed areas located on the medial and basal surfaces of the brain hemispheres, so as in deep brain structures, are not accessible for effective TMS stimulation [51].

References

1. Barker A.T. (1991), An introduction to the basic principles of magnetic nerve stimulation. *J. clin. Neurophysiol.* 8(1), 26-37.
2. Padeberg P., Großheinrich N., Schläpfer T.E. (2007), Depressive Erkrankungen. In: H. Siebner, U. Ziemann (ed.), *Das TMS-Buch. Handbuch der transkraniellen Magnetstimulation*. Springer Medizin Verlag, Heidelberg, 609-620.
3. Abrams A. (2002), Electroconvulsive therapy. Oxford University Press, Oxford.
4. Laarne P., Eskola H., Hyttinen J., Suihko V., Malmivuo J. (1995), Validation of a detailed computer model for the electric fields in the brain. *J. Med. Eng. Technol.* 19(2-3), 84-87.
5. Nilsson J., Panizza M., Grandori F. (ed.) (1996), Advances in magnetic stimulation. Mathematical modeling and clinical application. *Advances in Occupational Medicine & Rehabilitation. Aggiornamenti in medicina occupazionale e riabilitazione* 2/2. Fondazione Salvatore Maugeri, Pavia.
6. Fink M. (1985), Convulsive therapy – theory and practice. Raven Press, New York.
7. Mantovani A., Lisanby S.H. (2007), Transcranial magnetic stimulation in major depression. In: M.S. George, R.H. Belmaker (ed.), *Transcranial magnetic stimulation in clinical psychiatry*. American Psychiatric Press, Washington, 113--152.
8. Swartz C.M. (2009), Electroconvulsive and neuromodulation therapies. Cambridge University Press, New York.
9. Ollendorf F. (1963), Beiträge zur Elektrodynamik des Elektroschoks. II. Ausgleichvorgänge beim Schalten des Schockstromes. *Archiv für Elektrotechnik* XLVII(6), 333-356.
10. Rush S., Driscoll D.A. (1968), Current distributon in the brain from surface electrodes. *Anesth. Analg.* 47, 717-723.
11. Ferdjallah M., Bostick F.X., Barr R.E. (1996), Potential and current density distributions of cranial electrotherapy stimulation (CES) in a four-concentric-spheres model. *IEEE Trans. Biomed. Eng.* 9, 939-943.
12. Grandori F. (1988), Intracranial electric fields during transcranial brain stimulation: modelling and simulations. In: P.M. Rossini, C.D. Marsden (ed.), *Non-invasive stimulation of the brain and spinal cord. Fundamentals and clinical applications. Neurology and Neurobiology* 41. Proceedings of a Workshop Held in Sorrento, Italy, May 24-29, 1987. Allan R. Liss Inc., New York, 145-158.
13. Malmivuo J., Plonsey R. (1995), Magnetic stimulation of neural tissue. In: J. Malmivuo, R. Plonsey (ed.), *Bioelectromagnetism*. Oxford University Press, New York, 375-384.
14. Roth B.J., Saypol J.M., Hallett M., Cohen L.G. (1991), A theoretical calculation of the electric field induced in the cortex during magnetic stimulation. *Electroenceph. clin. Neurophysiol.* 81(1), 47-56.
15. Tofts P.S. (1990), The distribution of induced curents in magnetic stimulation of the nervous system. *Phys. Med. Biol.* 35(8), 1119-1128.
16. Nadeem M., Thorlin T., Gandhi O.P., Persson M. (2003), Computation of electric and magnetic stimulation in human head using the 3-D impedance method. *IEEE Trans. Biomed. Eng.* 50(7), 900-907.
17. Krawczyk A., Wiak S., Drzymała P., Zyss T. (1998), Modelling of eddy currents applied to human brain. *IEEE Trans. Magn.* 34(5), 3471-3474.
18. Höflich G., Kasper S., Hufnagel A., Ruhrmann S., Möller H.-J. (1993), Application of transcranial magnetic stimulation in treatment of drug-resistant major depression – a report of two cases. *Human Psychopharmacology* 8, 361-365.
19. Sawicki B., Szmurło R., Starzyński J., Wincenciak S., Zyss T. (2005), Porównanie wyników symulacji terapii EW i TMS dla rzeczywistych parametrów urządzeń stymulujących (Comparison between results of ECT and TMS simulation for the true parameters of stimulation devices). *Przegląd Elektrotechniczny (Electrotechnical Review)* LXXXI/12, 31--34.
20. Starzyński J., Sawicki B., Wincenciak S., Krawczyk A., Zyss T. (2002), Simulation of magnetic stimulation of the brain. *IEEE Trans. Magn.* 38(2), 1237-1240.
21. Zyss T., Starzyński J., Krawczyk A. (1999), Trójwymiarowy stereotaktyczny model głowy ludzkiej dla badań symulacyjnych nad techniką przezczaszkową stymulacją magnetyczną mózgu (Tree dimensional stereotactic model of human head for stimulation research on technique of transcranial magnetic stimulation). *Annales Academiae Medicae Lodzensis* 40/3, 101-109.
22. Zyss T., Krawczyk A., Drzymała P., Starzyński J. (1999), Zabiegi elektrowstrząsowe a technika przezczaszkowej stymulacji magnetycznej. Wstępne wyniki modelowania komputerowego (ECT versus transcranial magnetic stimulation (TMS): preliminary data of computer modeling). *Psychiatria Polska* XXXIII/6, 909-923.
23. Zyss T., Sawicki B., Starzyński J., Szmurło R., Wincenciak S., Krawczyk A. (2005), Zagadnienia numeryczne dotyczące zjawisk fizykalnych zachodzących w trakcie zabiegów elektrowstrząsowych i przezczaszkowej stymulacji magnetycznej (Numerical problems referring physical phenomena occurring during electroshock treatment and transcranial magnetic stimulation). V Conference „Computer methods and systems" CMS'05, Kraków. In: R. Tadeusiewicz, A. Ligęza, M. Szymkat (ed.), *Computer Methods and Systems*. Vol. 2. ONT, Kraków, 479-482.
24. Zyss T., Szmurło R., Sawicki B., Starzyński J., Wincenciak S., Krawczyk A., Zięba A. (2005), Komputerowa symulacja elektrod do zabiegów elektrowstrząsowych (Computer simulation of electrodes for ECT). XII National Conference „Computer support in scientific research", Wrocław – Polanica Zdrój: XII KK Kowban, 295-300.
25. Magstim. Technical and information materials. Spring Gardens: Magstim Company (2009), http://www.magstim.com/index.html.
26. MagVenture. Technical and information materials. Farum: Dantec/MagVenture (2009), http://www.magventure.com/.
27. MECTA. Spectrum – Instruction manual. Lake Oswego: MECTA Corp (1997).
28. Somatics: Thymatron®System IV – Instruction manual. Lake Bluff: Somatics Inc. (2006).
29. Giljarowski V.A., Liwenzew N.M., Segal J.J., Kirillowa S.A. (1956), *Elektroschlaf*. Verlag Volk u. Gesundheit, Berlin.

30. Klawansky S., Yeung A., Berkey C., Shah N., Phan H., Chalmers T.C. (1995), Meta-analysis of randomized controlled trials of cranial electrostimulation. Efficacy in treating selected psychological and physiological conditions. *J. Nerv. Ment. Dis.* 183(7), 478-484.
31. Paulus W. (2003), Transcranial direct current stimulation (tDCS). In: W. Paulus, F. Tergau, M.A. Nitsche, J.C. Rothwell, U. Ziemann, M. Hallett (ed.), *Transcranial magnetic stimulation and transcranial Direct Current Stimulation. Proceedings of the 2nd International on Magnetic Stimulation (TMS) and Transcranial Direct Current Stimulation (tDCS) Symposium, Göttingen, 11-14 June 2003*. Elsevier, Amsterdam. *Clin. Neurophysiol.* 56, 249-254.
32. Zyss T., Sawicki B., Starzyński J., Szmurło R., Wincenciak S., Krawczyk A., Zięba A., Dudek D. (2006), Komputerowe modelowanie w ocenie efektywności terapeutycznej techniki TMS. XII National Conference „Computer support in scientific research", Wrocław – Polanica Zdrój: XIII KK Kowban, 201-206.
33. Zyss T., Sawicki B., Krawczyk A. (2007), Jak komputerowe modelowanie pomaga zrozumieć przyczyny klinicznej nieefektywności techniki przezczaszkowej magnetycznej stymulacji mózgu TMS w leczeniu depresji? (How does computer modeling help to understand the cause of clinical ineffectiveness of the trancranial magnetic stimulation (TMS) technique in treatment of depression?). IV Cracow Workshop of Medical Engineering, Kraków. *Przegląd Lekarski (Medical Review)* 64, 220-228.
34. Loo C. (2008), TMS in the treatment of major depressive disorder. In: E.M. Wassermann, V. Walsh, C.M. Epstein, T. Paus, U. Zieman, S.H. Lisanby, *The Oxford Handbook of Transcranial Stimulation*. Oxford University Press, Oxford, 633-660.
35. Padberg F., Grossheinrich N., Pogarell O., Möller H.-J., Fregni F. (2007), Efficacy and safety of prefrontal repetitive transcranial magnetic stimulation in affective disorders. In: M.A. Marcolin, F. Padberg (ed.), Transcranial brain stimulation for treatment of psychiatric disorders. *Advances in Biological Psychiatry* 23. Karger AG, Basel, 53-83.
36. Trąbka W. (1990), Regulacyjna interpretacja mechanizmów występowania padaczkowej aktywności w sieciach neuronowych. Rozprawa habilitacyjna. AM, Kraków.
37. Sawicki B., Szmurło R., Starzyński J., Wincenciak S., Zyss T. (2006), Numeryczne projektowanie układu wzbudzenia silnego pola magnetycznego dla przezczaszkowej stymulacji magnetycznej. In: A. Krawczyk, T. Zyss (ed.), *Bioelektromagnetyzm – teoria i praktyka*. CIOP – PIB, Warszawa, 59-66.
38. Zyss T. (ed.) (2009), *Technika przezczaszkowej stymulacji magnetycznej – zagadnienia aparaturowe*. Wydawnictwo Medyczne, Kraków.
39. Hyrman V., Palmer L.H., Cernik J., Jetelina J. (1985), ECT: the search for the perfect stimulus. *Biol. Psychiatry* 20(6), 634-645.
40. Mihailovic L., Delgado J.M. (1956), Electrical stimulation of monkey brain with various frequencies and pulse durations. *J. Neurophysiol.* 19(1), 21-36.
41. Classen J., Witte O.W., Schlaug G., Seitz R.J., Holthausen H., Benecke R. (1995), Epileptic seizures triggered directly by focal transcranial magnetic stimulation. *Electroenceph. clin. Neurophysiol.* 94(1), 19-25.
42. Wassermann E.M. (1998), Risk and safety of repetitive transcranial magnetic stimulation: report and suggested guidelines from the International Workshop on the Safety of Repetitive Transcranial Magnetic Stimulation, June 5-7, 1996. *Electroenceph. clin. Neurophysiol.* 108(1), 1-16.
43. Zyss T., Zięba A., Dudek D., Sawicki B., Krawczyk A., Starzyński J., Szmurło R., Wincenciak S., Siwek M., Wróbel A., Datka W., Grabski B. (2006), Dwa przypadki ujawnienia się czynności napadowej EEG w przypadku zastosowania stymulacji magnetycznej mózgu z częstością 50 Hz (Two cases of the EEG seizure activity in humans by applying of transcranial magnetic stimulations at frequency of 50 Hz). XVI Jubilee Environmental Symposium of PTZE, Wisła, 237-240.
44. Rigucci S., Serafini G., Pompili M., Kotzalidis G.D., Tatarelli R. (2009), Anatomical and functional correlates in major depressive disorder: The contribution of neuroimaging studies. *World J. Biol. Psychiatry* 9, 1-16.
45. Drevets W.C., Price J.L. (2005), Neuroimaging and neuropathological studies of mood disorders. In: J. Licinio, M.-L. Wong (ed.), *Biology of depression. From novel insights to therapeutic strategies*. Vol. 1. Wiley-VCH Verlag GmbH & Co. KGaA, Weinheim, 427-465.
46. Mayberg H.S., Lozano A.M., Voon V., McNeely H.E., Seminowicz D., Hamani C., Schwalb J.M., Kennedy S.H. (2005), Deep brain stimulation for treatment-resistant depression. *Neuron* 45(5), 651-660.
47. Cohen L.G., Roth B.J., Nilsson J., Dang N., Panizza M., Bandinelli S., Friauf W., Hallett M. (1990), Effects of coil design on delivery of focal magnetic stimulation. Technical considerations. *Electroenceph. clin. Neurophysiol.* 75(4), 350-357.
48. Lisanby S.H., Husain M.M., Rosenquist P.B., Maixner D., Gutierrez R., Krystal A., Gilmer W., Marangell L.B., Aaronson S., Daskalakis Z.J., Canterbury R., Richelson E., Sackeim H.A., George M.S. (2009), Daily left prefrontal repetitive transcranial magnetic stimulation in the acute treatment of major depression: clinical predictors of outcome in a multisite, randomized controlled clinical trial. *Neuropsychopharmacology* 34(2), 522-534.
49. Dell'Osso B., Mundo E., D'Urso N., Pozzoli S., Buoli M., Ciabatti M., Rosanova M., Massimini M., Bellina V., Mariotti M., Altamura A.C. (2009), Augmentative repetitive navigated transcranial magnetic stimulation (rTMS) in drug-resistant bipolar depression. *Bipolar Disord.* 11(1), 76-81.
50. Herwig U., Schönfeldt-Lecuona C., Wunderlich A.P., von Tiesenhausen C., Thielscher A., Walter H., Spitzer M. (2001), The navigation of transcranial magnetic stimulation. *Psychiatry Res.* 108(2), 123-131.
51. Zyss T. (ed.) (2009), *Zabiegi elektrowstrząsowe i przezczaszkowa stymulacja magnetyczna – porównanie technik przy pomocy modelowania komputerowego* (Electroconvulsive treatment and transcranial magnetic stimulation – comparison with help of computer modeling). (Krakowskie) Wydawnictwo Medyczne, Kraków.

BIO-ALGORITHMS AND MED-SYSTEMS
JOURNAL EDITED BY MEDICAL COLLEGE – JAGIELLONIAN UNIVERSITY
Vol. 6, No. 12, 2010, pp. 75–80.

COMPUTER DIAGNOSIS OF LARYNGOPATHIES BASED ON TEMPORAL PATTERN RECOGNITION IN SPEECH SIGNAL

Jarosław Szkoła[1], Krzysztof Pancerz[1], Jan Warchoł[2]

[1]Institute of Biomedical Informatics, University of Information Technology and Management in Rzeszów, ul. Sucharskiego 2, 35-225 Rzeszów, Poland
[2]Department of Biophysics, Medical University of Lublin, ul. Jaczewskiego 4, 20-090 Lublin, Poland

Abstract: The research concerns designing computer methods of a non-invasive diagnosis of selected larynx diseases. The proposed approach is based on a signal analysis in the time domain. Two diseases are considered: Reinke's edema and laryngeal polyp. The paper presents a medical background, basic problems, a proposed procedure for the computer tool, and experiments carried out using this procedure.
Keywords: diagnosis support system, laryngopathies, temporal patterns, neural networks

Introduction

The research concerns designing methods of a non-invasive diagnosis of selected larynx diseases. Two diseases are considered: Reinke's edema and laryngeal polyp. The diagnosis is based on an intelligent analysis of selected parameters of a patient's speech signal (phonation). Computer tools supporting medical diagnosis become increasingly more popular worldwide. One of their advantages is automation of a diagnosis process. Moreover, such systems are based on objective measurements and observations of selected parameters. The proposed approach is non-invasive. Comparing it to direct methods shows that it has several advantages. It is convenient for the patient, because the measurement instrument (in this case, a microphone) is located outside the voice organ. This enables free articulation. Moreover, different physiological and psychological patient factors impede making a diagnosis with using the direct methods. From the clinical point of view, an early diagnosis enables taking an effective treatment without surgical procedures. The problem of larynx diseases has become an increasingly serious health problem in different occupational groups.

The majority of methods proposed to date are based only on the statistical analysis of the speech spectrum as well as the wavelet analysis. An application of such methods does not always adjudicate the patient classification in a unique way (compare spectrums in Figure 1 and Figure 2). Therefore, in our research, we propose a hybrid approach, which is additionally based on a signal analysis in the time domain. Hybridization means that a decision support system will have a hierarchical structure, based on multiple classifiers working on signals in time and frequency domains. Preliminary observa-

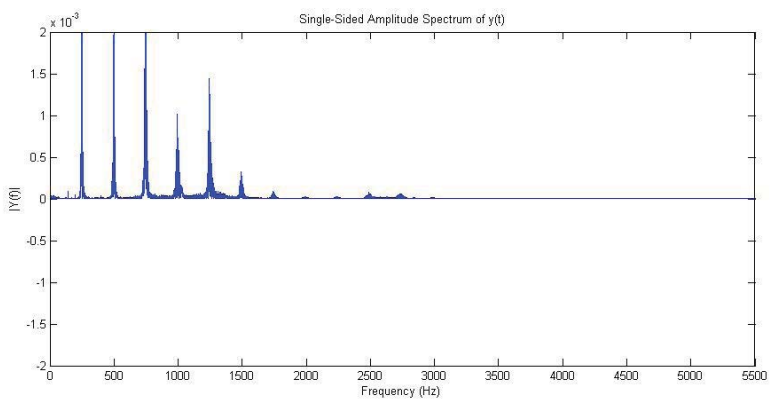

Fig. 1. An exemplary speech spectrum for a patient from a control group

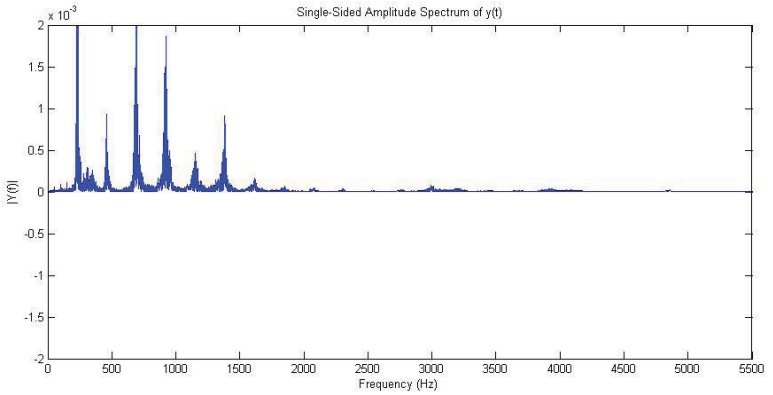

Fig. 2. An exemplary speech spectrum for a patient with polyp

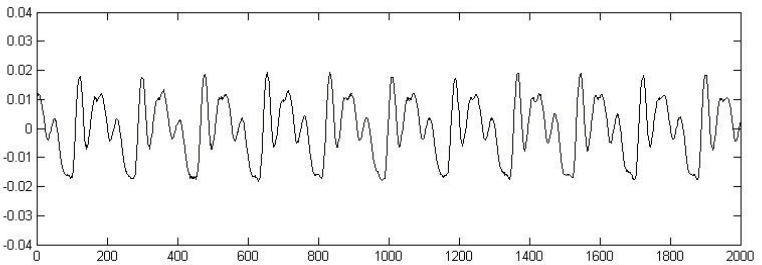

Fig. 3. An exemplary speech signal (fragment) for a patient from a control group

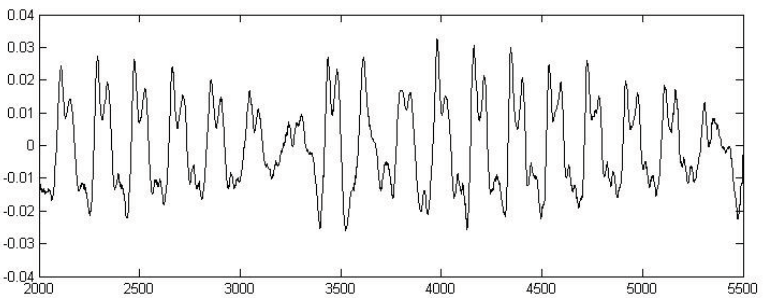

Fig. 4. An exemplary speech signal (fragment) for a patient with polyp

tions of signal samples for patients from a control group and patients with a confirmed pathology clearly indicate deformations of standard articulation in precise time intervals (see Figures 3 and 4).

An application of the spectrum analysis does not enable detection of individual disturbances in a speech signal. In the proposed approach, designing a way for recognition of temporal patterns and their replications becomes the key element. It enables detecting all non-natural disturbances in articulation of selected phonemes. This is the basis for diagnostic classification of patients. In the hybrid system, we propose to use neural networks conditioned by time, i.e., networks with the capability of extracting the phoneme articulation pattern for a given patient (articulation is an individual patient feature) and the capability of assessment of its replication in the whole examined signal. Preliminary observations show that significant replication disturbances in time appear for patients with the clinical diagnosis of disease.

Sound samples were analyzed. Experiments were carried out on two groups of patients. The first group included patients without disturbances of phonation. It was confirmed by phoniatrist. Patients came from different social groups. All patients were non-smoking, so they did not have contact with toxic substances which can have an influence on the physiological state of vocal folds. The second group included patients of Otolaryngology Clinic of the Medical University of Lublin in Poland. They had clinically confirmed dysphonia as a result of Reinke's edema or laryngeal polyp. Experiments were carried out by a course of breathing exercises with instruction about the way of articulation.

Our paper is organized as follows. First, we introduce some relevant medical background related to larynx diseases (Sec-

tion 2). In Section 3, we indicate basic problems in examination of a speech organ function for medical diagnosis. Section 4 describes a computer procedure based on the Elman neural network for supporting diagnosis of laryngopathies. In Section 5, we present results obtained by experiments done on real-life data. Some conclusions and final remarks are given in Section 6.

Medical Background

A model of speech generation is based on the "source – filter" combination. The source is larynx stimulation, i.e., passive vibration of the vocal folds as a result of an increased subglottis pressure. Such a phenomenon of making speech sonorous in the glottis space is called phonation. The filter consists of the remaining articulators of the speech canal, creating resonance spaces. A signal of larynx stimulation is shaped and modulated in these spaces. The final product of this process is called speech. Pathological changes appearing in the glottis space entail a bigger or smaller impairment of the phonation functions of the larynx. The subject matter of the presented research concerns diseases, which appear on the vocal folds, i.e., they have a direct influence on phonation. We are interested in two diseases: Reinke's edema (*Oedema Reinke*) and laryngeal polyp (*Polypus laryngis*).

Reinke's edema appears often bilaterally and usually asymmetrically on the vocal folds. It is created by transudation in a slotted epithelial space of folds devoid of lymphatic vessels and glands, called the Reinke's space. In the pathogenesis of disease, a big role is played by irritation of the laryngeal mucosa by different factors like smoking, excessive vocal effort, inhalatory toxins or allergens. The main symptoms are the following: hoarseness resulting from disturbance of vocal fold vibration or, in the case of large edemas, inspiratory dyspnea. In the case of Reinke's edemas, conservative therapy is not applied. They are microsurgically removed by decortication with saving the vocal muscle.

Laryngeal polyp is a benign tumor arising as a result of gentle hyperplasia of fibrous tissue in mucous membrane of the vocal folds. In the pathogenesis, a big role is played by factors causing chronic larynx inflammation and irritation of the mucous membranes of the vocal folds: smoking, excessive vocal effort, reflux, etc. The main symptoms are the following: hoarseness, aphonia, cough, tickling in the larynx. In the case of very big polyps, dyspnea may appear. However, not big polyps may be confused with vocal tumors, especially when the patient's voice is overloaded. The polyp may be pedunculated or may be placed on the wide base. If it is necessary, polyps are microsurgically removed with saving a free edge of vocal fold and vocal muscle.

Basic Problems

The research proves that a subjective assessment of voice is always reflected in the basic acoustic parameters of a speech signal. Sound parameters correlating with the anatomical structure and functional features of the voice organ are a subject of interest for researchers. However, the diversity of anatomical forms, inborn phonation habits, and the diversity of an exploratory material cause that researches are performed on different grounds. The voice generation is conditioned by a lot of factors, which give the voice an individual, peculiar character. However, the analysis of individual features of a speech signal in an appropriate group of people, suitably numerous, shows some convergence to values of tested parameters. This enables differentiation of changes of characteristics of the source (larynx stimulation) caused by different pathologies. Since a colloquial speech is a stochastic process, an exploratory material is made up often by vowels uttered separately with extended articulation. Together with the lack of intonation, it enables eliminating phonation habits.

We can distinguish two types of the acoustic measurement methods: objective and subjective. Both of them belong to indirect exploratory methods. Comparing them to direct methods (e.g., computer roentgenography, stroboscopy, bioelectrical systems) shows that they have several advantages. They are convenient for the patient, because the measurement instrument (in this case, a microphone) is located outside the voice organ. This enables free articulation. The advantage of acoustic methods is the possibility of automating measurements by using computer technique. It is also possible to visualize individual parameters of a speech signal. Subjective auscultatory methods are used, among others, in laryngology and phoniatrics in the case of both correct or pathological voice emission. Objective methods are based on physical features of the voice. They become especially popular when a computer technique reaches a high extent of specialization. They enable an objective assessment of voice and deliver information in the case of pathology and rehabilitation of the voice organ. Examined parameters aid the doctor assessment of the patient's health state.

In the literature, we may notice that parameters of the source (larynx stimulation) are often examined, e.g. [5]. However, it is possible to modify an exploratory method so that it encompasses wider range of the material analyzed. A crucial role is played by further mathematical processing of basic acoustic parameters. In this way, we can take into consideration and examine dynamic changes during the phonation process, resulting from functions of the speech apparatus as well as from additional acoustic effects occurring in the whole voice organ.

Computer Procedure

A computer procedure proposed in this paper is based on the Elman neural network. The Elman network is a kind of the globally feedforward locally recurrent network model proposed by Elman [3]. The main reason for choosing the Elman network from amongst several neural networks is that it has the advantageous time series prediction capability because of its memory nodes, as well as local recurrent connections. Thus, it has certain dynamic characteristics over static neural networks [1]. In the Elman network, the input layer has a recurrent connection with the hidden one. Therefore, at each time step the output values of the hidden units are copied to the input ones, which store them and use them for the next time step. This process allows the network to memorize some information from the past, in such a way to better detect periodicity of the patterns. Such capability can be exploited in our problem to recognize temporal patterns in the examined speech signals.

According to time-dependent signal, only recurrent neural networks can be used in a classification process. Selection of the net structure springs from a compromise between complexity and classification accuracy. The Elman networks are successfully used in different prediction problems (speech recognition, stock market quotation, exchange rates quotation). Simultaneously, they have relatively simple structures. Another simple recurrent network, called the Jordan network, cannot be used in our approach due to feedback between an output layer (with one output) and a context layer. Similarly, the Hopfield network is excluded. In the further research, combining the Elman and Jordan networks, resonance networks (ART2) as well as impulse networks will be considered.

The structure of the Elman neural network used in our experiments is illustrated in Figure 5. z^{-1} is a unit delay here. It is easy to observe that the Elman network consists of four layers: input layer (in our model: the neuron I_1), hidden layer (in our model: the neurons H_1, H_2, ..., H_{50}), context layer (in our model: the neurons C_1, C_2, ..., C_{50}), and output layer (in our model: the neuron O_1). The number of hidden and context neurons was chosen experimentally. Experiments showed that 50 neurons have the ability of learning time patterns in the examined speech signals. In general, they needed up to 200 epochs to learn with the error smaller than 0.01. The Elman network used in experiments had tan-sigmoid neurons in its hidden layer, and linear neurons in its output layer. The gradient method was used to update the weights with the back-propagation training function.

In our approach, we divide the speech signal of an examined patient into time windows corresponding to phonemes (a single window is limited by peaks). At the current stage, the windowing method is not automatic. A part of samples corresponding phonemes is strongly noised, especially at the beginning and at the end, and this part cannot be provided to the neural network input. Next, we select randomly a number of time windows. This set of selected windows is used for determining some coefficient characterizing deformations in the speech signal. This coefficient is constituted by an error obtained during testing the Elman neural network. We propose to use the approach similar to the cross-validation strategy. One time window is taken for training the neural network and the remaining ones for testing the neural network. The network learns a selected time window. If the remaining windows are similar to the selected one in terms of the time patterns, then for such windows an error generated by the network in a testing stage is small. If significant replication disturbances in time appear for patients with the larynx disease, then an error generated by the network is greater. In this case, the time pattern is not preserved in the whole signal. Therefore, the error generated by the network reflects non-natural disturbances in the patient phonation. Our procedure can be expressed formally as it is shown in Algorithm 1. We use the following notation: *train* denotes a training function of the neural network, *test* denotes a testing function of the neural network, *mean_squared_error* denotes a function calculating the mean squared error. Our experiments described in Section 5 were performed using the neural network toolbox in the MATLAB environment [2].

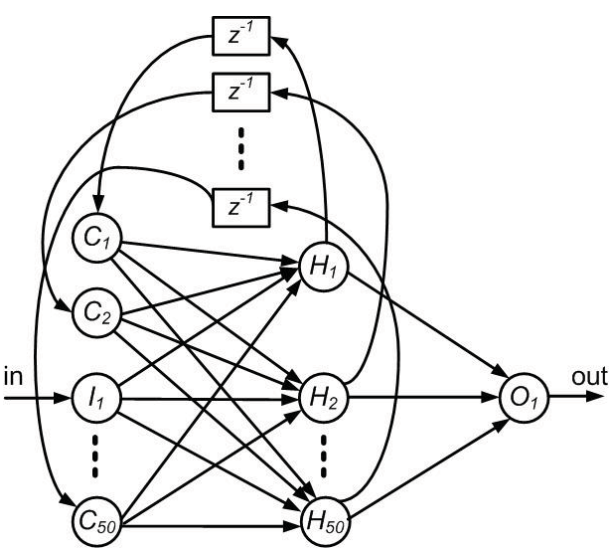

Fig. 5. A structure of the trained Elman neural network

Algorithm 1

INPUT: a speech signal of a given patient.
OUTPUT: an error coefficient characterizing deformations in the speech signal.

F_{all} ← divide the speech signal into time windows corresponding to phonemes;
F_{rand} ← select randomly a number of time windows from F_{all};
error = 0;
es = 0;
i = 0;
for each f in F_{rand} **do**
    N ← train(N, f);
    for each f* in F_{rand} **do**
        if f* ≠ f **then**
            e ← mean_squared_error(test(N, f*));
            es ← es+e;
            i ← i+1;
        end
    end
end
error ← es/i;

Experiments

In the experiments, sound samples were analyzed. The experiments were carried out on two groups of patients [6]. The first group included patients without disturbances of phonation. This was confirmed by phoniatrist's opinion. Patients came from different social groups (students, laborers, office workers). They were classified into four age categories. All patients were non-smoking, so they did not have contact with toxic substances which can have an influence on the physiological state of vocal folds. The second group included patient of Otolaryngology Clinic of the Medical University of Lublin in Poland. They had clinically confirmed dysphonia as a result of Reinke's edema or laryngeal polyp. The information about diseases was received from patient documentations.

Experiments were carried out by a course of breathing exercises with instruction about a way of articulation. A task of all

examined patients was to utter separately polish vowels: "A", "I", and "U" with extended articulation as long as possible, without intonation, and each on separate expiration.

The microphone ECM-MS907 (Sony) was used during recording. It is an electret condenser microphone with directional characteristics. Each sound sample was recorded on MiniDisc MZ-R55 (Sony). In MiniDisc, an analog signal is converted into digital signal according to the CD (Compact Disc) standard (16 bits, 44.1 kHz), and next it is transformed by means of the ATRAC (Adaptive Transform Acoustic Coding for MiniDisc) system. It is the compression system proposed by Sony. A data size is reduced in the ratio of 5 to 1. Psychoacoustic effects, like audibility threshold and masking quiet sounds by strong neighboring sounds, are the basis for compression. Compression system is based on separating harmonics, to which a human is most sensitive. Such harmonics are encoded with high precision. However, the less significant the harmonics, they are encoded with the higher compression ratio.

In the case of acoustic experiments, the most precise mapping of a speech signal is important. In the ATRAC system, the majority of compression is performed for sounds over 5.5 kHz. The voice examination encompasses sounds below 4 kHz. Therefore, the MiniDisc can be used successfully. Effectiveness of such analysis was confirmed by Winholtz and Titze in 1998 [8]. They compared recording of speech using the MiniDisc and recording of speech without compression using DAT (Digital Audio Type), taking into consideration perturbations and the shape of the acoustic wave. The analysis did not reveal any significant differences.

Samples are normalized to the interval [0.0,1.0] before providing them to the neural network input. After normalization, samples (as double numbers) are provided consecutively to the neural network input.

In [7], we presented the approach to computer diagnosis of laryngopathies based on the speech spectrum analysis. A simple statistical parameter was calculated. This parameter expressed distribution of harmonics in the speech spectrum. Clinical experience showed that harmonics in the speech spectrum of a healthy patient are distributed approximately steadily. However, larynx diseases may disturb this distribution [6]. The disturbance of distribution was expressed by the parameter called SDA based on a standard deviation. The quality of the proposed method was unsatisfactory.

Now, we present selected results of experiments obtained using the approach based on the Elman neural network described in Section 4. In Table 1, we can compare results of both approaches (i.e., the SDA parameter and the error E_{ENN} of the Elman neural network) for women from the control group and women with laryngeal polyp. It is easy to see that the value of E_{ENN} significantly discriminates the control group from the diseased group. The majority of results differ one order of magnitude. The proposed approach will be a part of a hybrid system based on multiple classifiers working on signals in time and frequency domains. The use only of the Elman networks is not enough for making a diagnostic decision. In the further work we will try to build multiple classifiers for distinction of patients with polyp, patients with Reinke's edema and patients with articulation disturbances caused by another factors. Especially the last case should not be rejected.

Another important problem is the time efficiency of the Elman network. In our experiments the net needed up to 200 epochs to learn patterns. In real-time decision making acceleration of a learning process is very important.

Tab. 1. Selected results of experiments

Women from the control group			Women with laryngeal polyp		
ID	*SDA*	E_{ENN}	*ID*	*SDA*	E_{ENN}
W_{CG1}	0.311	0.00059	W_{P1}	0.084	0.00240
W_{CG2}	0.159	0.00032	W_{P2}	0.138	0.01410
W_{CG3}	0.167	0.00068	W_{P3}	0.147	0.00390
W_{CG4}	0.012	0.00030	W_{P4}	0.840	0.00082
W_{CG5}	0.139	0.00072	W_{P5}	0.200	0.00070
W_{CG6}	0.205	0.00041	W_{P6}	0.333	0.00210
W_{CG7}	0.118	0.00073	W_{P7}	0.169	0.00220
W_{CG8}	0.127	0.00065	W_{P8}	0.219	0.00240
W_{CG9}	0.008	0.00039	W_{P9}	0.191	0.00100
W_{CG10}	0.129	0.00052	W_{P10}	0.501	0.00590

Conclusions

In the paper, an approach to diagnosis of larynx diseases has been shown. This approach is based on the analysis of a speech signal in the time domain. We have presented the usage of the Elman neural network in solving the problem of detection of disturbances in articulation of selected phonemes by patients. Further work will be concentrated on implementing effective preprocessing methods, adequate signal analyzing and processing methods, as well as efficient decision support methods based on computational intelligence methodologies, especially different kinds of neural networks. In the future work, a computer tool supporting diagnosis of larynx diseases will be developed. Therefore, presented results shall be helpful for selection of suitable techniques and algorithms for this tool. The application of proper models of neural networks seems to be a promising approach.

Acknowledgments

This research has been supported by the grant No. N N516 423938 from the Polish Ministry of Science and Higher Education. The remarks of an anonymous reviewer for improvements of this paper are also greatly appreciated.

References

1. Cheng Y.-C., Qi W.-M., Cai W.-Y. (2002), Dynamic properties of Elman and modified Elman neural network. Proceedings of the First International Conference on Machine Learning and Cybernetics. Beijing, China, 637-640.
2. Demuth H., Beale M. (2001), Neural Network Toolbox for Use with MATLAB. User's Guide. Version 4. The Math--Works.
3. Elman J.L. (1990), Finding Structure in Time. *Cognitive Science* 14, 179-211.

4. Greenes R.A. (2007), Clinical Decision Support: The Road Ahead. Elsevier Inc.
5. Orlikoff R., Baken R., Kraus D. (1997), Acoustic and physiologic characteristics of inspiratory phonation. *Journal of the Acoustical Society of America* 102(3), 1838-1845.
6. Warchoł J. (2006), Speech Examination with Correct and Pathological Phonation Using the SVAN 912AE Analyser (in Polish). PhD Thesis. Medical University of Lublin.
7. Warchoł J., Szkoła J., Pancerz K. (2010), Towards Computer Diagnosis of Laryngopathies Based on Speech Spectrum Analysis: A Preliminary Approach. In: A. Fred, J. Filipe, H. Gamboa (eds.), Proceedings of the Third International Conference on Bio-inspired Systems and Signal Processing (BIOSIGNALS'2010). Insticc, Valencia, Spain, 464-467.
8. Winholtz W.S., Titze I.R. (1998), Suitability of minidisc (MD) recordings for voice perturbation analysis. *Journal of Voice* 12(2), 138-142.

BIO-ALGORITHMS AND MED-SYSTEMS
JOURNAL EDITED BY MEDICAL COLLEGE – JAGIELLONIAN UNIVERSITY
Vol. 6, No. 12, 2010, pp. 81–84.

EOG BASED INTERFACE FOR PEOPLE WITH PHYSICAL DISABILITIES

JACEK CHODAK

Faculty of Physics and Applied Computer Science, AGH University of Science and Technology, Krakow, Poland, chodak@novell.ftj.agh.edu.pl

Abstract: In this paper EOG (electrooculography) based interface for people with physical disabilities has been described. The interface was implemented using an AC amplifier (EEG device) and four electrodes made of gold. The electrode placement was planned in such way that it would be possible in the future to install them in glasses. Eight selections operations were realized by circular interface, displayed on a screen monitor, which was divided into eight parts. Each part may be selected by targeting sight into one of the eight defined directions: up, up-right, right, bottom-right, down, down-left, left, up and left. This interface is an alternative for people, whose disability prevents them from using interfaces designed for a physically fit person. The interface configuration allows assigning different functions to the parts of circle, what allows using it in different circumstances. Virtual keyboard or a on/off switch for household appliances are examples of practical application of the described interface.
Keywords: electrooculography (EOG), human-computer interface (HCI), artificial neural networks (ANN), signal processing

Introduction

The ability to communicate with other people is essential to coexist in a society. For people with significant physical disabilities this is a serious problem. The opportunity to communicate in the misfit environment is often limited to a minimum. If the disabled person is unable to move, then the activity which can be performed by a normal person without any problem, such as turning on a device, can be an insurmountable obstacle for them.

Different technologies are used to assist people with physical disabilities, using the proper motor functions as a supplement for them. In severe cases of disability often the only organ that retains the motor functions are eyes. Different methods are used to determine the eye movements:

- videooculography, which allows to track eye movements by analyzing the images taken by a video camera,
- photoelectric, based on measuring infrared light reflected from the apple of the eye,
- electrooculography (EOG), measuring differences of the potential that are between the retina and the cornea of the eye.

To create an interface the last of these methods was used. The signal was measured by electrophysiology signal amplifier AC type and four gold electrodes. The method results and conclusions are shown below.

Method of an eye movement measurement

Eye behaves as a single electrical dipole, the cornea of the eye is electrically positive relative to the retina, therefore this dipole is oriented form the retina to the cornea. During teye movements the dipole also changes its position and rotates adequately. Thanks to these signals, measurements of eye movements are possible.

Fig. 1 presents measure of horizontal eye movements. Two electrodes are placed outside of the left and right eye. If the eye remains immobile, the electrodes have effectively the same potential and no voltage is recorded. The movement (rotation) of the eye causes change of the potential of the electrodes. For example, if eye rotates to the right, the right electrode is relatively positive to the second (left) electrode. The opposite move gives opposite effect, as have been shown on fig. 1. It is expected that the difference of the measured potential on the electrodes would be proportional to the angle rotation, but when angle is growing beyond 30 degrees the linearity becomes progressively worse [1].

When eye movements are recorded with EOG technique, the EMG (electromyography) signals can be recorded by the same electrodes. One of EMG signals are eye blinks, which can be classified into two categories: involuntary eye blink, which occurs frequently, and voluntary, caused by intentional eye closing.

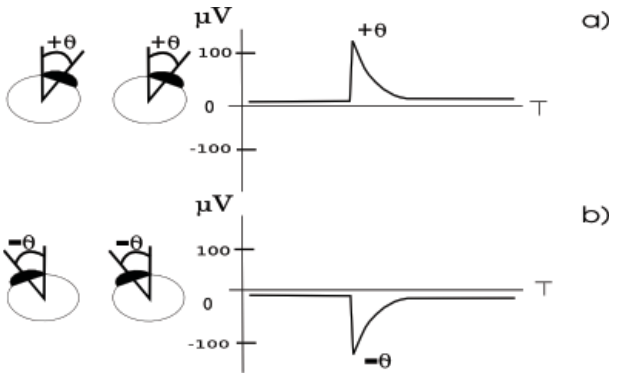

Fig. 1. Signal corresponding to the angle of eye rotation

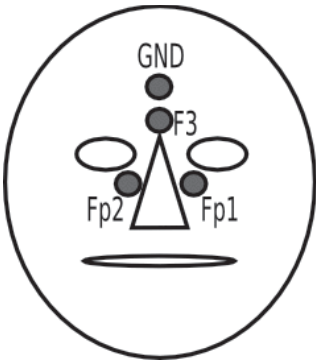

Fig. 2. Placement of electrodes

Acquisition takes place at a frequency 500 Hz by using the electrophysiology signal amplifier ISO-1032CE Braintronics's [2] and four gold electrodes.

Electrodes were arranged [3] in a way that reminds arrangement of glasses on the nose fig. 2. Horizontal and vertical signal were obtained from the difference of signals on the electrodes, and then filtered by bandpass elliptical filter (IIR).

EOG signal processing

The horizontal EOG signal obtained from proposed setup of electrodes is defined by the equation (1)

$$X_{raw} = Fp1 - Fp2 \tag{1}$$

and the vertical one is defined as (2)

$$Y_{raw} = \boldsymbol{B} - Fp1 \tag{2}$$

where $Fp1, Fp2, \boldsymbol{B}$ are measured signals from electrodes.

Raw EOG signal is very noisy and requires preprocessing. In this study a set of 3 bandpass elliptic filters was used with edge frequency:

- 140 Hz – 150 Hz to detect EMG artifacts,
- 35 Hz – 45 Hz to detect closed eyes,
- 0.05 Hz – 10 Hz to obtain EOG signals.

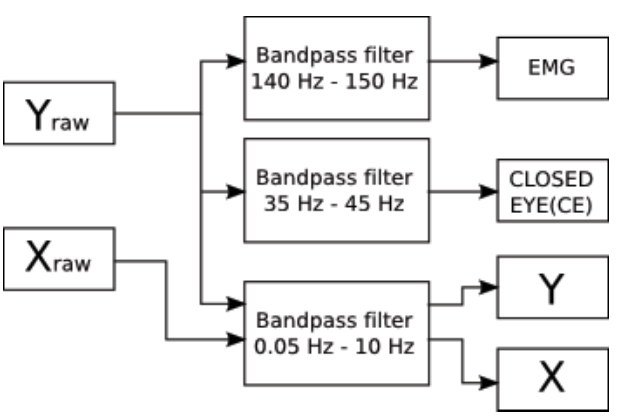

Fig. 3. Signal flow diagram through the filters

As presented on the fig. 3, for Y_{raw} signal all 3 filters were applied and for X_{raw} only last one. After filtering X and Y signals were under further processing if no EMG signal occurred (not exceeded threshold) or eyes were open. If eyes were closed, then signal CE exceeded threshold (fig. 4). This allowed detect closed eyes.

If no EMG and CE signals occurred, X and Y were thresholded, by proposed algorithm presented on the fig. 5, to detect saccades. With the decline in the quality of electrodes placement, the quality of the recorded signal decreased. This can be seen in the fig. 6. In such distorted signal the spikes, which are the evidence of inclination of the eye (saccade), had to be found. Therefore, the thresholding algorithm was proposed, which gives on the output value of the sudden spikes in the signal. In the proposed algorithm very important factors are the size of the buffer and threshold. The value of the dete mined threshold affects the sensitivity of the algorithm to sudden drops in signal. However, the size of the buffer affects the accuracy of the time interval in which the spike signal occurred. The results of this saccades detection are presented on fig. 6.

Calibration of the interface

Calibration is one of the main problems in a human-computer interface (HCI). When applying EOG, signal measurement differs each time of the deployment of the electrodes. Changing the position of electrodes causes a necessity of recalibration of the interface before the next use, because received signals may be different from the previous ones.

Calibration procedure consists of showing a point, which appears randomly in one of the eight sections of the circle (fig. 7). After each presentation, the point returns to the center of the circle. Each section is 1/8 of the full circle. Number of displays for each section in the series is equal. The multiplicity of the series depends on the results of particular calibration.

In order to calibrate the interface, a feedforward backpropagation artificial neural network (ANN) [4] has been applied. For each X and Y signals a separate ANN was used. The ANN consisted of one hidden layer with 4 neurons and a log-sigmoid transfer function. The output layer consisted of a single neuron with linear transfer function. The structure of the ANN was set experimentally.

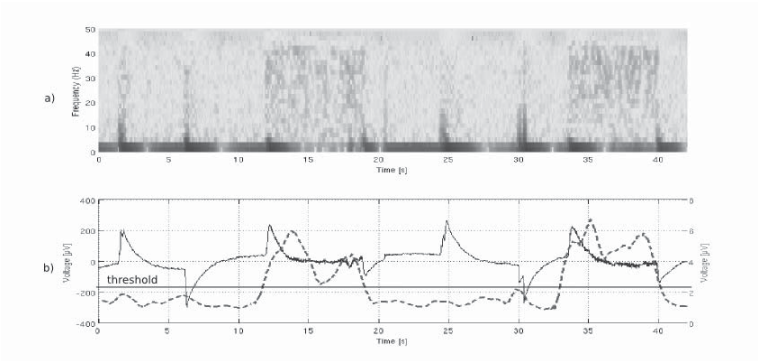

Fig. 4. Example of signal filtered by bandpass filter (0.01 Hz – 40 Hz) spectrogram a) and signal in time represented by solid line and CE signal represented by dashed line b)

The task of the networks was to map X or Y signal to the range of coordinates (-1;1). Sample output of the artificial neural network is shown on the fig. 7.

Results

The circular menu is divided into eight equal parts (fig. 7). The action of selecting takes place when the user directs vision into the proper section of the circle and back to the center. The center is a dead zone, in which all eye movements are ignored. Its size is determined during the calibration stage. The menu item selection is displayed in the zone. Its approval is followed by intentional closing eyes for a specified period of time.

In order to evaluate capabilities of the interface in respect of accuracy of the menu item selection, the formula defined in publication [5] was selected as correctness of choice (3)

$$accuracy = \frac{correctchoices}{totalnumberofchoices}100[\%] \quad (3)$$

and the formula defined in publication [5] was selected as error of choice (4)

$$error = \frac{wrongchoices}{totalnumberofchoices}100[\%] \quad (4)$$

The study was conducted on two people who chose the items from the menu within a limited period of time. The results concerning the correctness of the choice are slightly different between individual examinees (fig. 8).

Discussion and Conclusion

During the work on the interface many problems were noted. Some of them arose from the method of eye signal acquisition. The measurement of signals by the EOG is very sensitive to disturbance associated with the movement of muscles. Clamping teeth or even a slight limb movement cause significant disorder of the signal. However, some of the signals associated with the movement of muscles can be used to handle this HCI, such as closing the eyelids. This signal was used in the proposed interface as a confirmation of the selection.

With the acquisition by the EOG, it is necessary to pay great attention to the precision of electrodes placement on the

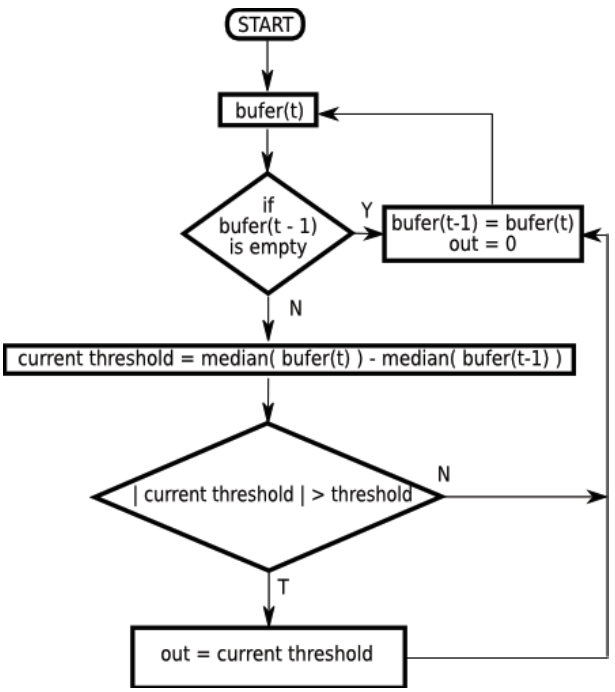

Fig. 5. Diagram of threshold algorithm

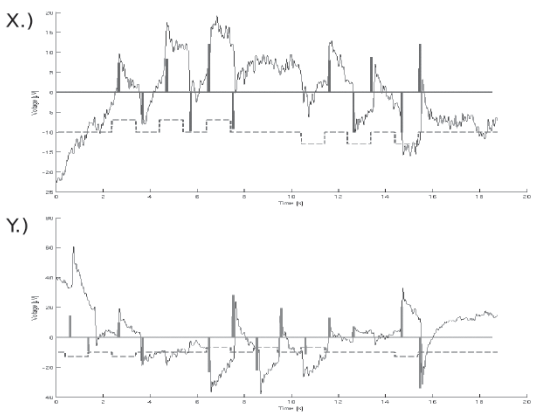

Fig. 6. X and Y signal before (straight line with spikes) and after thresholding (jagged curve). Dashed line represents the time at which the event should occur

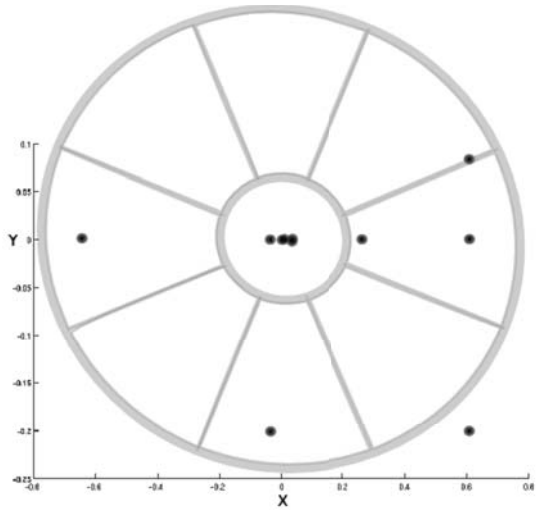

Fig. 7. Results of mapping X and Y signals to coordinate system of the interface by neural network

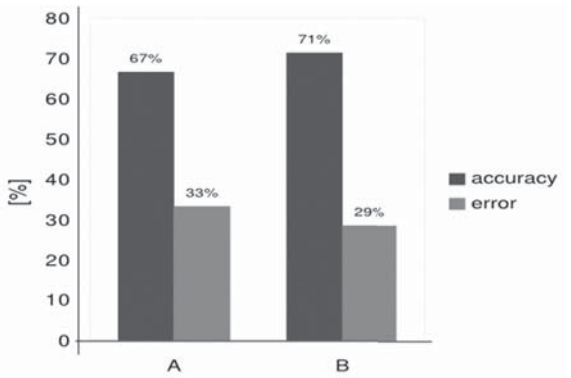

Fig. 8. Accuracy and error for two subjects A and B in eight directional circle menu

body of the person under test. In these studies the comfort of user has been posed emphasis. Therefore the quality of the placement of electrodes decreased.

The proposed interface best suits its purpose, if the person using it does not move. If there is too much disruption to the movement of muscles, the drop of the interface efficiency can be expected. Further work will be focused on the possibilities of eliminating distortions associated with the movement of muscles.

References

1. Malmivuo J., Plonsey R. (1995), Bioelectromagnetism: Principles and Applications of Bioelectric and Biomagnetic Fields. Oxford University Press, New York.
2. Braintronics ISO-1032CE Amplifier: http://www.braintronics.nl/DocumentDatabase/860107.pdf.
3. Goto S., Yamada A., Hashimoto W., Sugi T., Nakamura M. (2007), Determination of Target Position of Meal Assistance Orthosis. Using EOG Signal and Dish Image. Saga University, Saga.
4. Coughlin M.J., Cutmore T.R.H., Hine T.J. (2004), Automated eye tracking system calibration using artificial neural networks. *Computer Methods and Programs in Biomedicine* 76.
5. Yamagishi K., Hori J., Miyakawa M. (2006), Development of EOG-Based Communication System Controlled by Eight-Directional Movements. Proceedings of the 28th IEEE, EMBS Annual International Conference.

BIO-ALGORITHMS AND MED-SYSTEMS
JOURNAL EDITED BY MEDICAL COLLEGE – JAGIELLONIAN UNIVERSITY
Vol. 6, No. 12, 2010, pp. 85–90.

MYOCARDIAL SEGMENTATION BASED ON MAGNETIC RESONANCE SEQUENCES

TOMASZ PIECIAK

AGH University of Science and Technology, Institute of Automatics, Bio-Cybernetics Laboratory, al. Mickiewicza 30, 30-059 Krakow, Poland, pieciak@agh.edu.pl

Abstract: A strain analysis is a new diagnostics method used in the cardiology. The advanced regional quantitive analysis of the myocardium during a systole and a diastole allows to diagnose a cardiac cycle. Realization of the analysis requires a myocardial segmentation algorithm.
In this paper the myocardial segmentation method from the cardiovascular magnetic resonance sequences (CMR) has been presented. The endocardium areas are calculated using active contour algorithm with the gradient vector flow forces (GVF). Apart from that, the algorithm uses fuzzy logic approach to detect the edges. As a result, the curve matches to image contents. The epicardium boundaries are being designated and supplemented by the surrounding analysis and Fourier descriptors. Based on the endocardium and the epicardium boundaries which limit the myocardium, it is possible to realize analysis a local stenosis detection and the directional strain during the cardiac cycle. The analysis is based on the CMR images of the left ventricle, which were acquired in short axis of left ventricle and radial direction.
The most important achievements presented in this paper are fuzzy logic application in the image processing, the active contour segmentation method improvements and the formal descriptions of the myocardium boundaries.
Keywords: myocardial segmentation, active contour, myocardial strain, fuzzy logic, Fourier descriptors, cardiovascular magnetic resonance

Introduction

Computer image processing and analysis might be of indispensable help for the cardiologists who are to make diagnosis of the condition of the patients, where it is impossible to achieve by objective judgment of medical images or requires certain quantitative calculations. One of the examples of the quantitative analysis is a local deformation analysis (strain) and speed of deformation of myocardium (strain rate), in particular the left ventricle of the heart. In order to carry out the analysis, it is essential to fulfill the stage of segmentation of myocardium in all cycle of the action of the heart. It is quite difficult to deal with this issue as in the standard examination, as there are many imaging planes. The images which present the left ventricle of the heart on the various planes possess a diverse morphological structure and are located in different places. Such images can cause difficulties in interpretation by cardiologists, because they contain papillary muscles as well as non- continuous and blurred boundaries. So far the marking of myocardial area has been carried out manually by drawing landmarks on the boundary of the myocardium.

A number of approaches has been proposed to segment Cardiac Magnetic Resonance images. The method proposed in [1] uses active contour model [2] based on the generalized gradient vector flow (GGVF) [3] and contour prediction model. Initial contours for endo- and epicardial wall are being drawn manually on the first slice and active contour method is applied. Method predicts initial contours of the next image from the segmentation results of the previous image by cross profile correlation matching method (CPCM) and mixed interpolation model. Then, endo- and epicardial wall are extracted by snake deformation model with GGVF force. Ciofolo et al. in [4] proposed an automatic method based on multi-step approach to segment the myocardium in late-enhacement MRI. In the first stage, myocardial contours are being found in each slice of the LE CMR volume by deformation of geometrical template. Second stage corrects inaccuracies along the myocardium borders, using shape prior of the left ventricle from cine MR sequence. Carranza et al. in [5] presented motion estimation and segmentation method of tagged CMR images. The variational method based on total variation approach (norm L^1) is used for motion estimation. On the other hand, level set method with variational formulation of embedding function is applied for endocardial wall segmentation. These two systems integrated together increase accuracy of the segmentation and minimize computational cost of the segmentation process.

There are many more articles describing cardiac segmentation in short axis, inclusive of graph cuts technique [6], 3-D active appearance model (AAM) [7], 3-D active shape model

(ASM) [8], Markov random field model [9] and iterative thresholding with active contour model [10].

In the paper [11] authors apply nearing approach to the presented method. In comparison to this paper, method presented in that paper also uses active contour model [2] with GVF forces [12, 13] to extract endocardial contour. Firstly, the algorithm uses open and close morphology operations to include the papillary muscles into the cavity. This operation is performed only on the segments, which are greater than λ, which in turn is changing despite of the slice level. To delineate endocardium area, the algorithm uses the GVF snake algorithm with edges previously detected by the Canny operator. Also, additional parameter κ_p controls the force orthogonal to the contour force. The results of the first snake are then used for the second as a initialization curve. In this case snake is being used with lower deformation parameters to minimize the distance between the curve and real endocardium border. In turn, the epicardial delineation method approximate the contour by peak detection based on gradient image. After this operation, snake algorithm is being used with previously estimated points as the initialization curve. In this paper, endocardium detection algorithm uses surrounding analysis and Fourier descriptors as a fitting stage.

The proposed algorithm uses sequence of images which are created in a research by cardiovascular magnetic resonance in short axis (Figure 1). The example of the myocardial area is marked with white arrows.

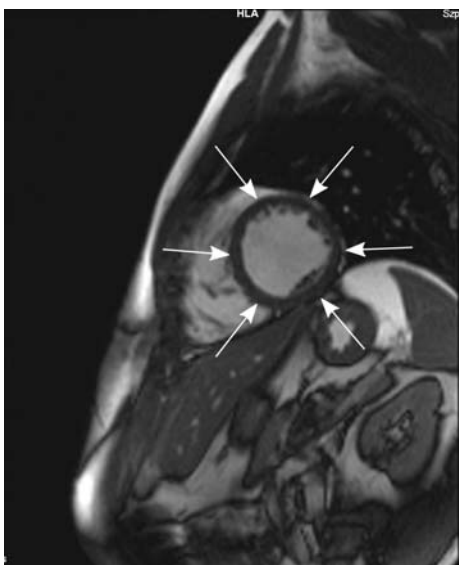

Fig. 1. The example of single image in short axis view. The arrows show the myocardium region

Myocardial area segmentation

The segmentation method is divided into two stages. Firstly, the algorithm detects an endocardium boundary and then extracts epicardium boundary by "designated radius" algorithm. Myocardial area is limited in both sides, the endocardium and the epicardium boundaries respectively.

Proposed method is based on the active contour approach (snake), originally introduced in [2]. From the geometrical point of view, snake is a parametric curve described as $v(s) = (x(s), y(s)),\ s \in [0, 1]$. The curve moves in the image plane to the functional minimization [2]

$$E = \int_0^1 \left(E_{int}(v(s)) + E_{ext}(v(s))\right) ds$$

For closed curves, $s(0) = s(1)$. Internal energy E_{int} is defined as [14, 15]

$$E_{int} = \frac{1}{2}\left(\alpha \left|\frac{\partial v}{\partial s}\right|^2 + \beta \left|\frac{\partial^2 v}{\partial s^2}\right|^2\right)$$

where α controls the tension and β controls the rigidity of the curve. The external energy E_{ext} depends on the image content and attracts the curve to the object's boundary. As a rule E_{ext} can be defined as [12, 13]

$$E_{ext}(x, y) = -|\nabla I(x, y)|^2$$

$$E_{ext}(x, y) = -|\nabla (G_\sigma(x, y) * I(x, y))|^2$$

where $\nabla I(x, y)$ is an image gradient, and $G_\sigma(x, y)$ is a two-dimensional Gaussian's function with a standard deviation σ.

In this paper, the method uses GVF forces (Gradient Vector Flow) defined in [12, 13]. GVF forces make homogenous gradient field instead of dependent image content E_{ext} field. For edge detection of the image, fuzzy logic approach is used defined in [16] based on gradient and standard deviation of image.

The curve, which minimizes the energy, must satisfy the Euler-Lagrange equation [14]

$$\frac{\partial}{\partial s}\left(\alpha \frac{\partial v}{\partial s}\right) + \frac{\partial}{\partial s^2}\left(\beta \frac{\partial^2 v}{\partial s^2}\right) - \nabla E_{ext} = 0$$

where

$$-\nabla E_{ext} = \begin{bmatrix} f_x \\ f_y \end{bmatrix}$$

$$f_x = -\frac{\partial E_{ext}}{\partial x}$$

$$f_y = -\frac{\partial E_{ext}}{\partial y}$$

Shape of the curve is represented by two vectors, in the following iteration it is described as two independent matrix equations [2, 17]

$$X_{k+1} = (I - \xi A)^{-1}\left(X_k + \xi f_x(X_k, Y_k)\right)$$

$$Y_{k+1} = (I - \xi A)^{-1}\left(Y_k + \xi f_y(X_k, Y_k)\right)$$

where A is symmetric pentadiagonal matrix. Constant parameter ξ determines the convergence of the curve to desirable shape boundary. In this paper, the author proposes to get variable α and ξ parameter.

After modification of the α parameter due to iteration number, the curve achieves the endocardium boundary (Figure 2). On one hand, a low value of $\boldsymbol{\alpha}$ parameter (tension) at the beginning prevents collapsing the area. On the other hand, the curve fits in the concaved area due to the increasing value of $\boldsymbol{\alpha}$. The parameter α is defined as

$$\alpha_k = \frac{1}{10}\left(1 - e^{-\frac{1}{4}k}\right), \qquad k = 1, 2, 3, \ldots$$

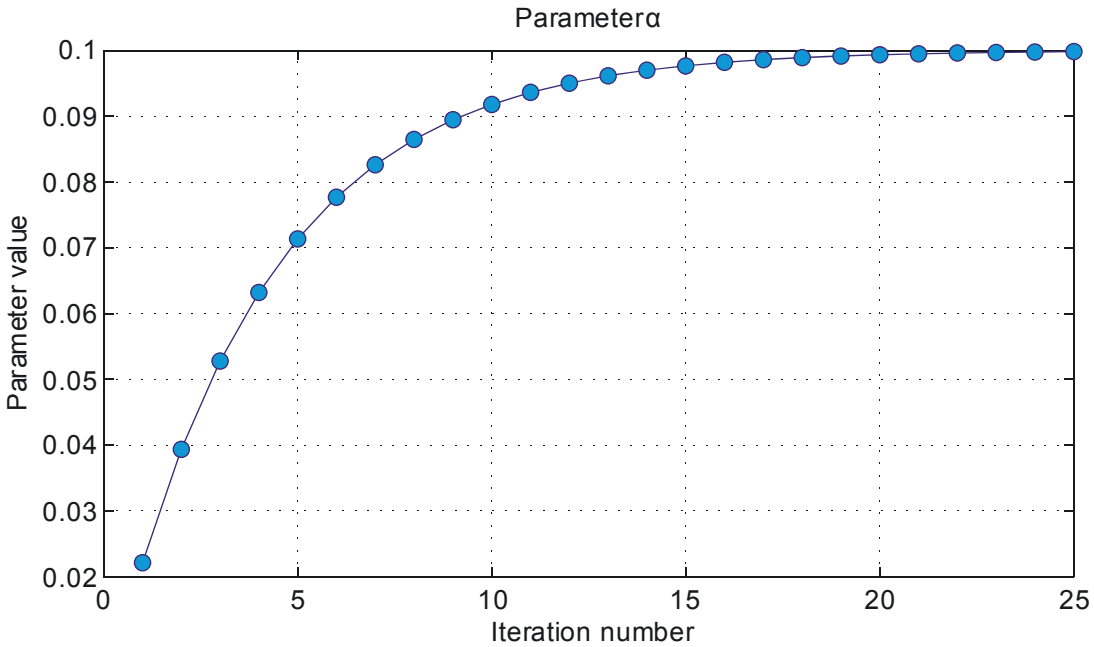

Fig. 2. Parameter α in function of iteration number

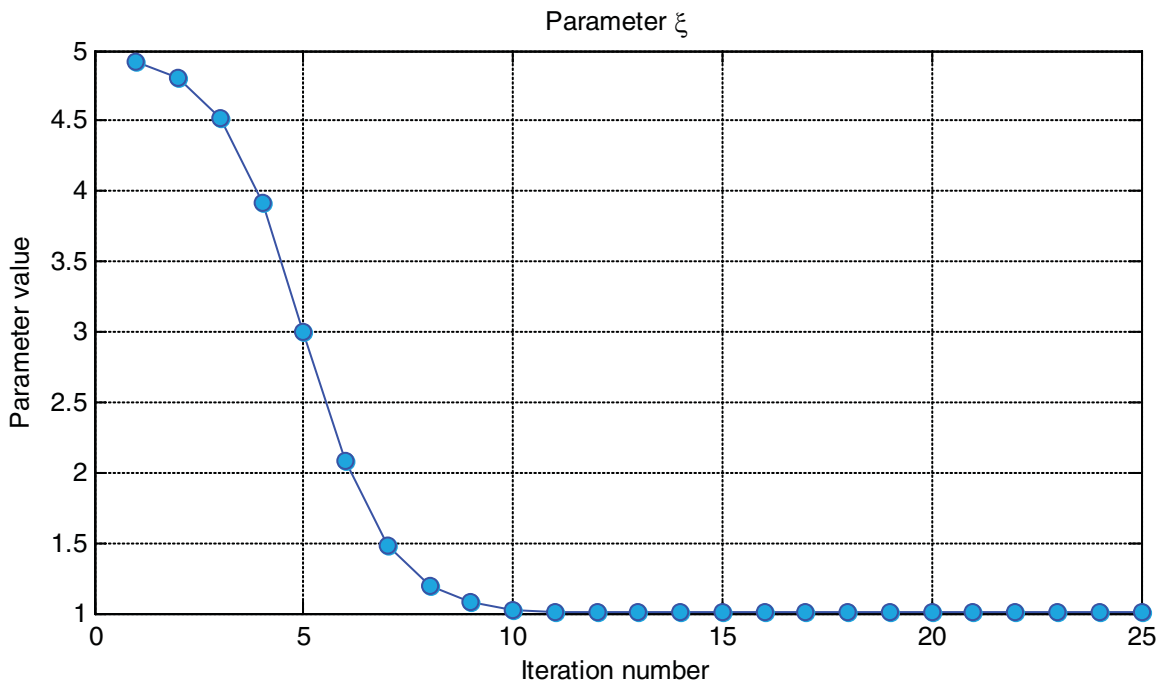

Fig. 3. Parameter ξ in function of iteration number

More important parameter is ξ, which directly determines the speed of curve's convergence (Figure 3). Manipulating of this parameter we can easily fall into the trap, because the curve might start oscillating. The high value of ξ parameter speeds up the curve convergence. After few iterations the contour probably will have reached the area closed to the real endocardium boundary. In this case, the value of ξ is instantly decreasing. As a result, oscillating of the curve is prevented. Parameter ξ is defined as

$$\xi_k = \frac{5e^{-(k+5)} + 1}{e^{-(k+5)} + 1}, \qquad k = 1, 2, 3, \ldots$$

An initial curve for matrix equation is a circle with middle point indicated manually. The algorithm stops after 30 itera-

tions or after sum of Euclidean distance between the curve and the previous curve is less than $\varepsilon = 5$. The tension parameter β is set to 10, which produces the curve inflexible enough. As a result, the endocardium area is marked in the single image (Figure 4).

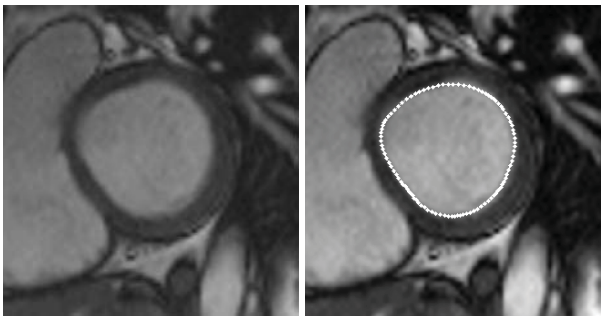

Fig. 4. Comparison of the real image (left) and the segmented cavity (right). It is worth mentioning that the endocardium boundary is non-continuous

After that, the proposed "designated radius" algorithm is applied. From the middle of the cavity, a line is created through every point on the endocardium curve. Then, along the line, pixels luminosity from the edge image is read. It means that the values of the points on the curve belong to set C_i

$C_i \epsilon \{0, 1\}$

Figure 5 shows luminosity of example radius line.

Reading luminosity along the line, the algorithm searches for the first point which value equals 1 (the edge) leaving first ten points at the beginning. It has direct connection with detected multiple edges of the myocardial area. The proposed method can lead to wrong landmarks because the discrete line might miss the real boundary line (the edge) (Figure 6).

The landmarks which were detected initially by the algorithm representing the boundary of the myocardium have to be corrected. For every point 'X' on the every line the condition is checked whether in its surrounding the edge exists. The twelve surroundings points are taken into consideration. The order of the examined points is marked with numbers (1-12) (Figure 7). Consequently, the chances of detecting wrong points decreases.

Finally, the Fourier descriptors [18, 19] is applied to the points produced by the "designated radius" algorithm. The Fourier descriptors act as a low-pass filter. The points coordinates of the curve v are being mapped into complex vector F as follows

$$F = \begin{bmatrix} x_0 + jy_0 \\ x_1 + jy_1 \\ \vdots \\ x_{n-1} + jy_{n-1} \end{bmatrix}$$

After transformation the vector to the frequency domain, only 10 of the first coefficients are not set to zero. The Inverse Fourier Transform converts partially reset complex vector into coordinates vector. In result, the curve is smooth, and covers the external boundary of myocardium (Figure 8).

In next stage the final internal curve (representing endocardium) is a starting point for active contour algorithm. In that case, the curve is matched with the whole sequence (Figure 9). The external curve (representing epicardium) is calculated by the same "designated radius" algorithm as mentioned.

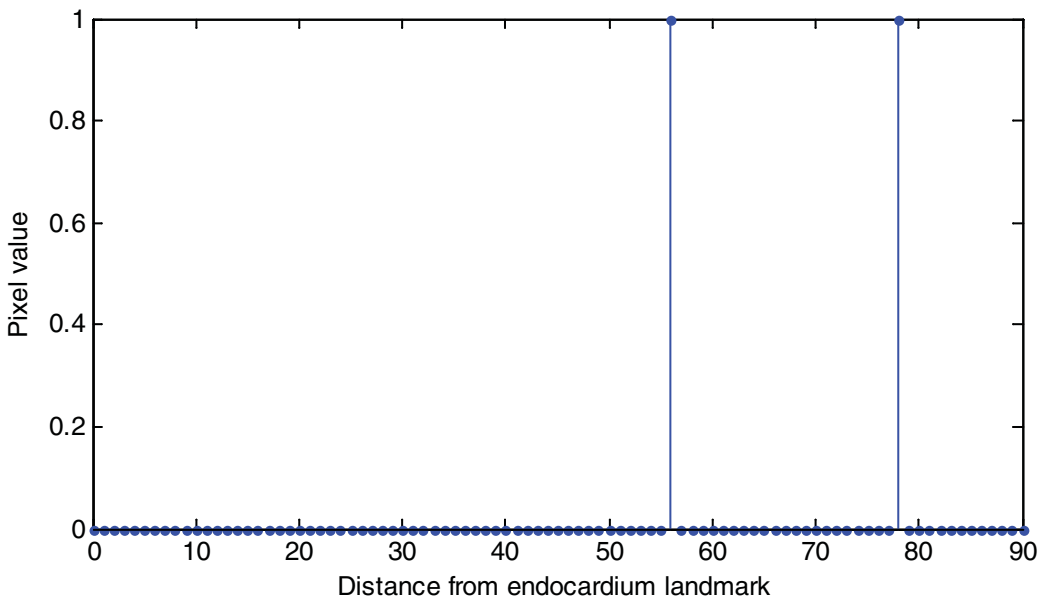

Fig. 5. Luminosity of example radius line. First point of the plot corresponds endocardium marker

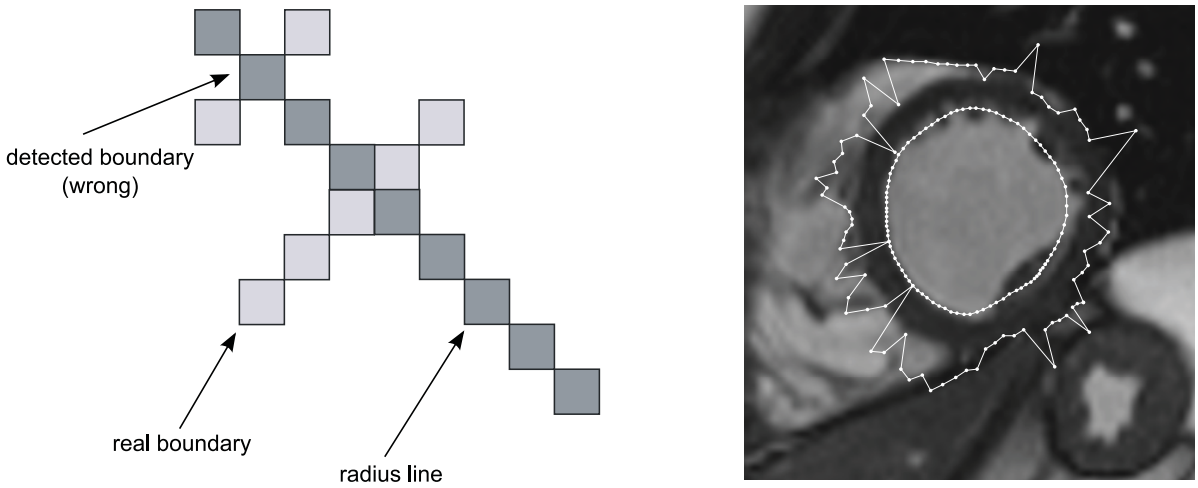

Fig. 6. Scheme of the wrong boundary detection (left) and the detected points (right)

		11		
	5	3	6	
9	1	X	2	10
	7	4	8	
		12		

Fig. 7. The order of the examined points surrounding 'X'

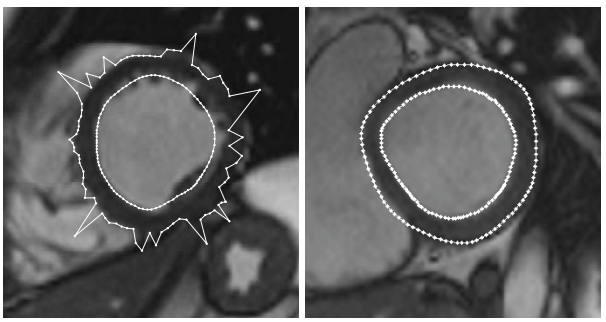

Fig. 8. The curve after the correction (left) and the final epicardium (right)

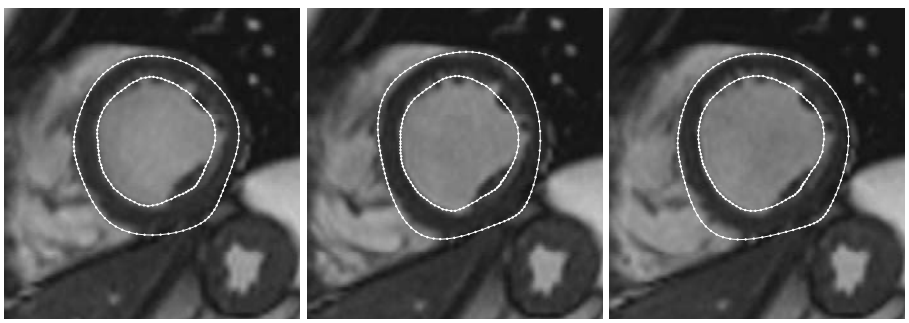

Fig. 9. The example results from the sequence. The sequence contains 25 images

Results

Due to very complicated and long term examination curried by cardiac MRI (acquisition takes about 1.5 hour), the algorithm has been tested in few sequences. The method works properly on twelve image sequences which were tested. In the future an algorithm is being planned to be tested on more sequences containing pathological examples of the images. The other possibility is to compare results of the algorithm to manually marked boundaries by a cardiology expert.

One of the most important issues connected with segmentation of medical images in active contour method is setting of the parameters directly to dedicated problem. These parameters has been set in experimental way. The second problem is the initial curve, which should be closed to real boundaries. It can be estimated based on the statistics or the expert examples.

For method evaluation two factors has been calculated separately for endo- and epicardium wall as follows

MaxDD – Maximum distance difference

$$MaxDD = \max_i |P_i' - P_i|$$

MeanDD – Mean distance difference

$$MeanDD = \frac{1}{N}\sum_i |P_i' - P_i|$$

where
P_i' – contour points appointed manually
P_i – contour points appointed automatically by an algorithm

Tab. 1. Comparison between automatic and manual segmentation, respectively for endo- and epicardium borders. The distance has been calculated in pixels

	MaxDD	MeanDD
Epicardium	8.5 ± 4.8	3.4 ± 1.1
Endocardium	9.2 ± 6.6	3.3 ± 0.4

References

1. Shin I. et al. (2002), Segmentation and visualization of left ventricle in MR Cardiac images. International Conference on Image Processing, Vol. 2, II-89-II-92.
2. Kass M. et al. (1987), Snakes: active contour models. *International Journal of Computer Vision* 1, 321-331.
3. Xu C., Prince J. L. (1998), Generalized Gradient Vector Flow External Forces for Active Contours. *Signal Processing an International Journal* 71(2), 131-139.
4. Ciofolo C. et al. (2008), Automatic myocardium segmentation in late-enhacement MRI. 5th IEEE International Symposium on Biomedical Imaging, 225-228.
5. Carranza N. et al. (2008), Motion Estimation and Segmentation of Cardiac Magnetic Resonance Images Using Variational and Level Set Techniques. 16th European Signal Processing Conference.
6. Jie Zhu-Jacquot Zabih R. (2008), Segmentation of the left ventricle in cardiac MR images using graph cuts with parametric shape priors. IEEE International Conference on Acoustics, Speech and Signal Processing, 521-524.
7. Mitchell S. C. et al. (2002), 3-D active appearance models: segmentation of cardiac MR and ultrasound images. *IEEE Transactions on Medical Imaging* 21(9), 1167-1178.
8. van Assen H. C. et al. (2008), A 3-D Active Shape Model Driven by Fuzzy Inference: Application to Cardiac CT and MR. *IEEE Transactions on Information Technology in Biomedicine* 12(5), 595-605.
9. Wang G. et al. (2009), A Novel Segmentation Method for Left Ventricular from Cardiac MR Images Based on Improved Markov Random Field Model. 2nd International Congress on Image and Signal Processing, 1-5.
10. Hae-Yeoun L. et al. (2010), Automatic Left Ventricle Segmentation Using Iterative Thresholding and an Active Contour Model with Adaptation on Short-Axis Cardiac MRI. *IEEE Transactions on Biomedical Engineering* 57(4), 905--913.
11. El Berbari R. et al. (2007), An automated myocardial segmentation in cardiac MRI. Proceedings of the 29th Annual International Conference of the IEEE EMBS.
12. Xu Ch., Prince J. L. (1997), Gradient Vector Flow: A New External Force for Snakes. IEEE Computer Society Conference on Computer Vision and Pattern Recognition (CVPR'97), 66.
13. Xu Ch., Prince J. L. (1998), Snakes, Shapes, and Gradient Vector Flow. *IEEE Transactions on Image Processing* 7/3.
14. McInerney T., Terzopoulos D. (2009), Deformable Models. In: I. N. Bankman (ed.), Handbook of Medical Image Processing and Analysis. Elsevier.
15. Das B., Banerjee S. (2007), Parametric Contour Model in Medical Image Segmentation. In: J. S. Suri, A. Farag (eds.), Deformable Models II: Theory & Biomedical Applications. Springer.
16. Barkhoda W. et al. (2009), Fuzzy Edge Detection Based on Pixel's Gradient and Standard Deviation Values. Proceedings of the International MultiConference on Computer Science and Information Technology, 7-10.
17. Acton S. T., Ray N. (2009), Biomedical Image Analysis: Segmentation. Morgan & Claypool Publishers.
18. Gonzales R. C., Woods R.E. (2008), Digital Image Processing. Pearson Education.
19. Suri J. S. et al. (2002), Advanced Algorithmic Approaches to Medical Image Segmentation. State-of-the-art Applications in Cardiology, Neurology, Mammography and Pathology. Advances in Pattern Recognition. Springer, London.

BIO-ALGORITHMS AND MED-SYSTEMS
JOURNAL EDITED BY MEDICAL COLLEGE – JAGIELLONIAN UNIVERSITY
Vol. 6, No. 12, 2010, pp. 91–97.

NITANO – NOVEL INTER/INTRAMOLECULAR COLOCATION CALCULATOR

JACEK KUŚKA[1,4], JACEK LELUK[2,4], BOGDAN LESYNG[3,4]

[1]*Faculty of Biology, Warsaw University, Poland, e-mail: biochemon@biol.uw.edu.pl*
[2]*Faculty of Biological Sciences, University of Zielona Gora, Poland*
[3]*Faculty of Physics, University of Warsaw, Poland*
[4]*CoE BioExploratorium, Warsaw University, Poland*

Abstract: Nitano is a stand-alone Windows application. The main purpose of this software is to calculate the intra- or intermolecular residue colocations. A PDB file is used as input file. The application is to detect and analyse the intramolecular contacts as well as the contacts between residues from two separate chains/molecules (see Fig. 2). Nitano can be used for study the proteins and nucleic acids. The output files contain names, numbers and distances between the atoms that reveal collocation. The application gives two types of maps that show the structure on a two-dimensional image. Nitano allows to perform basic statistical analysis of obtained results. This application is a useful tool supporting the work of drug designers in creating more specific ligands. The application is freely available for educational and academic purposes at: http://www.bioware.republika.pl. Nitano is a user friendly application and does not require any advanced course to be applied for any kind of analysis.
Keywords: residue colocation, contact map, intermolecular/intramolecular interaction

Background

Contact maps provide the information about protein structure [Biro 2006, Biro and Fordos 2005]. The structure analysis by contact map study is easier to perform and gives more information concerning the intramolecular interactions than study of the molecule structure with any 3D browser [Sonnhammer and Wooton 1998, Vullo et al. 2006]. Nitano is a software designed for this purpose. It is provided with intuitive GUI (Fig. 1) and is able to generate the inter- and intramolecular contact maps. The application does not require the advanced knowledge concerning the computer science, it is easy to use by any average PC user.

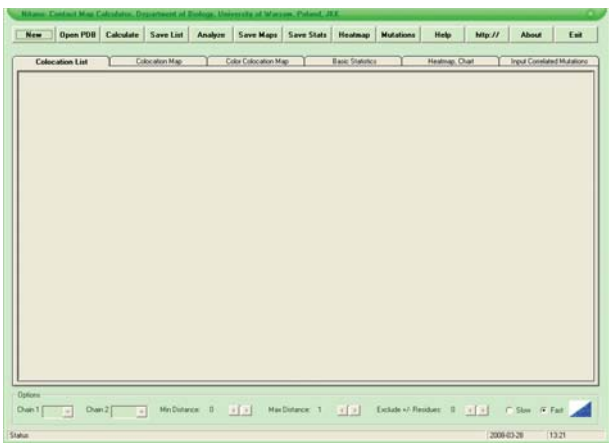

Fig. 1. Nitano's GUI

Implementation

In order to analyze a protein, DNA/RNA or a complex composed of a protein and nucleic acid the appropriate PDB file is used as input file. The PDB file should fulfill all reqirements of this format, otherwise the application would not work properly. Nitano detects intramolecular colocations and colocations between two subjects: protein/DNA/RNA and protein/DNA/RNA/non standard groups such as enzyme substrates, products or inhibitors. Prior to analysis some treshold values must be specified, such as a minimum as well as maximum distance in Angroms that are significant for a study. The upstream and downstream colocations can be excluded from calculation in order to avoid analysis of neighbor residues in sequence. The recommended default values for proteins are: 0 as the minimum distance, 5-6 as the maximum distance and exclude up to 5 neighboring positions upstream and downstream the sequence. The exclusion of neighboring positions in sequence from colocation analysis significantly reduces the computing time (Fig. 3). After all parameters are set the caculation pro-

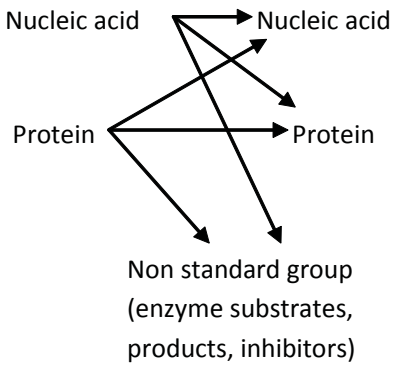

Fig. 2. Possible intra- as well as intermolecular searches

cedure is executed by clicking on the 'Find' button. During the analysis Nitano ignores water molecules that are included in a PDB input file provided by the user. The distances are calculated by the simple Pythagoras theorem.

Results

Nitano has been succesfully used in the study of cAMP dependent protein kinases, hexokinases, insulin receptor tyrosine kinases and non-receptor tyrosine kinases (JAKs). As input files there were used crystallographic models deposited in the Protein Data Bank [Berman et al. 2000] and the structures generated theoretically with the aid of commonly available modelling techniques and deposited in ModBase [Pieper et al. 2004, Pieper et al. 2006]. Nitano was applied to investigate the intramolecular colocations involved in protein folding as well as the intermolecular atom colocations that appear the complex with inhibitor or substrate. Example of intramolecular interactions is shown on Fig. 4. Figures 5 and 6 show the examples of intermolecular interactions for protein-protein and protein-substrate complexes. Nitano is supported with some basic tools for further analysis of the obtained colocation results Fig. 4-8.

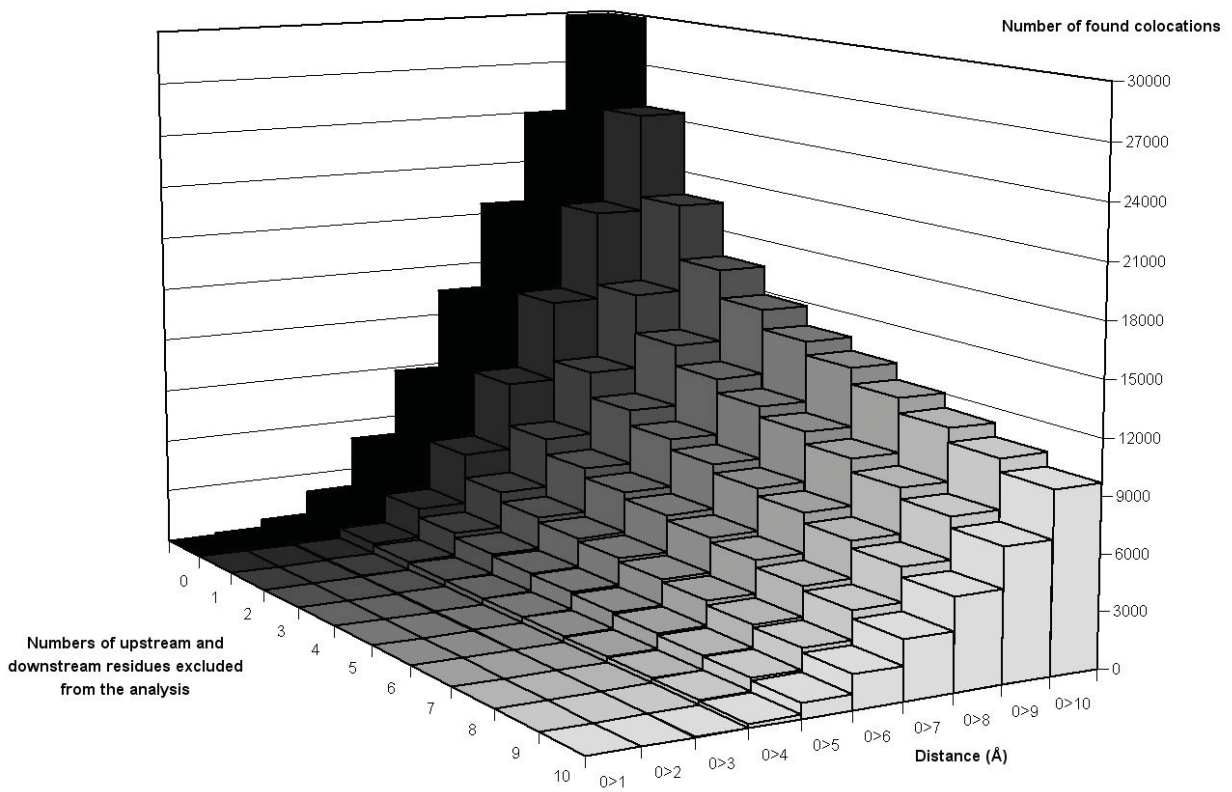

Fig. 3. The correlation between the number of colocations (the time of analysis), the distance and the number of residues that are excluded from the analysis (upstream and downstream)

```
Start of analysis: 2009-12-20 16:50:27
Type of calculation: Intramolecular
Minimum Distance: 0
Maximum Distance: 6
Exclude +/- residues:0
1     |     1 |  N   |  981 | SER |   |   1.00 |     7 |  N   |  982 | SER |   |   1.00 | 3,22214
2     |     1 |  N   |  981 | SER |   |   1.00 |     8 |  CA  |  982 | SER |   |   1.00 | 4,52968
3     |     1 |  N   |  981 | SER |   |   1.00 |     9 |  C   |  982 | SER |   |   1.00 | 5,51382
4     |     1 |  N   |  981 | SER |   |   1.00 |    11 |  CB  |  982 | SER |   |   1.00 | 5,44495
5     |     1 |  N   |  981 | SER |   |   1.00 |    12 |  OG  |  982 | SER |   |   1.00 | 5,29272
Part of this file was removed for brevity
8752  |   374 |  CG2 | 1029 | VAL |   |   1.00 |   363 |  N   | 1028 | ALA |   |   1.00 | 4,61016
8753  |   374 |  CG2 | 1029 | VAL |   |   1.00 |   364 |  CA  | 1028 | ALA |   |   1.00 | 4,49877
8754  |   374 |  CG2 | 1029 | VAL |   |   1.00 |   365 |  C   | 1028 | ALA |   |   1.00 | 3,45777
8755  |   374 |  CG2 | 1029 | VAL |   |   1.00 |   366 |  O   | 1028 | ALA |   |   1.00 | 3,68856
8756  |   374 |  CG2 | 1029 | VAL |   |   1.00 |   367 |  CB  | 1028 | ALA |   |   1.00 | 5,89182
End of Analysis: 2009-12-20 17:16:05
```

Fig. 4. An example of intramolecular calculation for Tyrosine Kinase Domain of the Human Insulin Receptor (PDB code: 1IRK). Search for residues distant from each other by less than 6 Angstroms without any limitation in the primary structure

```
Start of analysis: 2009-12-29 18:36:41
Type of calculation: Intermolecular
Minimum Distance: 0
Maximum Distance: 5
Exclude +/- residues:0
1     |   296 |  CA  |   50 | GLY | E |   1.00 |  2876 |  NH2 |   18 | ARG | I |   1.00 | 4,58706
2     |   297 |  C   |   50 | GLY | E |   1.00 |  2876 |  NH2 |   18 | ARG | I |   1.00 | 4,69623
3     |   299 |  N   |   51 | THR | E |   1.00 |  2874 |  CZ  |   18 | ARG | I |   1.00 | 4,27944
4     |   299 |  N   |   51 | THR | E |   1.00 |  2875 |  NH1 |   18 | ARG | I |   1.00 | 4,11532
5     |   299 |  N   |   51 | THR | E |   1.00 |  2876 |  NH2 |   18 | ARG | I |   1.00 | 3,82460
Part of this file was removed for brevity
626   |  2600 |  OH  |  330 | TYR | E |   1.00 |  2872 |  CD  |   18 | ARG | I |   1.00 | 3,55140
627   |  2600 |  OH  |  330 | TYR | E |   1.00 |  2873 |  NE  |   18 | ARG | I |   1.00 | 3,41042
628   |  2600 |  OH  |  330 | TYR | E |   1.00 |  2874 |  CZ  |   18 | ARG | I |   1.00 | 3,42074
629   |  2600 |  OH  |  330 | TYR | E |   1.00 |  2875 |  NH1 |   18 | ARG | I |   1.00 | 3,50369
630   |  2600 |  OH  |  330 | TYR | E |   1.00 |  2876 |  NH2 |   18 | ARG | I |   1.00 | 4,10538
End of Analysis: 2009-12-30 05:07:21
```

Fig. 5. An example of protein intermolecular search of residues distant from each other within 5 Angstroms. Results for the complex of cAMP- Dependent Protein Kinase Complexed with mnATP and a peptide inhibitor, pdb code: 1ATP

```
Start of analysis: 2010-01-08 15:47:25
Type of calculation: Intermolecular
Minimum Distance: 0
Maximum Distance: 3
Exclude +/- residues:0
1     |   310 |  N   |   53 | SER | E |   1.00 |  2938 |  O1G |    1 | ATP |   |   1.00 | 2,77225
2     |   316 |  N   |   54 | PHE | E |   1.00 |  2943 |  O2B |    1 | ATP |   |   1.00 | 2,95500
3     |   327 |  N   |   55 | GLY | E |   1.00 |  2943 |  O2B |    1 | ATP |   |   1.00 | 2,81258
4     |   470 |  NZ  |   72 | LYS | E |   1.00 |  2942 |  O1B |    1 | ATP |   |   1.00 | 2,59583
5     |   470 |  NZ  |   72 | LYS | E |   1.00 |  2946 |  O1A |    1 | ATP |   |   1.00 | 2,52474
6     |   924 |  OE2 |  127 | GLU | E |   1.00 |  2954 |  O3* |    1 | ATP |   |   1.00 | 2,98523
7     |   924 |  OE2 |  127 | GLU | E |   1.00 |  2956 |  O2* |    1 | ATP |   |   1.00 | 2,64585
8     |  1279 |  NZ  |  168 | LYS | E |   1.00 |  2939 |  O2G |    1 | ATP |   |   1.00 | 2,43815
9     |  1290 |  O   |  170 | GLU | E |   1.00 |  2954 |  O3* |    1 | ATP |   |   1.00 | 2,71296
10    |  1407 |  OD1 |  184 | ASP | E |   1.00 |  2942 |  O1B |    1 | ATP |   |   1.00 | 2,92991
11    |  1408 |  OD2 |  184 | ASP | E |   1.00 |  2940 |  O3G |    1 | ATP |   |   1.00 | 2,99367
12    |  1408 |  OD2 |  184 | ASP | E |   1.00 |  2942 |  O1B |    1 | ATP |   |   1.00 | 2,82930
13    |  1408 |  OD2 |  184 | ASP | E |   1.00 |  2947 |  O2A |    1 | ATP |   |   1.00 | 2,90385
End of Analysis: 2010-01-08 15:47:45
```

Fig. 6. An example of intermolecular search of amino acid residues that are distant within 5 Angstroms from nmATP and the protein inhibitor. Results for cAMP- Dependent Protein Kinase complexed with mnATP and a peptide inhibitor, pdb code: 1ATP

Total amount of found colocations.

4288	ALA	ARG	ASN	ASP	CYS	GLN	GLU	GLY	HIS	ILE	LEU	LYS	MET	PHE	PRO	SER	THR	TRP	TYR	VAL
ALA	32	15	14	9	0	0	49	0	12	8	12	7	29	1	7	20	3	0	9	16
ARG	15	0	8	21	1	2	43	7	8	6	37	10	21	0	28	15	14	6	8	21
ASN	14	8	16	9	12	0	33	7	0	1	21	8	2	8	16	9	2	0	0	16
ASP	9	21	9	12	0	8	9	30	9	12	31	15	14	15	12	10	14	0	11	0
CYS	0	1	12	0	0	0	0	0	9	0	1	0	12	0	8	0	5	6	0	1
GLN	0	2	0	8	0	0	19	21	1	8	6	1	9	7	23	2	0	8	8	8
GLU	49	43	33	9	0	19	14	12	0	30	21	9	18	9	26	24	14	20	14	15
GLY	0	7	7	30	0	21	12	26	6	5	24	34	20	27	6	8	0	2	7	25
HIS	12	8	0	9	9	1	0	6	12	1	7	1	1	7	8	10	0	0	0	13
ILE	8	6	1	12	0	8	30	5	1	12	3	18	10	0	0	0	12	0	6	9
LEU	12	37	21	31	1	6	21	24	7	3	46	29	13	14	7	32	17	8	22	28
LYS	7	10	8	15	0	1	9	34	1	18	29	14	16	14	8	13	5	0	1	14
MET	29	21	2	14	12	9	18	20	1	10	13	16	4	0	0	0	9	14	0	31
PHE	1	0	8	15	0	7	9	27	7	0	14	14	0	14	8	32	23	0	0	28
PRO	7	28	16	12	8	23	26	6	8	0	7	8	0	8	38	6	16	2	7	16
SER	20	15	9	10	0	2	24	8	10	0	32	13	0	32	6	24	14	8	9	34
THR	3	14	2	14	5	0	14	0	0	12	17	5	9	23	16	14	16	1	1	18
TRP	0	6	0	0	6	8	20	2	0	0	8	0	14	0	2	8	1	0	0	1
TYR	9	8	0	11	0	8	14	7	0	6	22	1	0	0	7	9	1	0	10	7
VAL	16	21	16	0	1	8	15	25	13	9	28	14	31	28	16	34	18	1	7	54

Fig. 7. The example of the distribution of all possible amino acid pairs calculated by Nitano

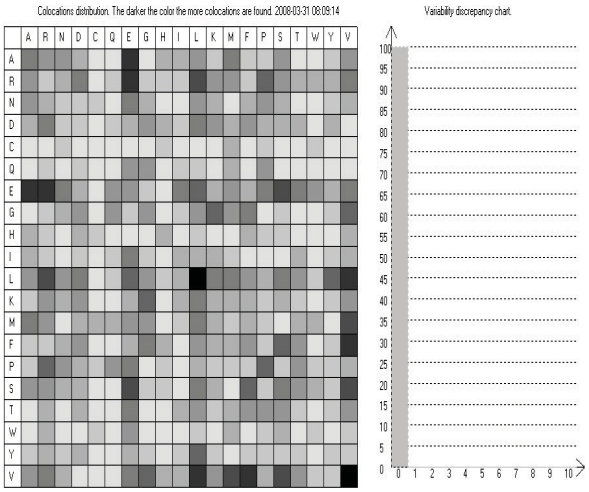

A B

Fig. 8. Amino acid heatmap (A). The darker colour means the more collocations are found. (B) The chart presenting correlation between average variability difference between residues that form collocation. Variability for this chart is calculated with the aid of another application Talana [unpublished data]

Nitano generates the text data concerning detected colocations and also draws two maps of colocations. The first map is a contact map. The horizontal axis and the vertical axis represent the protein sequence. The coordinates of the plotted dots refer to the numbers in the sequence ofthe residues that accomplish the distance treshold declared by user (minimum and maximum distance, exclusion of upstream and downstream residues) (Fig. 9A, Fig. 10B, Fig. 11A, Fig. 12A). This map allows to analyze both secondary and tertiary structure of a given protein. Another type of maps created by Nitano are the distance maps (Fig. 9B, Fig. 10A, Fig. 11B, Fig. 12B). These maps show each pair of residues with respect to the mutual distance of two atoms forming the colocation. The red color represents residues distant from each other by less than 3Å, the orange color shows a distance from 3 to 6Å, yellow – 6 to 9Å, green 9 to 12Å, light blue – 12 to 15Å and blue colour is for more than 15Å. The important feature of the software is the ability to analyse both the intermolecular and intramolecular contacts. The maps cannot be drawn only for protein/DNA/RNA complexes and small non-protein molecules such as ATP or glucose. The time of analysis can be reduced by excluding the upstream and downstream residues as it was mentioned before. The application is based on two similar algorithms for distance calculation. Let us consider a theoretical colocation between GLU12 and LYS16. The first algorithm (the slow one) finds two colocations for this pair: GLU12 vs. LYS16 and LYS16

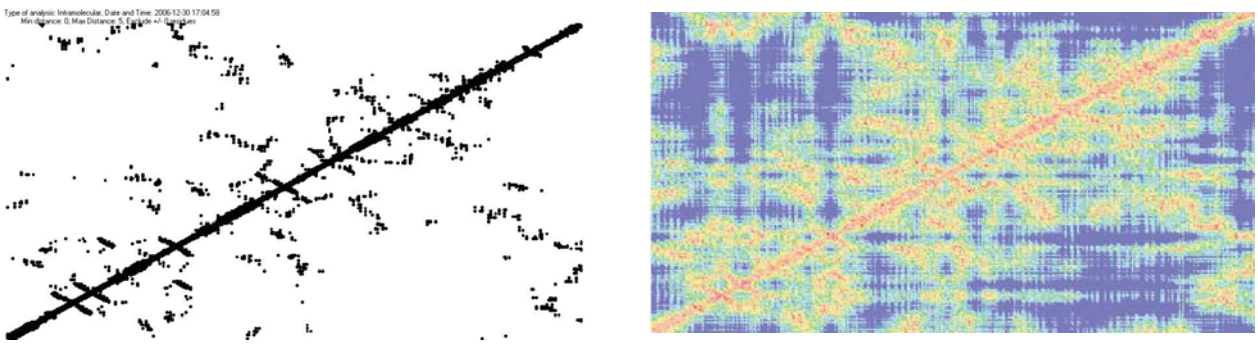

A B

Fig. 9. Example of intramolecular contact map with colocations within 5 Angstroms (A) obtained with the aid of Nitano. In the coloured map (B) the red color represents residues distant from each other by less than 3Å, the orange color shows a distance from 3 to 6Å, yellow – 6 to 9Å, green 9 to 12Å, light blue – 12 to 15Å and blue colour is for more than 15Å

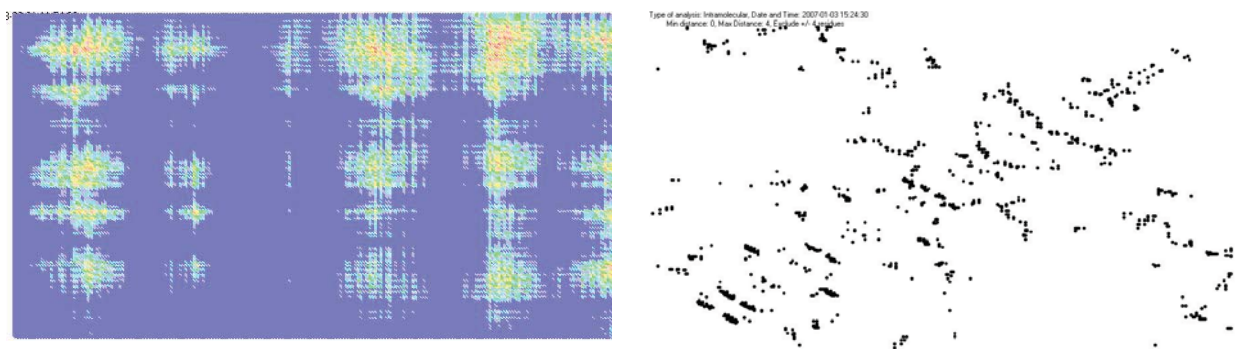

A B

Fig. 10. Intermolecular distance map (A). A map between kinase (PDB code 1ATP) and a peptide inhibitor bound to the chain. The effect of upstream and downstream exclusion of 4 residues (B), which allows the investigation of only these interactions that are not involved in neighbors contacts

vs. GLU12. This case is an example of duplicated data. The second algorithm (the fast one) considers only one direction, e.g. LYS16 vs. GLU12. Although the faster algorithm reduces the time of computing, the 'slower' algorithm is useful in some special cases. An example of faster analysis is presented on Fig. 11 A and B. Another feature of Nitano enables to study the phenomenon of correlated mutations [Kass and Horovitz 2002, Neher 1993, Valencia and Pazos 2002]. Correlated mutations detected by another application (Keram) are used as input data to Nitano in order to be visualized on the contact black-and-white or color map. Moreover, Nitano has also ability to construct a PDB file that can be used to visualize the mutations on the tertiary protein structure (Fig. 13B).

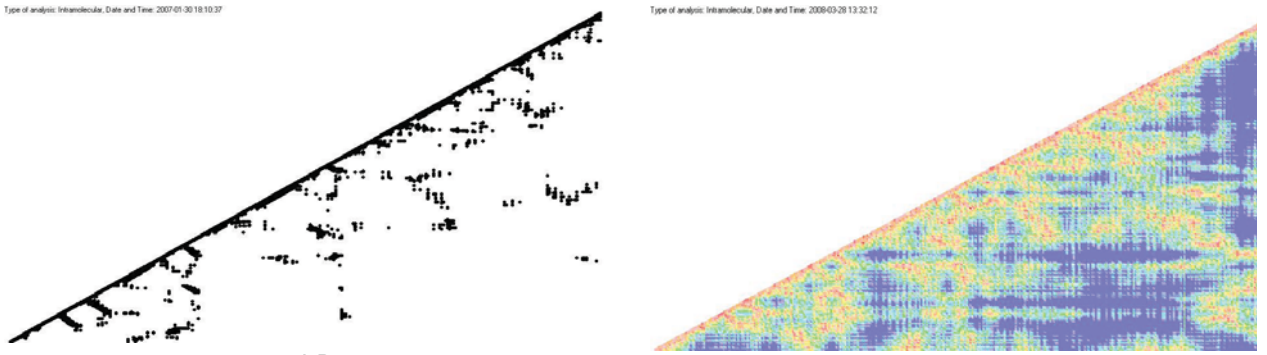

A B

Fig. 11. Intramolecular maps calculated with the 'faster' algorithm of Nitano. Contact map (A). Ditstance map (B)

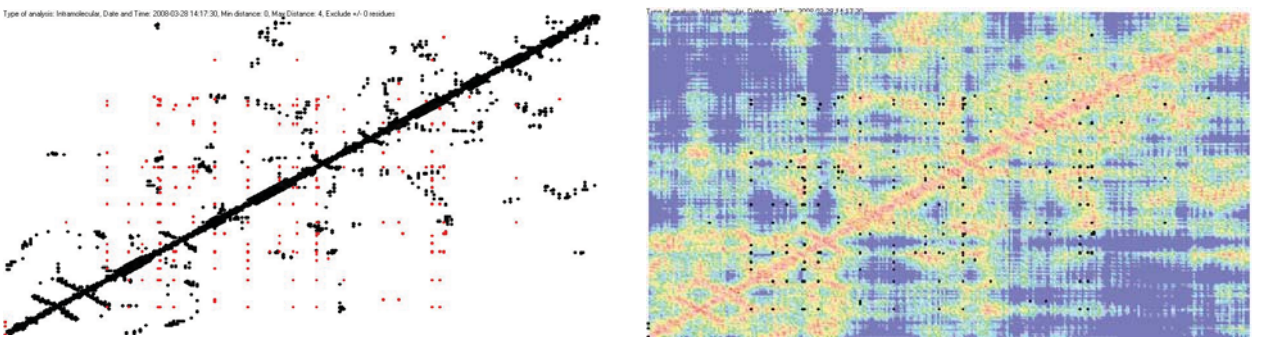

A B

Fig. 12. Contact (A) and color map (B) with visualized correlated mutations detected by KERAM [unpublished data]. Mutationally correlated positions are marked with red dots (A) or black dots (B)

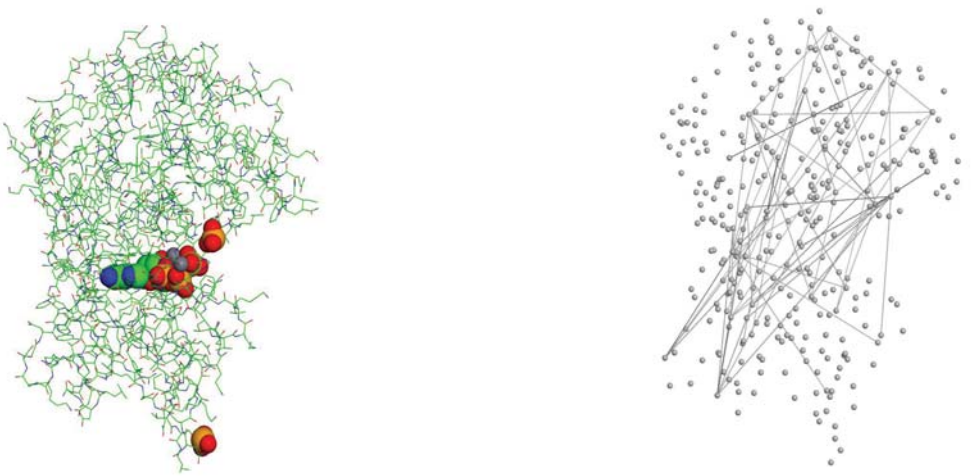

A B

Fig. 13. Protein structure (A) vs. correlated mutations (B) detected by Keram [unpublished data]. The lines connect the CA atoms of the correlated positions

Conclusions

Nitano is a user friendly application that provides significant structural data. Currently it is more specific than other available freeware. The application is designed to investigate the intramolecular and intermolecular interactions between proteins, nucleic acids and other compounds such as cofactors, substrates or inhibitors. There are implemented two independent algorithms that give the possibility of appropriate choice of the calculation with respect to the user's needs. The software generates informative output data and prints the inter- or intramolecular maps of interaction that can be used for more advanced analysis. It provides some basic important statistical calculations as well. Nitano is a useful application for drug designers concerning search for very specific ligands, for thorough protein structure analysis and for the interactome purposes.

Acknowledgements

This work was supported by the PBZ-MIN-014/P05/2005 grant and by CoE BioExploratorium.

References

1. Berman H.M., Westbrook J., Feng Z., Gilliland G., Bhat T.N., Weissig H., Shindyalov I.N., Bourne P.E. (2000), The Protein Data Bank. *Nucleic Acids Research* 28, 235-242.
2. Biro J.C. (2006), A novel intra-molecular protein – protein interaction code based on partial complementary coding of co-locating amino acids. *Medical Hypotheses* 66, 137-142.
3. Biro J.C., Fördös G. (2005), SeqX: a tool to detect, analyze and visualize residue co-locations in protein and nucleic acid structures. *BMC Bioinformatics* 6, 170.
4. Kass I., Horovitz A. (2002), Mapping pathways of allosteric communication in GroEL by analysis of correlated mutations. *Proteins: Struct. Funct. & Genet.* 48, 611-617.
5. Main E.R.G., Jackson S.E., Regan L. (2003), The folding and design of repeat proteins: reaching a consensus. *Current Opinion on Structural Biology* 13, 482-489.
6. Neher E. (1993), How frequent are correlated changes in families of protein sequences. *Proc. Natl. Acad. Sci. USA* 91, 98-102.
7. Oliveira L., Pavia A.C.M., Vriend G. (2002), Correlated Mutation Analyses on Very Large Sequence Families. *Chembiochem* 3(10), 1010-1017.
8. Pieper U., Eswar N., Braberg H., Madhusudhan M.S., Davis F., Stuart A.C., Mirkovic N., Rossi A., Marti-Renom M.A., Fiser A., Webb B., Greenblatt D., Huang C., Ferrin T., Sali A. (2004), MODBASE, a database of annotated comparative protein structure models, and associated resources. *Nucleic Acids Research* 32, D217-D222.
9. Pieper U., Eswar N., Davis F.P., Braberg H., Madhusudhan M.S., Rossi A., Marti-Renom M., Karchin R., Webb B.M., Eramian D., Shen M.Y., Kelly L., Melo F., Sali A. (2006), MODBASE, a database of annotated comparative protein structure models and associated resources. *Nucleic Acids Research* 34, D291-D295.
10. Sonnhammer E.L.L., Wooton J.C. (1998), Dynamic contact maps of protein structure. *Journal of Molecular Graphics and Modelling* 16, 1-5.
11. Valencia A., Pazos F. (2002), Computational methods for the prediction of protein interactions. *Current Opinion in Biology* 12, 368-373.
12. Vullo A., Walsh I., Pollastri G. (2006), A two-stage approach for improved prediction of residue contact maps. *BMC Bioinformatics* 7, 180.

BIO-ALGORITHMS AND MED-SYSTEMS
JOURNAL EDITED BY MEDICAL COLLEGE – JAGIELLONIAN UNIVERSITY
Vol. 6, No. 12, 2010, pp. 99–104.

THE BIOINFORMATICS IN VIETNAMESE ACADEMIC EDUCATION. SOFTWARE RESOURCES, RELIABILITY AND DEVELOPMENT

JACEK LELUK

Faculty of Biological Sciences, University of Zielona Góra, Poland

Abstract: Since 2005 the education program at bioinformatics an molecular modeling is being developed in Vietnam national universities with the cooperation of the University of Zielona Góra (Poland). This program requires good support concerning the biological databases and bioinformatics software. A number of good quality and comprehensive genomic an protein sequence databases and protein structure database are freely accessible online for academic use and scientific research. Also there are accessible the specialized genomic databases, kindly provided by Human Genome Center at Tokyo University. Similar situation concerns the bioinformatics software. However, the quality and reliability of the accessible software is not always very good. Therefore the Polish group cooperating with the Vietnam National University has elaborated and supplied the academic community in Vietnam with the new and original applications. They replenish the current needs of the users studying bioinformatics and raise the quality of the obtained results. The original applications, which enrich the VNU bioinformastics resources (an are solely available only in bioinformatics centers in Hanoi and Poland), are:
GEISHA – a nonstatistic application for sequence multiple alignment based on genetic semihomology algorithm.
Corm – application for locating and analysing the intramolecular correlated mutations.
Consensus Constructor – program for consensus sequence construction.
SSSS – program for sequence similarity significance estimation.
Talana – protein variability/conservativity analyzer and visualiser.
Nitano – detection of intra- and intermolecular residue colocations, protein contact map creator.
Keram – program to detect and analyze correlated mutations.
Retamgar – calculator of 2D, 3D, 4D points distance within a protein molecule.
Cylanu – PDB file modifier.
SecMaker – random protein sequence generator.
Byrnik – program for sequence comparison.
MMCC – molecule mass centre calculator.
Hypro – protein hydrophobicity profiler.
These resources contributed in the formation of the first academic Bioinformatics Center in this region of Asia, located at Hanoi University of Science. Within two last years the cooperation has been developed and extended by the long term study program for Vinh University students at University of Zielona Góra. At present two other universities joined the cooperation – Hanoi University of Agriculture and International University of HCMC. In all cases the bioinformatics and molecular modeling play the leading role in both educational and scientific activity.
Keywords: e-learning, education, bioinformatics software, software reliability, Vietnam universities

Introduction

In 2006 a group of lecturers from University of Zielona Góra in cooperation with 4System Company worked out the complete e-learning program for biology and environmental protection students. The translated English version of this material is being elaborated for educational use at Vietnam National University (VNU) in Hanoi and Hanoi University of Agriculture. The mirror of the initial e-learning material is installed on server of the Computer Center of the VNU College of Technology (http://www.coltech.vnu.vn).

The e-learning service in its complete form is intended to be open for biology students in Vietnam in academic year 2010/2011 [1]. The material provided by Polish scientists (from (University of Zielona Góra, University of Wrocław, Polish Academy of Sciences in Warsaw) includes 41 subjects, but the first version at VNU will consist of 12-15 subjects. The official language will be English. The technical support, mirror site and all infrastructure will be placed at Xuan Thuy Campus of VNU in Hanoi. The service is planned to have a global range. It will support all national universities in Vietnam that will declare the intention to include this program to their educational system. Also it is planned to support with this material the universities of other countries in the East Asian region upon the regulations established in the future. It especially concerns the countries where agriculture plays essential role in economics and fast

developing the qualifications in biological sciences will have important influence on the status of economy and social life.

The e-learning material is particularly focused on the modern fields of biological sciences and interdisciplinary sciences. A special place among them has the education material for bioinformatics and molecular modeling.

The Bilateral Cooperation between Universities in Vietnam and University of Zielona Góra, Poland

In 2008 there was officially ratified the bilateral cooperation between University of Zielona Góra (Poland) and two universities in Hanoi: Hanoi University of Science and Hanoi University of Agriculture. The cooperation concerns the broad activity within educational program and scientific research. This agreement concerns all faculties of the University of Zielona Góra and the universities in Hanoi. The partners will cooperate in following fields:

- exchange of academic staff in order to conduct joint research, deliver presentations, lectures and seminars;
- joint publications;
- exchange of information, specialized literature and library materials;
- cooperation in the fields of curricula and teaching methods;
- exchange of students in order to conduct studies, training and research;
- joint research projects;
- organization and participation in joint scientific undertakings, such as conferences, seminars, symposia etc.;
- cooperation within the international programmes.

A special role in this cooperation has development of the e-learning project and the development of the well supported Bioinformatics Center in Hanoi. Within this activity at both universities in Hanoi there have already been started the lectures on bioinformatics/molecular modeling for students of biology, computer science and mathematics and training courses on bioinformatics for the academic staff.

In 2009 there was signed another cooperation agreement between Vinh University and University of Zielona Góra. The cooperation with Vinh University concerns mainly the study program for Vietnamese students conducted by academic staff of the University of Zielona Góra at undergraduate, graduate and postgraduate level. The study program will be accomplished in compliance with the UE educational standards, partially in the parent university in Vietnam and partially in the University of Zielona Góra. For example, the undergraduate study program will be executed within the system 2+2 (first two years at Vinh University, and the last two years in Poland). The students attending the course will be awarded with the diploma of University of Zielona Góra, recognized by UE system and accomplishing the UE requirements. This will give the opportunity for Vietnamese students to continue their further studies at European universities and also facilitate the job opportunities in academic and research centers in Europe.

The cooperation with Vietnamese academic and research institutions has been extended within last 2 years by International University of Ho Chi Minh City (which is also a VNU member) and Saigon Hi-Tech Park. The cooperation with Ho Chi Minh City concerns especially the educational and research activity within the modern topics of biological sciences such as bioinformatics, molecular modeling, protein design, genomics and molecular phylogenetics.

Access to the Biological Databases at VNU

The contents of the biological databases are freely accessible by internet. However, the slow data speed transfer between Vietnam and original database servers may occur. This often makes the work with the databases less efficient and more time consuming. For that reason the most commonly used databases and online bioinformatics services will be installed locally as the continually updated mirrors in the Computer Center of VNU for convenience of the students and researchers working on the campus of Hanoi University of Science and Hanoi University of Agriculture. The set of the mirror databases at the first period will comprise the selected genomic and protein sequence databases, the Protein Data Bank (PDB) [2-4] and two specialized genomic databases of the transcription start sites – DBTSS [5-6] and DBTBS [7]. Among the on-line applications that require powerful computer units, a mirror of BLAST [8] package will be installed, for biological sequence comparative studies and searching the protein and genomic sequence databases.

The Bioinformatics Software Resources at VNU

A huge number of software applications for bioinformatics, genomics, proteomics and molecular modeling are freely accessible as online applications or downloadable software. They will be used for academic use, scientific research and educational purposes within the program developed at VNU. The available software is usually user friendly and is supported by high quality graphic user interface. These applications are commonly used worldwide. However, the quality and reliability of this software is not always very good. Therefore, the Polish group cooperating with the VNU staff has elaborated and supplied the University in Hanoi with the new and original applications. They replenish the current needs of the users studying bioinformatics and raise the quality of the obtained results. The original applications significantly enrich the VNU bioinformastics resources and are solely available only in bioinformatics centers in Hanoi and Poland. The list of the original applications is as follows:

GEISHA – a nonstatistic application for sequence multiple alignment based on genetic semihomology algorithm [9-13].

Corm – application for locating and analysing the intramolecular correlated mutations [14].

Consensus Constructor – program for consensus sequence construction [15].

SSSS – program for sequence similarity significance estimation [16-17].

Talana – protein variability/conservativity analyzer and visualiser [18].

Nitano – detection of intra- and intermolecular residue colocations, protein contact map creator [18].

Keram – program to detect and analyze correlated mutations [18].

Retamgar – calculator of 2D, 3D, 4D points distance within a protein molecule [18].

Cylanu – PDB file modifier [18].

SecMaker – random protein sequence generator [18].

Byrnik – program for sequence comparison [18].

MMCC – molecule mass centre calculator [18].

Hypro – protein hydrophobicity profiler [18].

Below is the brief description of some of the applications provided by the Polish group of biologists and computer scientists.

GEISHA and genetic semihomology algorithm

GEISHA (GEnetIc SemiHomology Algorithm) [13] is a program for protein sequence pairwise and multiple alignment. The alignment procedure uses the algorithm of genetic semihomology [9-12], which is a entirely different approach from the stochastic mutation matrices implemented in almost all available multiple alignment applications. The GEISHA application consists of two parts. One is to make a pairwise alignment with the detailed analysis and verification of the results. The other constructs the multiple sequence alignemnt and provides the data of the evolutionary distance between aligned sequences, which can be used for phylogentic tree construction.

The important feature of the algorithm of genetic semihomology concerns the minimal initial assumptions. It assumes the general codon-to-amino acid translation table, and the single point mutation as the basic and most common mechanism of protein differentiation [9]. This approach is not limited to single point mutation mechanism only. It may be used to localize those fragments which undergo other kind of mutation.

It is admitted that from evolutionary point of view the genetic code and amino acid “language” have evolved simultaneously. They also act with strict coherence with each other. Therefore in analysis of protein differentiation and variability, both of them should be considered as well.

The sense of this algorithm is not the scoring the comparison results but explaining the way of amino acid replacement and the mechanism of variability at both, amino acid and genetic code, levels. For that reason the algorithm of genetic semihomology should be treated separately from other algorithms, especially statistical ones. This interpretation is often consistent with the amino acid replacement indices data. Theoretical results obtained by algorithm of genetic semihomology and mutation data matrix scoring support each other. This coincidence is very important for correct interpretation of the mechanism of protein variability.

The goal of minimization of the initial assumptions in the algorithm of genetic semihomology is to 1) makes the algorithm universal for any group of proteins and 2) avoids errors and misinterpretation of the results. Basically, the algorithm assumes three general establishments. One of them is the codon-amino acid translation table, which is undoubtedly considered as true.

The second is the statement that single nucleotide replacement is the most often and easiest mechanism of mutational variability. The last general establishment comprises the three-dimensional diagram of amino-acid replacements by single point mutation.

A single nucleotide replacement concerns two types of replacements – transition and transversion. Another question is the position-dependence of replacement within the codon and its further consequence. The third nucleotide of the codon is known as the most tolerant and most flexible encoding unit. Most amino acids are encoded by first two nucleotides, while the third position is optional.

Amino acid residues as the products of genetic code translation are not equal units, when we consider both nucleotide and protein levels simultaneously. They are encoded by different number of codons from 1 to 6. That implies the difference in probability of their replacement by single point mutation. Such differentiation causes the fact that amino acids themselves cannot be treated uniformly in terms of mutational variability. It is important which exactly codon encodes a certain amino acid for its further transformation to another one. That reveals inconsistency of amino acid mutational substitution with the Markovian model which establishes all exchange probabilities as independent on the previous history [21]. Markovian model, however, is assumed in most statistical matrices of protein mutational variability.

Corm

Corm [14] is a Java application for locating and analyzing the correlated mutations that occur within a protein molecule. Correlated mutations are the phenomenon of several mutations occurring simultaneously in a protein molecule and dependent on each other. This phenomenon exists as a natural mechanism to preserve the significant structure properties and biological activity upon mutational variability process.

Corm is a fully automatic procedure to find all correlated position clusters within a protein upon the declared threshold parameters of search. This is the unique program for correlated mutation analysis.

Consensus Constructor

Consensus Constructor [15] is a user friendly Java application for a clear representation of the sequence multiple alignment constructed by other programs. It gives the output file in rtf format, with the black and gray boxes indicating the conservative and typical residues defining a homologous protein family. The scientific value of the program is the ability of the consensus sequence construction by adjusting the three parameters defining the conservativity, frequent occurence of a certain amino acid type and the gaps.

This program is used to design the proper consensus sequence that defines all significant characteristics of a homologous family and can be applied as a query sequence for BLAST search for the family new members.

SSSS

The correct estimation of significant sequence similarity is a very important initial step for any theoretical comparative studies on nucleic acids and proteins. The selection of the truly related sequences is the basic condition for multiple alignment and consensus sequence construction, for monitoring the molecular evolution and homology determination. The successful protein similarity search depends on adequate estimation whether the observed similarity is actual or casual. Although many applications for sequence similarity allow to estimate the degree of similarity and possible homology, they are not universally standardized and they not always consider all essential criteria. Moreover, quite often only percentage of identity is assumed as a decisive factor of sequence possible relationship. The SSSS (Sequence Similarity Significance Statement) program [16-17] enables explicitly to estimate the significance of the observed similarity at the level of primary structure. This approach is applicable to any protein family as well as for comparative studies on nucleic acids.

- There are following fundamental criteria of the sequence similarity estimation at optimal alignment:
- The percentage of identity (relative contribution of the corresponding positions occupied by identical units)
- The length of the compared sequences
- Distribution of the identical positions along the analyzed sequences
- The type of units occupying conservative positions (for protein sequences)
- Genetic relationship structural similarity and/or statistical estimation of the replacement frequency of the units at corresponding but non-identical positions (for protein sequences)

First three criteria refer to any biological sequences, the last two criteria are used for protein sequences only. The program SSSS exists in a few versions. The version SSSSg [17] evaluates the similarity significance on the basis of all three general criteria. The output gives several values, one of which is used as an evolutionary distance between the compared sequences and serves to create the phylogenetic tree.

If the protein sequence similarity significance is still uncertain, the final step considers a thorough analysis of genetic semihomology of non-identical fragments [9-12]. This step may be additionally supported by side chain structural similarity of the corresponding amino acids.

Talana

Talana [18] is a stand alone application that runs under Windows and is aimed at calculating variability/conservativity. The calculation is based on multiple sequence alignment of related sequences provided by the user. Talana returns the number that represents the amount of different aminoacids or bases that occupy particular position. It also creates a script file that is calculated on the basis of the alignment and latter can be applied by the user to visualize the variability/conservativity in three dimensional space. This application is useful to identify the significant sites that form a catalytic cavity, it is helpful to locate and analyse the conservativity of hydrophobic protein core. Talana can be used not only for identification of crucial sites in the biological macromolecules, but also to design the new drugs of a desired specific activity. Talana significantly improves the speed and quality of analysis of multiple sequence alignments. With this software the identification as well as visualization of crucial residues (from both structural and functional point of view) is considerably easy.

Talana is freely available for educational users at http://www.bioware.republika.pl. The application requires Windows (XP/2000) with Pentium processor with at least 512MB of RAM and Internet Explorer (optional) to view its website and help file.

Nitano

The main destination of Nitano [18] is the calculation of residue colocations. The input file is any PDB file. It allows not only to search the contacts that exist within one protein chain but also the contacts responsible for interaction between two separate protein chains. Nitano recognizes the nucleic acids as well as proteins in analyzed PDB file. As output file of Nitano gives distances of found collocations and two contact maps that visualize protein structure on a 2D surface. This application is capable of performing basic statistical analysis of obtained results. The application is freely available for educational users at http://www.bioware.republika.pl. Nitano is available in two versions – slower but giving the more detailed output file and faster, providing the simplified graphics of output. The application requires Windows (XP/2000) with Pentium 2GHz or higher with at least 512MB of RAM and Internet Explorer (optional).

Nitano is a very user friendly application. Currently it is more specific than other freeware sofware available. Moreover, Nitano does not require the user to have any programming knowledge. The application is capable of investigating interactions between two proteins, two DNA strand, protein and DNA, protein and nonstandard residues such as cofactors, substrates, or specific inhibitors.

Keram

Keram [18] serves to detect and analyze the correlated mutations [19-20] within the protein molecule. It is assumed that this phenomenon contains the information about protein structures as well as the information about the formation of protein complexes. It is commonly accepted that the mechanism of compensation explains the mutations that occur simultaneously. The fundamental destination of this software is to detect correlations on the basis of sequence alignments. The output files created by Keram consists of a list of all detected correlations and tables containing some other important data. This application is useful to detect the mutations that occur simultaneously. The computing time is very short. The program can be run offline. Keram is available for free for the non-commercial user at http://www.republika.pl/bioware or at http://www.bioexploratorium.edu.pl. Also the source code is available from the authors upon direct request.

Retamgar – calculator of 2D, 3D, 4D points distance within a protein molecule

Retamgar [18] is an application that calculates distance between two points within a molecule. These points can be plotted on 2D, 3D or even 4D space. Output is a txt file including the coordinates and calculated distances. The program is freely accessible at the address http://www.bioware.republika.pl/retamgar.html.

Cylanu – PDB file modifier

Cylanu [18] is a PDB file editor for PDB (ENT) files. It modifies the PDB files according to the users requirements. By this application it is easy to find the search field of the file to be modified, extract the sequence(s) and calculate the contribution of residues in a molecule and atoms of a particular residue in the sequence. The program is freely accessible at the address http://www.bioware.republika.pl/cylanu.html.

SecMaker – random protein sequence generator

SecMaker [18] is an application that creates a random sequence. It generates RNA/DNA or protein sequences. The user can specify the lenth of your sequence or the sequence lenght can be declared as random. The output txt file contains the sequence in FASTA format. The program is freely accessible at the address http://www.bioware.republika.pl/secmaker.html.

Byrnik – program for sequence comparison

Byrnik [18] is a dotplot application that uses the algorithm of genetic semihomology [9-12] for sequence comparative studies. The advanced analysis concerns the positions occupied by the amino acids that can be replaced one to another by single transition/transversion. The program is freely accessible at the address http://www.bioware.republika.pl/byrnik.html.

MMCC – molecule mass centre calculator

MMCC [18] is an application for the mass centre analysis in PDB files. The application calculates the correlation between each residue mass centre and the entire molecule's mass centre. MMCC draws charts, writes script files as well as text files that can be used for more advanced analysis. The program is freely accessible at the address http://www.bioware.republika.pl/mmcc.html.

Hypro – protein hydrophobicity profiler

HyPro [18] (Hydrophobicity Profilier) is an application designed to analyze hydrophobicity of one or two protein sequences. It can be freely downloaded for academic use from http://www.bioware.republika.pl/hypro.html.

References

1. Leluk J. (2007), E-learning: the past, present and future perspectives. International Conference Hanoi Forum on Information-Communication Technology (ICT), 5-7 December 2007, Hanoi, Vietnam, Abstracts.
2. Berman H.M., Westbrook J., Feng Z., Gilliland G., Bhat T.N., Weissig H., Shindyalov I.N., Bourne P.E. (2000), The Protein Data Bank. *Nucl. Acids Res*. 28, 235-242.
3. Berman H.M., Henrick K., Nakamura H. (2003), Announcing the worldwide Protein Data Bank. *Nature Structural Biology* 10, 980.
4. Bernstein F.C., Koetzle T.F., Williams G.J.B., Meyer E.F., Jr., Brice M.D., Rodgers J.R., Kennard O., Shimanouchi T., Tasumi M. (1997), The Protein Data Bank: a computer-based archival file for macromolecular structures. *J. Mol. Biol.* 112, 535-542.
5. Suzuki Y., Yamashita R., Nakai K., Sugano S. (2002), DBTSS: DataBase of human Transcriptional Start Sites and full-length cDNAs. *Nucl. Acids Res*. 30, 328-331.
6. Suzuki Y., Yamashita R., Sugano S., Nakai K. (2004), DBTSS: DataBase of Transcriptional Start Sites: progress report 2004. *Nucl. Acids Res.* 32.
7. Ishii T., Yoshida K., Terai G., Fujita Y., Nakai K. (2001), DBTBS: a database of Bacillus subtilis promoters and transcription factors. *Nucl. Acids Res.* 29, 278-280.
8. Altschul S.F., Gish W., Miller W., Myers E.W., Lipman D.J. (1990), Basic local alignment search tool. *J. Mol. Biol.* 215, 403-410.
9. Leluk J. (1998), A new algorithm for analysis of the homology in protein primary structure. *Computers & Chemistry* 22, 123-131.
10. Leluk J. (2000), A non-statistical approach to protein mutational variability. *BioSystems* 56, 83-93.
11. Leluk J. (2000), Regularities in mutational variability in selected protein families and the Markovian model of amino acid replacement. *Computers & Chemistry* 24, 659-672.
12. Leluk J., Hanus-Lorenz B., Sikorski A.F. (2001), Application of genetic semihomology algorithm to theoretical studies on various protein families. *Acta Biochim. Polon.* 48, 21-33.
13. Górecki A., Leluk J., Lesyng B. (2004), A Java-implementation of a genetic semihomology algorithm (GEISHA), and its applications for analyses of selected protein families. 29th FEBS Congress, 26 June – 1 July 2004, Warsaw, Poland. *Eur. J. Biochem.* 271, Supplement, 30.
14. Kuśka J., Leluk J., Lesyng B. (2008), Novel analysis of correlated mutations in kinases and its potential applications. Bioinformatics 2008 Conference, 24-27 April, 2008, Warsaw, Poland, Abstracts, 45.
15. Fogtman A., Leluk J., Lesyng B. (2005), β-Spectrin consensus sequence construction with variable threshold parameters: verification of their usefulness. The International Conference Sequence-Structure-Function Relationships; Theoretical and Experimental Approaches, 6-10 April, 2005, Warsaw, Poland. Abstracts, 12.
16. Leluk J., Mikołajczyk A. (2004), A new approach to sequence comparison and similarity estimation. 29th FEBS Congress, 26 June – 1 July 2004, Warsaw, Poland. *Eur. J. Biochem*. 271, Supplement, 29.

17. Gajewska E., Leluk J. (2005), An Approach to Sequence Similarity Significance Estimation. *Bio-Algorithms and Med-Systems* 1, 121-124.
18. Kuśka J., Leluk J. (2007), BIOW@RE: A package of applications for intra/intermolecular interaction studies. 5th International Conference "Inhibitors of Protein Kinases". *Acta Biochim. Polon.* 54, Supplement 3, 61-62.
19. Neher E. (1993), How frequent are correlated changes in families of protein sequences. *Proc. Natl. Acad. Sci. USA* 91, 98-102.
20. Oliveira L., Pavia A.C.M., Vriend G. (2002), Correlated Mutation Analyses on Very Large Sequence Families. *Chembiochem* 3(10), 1010-1017.
21. George D.G., Barker W.C., Hunt L.T. (1990), Mutation data matrix and its uses. In: R.F. Doolittle (ed.), *Methods in Enzymology*. Academic Press, San Diego, CA, 183, 337.

BIO-ALGORITHMS AND MED-SYSTEMS
JOURNAL EDITED BY MEDICAL COLLEGE – JAGIELLONIAN UNIVERSITY
Vol. 6, No. 12, 2010, pp. 105–111.

SIMULATION BASED VERIFICATION OF THE BAYESIAN APPROACH IN SINGLE-POOL HEMODIALYSIS MODELLING

Przemysław Korohoda

Chair of Electronic, AGH University of Science and Technology, Cracow, Poland

Abstract: In the paper an intensive computational comparative study has been described. With use of a hundred thousand pseudo-randomly generated hemodialysis sessions, a comparison between the efficiency of the Bayesian approach and the classic RMSE optimisation used in the urea kinetic modelling has been performed. The studied procedure of kinetic modelling utilized asingle-pool model to find from a number of measured urea concentration values: a) clearance *K*, b) generation rate *G*, c) distribution volume *V*. The obtained results indicate that the Bayesian approach, while in general being better than the classic one, is very sensitive to errors in the assumed *a priori* distributions parameters, and in such cases it may also lead to considerably unreliable results. Additionally, a strong critique emerged against the classic optimisation used for the studied task. The above observations indicate a need to design a specific optimisation technique, relevantly suited for the studied problem.
Keywords: urea kinetic modelling, Bayesian, comparative study

Streszczenie: W artykule opisano intensywne obliczeniowe studium porównawcze. Z wykorzystaniem stu tysięcy symulowanych sesji hemodializy skonfrontowano efektywność zastosowania w modelowaniu kinetycznym mocznika klasycznej optymalizacji z minimalizacją błędu średniokwadratowego i podejścia bayesowkiego. Poddana badaniom procedura modelowania kinetycznego wykorzystywała model jednokompartmentowy w celu wyznaczenia, na podstawie kilku wartości stężenia mocznika, następujących parametrów: a) klirensu *K*, b) tempa generacji *G* oraz c) objętości dystrybucji *V*. Uzyskane wyniki wykazały, iż podejście bayesowkie, chociaż generalnie lepsze od klasycznego, jest bardzo wrażliwe na błędy w założonych parametrach rozkładów i w takim przypadku może prowadzić do wyników w znacznym stopniu niewiarygodnych. Ponadto stwierdzono, że należy poddać poważnej krytyce klasyczną metodę optymalizacji, stosowaną typowo do postawionego zadania. Obserwacje te wskazują na konieczność opracowania nowej metody, odpowiednio dostosowanej do rozważanego zagadnienia.
Słowa kluczowe: modelowanie kinetyczne mocznika, podejście bayesowkie, studium porównawcze

Introduction

In the area of hemodialysis treatment, the procedure of urea kinetic modelling (UKM) is an important and helpful element, which provides a better understanding of the behaviour of the system patient-dialysis machine, and thus enables a more accurate assessment of the delivered dose and more efficient planning of further actions [1,2,3,5]. The most commonly used model in the clinical practice is a single pool model, in spite of the fact that the two-pool model much better represents some important features, like the rebound effect and overall equilibration of the system [3]. However, the crucial parameters required to adequately use the latter are not available in the way of direct measurement or simple calculations. Therefore, the basic model is still the single-pool with some later corrections [3]. In the process of modelling, the parameters of the model are obtained after some measurements and model tuning, so that the modelled values would be close to the measured ones. This procedure has been well known for some decades already [1], but the peculiar structure of the model and the limitations resulting from the reality of the dialysis units make it still the subject of investigation [4,6,7,8,11]. The so called Bayesian approach, well known in the field of farmacology [9,10], has been recently adapted to UKM and seems to attract growing attention [6,7,8]. However, the research described in the references has been typically performed on the clinical data, with the Bayesian approach used without clarifying the possible doubts about adequacy of this method. The only relevant references are either statistical works with rather optimistic description of the theory and examples significantly different from UKM [9], or describing computational comparative studies performed with limitations resulting from then up-to-date computing efficiency, which made the conclusions unconvincing [10]. Theseobservations motivated the author to design and perform a comparative experiment to state clearly the advantages of the newly rediscovered Bayesian approach as applied to UKM, in the realistic assumption of using a single-pool model. The presented study, performed on simulated hundred thousand hemodialysis sessions, compares the efficiency of the Bayesian approach and the classic mean square optimisation.

Modelling with the use of a single-pool model

The single pool model used in the UKM may be described by the differential equation [1]:

$$\frac{dC(t)}{dt} = \frac{-KC(t) + G}{V - Qt} \quad (1)$$

where
V – the urea distribution volume, expressed in liters [L];
C – concentration of the urea in the compartment, available for the direct measurement, in [mg/L];
G – urea generation rate in [mg/min];
K – clearance, expressing the sum of the residual renal activity and the hemodialysis blood filtering, in [L/min];
Q – the ultrafiltration rate – the speed of removing of the surplus of water accumulated in the patient's body between the treatments – available for measurement, in [L/min].

Note that the form of (1) may suggest that the number of unknown parameters (K,G and V) could be replaced with satisfactory accuracy by relevant ratios. However, for proper understanding of the whole process it is necessary to know the values separately and not in the form of ratios. Moreover, the Bayesian criterion (see the explanation below) introduces tuning of each of the just mentioned parameters.

Classic optimisation based on the RMSE

Typically [4,11], in the modelling session samples of urea concentration are taken at given time points, and then the model is being adjusted via finding the minimum of the root mean square error (RMSE), computed for the concentration values resulting from modelling referred to those coming from the measurement. Here, the following RMSE formula will be used:

$$RMSE_M = \sqrt{\frac{1}{M-1}\left(\sum_{m=2}^{M}\left(C_{test}(m) - C_{ref}(m)\right)^2\right)} \quad (2)$$

The concentration at t = 0 (indexed as m = 1) is not taken into account, because, as a starting point for the runs, it must be always correct. M is the number of measured concentration values.

Bayesian approach

Originally, in the Bayesian approach the maximum of the likelihood function has to be found [9]. However, for the Gaussian data distribution functions looking for the maximum of likelihood function is equivalent to finding the minimum of the following expression, presented here for G, K and V

$$Y = \frac{(K-\overline{K})^2}{\sigma_K^2} + \frac{(G-\overline{G})^2}{\sigma_G^2} + \frac{(V-\overline{V})^2}{\sigma_V^2} \quad (3)$$

where
$\overline{K}, \overline{G}, \overline{V}$ – the *a priori* known mean values of the distributions of the variables;
$\sigma_K, \sigma_G, \sigma_V$ – the *a priori* known standard deviations of the discussed distributions.

In the Bayesian approach, both criteria (2) and (3) are combined in the formula, derived in the same manner as in the model used in [10]. Additionally, the log-Gaussian distribution functions are applied for G, K and V, according to the properties observed in practice [10]. Finally, the optimised criterion is

$$Y_B = \frac{(\log(K) - \log(\overline{K}))^2}{\sigma^2_{\log K}} + \frac{(\log(G) - \log(\overline{G}))^2}{\sigma^2_{\log G}} + \frac{(\log(V) - \log(\overline{V}))^2}{\sigma^2_{\log V}} + RMSE_M \quad (4)$$

where log( ) means the natural logarithm and $\sigma_{\log G}$ denotes the standard deviation of the distribution of a given variable in the logarithm form, in this example: log(G).

Description of the experiment

The only referenced study comparing the effects of using Bayesian and other approach to a task closely resembling UKM has been provided in [10]. However, the authors could not use the computational power which is available now even on commonly available PC, especially armed with the Matlab tool, which made their study considerably reduced if compared with expectations which might be defined contemporarily. In [10] the single-pool model was studied: a) with the sample size inadequately small – the study was based on merely N = 100 simulations, b) the simulations assumed a single marker injection (instead of constant generation, typical for UKM), c) the volume remained constant during session (no ultrafitration was assumed), d) the study focused on the only one optimized parameter – clearance. Therefore, it appeared obvious that a similar relevant study without the mentioned above drawbacks should be performed.

Here, the data for the simulated sessions were generated with a pseudo-random generator with following assumptions.

The parameters cannot take negative values. Instead of introducing the limits, the log-Gaussian distribution function with use of the natural logarithm, log of K, G and V has been assumed, as suggested in [10]. The relevant mean and standard deviation values for all generated parameters are provided in Table 1. Note that the measurement noise for the concentration was just Gaussian distributed.

Tab. 1. The values describing the log-Gaussian distributions of randomly generated values for the experiments

parameter	log(K)	log(G)	log(V)	C noise [mg/L]
mean	log(180)	log(10)	log(40)	0
stand. dev.	log(20)	log(3)	log(10)	50

The ultrafiltration rate was assumed as closely related to the total volume: $Q = 0.05 \cdot V/td$, where the treatment time td was fixed to 240 minutes. To avoid unrealistic simulations, all cases where the Kt/V index [1,3], $Kt/V = \log(C(0)/C(td))$, was outside the range between 0.8 and 1.8, were skipped, and the

generation was repeated. The starting concentration was fixed: $C(0) = 2000$ mg/L.

After generating the *K*, *G*, *V* parameters, the urea concentration runs, $C(t)$, were computed according to the well known formulas [1], and at certain time points, after each 60 minutes, the concentration values were recorded. Then, the ideal concentration values were modified by the generated noise – see last column in Table 1.

Measured concentration values were used to find the – assumed as unknown – *K*, *G*, *V* parameters.

Four options were used to compare the optimisation efficiency.

$x = 1$ – classic solution, via finding minimum of the RMSE (2) formula;

$x = 2$ – Bayesian approach, assuming the values from Table 1 to be *a priori* known, with finding the minimum of (4);

$x = 3$ – Bayesian approach, almost the same as for $x = 2$, but with wrong mean values for *K* (0.12 L/min) and for *V* (60 L);

$x = 4$ – Bayesian approach, almost the same as for $x = 2$, but with wrong standard deviation values for *K* (0.06 L/min) and for *V* (30 L).

The efficiency of the tuning process was measured by the following criteria. The accuracy of the obtained concentration values at the measurement points, taking as a reference the values with noise added (C_n denotes the value of noise)

$$\mathrm{J}_x = \sqrt{\frac{1}{M-1}\left(\sum_{m=2}^{M}\left(\tilde{C}(m) - C_x(m)\right)^2\right)}$$
$$\tilde{C}(m) = C(m) + C_n(m) \qquad (5)$$
$$x = 1, 2, 3, 4$$

and without noise

$$\mathrm{I}_x = \sqrt{\frac{1}{M-1}\left(\sum_{m=2}^{M}\left(C(m) - C_x(m)\right)^2\right)} \qquad (6)$$
$$x = 1, 2, 3, 4$$

In this experiment: $M = 5$.

The found *K*, *G*, *V* parameters were compared with the assumed values with use of the relative error measure, expressed in %

$$\mathrm{RelErr} = 100\,\% \frac{X - X_{ref}}{X_{ref}} \qquad (7)$$

where *X* represents the relevant parameter: $X = K, G$ or V.

Results

General approach

The obtained results are described by the values summarized in the Tables and Figures below. Tables 2, 3 and 4 together with Fig. 1 indicate that in all four options the resulting concentration runs are very similar. However, note that according to Table 2 the values for $x = 1$ (the classic approach) are slightly smaller, which suggests this option to be the best choice, if we consider only the concentration values enriched with noise, which is the best approximation of the realistic case.

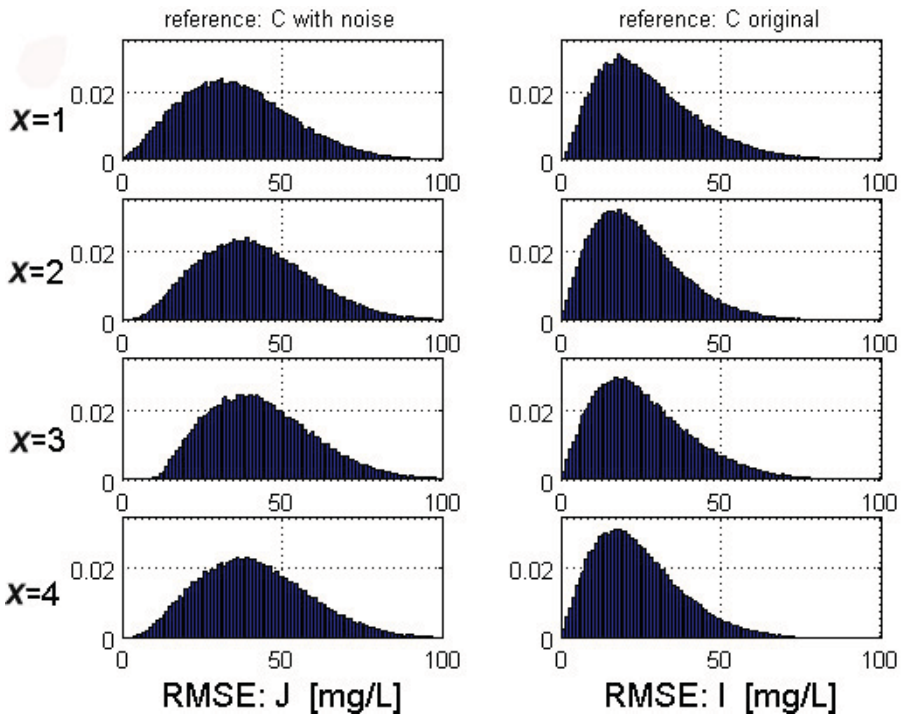

Fig. 1. The normalized histograms depicting experimental distribution functions of the RMSE values for N=100 000 simulations and four optimisation options (denoted by x). J refers to (5) and error computed with reference to the noised concentration values, and I (6) expresses error referred to the original concentration values, prior to adding Gaussian noise

Tab. 2. Mean (±standard deviation) of the RMSE concentration error according to (5) and (6)

x	1	2	3	4
J_x	36.0 (±17.3)	41.5 (±17.4)	43.4 (±16.6)	41.4 (±17.5)
I_x	27.2 (±15.3)	24.1 (±13.9)	26.1 (±15.3)	24.4 (±14.1)

Tab. 3. Correlation coefficients between J RMSE values (5) for the performed experiments with four options (denoted by *x*); all *p-values* were 0 up to the computational precision

x	1	2	3	4
1	1.0000	0.8714	0.8670	0.8699
2	0.8714	1.0000	0.9987	0.9999
3	0.8670	0.9987	1.0000	0.9983
4	0.8699	0.9999	0.9983	1.0000

Table 4. Correlation coefficients between I RMSE values (6) for the performed experiments with four options (denoted by *x*); all *p-values* were 0 up to the computational precision

x	1	2	3	4
1	1.0000	0.8144	0.6592	0.8255
2	0.8144	1.0000	0.8418	0.9876
3	0.6592	0.8418	1.0000	0.8013
4	0.8255	0.9876	0.8013	1.0000

The paired t-test exhibited the same distribution only while comparing between concentration errors for $x = 2$ and $x = 4$, only then the *p-value* was 0.1651. In other comparisons the test indicated different distributions, $p < 0.0001$. Such results prove the values in Table 2 to be reliable as indicators of expected differences between compared options, which, however, seem to be negligibly small from the practical point of view and rather support the thesis that all options are equivalent when considering the concentration adjustment.

The crucial comparison is presented in Fig. 2 and Table 5, where the differences in accuracy between options are clearly noticeable. Undoubtedly, for $x = 2$ (the Bayesian solution with proper *a priori* knowledge), the prediction of the *K*,*G* and *V* values is the best. The distracting effect of wrong *a priori* values is clearly visible (for $x = 3$ and $x = 4$). Note that *G* exhibits the smallest sensitivity to inaccurate *a priori* values, but on the other hand, the error for this parameter is the largest.

Tab. 5. Mean (±standard deviation) of the relative error (7) expressed in %, for *K*, *G* and *V* after all four options of experiment (denoted by *x*)

x	1	2	3	4
K	–11.2 (±39.1)	0.4 (±10.2)	–22.6 (±7.8)	8.6 (±20.2)
G	21.8 (±117.4)	4.7 (±32.1)	–0.9 (±30.4)	5.2 (±32.3)
V	–15.2 (±42.2)	1.1 (±11.9)	–22.3 (±9.2)	9.4 (±21.0)

The paired t-test indicated the same distribution only while comparing between *G* for $x = 2$ and $x = 4$, only then the *p-value* was 0.3588. In other comparisons the test indicated different distributions with $p < 0.0001$.

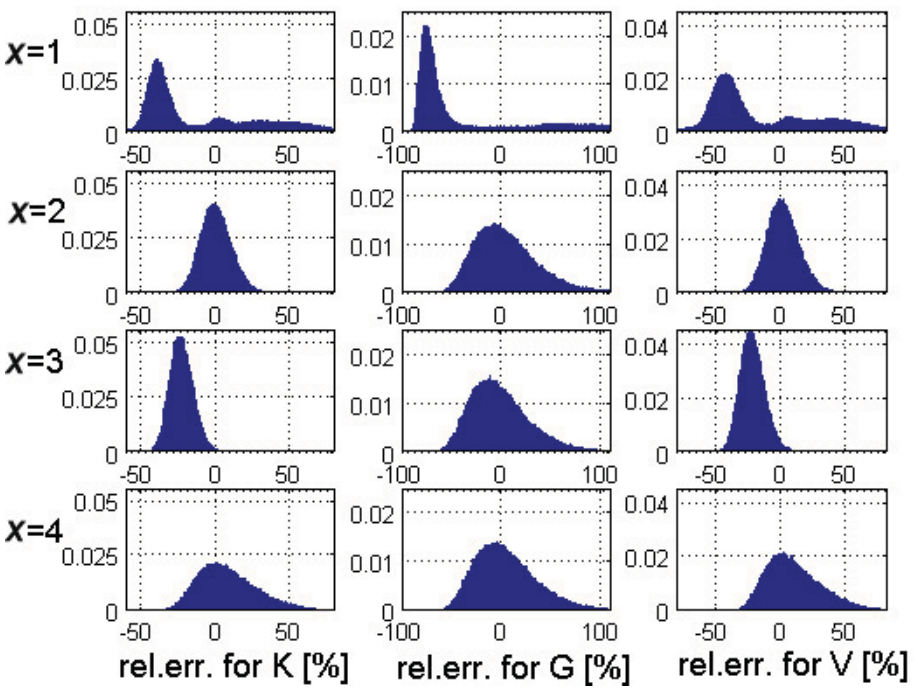

Fig. 2. The normalized histograms showing experimental distribution functions of the relative error (7) for three computed parameters, *K*, *G* and *V*, obtained after four optimisation options, denoted by *x*

To show the main, not always properly recognized, challenge of using UKM to predict the model parameters from the concentration samples, an example is presented in Fig. 3 and Table 6. Note that the observer would rather accept the result of optimisation, while considering the concentration runs, when simultaneously the resulting *K*,*G* and *V* parameters could be dramatically incorrect. Note also that in some cases the Bayesian part of the optimisation criterion (4) may force the process to select parameters resulting in the concentration runs clearly not matching the samples – see Fig.4. Also note, however, that in this example the pure concentration-based procedure leads to absurd values – see Table 7.

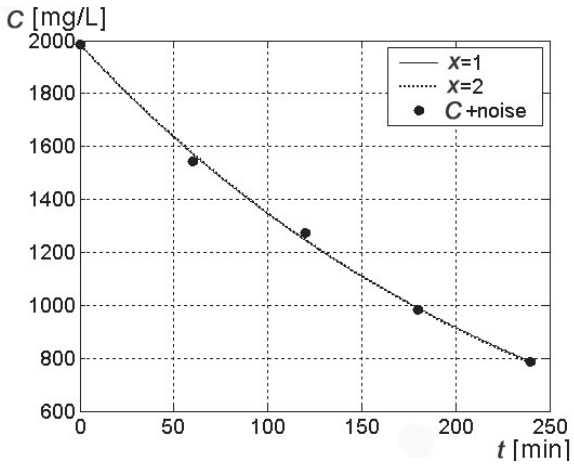

Fig. 3. An example of modelled concentration runs, resulting from two optimisation options – compare Table 6. Note that the runs for *x*=1 and *x*=2 are indistinguishable

Tab. 6. The computed parameters values for the runs depicted in Fig. 3; *x*=0 means the original values

x	0	1	2
K [L/min]	0.188	0.287	0.178
G [mg/min]	7.790	24.658	10.053
V [L]	44.718	67.703	42.359

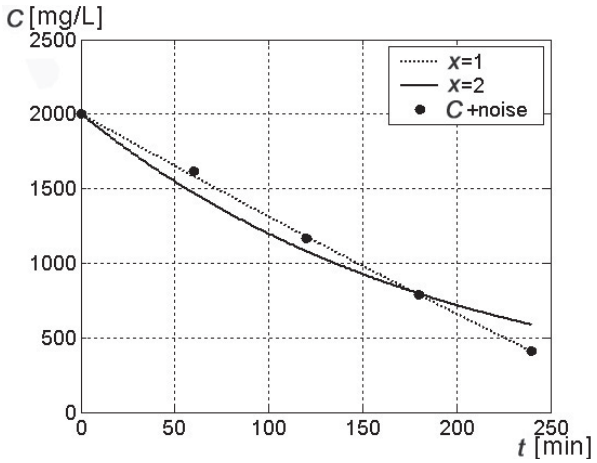

Fig. 4. An example of a relatively rare, but not impossible, case, compare Fig. 3, when the Bayesian part of criterion (4) made the role of concentration values noticeably reduced

Tab. 7. The computed parameters values for the runs depicted in Fig. 4; *x*=0 means the original values

x	0	1	2
K [L/min]	0.1460	0.1114	0.1866
G [mg/min]	6.3516	–1067.4	9.0961
V [L]	26.7821	180.4004	34.3035

Individualized approach

While treating the same patients for longer time, the parameters could be predicted in a more individualized manner. If we could assume that we know the *a priori* distribution functions relying on the previous modelling sessions for each patient, then the relevant experiment should be organized in a somewhat modified manner. In such case the mean values for distribution functions were not common for all sessions – as in the general approach – but the exact value was taken as *a priori* known mean value of the relevant distribution – *K*, *G* and *V*. The standard deviation values remained the same as in

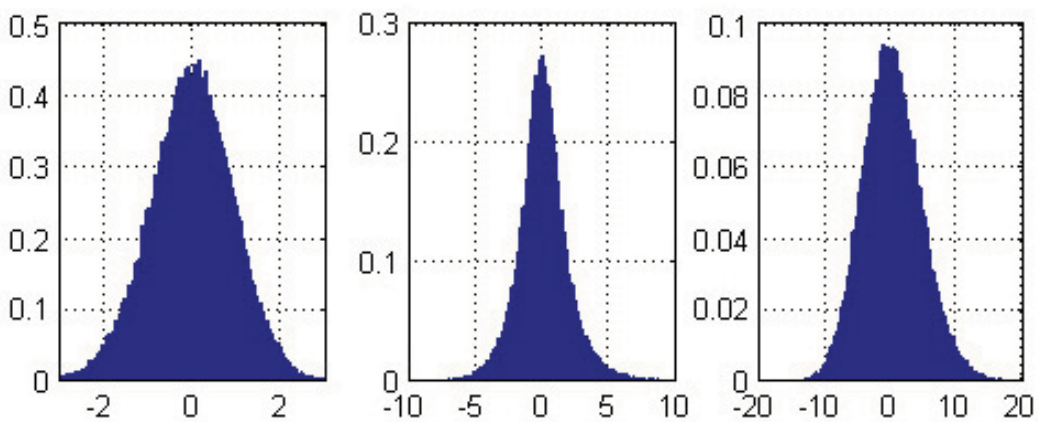

Fig. 5. The normalized histograms showing experimental distribution functions of relative errors (7) in %: (from left to right) *K*, *G* and *V*, when the *a priori* knowledge included the individual values for each simulated case – compare Fig. 2

Table 1. The obtained results for $x = 2$ are shown in Fig. 5 and within Tables 8 and 9. Comparing with the general approach, no improvement was observed in the concentration values, but the accuracy of predicting the *K*, *G* and *V* changed dramatically. Note that if we used the classic approach the results would be the same as in the general approach, so the superiority of the Bayesian solution is obvious, however, only under the condition that the *a priori* distribution functions have been properly assumed.

Tab. 8. Mean (±standard deviation) of the concentration RMSE, for J according to (5) and for I as defined by (6)

x	1	2	3	4
J_x	36.0 (±17.3)	41.4 (±17.5)	43.4 (±16.6)	41.3 (±17.45)
I_x	27.2 (±15.3)	24.0 (±13.9)	26.1 (±15.4)	24.3 (±14.1)

The paired t-test exhibited the same distribution only while comparing between concentration errors for $x = 2$ and $x = 4$, only then the *p-value* was 0.5884. In other comparisons the test indicated different distributions, $p < 0.0001$.

Tab. 9. Mean (±standard deviation) of the relative error (7) expressed in %, for *K*, *G* and *V* after all four types of experiment

x	1	2	3	4
K	–11.7 (±39.4)	–0.0 (±0.9)	–22.5 (±7.8)	–0.1 (±5.4)
G	23.2 (±116.1)	0.1 (±2.1)	–6.0 (±3.0)	0.1 (±2.2)
V	–15.8 (±42.3)	0.2 (±4.4)	–22.3 (±9.1)	–0.1 (±2.7)

The paired t-test exhibited the same distribution only while comparing between *G* for $x = 2$ and $x = 4$, only then the *p-value* was 0.4345. In other comparisons the test indicated different distributions, $p < 0.0001$.

Testing sensitivity to *a priori* knowledge

The high accuracy of the Bayesian approach in the individualized case suggested the third experiment, when for the same original parameters, the assumed mean values of the dsitribution functions would be changed over a larger range of values. The following exact values were taken: $K_0 = 0.18$ L/min; $G_0 = 10$ mg/min; $V_0 = 40$ L. Then the concentration run with noise measurement was implemented. Finally, ten thousand sessions were optimized, according to option $x = 2$, with randomly selected mean distribution values, but the same measurement data in all cases. Fig. 6 presents the distributions of the optimized values. Note that in all cases the original values were the same, only the *a priori* knowledge was changed. The graphs show clearly that for *K* and *G* the computed values tend to follow the mean values. This phenomena is not so strong for *V*, but in this case the accuracy is definitely the poorest.

Concluding comments

The presented study indicates that in spite of rather enthusiastic applications of the Bayesian approach in recent years, the use of it should be accompanied by relevant comparative verification. Otherwise, the obtained results may rather represent *a priori* assumptions than really tuned-in values. On the other hand, the Bayesian solution exhibits features making it definitely superior to the classic optimisation, where the results may be very far from the original values, and if not corrected in any way with use of some reference – like the anthropometric volume based on the body weight – may lead to considerable errors. The observed phenomenon may explain why in [11] the obtained volumes were considerably lower than expected from the anthropometric formulas. Thus, the study also shows that, in spite of being quite commonly used, the whole procedure is very sensitive to inevitable in the practical measurement, even if very small, errors, and, therefore, the *K*, *G* and especially *V* values resulting from it should be taken with great care and, if possible, verified with some other data. Note that when drawing the obtained concentration runs versus the measurement points, even after modelling with very erroneous parameters,

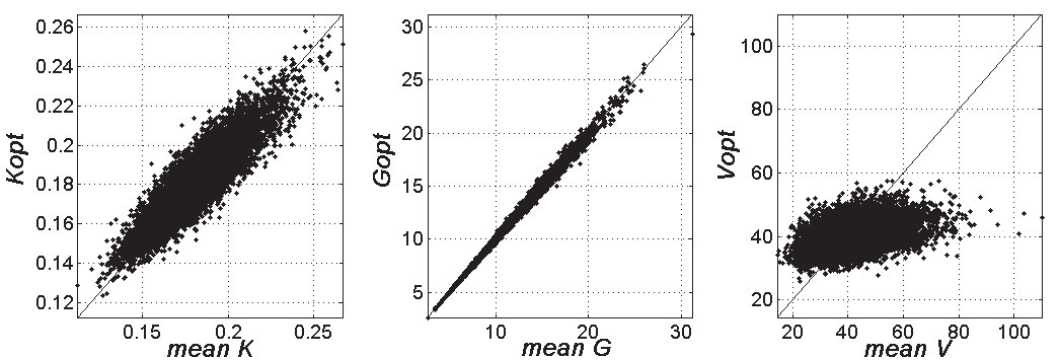

Fig. 6. The dependence of the optimized values on the assumed mean values of the log-Gaussian distribution functions, confirming strong sensitivity to the *a priori* knowledge, mainly for *K* and *G*

the wrong result may be indistinguishable by visual inspection from the good match, which consists a pitfall that may turn out very costly when used in clinical practice.

All presented results were obtained with the use of Matlab software [12].

References

1. Depner T.A. (1997), Prescribing Hemodialysis: A Guide to Urea Modeling. Kluwer Academic Publishers, Boston.
2. Dębowska M., Waniewski J. (2005), Comparison of dialysis adequacy indices calculated according to one and two compartment model. *Bio-Algorithms and Med-Systems* 1(1/2), 205-208.
3. Gotch F.A. (2001), Evolution of the Single-Pool Urea Kinetic Model. *Seminars in Dialysis* 14(4), 252-256.
4. Grandi F., Avanzolini G., Cappello A. (1995), Analytic solution of the variable-volume double-pool urea kinetic model applied to parameter estimation in hemodialyisis. *Computers in Biology and Medicine* 25(6), 505-518.
5. Korohoda P., Pietrzyk J.A., Schneditz D. (2010), Quantifying the discontinuity of haemodialysis dose with time-averaged concentration (TAC) and time-averaged deviation (TAD). *Nephrology Dialysis Transplantation* 25(3), 1011-1012.
6. Marsenic O., Zhang L., Zuppa A., Barrett J.S., Pfister M. (2010), Application of Individualized Bayesian Urea Kinetic Modeling to Pediatric Hemodialysis. *Journal of American Society for Artificial Internal Organs (ASAIO J)* 56(3), 246--53.
7. Pfister M., Uehlinger D.E., Hung A.M., Schaedeli F., Sheiner L.B. (2004), A new Bayesian method to forecast and fine tune individual hemodialysis dose. *Hemodialysis International* 8, 244-256.
8. Puñal Rioboó J., Sánchez-Iriso E., Ruano-Ravina A., Varela Lema M.L., Sánchez-Guisande D., González-Rodriguez L., Herrero J.A., Barril G., Maduell F., Hernández J., Otero A., Bajo M.A., Sánchez R. (2009), Short Daily verus Conventional Hemodialysis Quality of Life: A Cross-Sectional Multicentric Study in Spain. *Blood Purification* 28, 159-164.
9. Racine A., Grieve A.P., Flühler H. (1986), Bayesian Methods in Practice: Experiences in the Pharmaceutical Industry. *Applied Statistics* 35(2), 93-150.
10. Sheiner L.B., Beal S.L. (1982), Bayesian Individualization of Pharmacokinetics: Simple Implementation and Comparison with Non-Bayesian Methods. *Journal of Pharmaceutical Sciences* 71(12), 1344-1348.
11. Ziółko M., Pietrzyk J.A., Grabska-Chrząstowska J. (2000), Accuracy of hemodialysis modeling. *Kidney International* 57, 1152-1163.
12. Matlab: http://www.mathworks.com/.

BIO-ALGORITHMS AND MED-SYSTEMS
JOURNAL EDITED BY MEDICAL COLLEGE – JAGIELLONIAN UNIVERSITY
Vol. 6, No. 12, 2010, pp. 113–121.

MODELS OF ARTIFICIAL ARM ACTUATED BY PNEUMATIC MUSCLES ACTUATORS

Ryszard Dindorf

AGH University of Science and Technology, Krakow, e-mail: dindorf@agh.edu.pl
Kielce University of Technology, Kielce, e-mil: dindorf@tu.kielce.pl

Abstract: The paper deals with biomedical engineering (rehabilitation engineering) connected with the design and modelling of artificial arm (prosthetic arm, exoskeleton arm, bionic arm) actuated by pneumatic artificial muscles (PAMs), known also as pneumatic muscle actuators (PMAs). The kinematic and dynamic models of artificial arm are based on the model of the natural biceps–triceps system. The operation of two pneumatic muscles in bi-muscular driving system (BMDS) can be compared to that of natural agonistic-antagonistic muscles. The static model of PMA is determined on the basis of its physical and geometric properties. A phenomenological biomimetic dynamic model of PMA constructed on the basis of energetic–viscoelastic Hill-type muscle model is proposed. The virtual model and animation of artificial arm were conducted by means of Solid Works software. The presented models of artificial arm are used to design exoskeleton arm of weight and dimensions equivalent to those of human arm.
Keywords: artificial arm**,** artificial muscle system, pneumatic muscle actuators

Streszczenie: Pracy dotyczy zagadnienia inżynierii biomedycznej (rehabilitacyjnej), związanego z projektowaniem i modelowaniem sztucznego ramienia (protezy ramienia, egzoszkieletu ramienia lub ramienia bionicznego) poruszanego sztucznymi mięśniami pneumatycznymi (PAM), nazywanymi także pneumatycznymi aktuatorami mięśniowymi (PMA). Model kinematyczny i dynamiczny sztucznego ramienia bazuje na naturalnym modelu układu biceps-triceps. Praca dwóch muskułów pneumatycznych w układzie BMDS jest porównywalna do naturalnych mięśni agonistycznych-antagonistycznych. Określono model statyczny PMA, bazując na jego fizycznych i geometrycznych właściwościach. Zaproponowano fenomenologiczno biomimetyczny model dynamiczny PMA, który powstał na podstawie energetycznego wiskoelastycznego modelu muskułu typu Hilla. Wykonano wirtualny model i animacje sztucznego ramienia z użyciem programu SolidWorks. Przedstawione modele sztucznego ramienia zostały wykorzystane do projektowaniu egzoszkieletu ramienia o masie i wymiarach ludzkiego ramienia.
Słowa kluczowe: sztuczne ramię, sztuczny układ mięśniowy, pneumatyczne aktuatory mięśniowe

Introduction

Modelling of human motion is used in a wide range of applications, such as assessment of sport performance, diagnosis of pathogenic motion, assessing rehabilitation from traumatic events such as spinal cord injury or stroke, and control of prosthetic devices [1]. Therefore, it is important to achieve an accurate representation of human movement and be able to customize models to account for individual differences. Such modelling is often performed using biomechanical methods, where information on joint position is obtained using kinematic methods. Isometric muscle contractions, which are performed at a constant joint angle, have often been used for the development of biomechanical models, because joint position remains fixed, and the interaction between muscle activity and resulting force output can be observed more easily. Assessment of dynamic motion, such as in gait analysis, introduces more variables and thus may be more difficult to accurately determine model. Models to estimate joint torque can be developed using non-linear identification methods, such as dynamic models, biomimetic models and other methods. Building upon the classic work of A.V. Hill, Hill-based models reflect the neuromuscular behaviour of individual muscles and are commonly used for skeletal muscle modelling. The challenge is to separate the calculated net moment into individual muscle forces for each muscle acting on the elbow. Muscle force can be described as the result of "activation dynamics" and "contraction dynamics" as illustrated in Fig. 1. "Activation dynamics" refers to the activation of the contractile components of muscle tissue in response to neural signals from the Central Nervous System (CNS). "Contraction dynamics" describes the process of force generation in the contractile component of the muscle. Numerous models are used to estimate the force produced in muscles, including the Hill-muscle model.

A key parameter for upper arm muscles that has not been widely reported in the literature is the optimal joint angle asso-

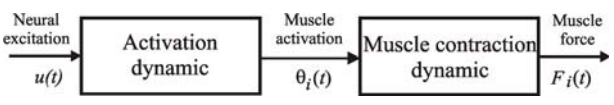

Fig. 1. Block diagram of process of muscle activation and contraction [9]

ciated with optimal muscle length. Many researchers provide muscle optimal length measurements from cadaver studies or estimates from biomechanical models. Some presented researchers have provided relationships between muscle length and joint angle, but only three studies were found that provided estimates of both the optimal muscle length and joint angle for the same subjects. Table 1 contains a summary of average joint angle values for upper arm muscles presented in the literature.

Tab. 1. Average joint angle for elbow muscles [9]

Muscle	Join angle (deg)
Biceps	67.4
Brachioradialis	59.7
Triceps	88.2

Flexion and extension of the elbow results from muscles acting across the elbow joint. These are classified into two categories: flexors (i.e. biceps brachii, brachioradialis and brachialis) which generate a moment about the elbow, causing the arm to bend, and extensors (i.e. triceps brachii and anconeous) which generate a moment in the opposite direction, causing the arm to straighten. Elbow joint motion is a result of the contraction of multiple muscles working together to create smooth and controlled joint rotation. The moment generated by each muscle is a function of the force produced by each muscle, and the moment arm of the muscle, which is defined as the minimum distance perpendicular to the line-of-action of the muscle, and the centre of the elbow joint. The net moment T in the elbow can be calculated as the sum of individual moments generated by each muscle, that is

$$T_{elbow} = \sum_{i=1}^{n} F_i L_i \quad (1)$$

where i represents an individual muscle, n is the number of muscles considered to be acting on the joint, F_i is the force generated by muscle i, and L_i is the length of muscle i.

The force at the wrist induced by a moment in the elbow can be measured using a force transducer positioned at the wrist, with the shoulder and wrist held in a fixed position. It is then possible to quantitatively determine the net moment T_{elbow} in the elbow from the force F_{wrist} measured at the wrist and using the length of the forearm $L_{forearm}$ as the moment arm as follows:

$$T_{elbow} = F_{wrist} L_{forearm} \quad (2)$$

The universally known lever principle as illustrated in Fig. 2 applies

$$T_{elbow} = T_{biceps} \quad (3)$$

$$F_w \sin \beta_w L_f = F_b \sin \beta_b L_b \quad (4)$$

Elbow joint angle is defined as external elbow angle θ, where zero degrees occurs when the arm is at full extension.

The classic A.V. Hill paper described muscle heat (energetic) measurements that were the basis of a model for the mechanical behavior of skeletal muscle [6]. The experimental

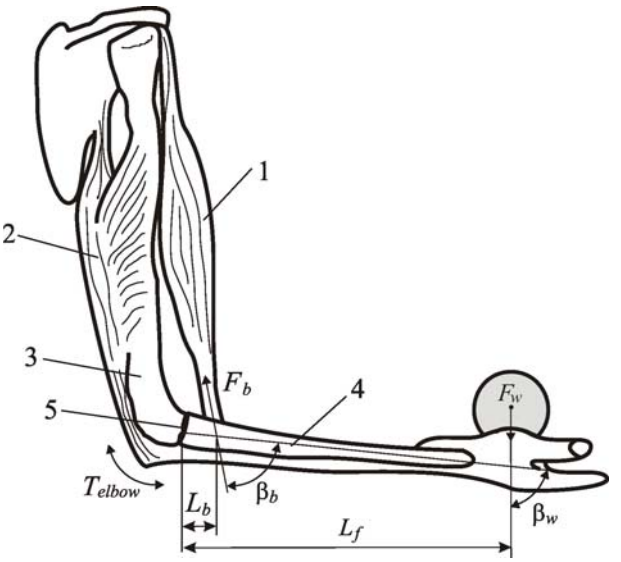

Fig. 2. Muscle configuration in the human arm: 1 – bicep, 2 – tricep, 3 – humerus 4 – ulna, 5 – elbow joint

technique itself involved muscle contractions experiencing external length changes (shortening) under a constant load (an isotonic type of muscle contraction). Hill's observations on heat liberation (energetics) can be directly converted into an equation on muscle mechanics [6]:

$$(F+a)(v+b)=b(F_0+a) \quad (5)$$

The mechanical variables are the muscle load force *F* and its velocity-of-shortening v. F_0 is an active state force, while *a* and *b* are coefficients used to obtain Eq.(5). The basic model that is described by Eq.(5) is known as the two-element model and is applicable to isotonic-type contractions.

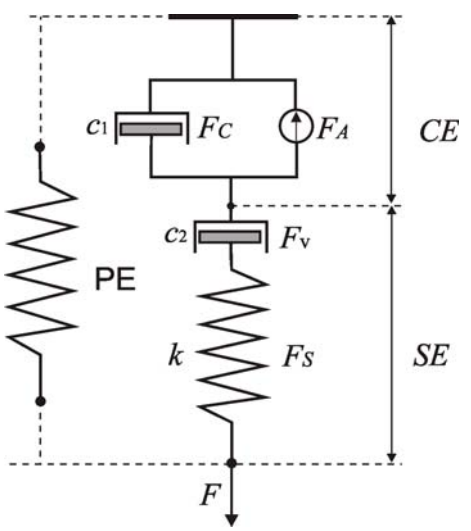

Fig. 3. Energetic-viscoelastic model [9]: F_S elastic force stored in the spring, F_v viscous force absorbed by the "passive" dashpot (c_2) of the series element *SE*, F_A active force generator, and F_C is the viscous force absorbed by the "active" dashpot (c_1) of the contractile element *CE*, *PE* parallel elastic element, which may be added to model the passive elastic properties of unstimulated muscle

Mathematical development of the energetic–viscoelastic muscle model is guided by the "law of parsimony" [13]. The most parsimonious skeletal muscle model describing the energetics and mechanics of isometric force twitch dynamics would be a first order linear ordinary differential equation with constant coefficients. The energetic–viscoelastic model (Fig. 3) introduces two additional elements into the Hill's model.

Pneumatic muscle actuator (PMA)

Pneumatic muscle is a relatively new actuator. It may be characterized as an elastic, single-acting, cylinder pulling the load in the axial direction. The structure of the muscle is based upon a special tube ending with two connectors. The action of the pneumatic muscle is often compared to that of the natural one and therefore, the pneumatic muscle finds application in mobile, anthropomorphic and humanoid robots, as well artificial arms, hand and limbs. The pulling force generated by pneumatic muscles is big in relation to their mass and cross-section. They perform smooth movements, do not show the effects of stroke movement, get deformed radially, are free of slip-stick and have natural properties of movement suppression. Artificial pneumatic muscle is constructed of a radially deformable pipe made of rubber, latex or silicone, braided with elastic radially tensile net. The net fixed to the muscle ends functions as a kind of artificial tendons. The muscle filled with compressed air deforms radially (expands) and gets shorter. The strains occurring in the muscle depend upon outer axial load. The force generated by pneumatic muscle is a function of pressure, initial length, contraction degree and its material properties. Initially big force decreases to zero after the critical contraction degree has been reached. Pressure control enables to change the degree of muscle's contraction and the value of pulling force. The pulling force of the pneumatic muscle in reference to its cross-section amounts to about 300 N/cm^2. It is much greater than the force of biological muscle which oscillates from 20 to 40 N/cm^2 [8]. The pneumatic muscle as a pneumatic actuator may be described as: light weight, lower cost, smooth, flexible, powerful, damped, compliant.

Table 2 shows the performance of biological muscle and this is compared with the pneumatic muscle actuator (PMA). From this table it can be seen that although the underlying mechanisms of operation are very different, the PMA can in most instances equal the natural behaviours of muscle while possessing excellent 'engineering' power, endurance and robustness. A particularly interesting feature of both the natural and artificial muscles is their ability to operate in antagonistic modes and thereby possess an inherent capacity to modulate compliance/impedance. This permits safer user interaction, more natural motion and control, and improved energy conservation through the spring elements of the actuators. Having noted that PMA has the potential to produce a biologically inspired actuator combining many, if not all, the best features of natural and technological science, the next stage was to incorporate these actuators into medical systems such as prosthetic limbs and aids for the disabled.

Tab. 2. Comparison of PMA and biological muscle [l2]

Parameter	Biological muscle	PMA
Displacement	35%	35%
Force/cm^2	20–40 N	100–500 N
Power/weight	40–250 W/kg	2 kW/kg
Efficiency	45–70%	32–50%
Rate of contraction	25–2000%/s	35–700%/s
Bandwidth		5Hz
Control	good	fair good
Temperature range	0–40◦C	−30–+80◦C
Robustness	excellent	fair good
Self repair-regeneration	yes	no
Antagonistic operation	yes	yes
Compliance control	yes	yes
Impedance control	yes	yes
Energy source	chemical	pneumatic
Environmental safe	ouputs CO_2	yes
Scalable from	μm–m	cm–m
Linear operation	yes	yes

The performance specification for the joints of the human arm are shown in Table 3, together with the achieved joint torque and range of motion for the PMA driven artificial arm.

Tab. 3. Performance of PMA in powered assist device [10]

Joint		**Human isometric strength**	**Artificial arm joint torque**
Shoulder	Flexion/extension	110 Nm	30 Nm
	Adduction/abduction	125 Nm	27 Nm
	Rotation	–	6 Nm
Elbow	Flexion/extension	72.5 Nm	6 Nm
	Supination/pronation	9.1 Nm	5 Nm
Wrist	Flexion/extension	19.8 Nm	4 Nm
	Adduction/abduction	20.8 Nm	4 Nm

PMAs reflect biological muscles with their high power to weight ratio, high power to volume ratio, and contraction mechanism. Biological muscle exhibits good position and force control. However, pneumatic muscle has shown slow advancements with control due to nonlinearities. Another limitation of PMAs includes a small contraction percentage of approximately 20%. However, this is comparable to skeletal muscles contraction ability. The PMA is not ideal for high precision task. Two distinct modeling approaches have been explored in order to characterize the PMA. They include a physical geometric model and biomimatic model.

Static model of PMA

The physical geometric model research strictly analyzes PMA behavior in a quasi-static state and incorporated no hysteresis (time) information [2]. The physical geometric models are not beneficial for real time control application, because the geometric structure is difficult to obtain during experiment. Bladder material properties were inserted into the physical geometric model. Around the rubber tubing of PMA there is a flexible sheathing formed from high strength interwoven (not bonded) nylon fibers. The braided structure of the external nylon shell implies that the muscle may be considered as a series of 2D (two dimensional) trapezoids. In design, as the actuator stretches or compresses, the interweave angle changes and the whole surface area of the muscle varies. Static physical geometric PMA model is presented in Fig. 4.

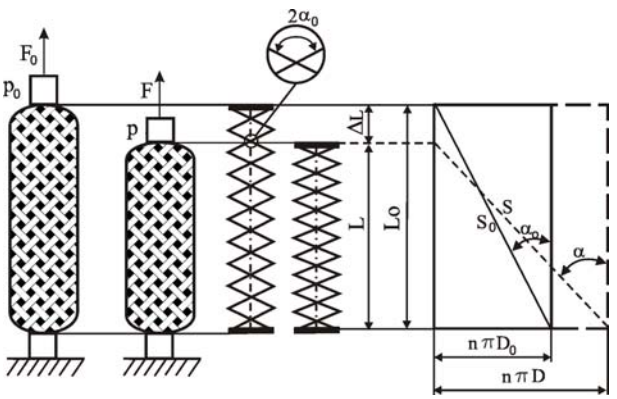

Fig. 4. Static physical geometric model of PMA

A PMA simplified static model is presented on the basis of geometrical relations of muscle's weave grid (Fig. 3):

$$\begin{cases} (n\pi D)^2 + L^2 = S^2 \\ L = S\cos\alpha \\ D = S\sin\alpha\,(n\pi) \end{cases} \quad (6)$$

$$\begin{cases} (n\pi D_0)^2 + L_0^2 = S_0^2 \\ L_0 = S_0\cos\alpha_0 \\ D_0 = S_0\sin\alpha_0\,(n\pi) \end{cases} \quad (7)$$

where: L, L_0 – length, D, D_0 – internal diameter, S, S_0 – thread length, α, α_0 – interweave angle, n – numbers of turns of thread of PMA.

From geometric relations (6) the formulas showing muscle volume V in relation to length L and angle α are obtained:

$$V(L) = \frac{\pi D^2}{4} L = \frac{L\left(S^2 - L^2\right)}{4\pi n^2} \quad (8)$$

$$V(\alpha) = \frac{S^3}{4n\pi} \sin^2\alpha \cos\alpha \quad (9)$$

From the energetic analysis of the pneumatic muscle the equation of work is obtained:

$$dW_{out} = dW_{in} \quad (10)$$

where: W_{out} – output work,

$$dW_{out} = -F\ dL \quad (11)$$

where: F – tensile force, dL – contraction,
dW_{in} – input work,

$$dW_{in} = p\ dV \quad (12)$$

where: p – pressure setting, dV – volume change.

After substituting relations (12) and (11) into Eg.(10) the following relation is obtained:

$$F = -p\frac{dV}{dL} = -p\frac{dV}{d\theta}\frac{d\theta}{dL} \quad (13)$$

Formula $dV/d\alpha$ is calculated from (9):

$$\frac{dV}{d\alpha} = \frac{S^3}{4\pi n^2}\left(2\sin\alpha\ \cos^2\alpha - \sin^3\alpha\right) \quad (14)$$

Formula $dL/d\alpha$ is calculated from (6):

$$\frac{dL}{d\alpha} = -S\sin\alpha \quad (15)$$

After substituting the derivatives $dV/d\alpha$ and $dL/d\alpha$ into (13) the equation for force F as a function of pressure p and angle α is written:

$$F = p\frac{\pi D^2}{4}\left(\frac{3\cos^2\alpha - 1}{1 - \cos^2\alpha}\right) \quad (16)$$

After substituting D and L from (6) into (16) the equation of force F as a function of pressure p and length L is obtained:

$$F = = \frac{p}{4\pi n^2}\left(3L^2 - S^2\right) \quad (17)$$

In the static analysis the contraction rate h of PMA is used:

$$h = \frac{\Delta L}{L_0} = \frac{L_0 - L}{L_0} \quad (18)$$

After introducing (18) into (17) the contraction force F as a function of pressure p and contraction rate h is calculated:

$$F = \frac{1}{4\pi n^2}\left[3L_0^2\left(1-h\right)^2 - S^2\right]p \quad (19)$$

Finally, formula for PMA's contraction force F in the range $0 \le h \le h_{\max}$ is presented in form:

$$F = A\ p\ \left[a_0\left(1-h\right)^2 - b_0 k_S^2\right] \quad (20)$$

where: $a_0 = \frac{3}{\tan^2\alpha_0}$, $b_0 = \frac{1}{\sin^2\alpha_0}$,

$$A = \frac{\pi}{4}D_0^2\ ,\ k_S = \frac{S(p)}{S_0}$$

The difference between experimental force and theoretical force for similar pressure is correlated with the coefficient k [11]:

$$F = A\ p\ \left[a_0\left(1-h\ k\right)^2 - b_0\ k_S^2\right] \tag{21}$$

To achieve the same approximation for smaller pressure, another correction function $\mu(k)$ and contraction $h(p)$ is added [12]:

$$F = \kappa(k)\ A\ p\ \left[a_0\left[1-h(p)\ k\right]^2 - b_0\ k_S^2\right] \tag{22}$$

To achieve the best approximation of the real muscle curve, the following correction functions are used:

$$\kappa(k) = a_k\ e^{-k\cdot p} - b_k \tag{23}$$

$$h(p) = a_h\ e^{-p} - b_h \tag{24}$$

where the coefficient a_h, b_h, a_k and b_k were determined using least squares method.

The extended static model PMA should take into account the real material properties of rubber bladder and braided shell including: bladder thickness, bladder thickness variation, nolinear elastic energy storage of the bladder, friction – inducted hysteresis.

Biomimetic model of PMA

Biological muscle is based on three components: pure force generator, elastic component and damping component. The biomimetic approach models the PMA by revising the Hill muscle model to include energetic and viscoelastic parameters. The energetic parameter refers to the chemo-mechanical energy conversion and viscoelastic refers to the internal-element stiffness variation. The research models the excitation and contraction of isometric skeletal muscle. The biomimetic model is a biophysical, biochemical, and biomechanical model of the contractions-excitations coupling during skeletal muscle isometric contraction. Both biological muscle and PMA generate force only by means of contraction. As pressure builds in up the PMA, it expands radially causing a force contraction in the axial direction mimicking biological muscle. From the biomimetic principle discussed above, a phenomenological biomimetic (biomechanical) model is proposed by Reynolds et al. [11]. Similarly to biological muscle, PMA experiences viscoelastic resistance as it expands which can be modeled as a dashpot and spring respectively. It combines the dashpot and spring in parallel with a damping element B and spring element K respectively. Using biomimetic principles, energetic-viscoelastic model (Fig. 2) can be applied to the PMA. However, the PMA model requires an additional element to describe the internal force. The contractile force element F_{CE}, explains the internal active contraction force source of the PMA. The contraction force F_{CE} opposes the action of the dashpot and spring. The configuration of elements in biomimatic model of PMA is presented in Fig. 5.

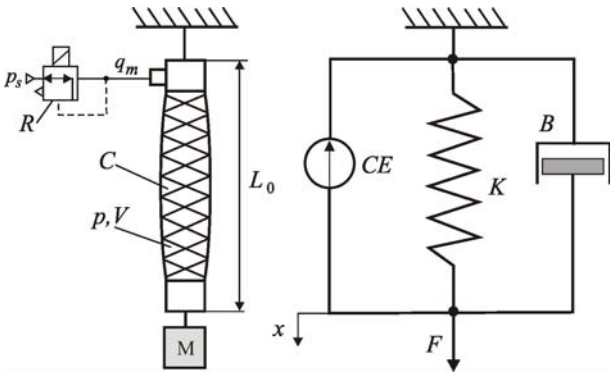

Fig. 5. Biomimetic model of PMA

The research focuses on characterizing the phenomenological biomimatic model of PMA with respect to dynamic motion [7]. The following equation is formulated to explain the dynamic motion of the vertical test system (Fig.5):

$$M\ \ddot{x} = -B\ \dot{x} - K\ x + F_{CE} - F \tag{25}$$

where: x – contraction of PMA, M – mass load, B – damping (dashpot) element coefficients, K – spring element coefficients, F – external force, $F = M{\cdot}g$; F_{CE} – effective muscle force provided by the contractile element CE.

To the equation (25) force F_{CE} of PMA obtained from Eg.(20) is introduced in the form:

$$\begin{aligned} F_{CE} &= A\ p\ \left[a_0\left(1-h\ \right)^2 - b_0\ \right] = \\ &= -\left(2\ h - h^2\right) A\ p + A\ p\ \left(a_0 - b_0\right) \end{aligned} \tag{26}$$

Finalny, Eg.(25) can be written in the form:

$$M\ \ddot{h} + B\ \dot{h} + -\left(2\ h - h^2\right) A\ p + M\cdot g = A\ p\ \left(a_0 - b_0\right) \tag{27}$$

Mass flow q_m through pressure control valve:

$$q_m = \frac{1}{R}\left(p_s - p\right) \tag{28}$$

where: p_s – supply pressure, R – valve resistance.

The equation dp/dt based on the first principle of thermodynamics after introducing V from formula (8), its derivative $\dot{V}$ and mass flow from (28), assumes the form:

$$\begin{aligned} \dot{p} &= \frac{\kappa}{V}\left[R\ T\ q_m - p\ \dot{V}\right] = \\ &= \frac{1}{R\ C}\left(p_s - p\right) - \kappa\ \frac{\left(S^2 - 3\ L^2\right)}{L\left(S^2 - L^2\right)}\ p\ \dot{L} \end{aligned} \tag{29}$$

where: C – capacitance of PMA;

$$C = \frac{V(L)}{\kappa\ \mathrm{R}\ T} \tag{30}$$

where: V– volume of the PMA tube, κ – adiabatic exponent, R – gas constant, T – temperature.

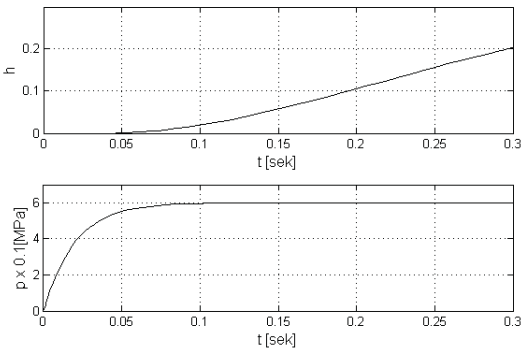

Fig. 6. Dynamic characteristic of PMA

The equation (29) in the first approximation is presented as low pass filter with the one parameter cut-off frequency $\omega = 1/R\,C$:

$$\dot{p} = \omega \left(p_s - p\right) \tag{31}$$

Dynamic characteristic of PMA on the basis of the biomimetic model (27) and (31) is presented in Fig. 6.

Model of artificial arm

Based on the model of the natural biceps–triceps system [5], two artificial muscles can be set into antagonism for defining an elbow joint according to the basic scheme of Fig. 7. The working principle of the pneumatic muscle actuator is as follows. The two identical muscles are initially contracted of a ratio $h_0 = h_{max}/2$ under a pressure of $p_0 = p_{max}/2$, where p_{max} is generally chosen equal to 0.6 or 0.8 MPa. The muscles are activated so one (flexor) of them is inflated to $p_1 = p_0 + \Delta p$ and

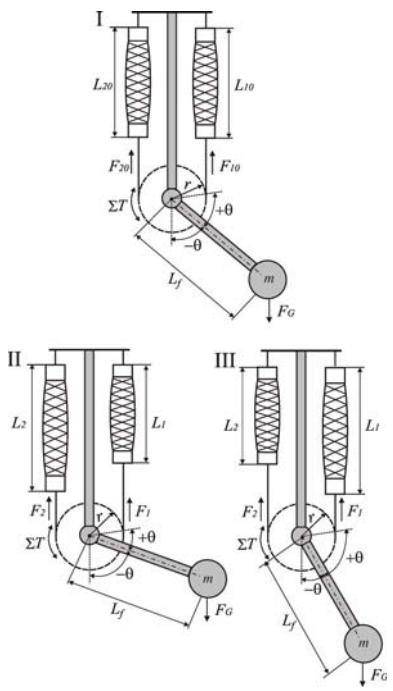

Fig. 7. Model of elbow joint: I – initial position forearm, II – forearm flexing, III– forearm extending

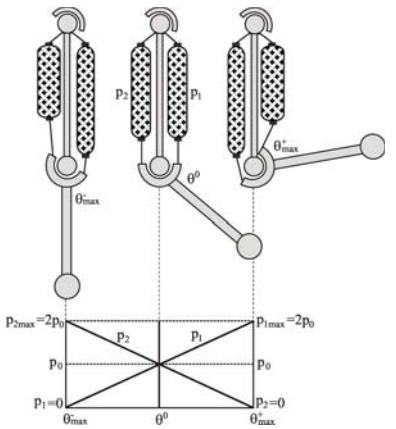

Fig. 8. Vertical forearm positions

the other one (extensor) is deflated to $p_2 = p_0 - \Delta p$. Thus, Δp is not the difference between the two muscles, but the distance to the initial pressure p_0. This kind of symmetric muscle activation has proved to be qualified in the past and will be used in the experiments. The advantage of this procedure is that while one muscle shortens, the second is extended by approximately the same length. This guarantees a high stiffness for the entire workspace of the joint.

The changes of elbow angle θ and the pressures p_1 in flexor and p_2 in extensor in relation to vertical positions of the forearm (bent and straight) are presented in Fig. 8.

I. Initial forearm position θ^0

$$L_{10} = L_{20},\ F_{10} = F_{20},$$

$$h_0 = h_{10} = h_{20},\ h_{10} = \frac{L_0 - L_{10}}{L_0},\ h_{20} = \frac{L_0 - L_{20}}{L_0},$$

$$p_1 = p_0,\ p_2 = p_0,\ \Delta p = 0.$$

II. Flexing the forearm θ^+

$$L_1 < L_{10} \quad L_2 > L_{20},$$

$$\Delta h_1 = h_1 - h_{10} = \frac{r\,\theta}{L_0},\ \Delta h_2 = h_2 - h_{10} = -\frac{r\,\theta}{L_0}$$

Force generated by the flexor

$$\Delta F_1(\theta, p_1) = A\ p_1 \left[a_0 \left(1 - \Delta h_1\right)^2 - b_0\right] = \tag{32}$$

$$= A\ p_1 \left[a_0 \left(1 - \frac{r\,\theta}{L_0}\right)^2 - b_0\right]$$

Force generated by the extensor

$$\Delta F_2(\theta, p_2) = A\ p_2 \left[a_0 \left(1 - \Delta h_2\right)^2 - b_0\right] = \tag{33}$$

$$= A\ p_2 \left[a_0 \left(1 + \frac{r\,\theta}{L_0}\right)^2 - b_0\right]$$

Torque for elbow joint angle θ^+ while flexing forearm:

$$T_{\theta^+} = r\left(\Delta F_1 - \Delta F_2\right) = \tag{34}$$

$$= K_{\alpha 2}\left(p_1 - p_2\right) \cdot \left(\theta^+\right)^2 - K_\alpha \left(p_1 + p_2\right)\theta^+ + K_p \left(p_1 - p_2\right)$$

where:

$$K_{\alpha 2} = A\frac{a_0 r^3}{L_0^2},\ K_\alpha = A\frac{2a_0 r^2}{L_0},\ K_p = A r (a_0 - b_0)$$

Assuming that: $p_1 = p_0 + \Delta p,\ p_2 = p_0 - \Delta p,$

we obtain the relation:

$$p_2 = 2\Delta p,\ p_1 + p_2 = 2 p_0$$

and after introducing it to the momentum equation we get:

$$T_{\theta^+} = 2 K_{\alpha 2} \Delta p (\theta^+)^2 - 2 K_\alpha p_0 \theta^+ + 2 K_p \Delta p \quad (35)$$

For the bent forearm:

$$p_2 = 0,\ p_{1\max} = 2\Delta p = 2 p_0,$$
$$\Delta p = p_0,\ \theta = \theta^+_{\max}.$$

maximum moment carries out:

$$T_{\theta^+_{\max}} = 2 K_{\alpha 2} p_0 (\theta^+_{\max})^2 - 2 K_\alpha p_0 \theta^+_{\max} + 2 K_p p_0 \quad (36)$$

III. Extending the forearm θ^-

$$L_1 > L_{10} \quad L_2 < L_{20}$$

$$\Delta h_1 = h_1 - h_{10} = -\frac{r\alpha}{L_0};\ \Delta h_2 = h_2 - h_{10} = \frac{r\alpha}{L_0}$$

Force generated by the flexor

$$\Delta F_1(\theta, p_1) = A\ p_1 \left[a_0 \left(1 + \frac{r\theta}{L_0} \right)^2 - b_0 \right] \quad (37)$$

Force generated by the extensor

$$\Delta F_2(\theta, p_2) = A\ p_2 \left[a_0 \left(1 - \frac{r\theta}{L_0} \right)^2 - b_0 \right] \quad (38)$$

Torque in elbow joint angle θ^- while straightening forearm:

$$T_{\theta^-} = r(\Delta F_2 - \Delta F_1) = \quad (39)$$
$$= K_{\alpha 2}(p_2 - p_1)(\theta^-)^2 - K_\alpha (p_1 + p_2)\theta^- + K_p (p_2 - p_1)$$

Assuming that: $p_1 = p_0 - \Delta p,\ p_2 = p_0 + \Delta p,$

we obtain the relations:

$$p_1 + p_2 = 2 p_0,\ p_2 - p_1 = 2\Delta p,$$

and after introducing them to the momentum equation we get:

$$T_{\theta^-} = 2 K_{\alpha 2} \Delta p (\theta^-)^2 - 2 K_\alpha p_0 \theta^- + 2 K_p \Delta p \quad (40)$$

For the straight forearm:

$$p_1 = 0,\ p_{2\max} = 2\Delta p = 2 p_0,$$
$$\Delta p = p_0,\ \theta = \theta^-_{\max}$$

maximum moment carries out:

$$T_{\theta^-_{\max}} = 2 K_{\alpha 2} p_0 (\theta^-_{\max})^2 - 2 K_\alpha p_0 \theta^-_{\max} + 2 K_p p_0 \quad (41)$$

In order to verify the design methodologies for actuation of artificial arm, a simple one DoF (Degree of Freedom) is considered as:

$$I\ddot{\theta} + B\dot{\theta} + F_G L_f \sin(\theta_{\max} \pm \theta) = T_\theta \quad (42)$$

where: I – torque of inertia, $I = m L_f^2$,
m – load mass, B – viscous friction coefficient, L_f – length of forearm, F_G – weight, $F_G = m \cdot g$, p_0 – initial pressure.

To the simulation model (42) of artificial arm was introducted: m = 0.35 kg, B = 5 Nms, L_f = 0.50 m, p_0 = 0.4 MPa; L_0 = 0.35, D_0 = 0.01, r = 0.15 m, a_0 = 22.64, b_0 = 8.54.

The simulation results obtained by means of model (41) are presented in Fig. 9, 10 and 11.

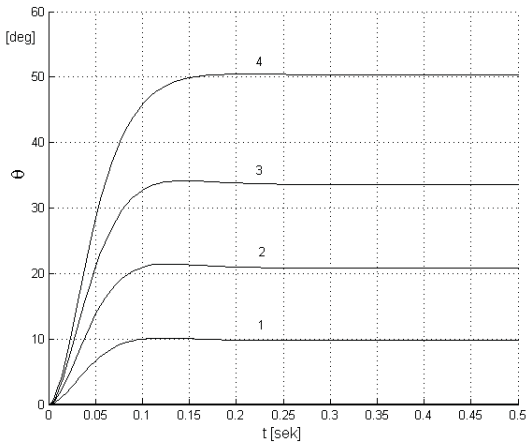

Fig. 9. Dynamic characteristics of elbow flexion angle $\theta(t)$ for actuation pressure Δp: 1 – 0,1 MPa, 2 – 0.2 MPa, 3 – 0.3 MPa, 4 – 0.4 MPa

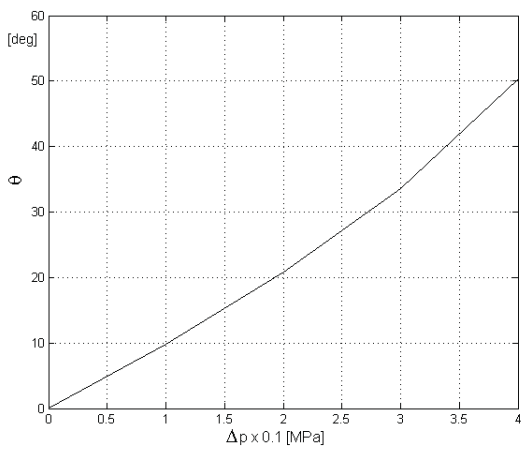

Fig. 10. Elbow flexion angle θ in relation to the actuation pressure Δp, $\theta = f(\Delta p)$

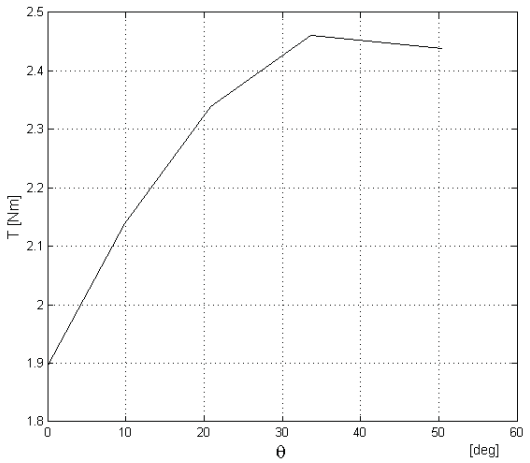

Fig. 11. Elbow flexion torque T in relation to the elbow flexion angle θ, $T = f(\theta)$

Virtual model of artificial arm

To construct virtual model of artificial arm, a physical geometric model and biomimatic model of PMA, described in preceding chapters, were used. The kinematic and virtual model of artificial arm is presented in Fig. 12.

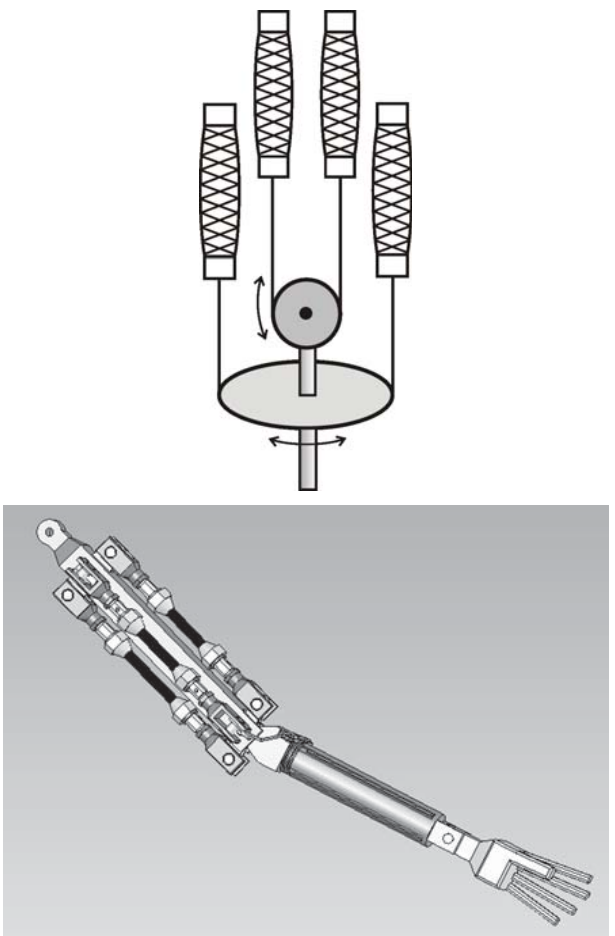

Fig. 12. Kinematic and virtual model of artificial arm [4]

The solid 3D CAD model and artificial arm animations were conducted by means of SolidWorks software. The virtual model of artificial arm consists of arm and forearm joined at the elbow joint. Since the accurate reconstruction of biological forearm movement is too difficult due to complex muscular system, the movement of artificial arm is simplified. Consequently, the forearm performs bending, straightening and rotary movements in elbow joint. To start the virtual model of artificial arm, an acutating system consisting of two pairs of pneumatic muscle actuators (PMA) constituting bi-muscular driving system (BMDS), comparable to the operation of natural antagonistic muscles, was proposed. [3]. The animation of virtual artificial arm, with the contraction and relaxation of pneumatic muscles exposed, clearly shows the operational principle of the designed artificial arm. After constructing the physical model of artificial arm, the research will be conducted with the use of intelligent control system – FLC (Fuzzy Logic Control), ANN (Artificial Neutral Network).

Summary

The paper deals with biomedical engineering (rehabilitation engineering) connected with the design and modelling of artificial arm (prosthetic arm, exoskeleton arm, bionic arm) actuated by pneumatic artificial muscles (PAMs), known also as pneumatic muscle actuators (PMAs). The qualities of pneumatic muscles (PMs) are compared with those of natural skeletal muscles. PMAs enable to decrease the mass and dimensions of prostheses and orthotics devices and exoskeletons, as well as minimize energy necessary for their actuation and controlling. PMA is constructed of a radially deformable pipe made of rubber, latex or silicone, braided with elastic radially tensile net. The net fixed to the muscle ends functions as a kind of artificial tendon. The static model of PMA is determined on the basis of its physical and geometric properties. From the static physical geometric model, the nonlinear force of PMA in the function of contraction rate and pressure is calculated. The inflating and deflating of PMA is controlled by electro-pneumatic pressure valves. A phenomenological biomimetic dynamic model of PMA constructed on the basis of energetic–viscoelastic Hill-type muscle model is proposed. This model consists of a spring, damping and contractile element arranged in parallel. To the biomimetic model of pneumatic muscle the mass force was added as external force. The mass flow rate equations through pneumatic coupling and dynamic pressure equation were introduced to the dynamic model of PMA. Static and dynamic models of PMA were applied in biologically inspired modelling of artificial arm. The kinematic and dynamic models of artificial arm are based on the model of the natural biceps–triceps system. In the artificial arm model two antagonistic pneumatic muscles are used. The model of artificial arm is actuated by simultaneous inflating (contraction) of one muscle and deflating (relaxation) the other one. Forearm flex angle in elbow joint depends upon contraction rate and relaxation rate of antagonistic pneumatic muscles. The forearm is being bent when muscle flexor (biceps) is inflating, and extensor muscle (triceps) is deflating. The forearm is being straightened when muscle flexor (biceps) is deflating, and extensor muscle (triceps) is inflating. Thanks to air pressure control inside the pneumatic muscle, the artificial arm movement with satisfactory precision is pos-

sible. The virtual model and animation of artificial arm were conducted by means of Solid Works software. The simplified model of artificial arm with a forearm in elbow joint flexing-extending and supination-pronation was analyzed. In the animation the system of two pairs of pneumatic muscle actuators (PMA) was used. The operation of two pneumatic muscles in bi-muscular driving system (BMDS) can be compared to that of natural agonistic-antagonistic muscles. The presented models of artificial arm (kinematic, static, dynamic and virtual) are used to design exoskeleton arm of weight and dimensions equivalent to those of human arm and can further the development of biomimetic models.

References

1. Caldwell D.G., Tsagarakis N. (2002), Biomimetic actuators in prosthetic and rehabilitation applications. *Technology and Health Care* 10.
2. Dindorf R. (2003), Static and dynamic models of pneumatic muscle actuator. Proc. The 18th International Conference on Hydraulics and Pneumatics, Prague, September 30 – October 1, 2003.
3. Dindorf R. (2010), Systemy biomechatroniczne. *Hydraulika i pneumatyka* 3.
4. Dindorf R. (2007), Wirtualny model ramienia bionicznego z pneumatycznymi aktuatorami mięśniowymi. *Pneumatyka* 1.
5. Dindorf R. (2005), Modelowanie sztucznych układów mięśniowych z aktuatorami pneumatycznymi. *Bio-Algorithms and Med-Systems* 1/2.
6. Hill A.V. (1938), The Heat of Shortening and the Dynamic Constants of Muscle. *Proc. R. Soc. London* B, 126.
7. Gerschutz M.J. (2008), Dynamic pneumatic muscle actuator control system for an augmented orthosis. Wright State University.
8. Klute G.K., Czerniecki J.M., Hannaford B. (2002), Artificial muscles: actuators for biorobotic systems. *International Journal of Robotics Research* 4.
9. Mountjoy K. (2008), Use of a Hill-based Muscle Model in the Fast Orthogonal Search Method to Estimate Wrist Force and Upper Arm Physiological Parameters. Master Thesis. Queen's University Kingston, Ontario, Canada.
10. Phillips C.A., Repperger D.W., Neidhard-Doll A.T., Reynolds D.B. (2005), Biomimetic model of skeletal muscle isometric contraction: I. An energetic-viscoelastic model for the skeletal muscle isometric force twitch. University of Nebraska, Lincoln. *Research* 24/4.
11. Reynolds D.B., Repperger D.W., Phillips C.A., Bandry G. (2003), Modeling the dynamic characteristics of pneumatic muscle. *Annals of Biomedical Engineering* 31.
12. Smagt P., Groen F., Schulten K. (1996), Analysis and Control of a Rubbertuator arm. *Biol. Cybernetics* 75.
13. Shin D., Khatib O., Cutkosky M. (2009), Design Methodologies of the Hybrid Actuation Approach for Human-friendly Robot. Proc. 2009 IEEE international conference on Robotics and Automation, Kobe, Japan, May 12-17, 2009.

BIO-ALGORITHMS AND MED-SYSTEMS
JOURNAL EDITED BY MEDICAL COLLEGE – JAGIELLONIAN UNIVERSITY
Vol. 6, No. 12, 2010, pp. 123–130.

MODELLING OF DELAY IN GLUCOSE-INSULIN DYNAMICS

JERZY BARANOWSKI

Akademia Górniczo-Hutnicza, Katedra Automatyki, Kraków

Abstract: In this paper a model of glucose-insulin dynamics is analysed. Since the model is in the form of a delay differential equation, a finite dimensional approximation is desirable. Two methods of such approximation are discussed. The first method is based on a discretisation and the second is based on Galerkin projections. Both methods are thoroughly described. A comparison of methods is executed for wide range of approximation orders and illustrated with graphs.

Introduction

Ultradian oscillations, with a period of about 100-200 minutes, are an interesting phenomenon occurring in human's insulin secretion. It was observed by Hansen in 1920's [7]. Up to this day many clinical trials and significant research are directed at determination of their cause and their overall analysis [28, 32, 33]. For example, the effect of aging was analysed in [30] and the abnormalities caused by type-2 diabetes in [34].

Experiments [36] have revealed that the release of insulin from the pancreas occurs in an oscillatory fashion with a typical period of 80-150 min. Hence, in healthy subjects the concentration of insulin in the plasma oscillates, and these oscillations are accompanied by variations in the plasma glucose concentration [32]. Superimposed on the slow (ultradian) oscillations, one can also observe more rapid pulses in the release of insulin with a period of 8-15 min. These oscillations are particularly visible in the portal vein, and they are assumed to have an important influence on several hepatic processes. These oscillations are smoothed out to a certain degree in the main blood compartment because of the relatively large volume of this compartment.

In 1995 Sturis et al. [7, 36] proposed a mathematical model of the arising oscillations in a form of a system of nonlinear differential equations. That model tried to explain the ultradian oscillations with a presence of a delay in the effect of insulin on glucose production. That model relied on a third order approximation of delay in order to obtain easily manageable ordinary differential equations. In [7] Drozdov and Khanina suggested that only using actual delays in equations guarantee the correctness of the model.

The model with delay (which is considered in this paper) was a base for significant amount of research. Among others: Bennet and Gourley [3] analysed global stability of a modified model (with simpler insulin dynamics), Li, Kuang and Mason [22, 23] extended the simplified model with an additional delay in insulin production, Wang, Li and Kuang used that model for modelling of insulin therapy [38].

Following, we will present the Sturis model in the Drozdov-Khanina version [7]. It should be noted that the model parameters are given in many sources [9, 23, 36, 38] however only [7] gives complete unit scaling and initial state justifications.

Let us introduce the notation: x is the amount of insulin level in plasma, y is the amount of insulin level in intercellular space, z is the amount of glucose in the plasma and intercellular space, u_g is the exogenous glucose supply. For more practical analysis we will also consider concentration values in appropriate volumes:

$$c_x(t) = \frac{x(t)}{V_p} \quad c_y(t) = \frac{y(t)}{V_i} \quad c_z(t) = \frac{0.1z(t)}{V_g}$$

The glucose insulin regulatory system dynamics is described by the following system of delay differential equations:

$$\dot{x}(t) = f_1(c_z(t)) - E(c_x(t) - c_y(t)) - \frac{x(t)}{T_p} \tag{1}$$

$$\dot{y}(t) = E(c_x(t) - c_y(t)) - \frac{y(t)}{T_i} \tag{2}$$

$$\dot{z}(t) = u_g(t) - (u_0 + c_z(t) f_2(c_y(t))) + f_3(c_x(t-\tau)) \tag{3}$$

Interpretation of these equations is as follows:

The term $f_1(c_z(t))$ is the rate of insulin secretion from pancreas, which is dependent on the glucose concentration.

The term $E(c_x(t) - c_y(t))$ is the rate of insulin exchange between blood and the intercellular space.

$\frac{x(t)}{T_p}$ and $\frac{y(t)}{T_i}$ represent the insulin degradation in the plasma and in the intercellular space.

The term $u_0 + c_z(t) f_2(c_y(t))$ represents the rate of utilisation of the glucose by different body parts.

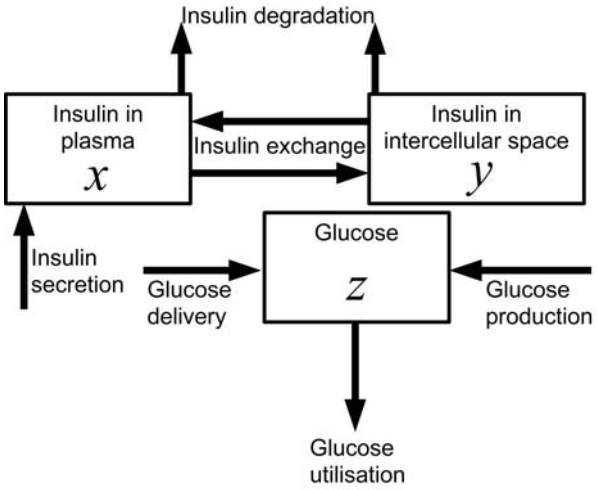

Fig. 1. Explanation of relations in system (1)-(3)

The function $f_3(c_x(t-\tau))$ is the rate of liver production of glucose, depending on the past insulin concentration.

A diagram explaining the compartmental character of this model is presented in figure 1.

Functions included in the equations (1)-(3) are given by the following formulas:

$$f_1(v) = \frac{R_m}{1 + \exp(\phi_{11} - \phi_{12} v)}$$

$$f_2(v) = U_0 + \frac{U_m - U_0}{1 + \exp\left(\phi_{21} + \phi_{22} \ln\left(\left(1 + \frac{V_i}{E T_i}\right) v\right)\right)}$$

$$f_3(v) = \frac{R_g}{1 + \exp(\phi_{31} v - \phi_{32})}$$

Model parameters with biological interpretation are collected in table 1, the rest of the parameters, which are a result of identification, are collected in table 2. All these parameters were experimentally determined by Sturis et al. (see for example [36]). The methodical analysis and correct unit scaling of the parameters can be found in [7].

It should be also noted that this model does not distinguish between hormonal and substrate aspects of insulin regulatory system and focuses on glucose-insulin relations. Regulatory effects of the neural system are not included and effects of different hormones (such as glucagon and somatostatin) are omitted. Additionally, no influence of amino acids indigestion is modelled. General information regarding more complicated relations in regulatory systems can be found in [35]. General survey of glucose dynamics models (including the Sturis model) can be found in [26] and [5], for a model including the effect of glucagon see [24].

Tab. 1. Parameters with direct biological interpretation

Parameter	Meaning	Unit	Value
V_p	volume of plasma	l	3
V_i	volume of interstitial liquid	l	11
V_g	distributional volume of glucose	l	10
E	diffusion rate	$\mathrm{l\ min^{-1}}$	0.2
T_p	time constant of insulin in plasma degradation	min	3
T_i	time constant of insulin in the intercellular space degradation	min	100
τ	time delay of the response of the hepatic glucose production to changes in the plasma insulin concentration	min	36

Tab. 2. Identification parameters

Parameter	Value
R_m	210
Φ_1	5.21
Φ_2	0.03
U_0	0.4
U_m	9.4
Φ_3	7.76
Φ_4	1.772
R_g	160
Φ_5	0.29
Φ_6	7.5
u_0	72

Motivation

The main difficulty in analysis of system (1) – (3) is the presence of delay in equation (3). Because of it the considered system is infinite dimensional. It is possible to obtain exact solutions of delay differential equations (DDE) numerically with the so called step method (see [8] page 6). It is, however, difficult to analyse these solutions and their qualitative behaviour. That is why a search for a finite dimensional approximation is desirable. In the applications of the discussed model a popular approach is to approximate the delay with a cascade of three identical first order dynamical systems, as it was historically

used in the works of Sturis [26, 36]. This delay-free system takes the form:

$$\begin{aligned}
\dot{x}(t) &= f_1(c_z(t)) - E(c_x(t) - c_y(t)) - \frac{x(t)}{T_p} \\
\dot{y}(t) &= E(c_x(t) - c_y(t)) - \frac{y(t)}{T_i} \\
\dot{z}(t) &= u_g(t) - (p_0 + c_z(t) f_2(c_y(t))) + f_3\left(\frac{\beta_3(t)}{V_p}\right) \\
\dot{\beta}_1(t) &= \frac{3(x(t) - \beta_1(t))}{\tau} \\
\dot{\beta}_2(t) &= \frac{3(\beta_1(t) - \beta_2(t))}{\tau} \\
\dot{\beta}_3(t) &= \frac{3(\beta_2(t) - \beta_3(t))}{\tau}
\end{aligned} \tag{4}$$

As it can be seen, it consists of ordinary differential equations (ODE). In the original works this representation of delay was chosen rather arbitrarily and is considered artificial [7]. It is however interesting if it approximates the delay properly.

This was a motivation to determine if this choice is a proper one and also how the order and type of approximation influence the model both qualitatively and quantitatively. It is especially important because system (1)-(3) is nonlinear.

Construction of finite dimensional approximations of time delay systems was a problem considered by many researchers. Generally attempts were divided into two groups: approximation in the frequency domain and approximation in the time domain. Frequency domain methods are generally more suited for linear systems, and are based on the approximation of the term $e^{-s\tau}$ in the transfer function with some kind of rational function. The most notable approach is the Padé approximation (see for example [27]), however, there were attemntps to create different methods. Gu, Khargonekar and Lee [12] used the Fourier series in H^∞ space, Yoon and Lee [39] constructed the approximation based on Frostman theorem, Makila and Partington [15] considered the approximant constructed with Laguerre and Kautz functions, Al-Amer and Al-Sunni [13] attempted to improve Padé approximation with optimisation of a weighted norm in the H^∞ space.

The other group of algorithms is based on approximations in the time domain. These approaches are generally easier to use with nonlinear systems. This class of approximations is much more versatile, and different methods can be developed. We can distinguish methods based on representation of delay as partial differential equation (PDE) and approaches using the approximation along with the step method (these are called spectral methods [19]).

Spectral methods were developed for linear systems with delays (possibly varying with time). This approach relies on Galerkin approximation of solution of DDE with a finite series of basis functions, sequentially on intervals $[k\tau, (k+1)\tau]$ (where k is an integer, and τ is a delay) and in this way reducing the DDE into a linear system of algebraic equations. Typical bases for approximations are shifted Legendre polynomials [15, 19] or Jacobi polynomials [14]. In certain cases these approaches can be very useful for determination of solution and its analysis, as the method can achieve potentially infinite precision [19]. They are, however, limited to the linear systems, and cannot be applied in our case.

Approaches based on using a PDE form are more useful for analysis of nonlinear systems, because only the delayed term is approximated and the nonlinearity of the original DDE does not influence the method. Here also we can find different methods of approximation. One approach is to discretise the PDE, with a difference quotient [16]. This method is especially interesting, because approximation (4) is a special case of such approximation. Other approaches are finite element methods, based on splines [2, 17] or continuous [6] and discontinuous [21] Galerkin projections using shifted Legendre polynomials. There is also a large number of works focused on approximation of DDE with system of ODEs constructed with some kind of Galerkin scheme. There are methods using splines of zero [11] and first [1, 20] order, these methods are generally based on abstract approximation theory (in case of linear semigroups the Trotter-Kato theorem is used). Final group of approximations uses Galerkin approximation of PDE with different bases. Ito and Teglas introduced the so called Legendre-tau approximation with shifted Legendre polynomials [18]. Different path to almost the same results was obtained through analysis of harmonic balance in oscillatory DDE. In [29] Saupe considered the basis of Fourier series, this approach was extended with an addition of first order polynomial by Wahi and Chatterjee [37] and also by Ghosh et al. in [10].

In this paper we focus on the PDE based approaches, i.e. on discretisation method, because it is a general case of (4) and a Galerkin method similar to Legendre-tau approximation, because it allows a high level of analytical computations even in the nonlinear case. Firstly, we will explain how a delay can be interpreted as a PDE and then we will describe both methods. Finally, we will present numerical comparisons of both approximations.

Interpretation of time delay as partial differential equation

Because of the fact that time delayed systems are infinite-dimensional, in order to obtain solutions for $t > 0$ we need to know the system history. We will focus on $x(t) \in R$, however, generalisation for $x(t) \in R^n$ is straightforward. In order to solve a delay differential equation we need an initial condition in a functional form, that is

$$x(t) = \varphi(t), \quad t \in [-\tau, 0] \tag{5}$$

For the rest of the paper we will assume that φ is continuous.

Because of the fact that for evaluation of right hand side of delay differential equation at given time instance t we need values of delayed variable x for time in interval $[t-\tau, t]$, it is reasonable to find some kind of representation of x on that interval. We define the following function of two variables

$$F(t, s) = x(t - s), \quad s \in [0, \tau] \tag{6}$$

Partial derivatives of (6) with respect to both variables are

$$\frac{\partial F(t,s)}{\partial t} = \dot{x}(t-s) \tag{7}$$

$$\frac{\partial F(t,s)}{\partial s} = -\dot{x}(t-s) \tag{8}$$

It can be easily seen that addition of equations (7) and (8) to each other produces the following partial differential equation (PDE)

$$\frac{\partial F(t,s)}{\partial t} = -\frac{\partial F(t,s)}{\partial s} \tag{9}$$

Definition (6) leads to a boundary condition for PDE (9)

$$F(t,0) = x(t) \tag{10}$$

and functional initial condition (5) gives an initial condition for for PDE (9)

$$F(0,\ s) = \varphi(-s), \quad s \in [0,\ \tau] \tag{11}$$

Solution of this PDE is equal to the state x, interpreted as a function on interval $[t-\tau, t]$. In the following sections we will consider two different approximations of solution of (9) and their applications for system (1)-(3).

Approximation through discretisation

The discretisation approach relies on the assumption that the PDE itself is approximated with a system of ODE. The solution of approximating finite dimensional system is then used to approximate the solution of the PDE. This type of approximation is a generalisation of the one introduced in the system (4). It is based on replacing the partial derivative of $F(t,s)$ with respect to s with a backward difference quotient

$$\frac{\partial F(t,s)}{\partial s} \approx \frac{F(t,s) - F(t,s-\Delta)}{\Delta}$$

Let us divide the interval $[0,\tau]$ into N equal parts. We can use this division to introduce a step

$$\Delta = \frac{\tau}{N}$$

that can be used in the difference quotient. Using the above approximation in PDE (9), we can obtain following equations for $k = 1, 2, \ldots, N$

$$\frac{\partial F\left(t, \frac{k\tau}{N}\right)}{\partial t} = \frac{N\left(F\left(t, \frac{(k-1)\tau}{N}\right) - F\left(t, \frac{k\tau}{N}\right)\right)}{\tau} \tag{12}$$

We can denote

$$\beta_k(t) = F\left(t, k\frac{\tau}{N}\right)$$

and then equations (12) will constitute the following system (in the first equation we use the boundary condition (10))

$$\dot{\beta}_1(t) = \frac{N}{\tau}(x(t) - \beta_1(t))$$

$$\dot{\beta}_2(t) = \frac{N}{\tau}(\beta_1(t) - \beta_2(t))$$

$$\vdots$$

$$\dot{\beta}_N(t) = \frac{N}{\tau}(\beta_{N-1}(t) - \beta_N(t))$$

or in a matrix form

$$\dot{\mathbf{b}}(t) = \frac{N}{\tau}\left(\mathbf{A}_1\mathbf{b}(t) + \mathbf{C}_1 x(t)\right)$$

where

$$\mathbf{A}_1 = [a_{ij}]_{N\times N},\ a_{ij} = \begin{cases} a_{ij} = -1, & j = i \\ a_{ij} = 1, & j = i-1,\ i > 1 \\ a_{ij} = 0, & \text{otherwise} \end{cases}$$

$$\mathbf{C}_1 = [c_i]_{N\times 1},\ c_i = \begin{cases} c_i = 1, & i = 1 \\ c_i = 0, & \text{otherwise} \end{cases}$$

$$\mathbf{b}(t) = [\beta_1(t)\ \beta_2(t) \ldots\ \beta_N(t)]^{\mathrm{T}}$$

with initial conditions

$$\beta_k(0) = \varphi\left(-k\frac{\tau}{N}\right), \quad k = 1, 2, \ldots, N$$

Because

$$x(t-\tau) = F(t,\tau)$$

we obtain approximation of delayed term

$$x(t-\tau) \approx \beta_N(t)$$

Finite dimensional approximation of system (1)-(3) of N-th order (introducing N additional equations), obtained through discretisation, takes the form of:

$$\begin{aligned} \dot{x}(t) &= f_1(c_z(t)) - E(c_x(t) - c_y(t)) - \frac{x(t)}{T_p} \\ \dot{y}(t) &= E(c_x(t) - c_y(t)) - \frac{y(t)}{T_i} \\ \dot{z}(t) &= u_g(t) - (u_0 + c_z(t)\, f_2(c_y(t))) + f_3\left(\frac{\beta_N(t)}{V_p}\right) \\ \dot{\mathbf{b}}(t) &= \frac{N}{\tau}\left(\mathbf{A}_1\mathbf{b}(t) + \mathbf{C}_1 x(t)\right) \end{aligned} \tag{13}$$

Approximation with Galerkin projections

This approach is based on the method of Galerkin and is very similar to Legendre-tau method of Ito and Teglas [18]. Instead of approximating the PDE it approximates its solution and then the system of ODE is constructed by substitution of the proposed solution into the PDE. We assume that (6) can be approximated as the following finite linear combination of orthogonal polynomials

$$F(t,s) \approx \sum_{i=0}^{N} \alpha_i(t)\, p_i(s) \tag{14}$$

where $\alpha_i(t)$ are time dependent coefficients and $p_i(s)$ are shifted Legendre polynomials [4]. These polynomials have following properties:

They fulfil the recurrence relation

$$(2n+1)\left(1-2\frac{s}{\tau}\right)p_n(s)-n\cdot p_{n-1}(s),\ n=1,2,\ldots$$

$$p_0(s)=1,\quad p_1(s)=1-2\frac{s}{\tau}$$

They are orthogonal on the interval $[0,\tau]$ with respect to the scalar product

$$(\gamma,\delta)=\int_0^\tau \gamma(s)\delta(s)\,\mathrm{d}s$$

that is

$$(p_i,p_j)=\begin{cases}\|p_i\|^2=\dfrac{\tau}{2i+1} & \text{for } i=j\\ 0 & \text{for } i\neq j\end{cases} \tag{15}$$

Their values on the boundary of interval $[0,\tau]$ are

$$p_i(0)=1,\quad p_i(\tau)=(-1)^i,\quad i=0,1,2,\ldots \tag{16}$$

Their first derivatives can be expressed as

$$\frac{\mathrm{d}}{\mathrm{d}s}p_i(s)=-\frac{2p_{i-1}}{\|p_{i-1}\|^2}-\frac{2p_{i-3}}{\|p_{i-3}\|^2}-\ldots$$

and

$$\left(p_j,\frac{\mathrm{d}}{\mathrm{d}s}p_i\right)=\begin{cases}-2\cdot((i-j)\bmod 2) & \text{for } i\geq j\\ 0 & \text{for } i<j\end{cases} \tag{17}$$

First five of described shifted Legendre polynomials are

$$p_0(s)=1$$

$$p_1(s)=1-2\frac{s}{\tau}$$

$$p_2(s)=1+\frac{6s^2-6s\tau}{\tau^2}$$

$$p_3(s)=1-\frac{20s^3-30s^2\tau+12s\tau^2}{\tau^3}$$

$$p_4(s)=1+\frac{70s^4-140s^3\tau+90s^2\tau^2-20s\tau^3}{\tau^4}$$

Let us substitute the approximation (14) in the PDE (9). It results in the following equation

$$\sum_{i=0}^{N}\dot{\alpha}_i(t)p_i(s)=-\sum_{i=0}^{N}\alpha_i(t)\frac{\mathrm{d}}{\mathrm{d}s}p_i(s) \tag{18}$$

Let us take the scalar products of equation (18) with shifted Legendre polynomials of degrees $j = 0, 1, \ldots, N-1$

$$\left(p_j,\sum_{i=0}^{N}\dot{\alpha}_i(t)p_i\right)=\left(p_j,-\sum_{i=0}^{N}\alpha_i(t)\frac{\mathrm{d}}{\mathrm{d}s}p_i\right)$$

Using orthogonality (15) and property (17) for $j = 0, 1, \ldots, N-1$ we will get equations

$$\frac{\tau}{2j+1}\dot{\alpha}_j(t)=2\sum_{i=j}^{N}((i-j)\bmod 2\cdot\alpha_i(t)) \tag{19}$$

We the consider the boundary condition (10). From (16) we can see that

$$x(t)=F(t,0)=\sum_{i=0}^{N}\alpha_i(t)=\mathbf{m}^{\mathrm{T}}\mathbf{a}(t) \tag{20}$$

where

$$\mathbf{a}(t)=[\alpha_0(t)\ \alpha_1(t)\ \ldots\ \alpha_N(t)]^{\mathrm{T}}$$

$$\mathbf{m}=[1\quad 1\quad \ldots\quad 1]^{\mathrm{T}}\in R^{N+1}$$

Differentiation of the above equality with respect to t leads to

$$\mathbf{m}^{\mathrm{T}}\dot{\mathbf{a}}(t)=\dot{x}(t) \tag{21}$$

We can now use the equation (1) of original system, with substitution

$$\mathbf{m}^{\mathrm{T}}\dot{\mathbf{a}}(t)=f_1(c_z(t))-\left(\frac{E}{V_p}+\frac{1}{T_p}\right)\mathbf{m}^{\mathrm{T}}\mathbf{a}(t)+Ec_y(t) \tag{22}$$

Finally, we can collect equations (19) for $j = 0, 1, \ldots, N-1$ and (22) in the following system

$$\mathbf{E}\dot{\mathbf{a}}(t)=\mathbf{A}_2\mathbf{a}(t)+\mathbf{C}_2\cdot\Phi(c_y(t),c_z(t),\mathbf{m}^{\mathrm{T}}\mathbf{a}(t)) \tag{23}$$

where

$$\mathbf{E}=[e_{ij}]_{(N+1)\times(N+1)},\ e_{ij}=\begin{cases}e_{ij}=\dfrac{\tau}{2j+1},\ j=i,\ i\leq N\\ e_{ij}=1,\ i=N+1\\ e_{ij}=0,\ \text{otherwise}\end{cases} \tag{24}$$

$$\mathbf{A}_2=[a_{ij}]_{(N+1)\times(N+1)},\ a_{ij}=\begin{cases}a_{ij}=2\cdot((j-i)\bmod 2),\ j\geq i\\ a_{ij}=0,\ \text{otherwise}\end{cases} \tag{25}$$

$$\mathbf{C}_2=[c_i]_{(N+1)\times 1},\ c_i=\begin{cases}c_i=1,\ i=N+1\\ c_i=0,\ \text{otherwise}\end{cases} \tag{26}$$

$$\Phi(v_1,v_2,v_3)=Ev_1+f_1(v_2)-\left(\frac{E}{V_p}+\frac{1}{T_p}\right)v_3 \tag{27}$$

Initial conditions for the auxiliary variables $\mathbf{a(0)}$ are determined through the approximation of the function φ with shifted Legendre polynomials and are given by

$$\alpha_i(0)=\frac{(p_i,\varphi^*)}{\|p_i\|^2},\quad \varphi^*(t)=\varphi(-t),\ t\in[0,\tau],$$

$$i=0,1,\ldots,N \tag{28}$$

From property (16) we get the approximation of the delayed term

$$x(t-\tau)\approx\sum_{i=0}^{N}(-1)^i\alpha_i(t)=\mathbf{d}^{\mathrm{T}}\mathbf{a}(t), \tag{29}$$

$$\mathbf{d}=[1\quad -1\quad 1\quad \ldots\quad (-1)^N]^{\mathrm{T}}\in R^{N+1}$$

Final approximated system takes then the following form

$$\dot{y}(t) = E\left(\frac{1}{V_p}\mathbf{m}^{\mathrm{T}}\mathbf{a}(t) - c_y(t)\right) - \frac{y(t)}{T_i} \tag{30}$$

$$\dot{z}(t) = u_g(t) - (u_0 + c_z(t)\, f_2(c_y(t))) + f_3\left(\frac{1}{V_p}\mathbf{d}^{\mathrm{T}}\mathbf{a}(t)\right) \tag{31}$$

$$\dot{\mathbf{a}}(t) = \mathbf{E}^{-1}(\mathbf{A}_2\mathbf{a}(t) + \mathbf{C}_2\Phi(c_y(t), c_z(t), \mathbf{m}^{\mathrm{T}}\mathbf{a}(t))) \tag{32}$$

$$x(t) = \mathbf{m}^{\mathrm{T}}\mathbf{a}(t) \tag{33}$$

As it can be seen, an explicit differential equation for $x(t)$ was removed, as the insulin blood level is now represented as a product $\mathbf{m}^{\mathrm{T}}\mathbf{a}(t)$. It should also be noted that the effective order of approximation is the highest order of polynomial, because even if we introduce $N+1$ new equations, we will eliminate one of the originals. Inverse $\mathbf{E}^{-1}$ can be computed analytically, but is not included here because of the space reasons.

Numerical results

In this section the comparison of methods of estimation will be presented. All simulations were performed for the same initial conditions, with initial function chosen in such way that it didn't have an exact representation in the polynomial basis. Glucose supply was set to a constant value. All the simulations were performed using a Runge-Kutta type method developed by Shampine (see [31]) of third order, with second order error estimator and dense output. This method was used in is classical variant ode23 and variant for delay differential equations dde23. All simulations were performed on a time window of 24 hours. In the following figures concentrations of insulin in plasma and glucose are presented.

At first, the comparison was made between system with the delay, the popular third order approximation (4) and Galerkin approximation of third order. Results on the entire time window can be seen in figures 2 and 3. What might be surprising, the popular approximation presents not only quantitatively but

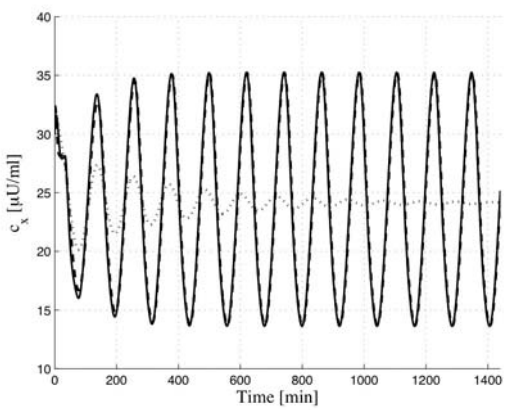

Fig. 2. Comparison of simulations – insulin concentration c_x – solid line is the actual time delay system, dotted is thr system (4) and dashed is the third order Galerkin projection

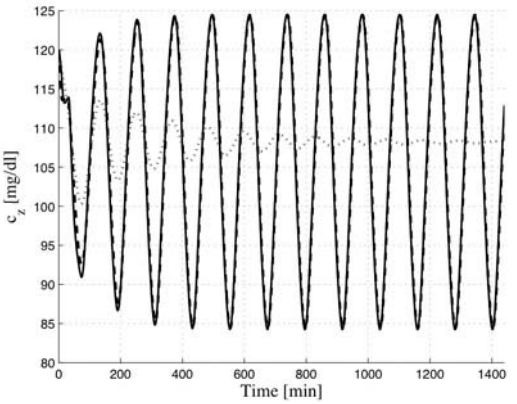

Fig. 3. Comparison of simulations – glucose concentration c_z – solid line is the actual time delay system, dotted is the system (4) and dashed is the third order Galerkin projection

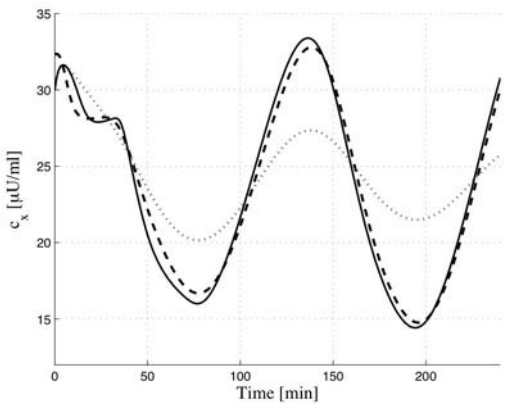

Fig. 4. Comparison of simulations on a shorter time window – insulin concentration c_x – solid line is the actual time delay system, dotted is the system (4) and dashed is the third order Galerkin projection

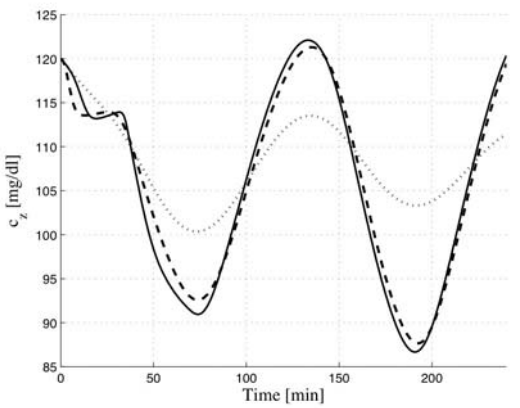

Fig. 5. Comparison of simulations on a shorter time window – glucose concentration c_z – solid line is the actual time delay system, dotted is the system (4) and dashed is the third order Galerkin projection

also qualitatively different results. Signals which should be oscillating are strongly dampened. The Galerkin approximation, on the other hand, with the same order gives results that are hardly distinguishable from the true results. In figures 4 and 5 the same signals are presented in shorter time window, where the differences are more visible. It should be concluded, however, that the results show superiority of Galerkin method.

The next task was to verify how approximations behave for different orders. ITo do so, a performance index was used in the form of square root of integral of square of approximation error. It took the form

$$\varepsilon_N = \sqrt{\int_0^T \left((c_x(t) - \hat{c}_{xN}(t))^2 + (c_z(t) - \hat{c}_{zN}(t))^2 \right) dt} \tag{34}$$

where $T = 24h$ and $\hat{C}xN$ were an approximated concentration with the approximation order N. Methodical simulations for discretisation were performed for orders up to 50. For Galerkin method, tests were limited to the order 15, because further increase in order results in poor conditioning of initial conditions. It should be noted, however, that Galerkin methods can be improved not only by increasing order, but also by introducing division of time interval into parts, and separate approximations are constructed for each of them (compare to finite element method). Results of this tests are presented in figures 6 and 7.

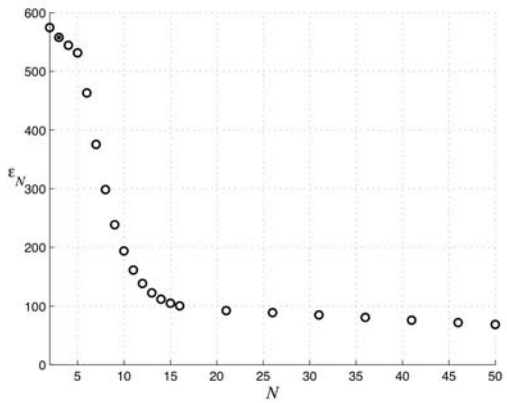

Fig. 6. Errors of discretisation approximation vs approximation order. Third order approximation is marked by a dot

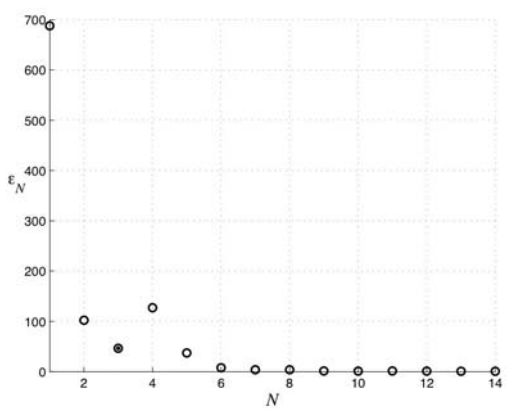

Fig. 7. Errors of Galerkin approximation vs approximation order. Third order approximation is marked by a dot

As it can be seen, differences between methods are substantial. Discretisation method converges very slowly and would require a very high order (up to thousands) to be comparable with higher order Galerkin methods. As it can be seen, the error for Galerkin approximations of order $N > 5$ is at least ten times better than discretisations. It should be noted that the first order Galerkin approximation does not have a corresponding discretisation, because the first order discretisation was not feasible for tests and figure 6 starts with the second order. It should be noted that the previously tested third order approximations are marked in these figures for easier reference.

Conclusions

In this paper different methods of delay approximations were considered. It was shown that more sophisticated (but still relatively simple) Galerkin approximation of a low order is much better approximation, both quantitatively and qualitatively, of the considered system. Approximation based on discretisation proved to be unreliable and slowly convergent. Further work will include analysis of approximated model in context of dynamical systems and control theory. Also the possibility of applying the method of characteristics as a way to improve the discretisation will be investigated.

The author would like to express his gratitude to staff of ePrints@IISc of Indian Institute of Science for help in accessing [37]. The work was financed by state science funds for 2008--2011 as a research project. Contract no. N N514 414034.

References

1. Banks H., Kappel F. (1979), Spline approximations for functional differential equations. *J. Differential Equations* 34(3), 496–522.
2. Bayly P. V., Halley J. E., Mann B. P., Davies M. A. (2003), Stability of Interrupted Cutting by Temporal Finite Element Analysis. *ASME Journal of Manufacturing Science and Engineering* 125, 220–225.
3. Bennet D., Gourley S. (2004), Global stability in a model of the glucose-insulin interaction with time delay. *Euro. Jnl of Applied Mathematics* 15, 203–221.
4. Bronsztejn I., Siemiendajew K., Musiol G., Mühlig H. (2004), Nowoczesne kompendium matematyki. PWN, Warszawa.
5. Chee F., Fernando T. (2007), Closed-loop Control of Blood Glucose. Lecture Notes in Control and Information Sciences. Springer, Berlin – Heidelberg.
6. Deng K., Xiong Z., Huang Y. (2007), The Galerkin continuous finite element method for delay-differential equation with a variable term. *Applied Mathematics and Computation* 186, 1488–1496.
7. Drozdov A., Khanina H. (1995), A model for ultradian oscillations of insulin and glucose. *Mathematical and Computer Modelling* 22(2), 23–38.
8. Elsgolts L. E., Norkin S. B. (1973), Introduction to the Theory and Application of Differential Equations with Deviating Arguments. *Mathematics in Science and Engineering* 105. Academic Press, New York. Translated from Russian by J. L. Casti.

9. Geraghty E. (2008), Delay differential equations in modeling insulin therapies for diabetes. Final year project submitted to the Dept. of Mathematics of the University of Portsmouth. Supervisor: Dr. Athena Makroglou.
10. Ghosh D., Saha P., Chowdhury A. R.(2007), On synchronization of a forced delay dynamical system via the Galerkin approximation. *Communications in Nonlinear Science and Numerical Simulation* 12, 928–941.
11. Gibson J. S. (1983), Linear quadratic optimal control of heraditary differential systems: Infinite dimensional Riccati equations and numerical approximation. *SIAM J. Contr. Optimiz.* 21(1), 95–139.
12. Gu G., Khargonekar P. P., Lee E. B. (1989), Approximation of infinite-dimensional systems. *IEEE Transactions on Automatic Control* 34(6), 610–618.
13. S. H. A.-A., F. M. A.-S. (2000), Approximation of time-delay systems. In: Proceedings of the American Control Conference. Chicago, Illinois, 2491–2495.
14. Horng I.-R., Chou J.-H. (1986), Analysis and parameter identification of time delay systems via shifted Jacobi polynomials. *International Journal of Control* 44(4), 935–942.
15. Hwang C., Chen M.-y. (1986), Analysis of time-delay systems using the Galerkin method. *International Journal of Control* 44(3), 847–866.
16. Insperger T., Stépán G. (2002), Semi-discretization Method for Delayed Systems. *International Journal for Numerical Methods in Engineering* 55(5), 503–518.
17. Insperger T., Mann B. P., Stépán G., Bayly P. V. (2003), Stability of Up-milling and Down-milling, Part 1: Alternative Analytical Methods. *International Journal of Machine Tools and Manufacture* 43(1), 25–34.
18. Ito K., Teglas R. (1986), Legendre-tau approximations for functional differential equations. *SIAM Journal on Control and Optimization* 24(4), 737–759.
19. Ito K., Tran H., Manitius A. (1991), A Fully-discrete Spectral Method for Delay-differential Equations. *SIAM Journal on Numerical Analysis* 28(4), 1121–1140.
20. Kappel F., Kunisch K. (1981), Spline approximations for neutral functional differential equations. *SIAM Journal on Numerical Analysis* 18(6), 1058–1080.
21. Li D., Zhang C. (2010), Nonlinear stability of discontinuous Galerkin methods for delay differential equations. *Applied Mathematics Letters* 23, 457–461.
22. Li J., Kuang Y. (2007), Analysis of a model of the glucose-insulin regulatory system with two delays. *SIAM J. Appl. Math.* 67(3), 757–776.
23. Li J., Kuang Y., Mason C. C. (2006), Modeling the glucose–insulin regulatory system and ultradian insulin secretory oscillations with two explicit time delays. *Journal of Theoretical Biology* 242, 722–735.
24. Liu W., Tang F. (2008), Modeling a simplified regulatory system of blood glucose at molecular levels. *Journal of Theoretical Biology* 252, 608–620.
25. Makila P. M., Partington J. R. (1999), Laguerre and Kautz shift approximations of delay systems. *International Journal of Control* 72(10), 932–946.
26. Makroglou A., Li J., Kuang Y. (2006), Mathematical models and software tools for the glucose-insulin regulatory system and diabetes: an overview. *Applied Numerical Mathematics* 56, 559–573.
27. Mitkowski W. (1991), Stabilizacja systemów dynamicznych. WNT, Warszawa.
28. O'Meara N. M., Sturis J., Cauter E. V., Polonsky K. S. (1993), Lack of control by glucose of ultradian insulin secretory oscillations in impaired glucose tolerance and in non-insulin-dependent diabetes mellitus. *Journal of Clinical Investigation* 92, 262–271.
29. Saupe D. (1983), Global bifurcation of periodic solutions to some autonomous differential delay equations. *Applied Mathematics and Computing* 13, 185–211.
30. Scheen A., Sturis J., Polonsky K. S., Cauter E. V. (1996), Alterations in the ultradian oscillations of insulin secretion and plasma glucose in aging. *Diabetologia* 39, 564–572.
31. Shampine L. F., Gladwell I., Thompson S. (2003), Solving ODEs with MATLAB. Cambridge University Press, New York.
32. Simon C., Brandenberger G. (2002), Ultradian oscillations of insulin secretion in humans. *Diabetes* 51(1), 258–261.
33. Sturis J., Cauter E. V., Blackman J. D., Polonsky K. S. (1991), Entrainment of pulsatile insulin secretion by oscillatory glucose infusion. *Journal of Clinical Investigation* 87, 439–445.
34. Sturis J., Polonsky K. S., Shapiro E. T., Blackman J. D., O'Meara N., Cauter E. V. (1992), Abnormalities in the ultradian oscillations of insulin secretion and glucose levels in Type 2 (non-insulin-dependent) diabetic patients. *Diabetologia* 35, 681–689.
35. Tatoń J., Czech A., Bernas M. (2008), Diabetologia kliniczna. Wydawnictwo Lekarskie PZWL, Warszawa.
36. Tolić I. M., Mosekilde E., Sturis J. (2000), Modeling the insulin-glucose feedback system: The significance of pulsatile insulin secretion. *Journal of Theoretical Biology* 207, 361–375.
37. Wahi P., Chatterjee A. (2005), Galerkin projections for delay differential equations. Transactions of the ASME. *Journal of Dynamic Systems, Measurement, and Control* 127, 80–87.
38. Wang H., Li J., Kuangb Y. (2007), Mathematical modeling and qualitative analysis of insulin therapies. *Mathematical Biosciences* 210, 17–33.
39. Yoon M. G., Lee B. H. (1997), A new approximation method for time-delay systems. *IEEE Transactions on Automatic Control* 42(7), 1008–1012.

BIO-ALGORITHMS AND MED-SYSTEMS
JOURNAL EDITED BY MEDICAL COLLEGE – JAGIELLONIAN UNIVERSITY
Vol. 6, No. 12, 2010, pp. 131–136.

RANDOMFOREST BASED ASSESSMENT OF THE HERG CHANNEL INHIBITION POTENTIAL FOR THE EARLY DRUG CARDIOTOXICITY TESTING

Barbara Wiśniowska[1], Aleksander Mendyk[2], Miłosz Polak[1], Jakub Szlęk[2], Sebastian Polak[1]

[1] Unit of Pharmacoepidemiology and Pharmacoeconomics Faculty of Pharmacy Jagiellonian University Medical College, Medyczna 9 Street, 30-688 Krakow, Poland
[2] Department of Pharmaceutical Technology and Biopharmaceutics Faculty of Pharmacy Jagiellonian University Medical College, Medyczna 9 Street, 30-688 Krakow, Poland

Abstract. Acquired long QT syndrome (LQTS) can lead to fatal ventricular arrhythmia and one of the most common reasons for developing LQTS seen in clinical settings as Torsade de Pointes (TdP) are drugs. LQTS syndrome and TdP are principally caused by the inhibition of the potassium channels encoded by hERG (the human ether-a-go-go related gene). The potassium channels and ionic currents ($I_{kr,}$ I_{to}, I_{ks} and others) together with calcium and sodium channels and currents (I_{CaL}, I_{Na} respectively) are the key elements of the electrophysiological interplay in heart. Drugs affinity to hERG channels and life-threatening interferences in heart electrophysiology resulted in withdrawal of many substances from the pharmaceutical market and some other drugs were black-boxed as potentially dangerous. Aim of the study was to develop reliable and easy to use model for the drug affinity to the hERG channel inhibition. Database used for the modeling purposes contains 447 records which were utilized during the modeling and validation levels. Dataset is freely available from the CompTox project website (www.tox-portal.net). Three various validation modes were applied to the model performance assessment to ensure highest possible reliability of the final model: standard 10-fold cross validation procedure (10-fold CV), enhanced 10-fold cross validation (whole drugs excluded from test sets) and validation on external test set of 62 records for both previously present (different in vitro models) and absent in native dataset drugs. Pre-processing included recalculation of the original output (IC50 value – concentration of a drug which causes 50% inhibition of the ionic current) derived from the in vitro experiments, with use of the scaling factors. Random Forest algorithm with either 10 or 50 or 100 generated trees and unlimited tree depth implemented in WEKA software was used. The input consisted of 1034 parameters describing in vitro setting (3), physico-chemical properties (7), and structure (so called chemical fingerprint – 1024). Output had a binary characteristic with IC50 equal to 1 ĘM concentration as the safety threshold value (encoded as 0-safe, 1- unsafe). The performance of the best model estimated in simple 10-fold CV was 85% (1-88%, 0-82%) with an average ROC accuracy of 0.92. Implementation of rigorous 10-fold CV procedure resulted in decrease in total accuracy to 72% (1-72%, 0-72%) with ROC value equal to 0.791. Test on the external set consists of three measures: all 62 records (total – 73%, 1-62%, 0-81%), 33 enew f records describing previously unknown drugs (total – 73%, 1-62%, 0-81%) and eold f records describing previously present drugs (total – 83%, 1-78%, 091%).
Keywords: RandomForest, decision tree, hERG, I_{kr} current inhibition, cardiotoxicity prediction, Torsade de Pointes

Introduction

Computational toxicology

Computational toxicology is a wide in meanings phrase which is commonly used for description of various scientific activities. One of the reasons for such situation lies in exploration of the relatively new fields and its innovativeness. The definition says that it comprises of the computational experiment, mathematical calculation, or scientific analysis of substances and organization of substance related data through a computer-based analysis [Valerio L.G., Jr. (2009),In silico toxicology for the pharmaceutical sciences. Toxicology and Applied Pharmacology 241(3), 356-370]. In practice it uses a variety of computer-based data analysis tools including computational algorithms (mathematical, chemical, and biological). They are designed to produce either predictions of toxicity or actual experimental toxicology-related data for use in scientific hypothesis testing or safety analysis [Merlot C. (2010), Computational toxicology–a tool for early safety evaluation. Drug Discovery Today 15(1-2), 16-22]. The endpoints being investigated include global toxicity like mutagenicity, carcinogenicity, cell toxicity, cardiotoxicity, hepatobiliary and urinary tract toxicities [Langham J.J., Jain A.N. (2008), Accurate and interpretable computational modeling of chemical mutagenicity. Journal of Chemical

Information and Modeling 48(9), 1833-9; Ursem C.J., Kruhlak N.L., Contrera J.F., et al. (2009), Identification of structure-activity relationships for adverse effects of pharmaceuticals in humans. Part A: use of FDA post-market reports to create a database of hepatobiliary and urinary tract toxicities. Regulatory toxicology and pharmacology: RTP 54(1), 1-22; Matthews E.J., Ursem C.J., Kruhlak N.L., et al. (2009), Identification of structure-activity relationships for adverse effects of pharmaceuticals in humans: Part B. Use of (Q)SAR systems for early detection of drug-induced hepatobiliary and urinary tract toxicities. Regulatory toxicology and pharmacology: RTP 54(1), 23-42; Matthews E.J., Kruhlak N.L., Benz R.D., et al. (2009), Identification of structure-activity relationships for adverse effects of pharmaceuticals in humans: Part C: use of QSAR and an expert system for the estimation of the mechanism of action of drug-induced hepatobiliary and urinary tract toxicities. Regulatory toxicology and pharmacology: RTP 54(1), 43-65], and more specific, better defined effects including receptor or ionic channels binding. Problems in gaining satisfactory results in the first approach lies in the wide range of possible connections between multiple dependent and independent variables. Two most often used approaches include various types of modeling and expert systems. The latter ones are the repositories of knowledge gathered and stored by experts. An example include EPISuite developed by U.S. Environmental Protection Agency (EPA) [Cohen Hubal E.A., Richard A.M., Shah I., et al. (2010), Exposure science and the U.S. EPA National Center for Computational Toxicology. Journal of Exposure Science & Environmental Epidemiology 20(3), 231-6]. Predictive systems are mainly based on the empirical modeling paradigm (statistical models or computational intelligence based models) and utilize the Quantitative Structure-Activity Relationships methodology (QSAR) [Mohan C.G., Gandhi T., Garg D., Shinde R. (2007), Computer-Assisted Methods in Chemical Toxicity Prediction. Mini Reviews in Medicinal Chemistry 7(5), 499-508]. Such approach mainly focuses on finding correlations between molecular descriptors (predictors and elements of the structure) and activity defined in various ways.

Drug toxicity assessment

Drug toxicity assessment is a compulsory and strictly controlled element of the drug development process. All New Chemical Entities tested as the potential drugs have to fulfill safety regulations. According to the International Conference of Harmonization guidelines toxicity studies include [http://www.ich.or]:

- Carcinogenicity studies
- Genotoxicity studies
- Toxicokinetics assessment
- General toxicity (after single or repeated doses)
- Pharmacology studies (including cardiac safety)
- Immunotoxicity studies

All listed above parameters are quantified based on either the in vitro or animal in vivo studies. Both groups remain gold standards and properly applied and carried deliver reliable results regarding potential toxic effects. It includes qualitative and semi-qualitative outcomes which can be further extrapolated to the human in vivo settings and used for example as the dose predictors for the first-in-human clinical studies. On the other hand wide implementation of such methods at the very early stage of the drug development wouldn ft be able due to relatively high cost and large number of molecules generated with use of the virtual chemical synthesis or combinatorial chemistry techniques. One of the propositions of the high throughput screening routines are in silico methods based on the mathematical models. They allow fast, efficient, and not expensive toxicity assessment. It is an element of the modernization of the drug development scientific approach proposed by the Food and Drug Administration in the FDA fs Critical Path White Paper [15].

Cardiotoxicity

Acquired long QT syndrome (LQTS) can lead to fatal ventricular arrhythmia. One of the most common reasons for developing LQTS seen in clinical settings as Torsade de Pointes (TdP) are drugs. LQTS syndrome and TdP are principally caused by the inhibition of the potassium channels encoded by hERG (the human ether-a-go-go related gene). The potassium channels and ionic currents (I_{kr}, I_{to}, I_{ks} and others) together with calcium and sodium channels and currents (I_{CaL}, I_{Na} respectively) are the key elements of the electrophysiological interplay in heart. Drugs affinity to hERG channels and life-threatening interferences in heart electrophysiology resulted in withdrawal of many substances from the pharmaceutical market and some other drugs were black-boxed as potentially dangerous. Nowadays regulations describing potential drugs studies require in depth assessment of the hERG affinity including various in vitro (rubidium-flux assays, radioligand binding assays, in vitro electrophysiology measurements, fluorescence-based assays based on the various cell lines) and in vivo (isolated hearts) tests [Gill S., Gill J., Lee S.S., Hesketh C., Fedida D., Rezazadeh S., Stankovich L., Liang D. (2003), Flux assays in high throughput screening of ion channels in drug discovery., Assay Drug Dev. Technol. 1(5), 709717; Finlayson K., Pennington A.J., Kelly J.S. (2001), [3H]Dofetilide binding in SHSY5Y and HEK293 cells expressing a HERG-like K+ channel?, Eur. J. Pharmacol. 412, 203212; Wang J., Della Penna K., Wang H., Karczewski J., Connolly T., Koblan K., Bennett P., Salata J. (2003), Functional and pharmacological properties of canine ERG potassium channels., Am. J. Physiol. Heart Circ. Physiol. 284(1), H256-H267; Witchel H., Milnes J., Mitcheson J., Hancox J. (2002), Troubleshooting problems with in vitro screening of drugs for QT interval prolongation using HERG K+ channels expressed in mammalian cell lines and Xenopus oocytes., J. Pharmacol. Toxicol. Methods 48(2), 65-80; Baxter D.F., Kirk M., Garcia A.F., Raimondi A., Holmqvist M.H., Flint K.K., Bojanic D., Distefano P.S., Curtis R., Xie Y. (2002), A novel membrane potential-sensitive fluorescent dye improves cell-based assays for ion channels., J. Biomol. Screen. 7(1), 79-85; Dorn A., Hermann F., Ebneth A., Bothmann H., Trube G., Christensen K., Apfel C. (2005), Evaluation of a high-throughput fluorescence assay method for hERG potassium channel inhibition., J. Biom. Screen. 10(4), 339-347; González J.E., Oades K., Leychkis Y., Harootunian A., Negulescu P.A. (1999), Cell-based assays and instrumentation for screening ion-channel targets., Drug. Discov. Ther. 4(9), 431-439].

Previously mentioned techniques are connected either with cost, effectiveness or ethical obstacles especially at the early

stage of the drug development. Therefore accurate screening tests of the drug candidates become appreciable and are widely used. The main objective of the work was to develop a reliable in silico screening model for the in vitro potassium channel inhibition prediction.

Materials and methods

Data

Database used for the modeling purposes was recently published [] and is freely available after registration from the CompTox project website [http://www.tox-portal.ne]. Preprocessing included recalculation of the original output (IC50 value – concentration of a drug which causes 50% inhibition of the ionic current) derived from the in vitro experiments, with use of the scaling factors described in a separate publication. Final set contained 447 records which were utilized during the modeling and validation levels. The input vector consisted of 1034 parameters as described in Table 1.

Output had a binary characteristic with IC50 equal to 1 ĘM concentration as the safety threshold value (encoded as 0-safe, 1- unsafe). The binarization procedure was conducted in MS Excel®. The database contained information for 175 drug and drug-like molecules from both groups – with proven hERG blocking activity and without it. All data were obtained experimentally during in vitro assays performed on HEK, CHO or XO cells. IC50 values, expressed in micro molar concentration, were obtained with use of the standard techniques – whole-cell patch clamp method for HEK and CHO and 2-electrode voltage clamp for XO. As the experimental settings, especially model applied and temperature maintained during the assays, can affect considerably on obtained IC50 measurement results, an inter-system and inter-temperature extrapolation factors were used in order to standardize the data []. Compounds characteristics as shown in Figure 1, correspond with chemical space of drug-like properties.

Two dimensional (2D) structures were represented by molecular fingerprint (substructure or hashed fingerprint) – a binary string of defined number bites. The core of the computational method used during the study was derived from the Chemical Descriptors Library project [http://cdelib.sourceforge.net/doc/fingerprints.html; last accessed 15.05.2010] with necessary changes and improvements in the code. The fingerprint depth – a maximum number of bonds separating two atoms – was set to 7 and the defined fingerprint length was 20.

Tab 1. Input vector characteristic

group	parameters	description (min ; max)
in vitro research settings (3)	depol_puls mV_measure protocol	Value of the depolarization pulse (-40; 70) Measurement point potential value (-140; 0) Type of protocol (five different protocols encoded as 1–5)
physico-chemical properties (7)	MW RBN nHDon nHAcc nHBonds TPSA ALOGP	Molecular Weight (94.13; 837.19) Rotatable Bond Number (0; 18) Number of H-bond donor (0; 8) Number of H-bond acceptor (1; 17) Number of intramolecular H-bonds (0; 5) Topological Polar Surface Area (3.24; 216.89) Calculated logP value (-2.171; 9.197)
structure (1024)		Chemical fingerprint

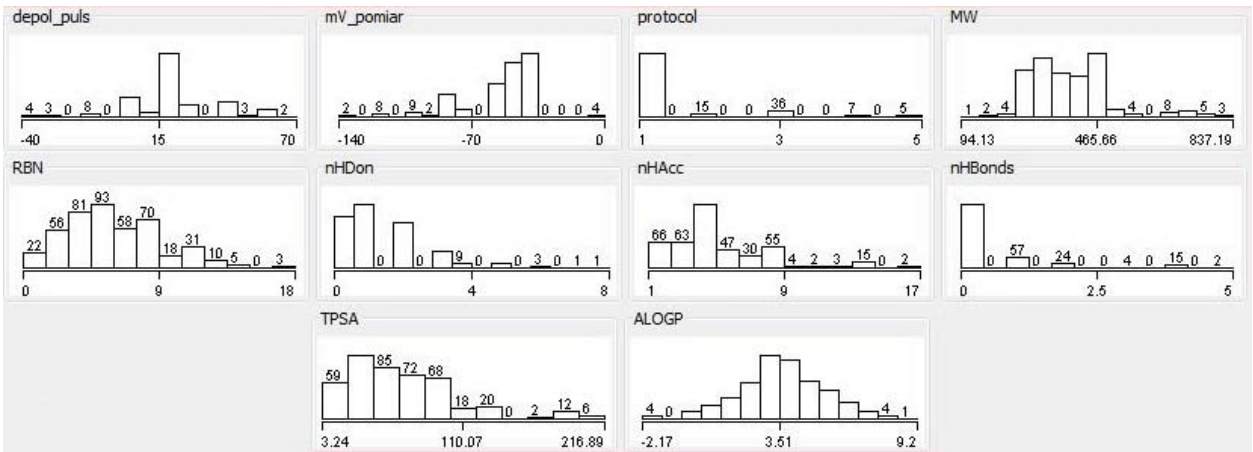

Fig. 1. Histogram of the molecular properties of the compounds in the training set

Validation procedures

Three various validation modes were applied to the model performance assessment to ensure highest possible reliability of the final model: standard 10-fold cross validation procedure (10-fold CV), enhanced 10-fold cross validation (whole drugs excluded from test sets) and validation on external test set of 62 records for both previously present (different in vitro models) and absent in native dataset drugs. Standard procedure was done with use of the WEKA built-in functionality. Enhanced procedure demanded development of the separate software solving multiple knapsack problem assigning to each test set at most 10% of the training set records assuming that elements of the test set were automatically excluded from the training set. 10 pairs were created as it is presented in Table 2.

Model assessment

Described problem is a typical classification problem with binary output. The chosen measure of the model performance was the ability of proper discrimination of the records from all test sets for both classes and all records separately. Additional measure used was the area under receiver-operator curve (ROC).

Software

Random Forest algorithm implemented in WEKA software, with either 10 or 50 or 100 generated trees and unlimited tree depth was used. WEKA (Waikato Environment for Knowledge Analysis) is a machine learning and data mining algorithms package developed at the University of Waikato in New Zealand [Witten I.H., Frank E. (2005), Data Mining: Practical machine learning tools and techniques., 2nd Edition, Morgan Kaufmann, San Francisco]. It is open source, publicly available scientific software implemented in Java and released under the GNU General Public License (GNU GPL). To calculate physicochemical parameters Dragon software was utilized. DRAGON is a collection of algorithms, for the molecular descriptors calculation, developed by the Milano Chemometrics and QSAR Research Group [18]. DRAGON version 5 allows calculation of more than 3200 different parameters from the simplest one as atom type, functional groups and fragment counts to the more sophisticated as charge, topological or geometrical descriptors

Tab. 2. Enhanced 10-fold cross validation test datasets

Test set	No. of records	No. of compounds	Compounds
1	51	3	Terfenadine Quinidine Dofetilide
2	50	4	Cisapride E4031 Fluoxetine Haloperidol
3	50	6	Thioridazine Verapamil Sotalol Moxifloxacin Pimozide Bupivacaine
4	44	6	Amitriptyline Erythromycin Amiodarone Loratidine Bepridil Astemizole
5	44	9	Azimilide Maprotiline Chlorpromazine Clozapine Diphenhydramine Propafenone Trifluoperazine Ropivacaine Ziprasidone
6	44	14	Halofantrine Sparfloxacin Berberine Chloroquine Doxazosin trazodone Clarithromycin naringenin Domperidone methadon Cocaine Ibutilide MK499 Ketanserin
8	44	23	Sertindole Propranolol Terazosin Vesnarinone Norfluoxetine Orphenadrine Mefloquine Nifekalant Levofloxacin Chlorpheniramine GF109203X (bisindolylmaleimide I) Lidoflazine Ajmaline Ketoconazole Droperidol FeXOfenadine Disopyramide Amsacrine Tolterodine Citalopram Grepafloxacin
8	44	34	Sildenafil olanzapine Flecainide Ciprofloxacin Ambasilide Diltiazem Risperidone Prazosin Dronedarone Prochlorperazine Epinastine Norpropoxyphene digoxin AVE0118 canrenoic_ acid Ranolazine Cetirizine LAAM Flunarizine Josamycin Papaverine Erythromycylamine DW286a 4-aminopyridine 5-hydroxypropafenone clomiphene Bertosamil miconazole Doxepin Perhexiline EDDP BRL-32872 N-desbutylhalofantrine Cocaethylene
9	44	44	Fluspirilene budipine Phenytoin Desloratidine pilsicainide Oleandomycin Ropinirole Trimethoprim Misolastine desbutyllumefantrine1 Digitoxin Ouabain Cibenzoline Dolasetron Perphenazine Quetiapine Spironolactone Mianserine Sulfamethoxazole Morphine Carvedilol Clemastine Mesoridazine lidocaine metoclopramide Imipramine Buprenorphine Meperidine Telithromycin Apomorphine Norastemizole lamotrigine Desmethylastemizole Cyamemazine Fentanyl morin vardenafil pentamidine Gatifloxacin Metoprolol Hesperetin Terodiline Ondansetron Lomefloxacin
10	32	32	Indomethacin Nicotine Propiverine Roxithromycin Pentobarbital Lumefantrine Methylecgonidine Nifedipine Irbesartan desmethylerythromycin Ofloxacin Phenobarbital MCI-154 Procainamide Pergolide Granisetron Terikalant Articaine Hydroxyzine Tamoxifen Ebastine Prenylamine Prucalopride Lovastatin Pyrilamine 4,4'-dimethyldiphenhydramine codeine Mepivacaine Sibutramine MDL74156 Fluvoxamine Propoxyphene

and some physicochemical properties (molecular weight, logP, number of rotatable bonds, H-donors/acceptors, topological surface area).

Results and discussion

The performance of the best model based on the 10 generated trees estimated in simple 10-fold CV was 85% (1-88%, 0-82%) with an average ROC accuracy of 0.92. Implementation of rigorous 10-fold CV procedure resulted in decrease in total accuracy to 72% (1-72%, 0-72%) with ROC value equal to 0.791. Test on the external set consisted of three measures: all 62 records (total – 73%, 1-62%, 0-81%), 33 enew f records describing previously unknown drugs (total – 73%, 1-62%, 0-81%) and 29 eold f records describing previously present drugs (total – 83%, 1-78%, 0_91%). Especially interesting and valuable was the enhanced validation procedure results as the most challenging for the algorithm. System had no previous information about the molecules and its work was pure extrapolation. To gain in depth knowledge about the best system performance all 10 test sets were strictly investigated. Results are presented below in Table 3.

Comparison of the data presented in Table 2 and Table 3 shows that the more various molecules in one dataset the more challenging problem for the algorithm to properly. It could be concluded that one of the most important factors influencing the final results is the construction of the learning-testing pairs and to avoid such bias test sets should be optimized not only for number of molecules but also diversity of data and such research will be done in the future.

The results prove that tools based on RandomForest algorithm can be useful for the fast assessment of the hERG potassium channel inhibition. Using relatively simple and easy to obtain molecule descriptors one can assess potential cardiotoxicity at the very early stage of drug development.

Conclusions

Developed RandomForest model due to its high specificity and sensitivity, relatively easy to obtain description of new chemical entity as well as flexibility (user-friendly) can be considered as the screening model for the cardiotoxicity testing purposes at the early stage of the drug development. Results can be further use for the ego-no go f decision justification and in vitro – in vivo extrapolation.

Tab. 3. Partial results of the best chosen prediction system

RandomForest 10				
Test set	a	b	<– classified as	
1	49	0	a = 1	1.00
	1	1	b = 0	0.50
2	24	25	a = 1	0.49
	0	1	b = 0	1.00
3	27	1	a = 1	0.96
	7	15	b = 0	0.68
4	18	6	a = 1	0.75
	4	16	b = 0	0.80
5	17	6	a = 1	0.74
	7	14	b = 0	0.67
6	14	9	a = 1	0.61
	6	15	b = 0	0.71
7	11	10	a = 1	0.52
	7	16	b = 0	0.70
8	9	4	a = 1	0.69
	12	19	b = 0	0.61
9	8	5	a = 1	0.62
	6	25	b = 0	0.81
10	2	5	a = 1	0.29
	6	19	b = 0	0.76

References

1. Valerio L.G., Jr. (2009), In silico toxicology for the pharmaceutical sciences. Toxicology and Applied Pharmacology 241(3), 356-370.
2. Merlot C. (2010), Computational toxicology – a tool for early safety evaluation. Drug Discovery Today 15(1-2), 16-22.
3. Langham J.J., Jain A.N. (2008), Accurate and interpretable computational modeling of chemical mutagenicity. Journal of Chemical Information and Modeling 48(9), 1833-1839.
4. Ursem C.J., Kruhlak N.L., Contrera J.F. et al. (2009), Identification of structure-activity relationships for adverse effects of pharmaceuticals in humans. Part A: use of FDA post-market reports to create a database of hepatobiliary and urinary tract toxicities. Regulatory toxicology and pharmacology 54(1), 1-22.
5. Matthews E.J., Ursem C.J., Kruhlak N.L. et al. (2009), Identification of structure-activity relationships for adverse effects of pharmaceuticals in humans. Part B: Use of (Q) SAR systems for early detection of drug-induced hepatobiliary and urinary tract toxicities. Regulatory toxicology and pharmacology 54(1), 23-42.
6. Matthews E.J., Kruhlak N.L., Benz R.D. et al. (2009), Identification of structure-activity relationships for adverse effects of pharmaceuticals in humans. Part C: use of QSAR and an expert system for the estimation of the mechanism of action of drug-induced hepatobiliary and urinary tract toxicities. Regulatory toxicology and pharmacology 54(1), 43-65.
7. Cohen Hubal E.A., Richard A.M., Shah I. et al. (2010), Exposure science and the U.S. EPA National Center for Computational Toxicology. Journal of Exposure Science & Environmental Epidemiology 20(3), 231-236.
8. Mohan C.G., Gandhi T., Garg D., Shinde R. (2007), Computer-assisted Methods in Chemical Toxicity Prediction. Mini Reviews in Medicinal Chemistry 7(5), 499-508.
9. Witten I.H., Frank E. (2005), Data Mining: Practical machine learning tools and techniques. 2nd Edition, Morgan Kaufmann, San Francisco.
10. Polak S., Wiśniowska B., Brandys J. (2009), Collation, assessment and analysis of literature in vitro data on hERG receptor blocking potency for subsequent modeling of drugs' cardiotoxic properties. Journal of Applied Toxicology 29(3), 183-206.
11. http://www.tox-portal.net; last accessed 15.05.2010.
12. http://www.ich.org; last accessed 15.05.2010.
13. Talete srl, DRAGON for Windows (Software for Molecular Descriptor Calculations). Version 5.5 – 2007: http://www.talete.mi.it; last accessed 15.05.2010.
14. Frid A.A., Matthews E.J. (2010), Prediction of drug-related cardiac adverse effects in humans: B: Use of QSAR programs for early detection of drug-induced cardiac toxicities. Regulatory toxicology and pharmacology 56(3), 276-289.
15. FDS Critical Path White Paper: www.fda.gov; last accessed 15.05.2010.
16. Cheng C.S., Alderman D., Kwash J., Dessaint J., Patel R., Lescoe M.K., Kinrade M.B., Yu W. (2002), A high-throughput HERG potassium channel function assay: An old assay with a new look. Drug. Dev. Ind. Pharm. 28(2), 177-191.
17. Gill S., Gill J., Lee S.S., Hesketh C., Fedida D., Rezazadeh S., Stankovich L., Liang D. (2003), Flux assays in high throughput screening of ion channels in drug discovery. Assay Drug Dev. Technol. 1(5), 709-717.
18. Finlayson K., Pennington A.J., Kelly J.S. (2001), [3H] Dofetilide binding in SHSY5Y and HEK293 cells expressing a HERG-like K+ channel? Eur. J. Pharmacol. 412, 203-212.
19. Wang J., Della Penna K., Wang H., Karczewski J., Connolly T., Koblan K., Bennett P., Salata J. (2003), Functional and pharmacological properties of canine ERG potassium channels. Am. J. Physiol. Heart Circ. Physiol. 284(1), H256-H267.
20. Witchel H., Milnes J., Mitcheson J., Hancox J. (2002), Troubleshooting problems with in vitro screening of drugs for QT interval prolongation using HERG K+ channels expressed in mammalian cell lines and Xenopus oocytes. J. Pharmacol. Toxicol. Methods 48(2), 65-80.
21. Baxter D.F., Kirk M., Garcia A.F., Raimondi A., Holmqvist M.H., Flint K.K., Bojanic D., Distefano P.S., Curtis R., Xie Y. (2002), A novel membrane potential-sensitive fluorescent dye improves cell-based assays for ion channels. J. Biomol. Screen. 7(1), 79-85.
22. Dorn A., Hermann F., Ebneth A., Bothmann H., Trube G., Christensen K., Apfel C. (2005), Evaluation of a high-throughput fluorescence assay method for hERG potassium channel inhibition. J. Biom. Screen. 10(4), 339-347.
23. González J.E., Oades K., Leychkis Y., Harootunian A., Negulescu P.A. (1999), Cell-based assays and instrumentation for screening ion-channel targets. Drug. Discov. Ther. 4(9), 431-439.
24. Wiśniowska B., Polak S. (2009), HERG in vitro interchange factors development and verification hERG in vitro interchange factors. Toxicology Mechanisms and Methods 19(4), 278-284.
25. http://cdelib.sourceforge.net/doc/fingerprints.html; last accessed 15.05.2010.

Statement. Research was funded from the Polish National Centre for Research and Development LIDER project number 187/L-1/09.

BIO-ALGORITHMS AND MED-SYSTEMS
JOURNAL EDITED BY MEDICAL COLLEGE – JAGIELLONIAN UNIVERSITY
Vol. 6, No. 12, 2010, pp. 137–139.

RELATIONSHIP BETWEEN MAXIMUM VALUE OF ANNUAL TREE STAND HEIGHT INCREMENT AND AGE OF ITS OCCURRENCE

PRZEMYSŁAW SYPKA

Department of Electronics, University of Science and Technology, al. Mickiewicza 30, 30-059 Kraków, sypka@agh.edu.pl

Abstract: The paper presents the analytical formula describing the relationship between the maximum value of an annual tree stand height increment and the age at which it takes place. The estimation of considered parameters was based on Czarnowski's theory of tree stand dynamics. The empirical data from 19 height growth benchmarks representing all site quality indexes of two species – beech and spruce – from experimental thinning plots were taken into consideration.
Keywords: tree-stand growth model; maximum value of annual stand growth increment; age of annual stand growth increment occurrence; tree stand management

Introduction

The tree stand dynamics are among the most important factors developing the components of water exchange balance between the atmosphere, tree stand, and the soil in various forests. There is a linear dependence between transpiration and the amount of biomass production; interception is directly proportional to the surface area of plants. In turn, the site quality index has a basic significance for the biometric features of the tree stand, which condition the energy of solar radiation reaching the litter level and the attenuation of wind velocity within the tree stand [6]. The site quality index is usually expressed by a Roman numeral (absolutely useless in modeling) or by the average height of a 100-year-old tree stand for the given species. There have also been some attempts to describe the site quality index in relation to the amount of biomass of over-ground parts of plants [1].

The objective of the paper is to find an analytical formula, combining the maximum value of an annual height increment (ΔH_m) and the age of its occurrence (A_m). The relationship of these biometrical features of tree stand is observed in the site surveys [1] [1] [3]:

- values of ΔH_m are dependent on tree species: the heliophilous species have bigger values of ΔH_m at an earlier age A_m than the shade-tolerant species,
- the higher the site quality index, the bigger the ΔH_m increments for a given species,
- the higher the site quality index, the earlier the age A_m of the maximum value of an annual tree stand height increment,
- values of ΔH_m and A_m may be influenced by silvicultural practices; for instance, thinning and also by violently affecting biotic and abiotic environments,
- the age A_m may be delayed when the analyzed tree stand was growing under forest canopy; this delay may have no influence on the value of ΔH_m.

The maximum value of an annual tree stand height increment and the age at which it takes place can be easily interpreted from the biological point of view. The culmination point of a height increment ΔH_m may be taken to mean a manifestation of stand growth ability and the A_m – age of the ΔH_m occurrence – may be understood as tree stand's response to growth conditions. The value of an annual height increment is high in early age on high-quality forest sites. If the site quality index is low, the growth activity of stand decreases and the culmination point occurs later.

There is a lack of formulae describing the relationship between ΔH_m and A_m which could be applied in forest practice. Such equations are essential for forest practice to anticipate and to describe effects of silvicultural practices [7] [8]. The goal of this paper is to express by a formula the field-noticeable interdependence between the maximum value of an annual height increment and the age of its occurrence.

Tree stand growth equations

Growth equations describe the change of height with age, which follows a sigmoid curve. In the beginning the curve is concave up, while it becomes convex in later life. But one

should remember that all mathematical models express just the idealized shape of the growth curve. Although many equations have been proposed to describe stand growth [5] [11] [13], most of them can be used only to supply an empirical fit. In turn, all parameters in such equations are not regarded as having any absolute significance for the theory of growth [5]. So the usefulness of any growth model should be verified not only by the values of goodness of fit, but above all the direct biological interpretation of parameters is essential [9].

Czarnowski's equation is one of a very few 'growth functions' directly based on biological premises. Referring to Czarnowski's theory [2], the height increment of an even-aged tree stand may be computed by the following formula:

$$\Delta H = \Delta H_m \left(1 - \left| \frac{A - A_m}{A + A_m} \right| \right) \qquad (1)$$

where: ΔH – an annual height increment [m] in consecutive growing years A, ΔH_m – the maximum annual height increment [m], which takes place at the age of A_m [years].

The formula (1) may be easily interpreted from a biological point of view, because both parameters in the equation are related to field-measurable biometric features of tree stands, especially of cone-shaped coniferous stands. The height of an even-aged tree stand may be calculated after the integration over the curve (1). It is essential to take into consideration that the function (1) has the singular point at the age of A_m, so the integration must be divided to two intervals delimitated by the value of A_m:

$$H(A) = \begin{cases} 2 \cdot \Delta H_m \cdot A_m \cdot \left[\frac{A}{A_m} - \ln\left(1 + \frac{A}{A_m} \right) \right] & \text{for } A \le A_m \\ 2 \cdot \Delta H_m \cdot A_m \cdot \left[\ln\left(1 + \frac{A}{A_m} \right) + 1 - 2 \cdot \ln(2) \right] & \text{for } A \ge A_m \end{cases} \qquad (2)$$

The Figure 1 presents the changeability of tree stand height and growth increment respectively, based on formulae (1) and (2). Although in a natural environment old trees are usually destroyed by different kinds of disasters such as a hurricane, a stroke of lightning or by a fire, some of them reveal the continuous increment. The annual increment of such trees is slight, but they manage to rich impressive dimensions. Moreover the tree height is often reduced by strong winds forcing trees to regenerate continuously. Such continuous ability to regenerate points out that trees are able to grow in height and in width until death [2].

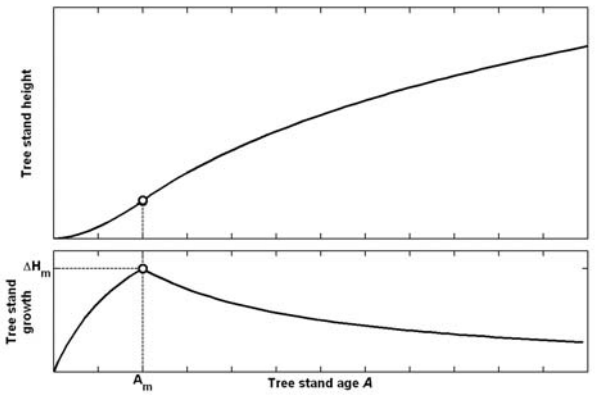

Fig. 1. Curve of tree stand height (above) and theoretical curve of tree stand height increment (below)

Relationship between ΔH_m and A_m

Two species of tree stands were analysed: a deciduous one (B type thinning beech) and a coniferous one (B type thinning spruce) – see Figure 2. All calculations were carried out on the basis of data on tree heights taken from the growth tables [12]. This means that data were referred to tangible tree stands with specific thinning techniques with similar intensity. Apart from the yield tables, the growth tables contain indisputable results of tree stand height measurements in experimental plots in the field. Such measurement results fulfil all requirements of empirical data. B type thinning describes the intensity of forest thinning that is the removal of growing trees carried out due to different criteria, for instance the tree height. It should be taken into consideration that the tree stand heights are in fact non-controversial in comparison to other features included in the yield tables. Moreover the average height of a tree stand is nearly independent of thinning intensity, but there is strong relation between the height and the size index [8]. One should remember that silvicultural practices have a direct influence on height growth benchmarks – if the lowest trees are thinned during the entire life of a tree stand, the average height of the tree stand is increased.

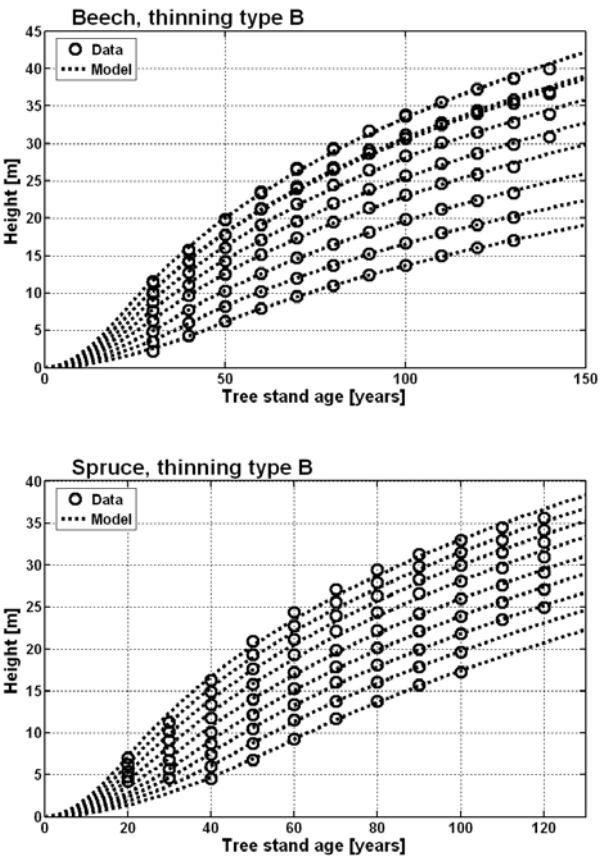

Fig. 2. Approximations of tree stand height by formula (2)

In the beginning, the pairs of parameters (A_m and ΔH_m) were estimated using the formula (2) for all stands growing benchmarks, separately for each species. The detailed results of approximation and the goodness of fit are presented in Table 1 and in Figure 2. The goodness of fit values for measured and estimated data prove that the tree stand dynamics are thoroughly expressed by Czarnowski's formula (2): (a) the variability of tree stand height is explained in almost 100% (parameter $100R^2$), (b) average estimation errors are usually lower than 0.5m, only in few cases for spruce stand errors are bigger, but still lower than 0.7m. The values of errors are bigger for the highest mature tree stand growing on the best sites, where accurate measurements of tree height are difficult.

The field-observed relationship between the maximum value of annual growth increment and the age of its occurrence is confirmed by the estimated pairs of parameters A_m and ΔH_m (Table 2) – the better the site index, the earlier the culmination point occurs. This relationship can be analytically expressed by the formula:

$$\Delta H_m = \frac{\alpha}{A_m - \beta} + \gamma \qquad (3)$$

where: ΔH_m – the maximum annual height increment [m], which takes place at the age of A_m [years], α, β, γ– coefficients to be calculated during the identification of the model equation. The results of identification of the formula (3) are presented in Table 2 and in Figure 3. The values of goodness of fit confirm that the form of equation (3) was correctly matched and, according to values of correlation coefficient R or $100R^2$, the variability of ΔH_m is explained in practically 100%. The standard deviation and the average error of estimation are so low that they can be simply omitted.

Conclusion

The empirical data from 19 height growth benchmarks representing all site quality indexes of two species: beech and spruce from experimental thinning plots were analysed in the paper. The field-noticeable relationship between the maximum value of an annual stand height increment and the age of its occurrence can be analytically expressed by the formula (3) with very high accuracy. The essential subject for the future research is to investigate the proper meaning of parameters α, β and γ from the biological point of view. On the other hand, the influence of the smoothing function (2) on parameters ΔH_m and A_m values should be also taken into consideration. Based on biological assumptions relationship between ΔH_m and A_m may allow to work out a formula to calculate a site quality class or annual biomass productivity from field measurements of tree stand height and age. Due to the type of considered data, the worked out function may be only applied to single-species and even-aged tree stands. It is also essential to investigate whether the presented relationship (3) may be used more generally and be applied to the uneven-aged tree stands [4].

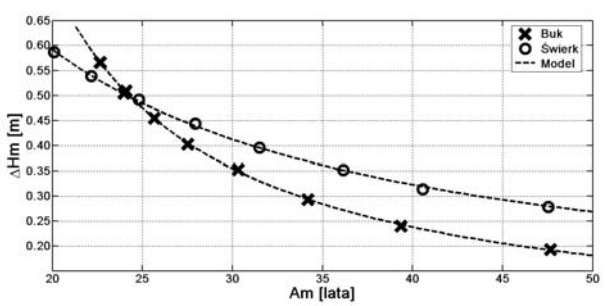

Figure 3. Relationship between ΔH_m and A_m

References

1. Assman E. (1968), Nauka o produkcyjności lasu. PWRiL, Warszawa.
2. Borowski M. (1974), Przyrost drzew i drzewostanów. PWRiL, Warszawa.
3. Czarnowski M. S. (1978), Zarys ekologii roślin lądowych. PWN, Warszawa.
4. Jaworski A., Szarawa J. (1981), Kształtowanie się wzrostu i przyrostu wysokości naturalnych odnowień jodły (Abies alba Mill.) na przykładzie wybranych powierzchni w lasach krynickich. *Acta Agr. Silv. ser. Silv.* 20, 17-40.
5. Peng Ch. (2000), Growth and yields models for uneven-aged stands: past, recent and future. *Forest Ecology and Management* 132, 259-279.
6. Richards F. J. (1959), A flexible growth function for empirical use. *Journal of Experimental Botany* 10, 290-300.
7. Suliński J. (1993), Modelowanie bilansu wodnego w wymianie między atmosferą, drzewostanem i gruntem przy użyciu kryteriów ekologicznych. *Zeszyty Naukowe AR Kraków*, Diss. 179.
8. Suliński J. (1997), Iloczyn maksymalnego rocznego przyrostu wysokości drzewostanu i wieku jego wystąpienia w świetle danych tabelarycznych. *Acta Agr. Silv. ser. Silv.* 55, 62-77.
9. Suliński J. (2007), Metoda obliczania rocznej produkcji biomasy w zbiorowisku leśnym w zależności od wysokości i wieku drzewostanu. *Acta Agr. Silv. ser. Silv.* 45, 89-119.
10. Sztencel I., Żelawski W. (1984), Modele matematyczne najczęściej stosowane w analizie wzrostu żywych organizmów. *Wiadomości Botaniczne* 28/3, 221-226.
11. Thurig E., Kaufmann E., Frisullo R., Bugmann H. (2005), Evaluation of the growth function of an empirical forest scenario model. *Forest Ecology and Management* 204, 51--66.
12. Tsoularis A., Wallace J. (2002), Analysis of logistic growth models. *Mathematical Bioscience* 179, 21-55.
13. Wiedemann E. (1957), Ertragstafeln wichtiger Holzarten bei verschiedener Durchforstung. Verlag M. u. H. Schaper, Hannover.
14. Zeide B. (1993), Analysis of Growth Equations, *Forest Science* 39/3, 594-616.

INSTRUCTION FOR AUTHORS

1. The original and one Photostat copy of the manuscript should be mailed to: Managing Editor Zdzisław Wisniowski. Authors are strongly urged to submit a CD containing the manuscript in Word for PCs format along with the hard copies. Articles already published or those under consideration for publication in other journals or periodicals should not be submitted.
2. Manuscripts should be in English. Usage of correct language is the responsibility of the author.
3. Submission of manuscripts to us implies that the copyright of the entire material except those already copyrighted by other publications like tables, figures etc and those permission the author(s) have already obtained, belongs to the publisher.

PRESENTATION

4. The text may be prepared from a good quality laser printer or electronic typewriter. It is to be typed (one side only) on a regular sheet of paper A4 size preferred with single line spacing. New Times Roman font of 12 point size is recommended. Authors are requested to paste figures and tables (if possible) at appropriate places in the text. If this is not possible, they may be given separately, in which case their exact locations in the text may be marked by pencil.
5. The article should begin with a short ABSTRACT followed by a short INTRODUCTION. The rest of the article ma be titled and arranged as per the wishes of the author.
6. REFERENCES should continue the last section of the article. In the text, references to other papers or books should be cited using consecutive numbers in parenthesis (e.g. [1,2]) and they should be listed numerically in the last section.

   Examples:

   I. Pyrczak W., Sarapata K.: Instructions for authors: references. Bio-Alghoritms and Med-Systems, 1, 386, 2005

   II. Tadeusiewicz R., Ogiela M.R.: Medical Image Understanding Technology. Springer Verlag, Heidelberg 2004

   Authors are to make sure that each reference appearing in the text appears in the list of references at the end and vice versa.
7. TITLE PAGE AND FIRST PAGE – The title page of the manuscript, the name(s) of author(s) and institution(s) where the work has been carried out should be typed out on a separate sheet of paper.
8. Section headings (ABSTRACT, INTRODUCTION etc.) are to be typed in upper case letters and placed on a separate line

1. Scientific names should be typed in italics or underlined
2. Tables should be numbered consecutively using Arabic numerals.
3. Illustrations should be limited to materials essential for the text. All figures should be numbered consecutively and should be submitted as sharp, high-quality prints. Figures that are to appear as a group should be photographed and mounted together. All figures and groups of figures should be trimmed at right angles and pasted directly on the typescript in the appropriate places. They should be of a size permitting photographic reduction by 25% together with text (not more than 15 cm across for page width and not higher than 20 cm). Legends to figures should appear directly below the respective figures.
4. In line drawings, all lines should be of uniform thickness; letters and numbers should be of professional quality and proper dimensions, approximately 1mm high when reproduced.
5. RUNNING TITLE – Please make sure to mention the running title (short title) of the article separately in the first page where the title, names of authors, their affiliations, etc. are given.
6. PREFFERED LENGTH – The length of the manuscript may be limited to 20-25 A4 size pages (20 cm width – 26 cms height) through this is not binding.
7. PERMISSION – Authors must obtain permission from other publishers if they use already published and copywrighted materials.
8. COLOUR FIGURES – Cost of printing color figures will be charged to the author at the rate of U.S. $ 125 per plate of four color pages.
9. REPRINTS – The order for reprints should be placed at the time of submission of the article itself, so that it may be out for printing without loss of time, if found suitable for order for not less than 100 reprints is to be made.

MANUSCRIPT SUBMISSION:

1. Electronic – the www.bams.cm-uj.krakow.pl address is available for all authors to submit manuscript. The instruction is available at each step of submission process.
2. The pdf or doc file with figures and tables incorporated into the manuscript body can be sent by email – address: bams@cm-uj.krakow.pl

www.akademicka.pl

ISSN 1895-9091